

ABSTRACT

Title of Dissertation: Quantitative Materials Contrast at High Spatial Resolution With a Novel Near-Field Scanning Microwave Microscope

Atif Imtiaz, Doctor of Philosophy, 2005

Dissertation directed by: Professor Steven M. Anlage
Department of Physics

A novel Near-Field Scanning Microwave Microscope (NSMM) has been developed where a Scanning Tunneling Microscope (STM) is used for tip-to-sample distance control. The technique is non-contact and non-destructive. The same tip is used for both STM and NSMM, and STM helps maintain the tip-to-sample distance at a nominal height of 1 nm.

Due to this very small tip-to-sample separation, the contribution to the microwave signals due to evanescent (non-propagating) waves cannot be ignored. I describe different evanescent wave models developed so far to understand the complex tip-to-sample interaction at microwave frequencies. Propagating wave models are also discussed, since they are still required to

understand some aspects of the tip-to-sample interaction. Numerical modeling is also discussed for these problems.

I demonstrate the sensitivity of this novel microscope to materials property contrast. The materials contrast is shown in spatial variations on the surface of metal thin films, Boron-doped Semiconductor and Colossal Magneto-Resistive (CMR) thin films. The height dependence of the contrast shows sensitivity to nano-meter sized features when the tip-to-sample separation is below 100 nm. By adding a cone of height 4 nm to the tip, I am able to explain a 300 kHz deviation observed in the frequency shift signal, when tip-to-sample separation is less than 10 nm. In the absence of the cone, the frequency shift signal should continue to show the logarithmic behavior as a function of height.

I demonstrate sub-micron spatial resolution with this novel microscope, both in tip-to-sample capacitance C_x and materials contrast in sheet resistance R_x . The spatial resolution in C_x is demonstrated to be at-least 2.5 nm on CMR thin films. The spatial resolution in R_x is shown to be sub-micron by measuring a variably Boron-doped Silicon sample which was prepared using the Focus Ion Beam (FIB) technique.

QUANTITATIVE MATERIALS CONTRAST
AT HIGH SPATIAL RESOLUTION WITH A
NOVEL NEAR-FIELD SCANNING
MICROWAVE MICROSCOPE

by

Atif Imtiaz

Dissertation submitted to the Faculty of the Graduate School of the
University of Maryland, College Park in partial fulfillment
of the requirements for the degree of
Doctor of Philosophy
2005

Advisory Committee:

Professor Steven M. Anlage, Chair/Advisor

Professor James R. Anderson

Professor Richard L. Greene

Professor Ichiro Takeuchi

Professor Frederick C. Wellstood

©Copyright by

Atif Imtiaz

2005

DEDICATION

“...My Lord! Bestow (on my parents) Your mercy as they did bringing me up.” [Al-Quran]

To my parents

ACKNOWLEDGMENTS

I begin in the name of Allah, the Beneficent and the Merciful. First of all, I thank the Lord, the Creator and the Sustainer of the universe, Allah (the Supreme) who granted me the opportunity to work on this project. I also thank Allah (the Supreme) for granting me a strong motivation towards science and technology. This motivation came while studying Quran during my teenager years, which in general encourages the human to study the creation and understand the fact that “...*Allah did not create this but in truth (for a purpose)...*” [Chapter 10: Verse 5].

Islam teaches me to thank all those people who benefit me. In this spirit, I would like to acknowledge my dissertation committee for taking interest in my research and providing me with valuable feedback to improve my thesis. I would like to give special thanks to Dr. Steven M. Anlage for his strong and diligent leadership over the course of my graduate life. I love the dynamic and determined environment that Dr. Anlage maintains in his laboratories.

I would like to thank Dr. Andrew R. Schwartz and Dr. Vladimir V. Talanov at Neocera for collaboration and many illuminating discussions. Their critical view on my work has been very important for me to develop into a professional scientist. It is with the help of these two scientists, that many barriers were overcome in modeling the microscope.

I would like to thank all my fellow students that I worked with in Dr. Anlage's laboratory. I thank Gus Vlahacos, David Steinhauer and Sheng-Chiang Lee with helpful discussions when I started the experiment. I thank Mike Ricci, Dragos Mircea, Sameer Hemmady, Yi Qi and Nathan Orloff for many good discussions on different physics problems. I thank Greg Ruchti, Marc Pollak and Akshat Prasad for help with numerical simulations.

I would like to thank Todd Brintlinger and Tarek Ghanem in Dr. Fuhrer's group as well. Todd helped me prepare many carbon nano-tube samples and I had many good discussions on physics and related issues with Tarek.

I would like to also thank Dr. John Melngailis, Dr. Andrei Stanishevsky and John Barry for helping with Focus Ion Beam technique to prepare different samples. Dr. Amlan Biswas, Dr. Eric Li and Todd Brintlinger helped me with preparing many samples for different experiments as well. Special thanks to Doug Bensen and Brian Straughn for help in many technical issues of machining and computing. I would like to thank Jane Hensing for her help with all the paper work over the years.

Last but not least, I would like to thank my parents, all my relatives and friends who are sharing with me the joy of completing my Ph.D. degree in physics.

TABLE OF CONTENTS

List of Tables	viii
List of Figure.....	ix
 Chapter 1 Introduction to Near-Field Microwave Microscopy.....	 1
1.1 Basic idea of near-field measurement	4
1.2 The novel microwave microscopy technique	10
1.3 Other ac-STM microscopes.....	17
1.4 Outline of the dissertation	22
 Chapter 2 Development of the Integrated STM and Microwave Microscope.....	 25
2.1 Introduction.....	25
2.2 Description of Scanning Tunneling Microscope (STM).....	26
2.3 Description of the Near-Field Scanning Microwave Microscope (NSMM) .	48
2.4 The geometry of the tips.....	62
 Chapter 3 Modeling of the novel Near-Field Microwave Microscope	 72
3.1 Introduction.....	72
3.2 Propagating waves or circuit models	72
3.3 Evanescent (non-propagating) waves	91
3.4 Numerical Simulations	115

3.5 Conclusions from different models of NSMM.....	122
Chapter 4 Contrast of Near-Field Microwave Signals	124
4.1 Introduction.....	124
4.2 Height dependant contrast of Δf and Q	125
4.3 Spatial (lateral) contrast of Δf and Q	140
4.4 Conclusion	144
Chapter 5 Imaging of sheet resistance (R_x) contrast with the NSMM.....	146
5.1 Introduction.....	146
5.2 The preparation of sample with FIB (Focus Ion Beam) technique.....	147
5.3 Scanning Tunneling Microscopy of FIB Boron doped Silicon sample	152
5.4 NSMM data on FIB Boron doped Silicon sample.....	153
Chapter 6 Imaging of local contrast in a correlated electron system	161
6.1 Introduction.....	161
6.2 Colossal Magneto-Resistive (CMR) thin $\text{La}_{0.67}\text{Ca}_{0.33}\text{MnO}_3$ film.....	161
6.3 Simultaneous STM and NSMM imaging	164
6.4 Conclusion	171
Chapter 7 Conclusions and Future Directions	173
7.1 Conclusions.....	173
7.2 The future directions with NSMM models	174

7.3 The future directions with NSMM experiments	175
Appendix A Few Issues in relation to the Scanning Tunneling Microscopy (STM)	177
A.1 Nominal height of tip above sample during tunneling	177
A.2 Effects of tip geometry on topography	179
Appendix B Determination of Microscope Q	182
B.1 Theory	182
B.2 Experimental Procedure	187
B.3 An example of calculation from the file Q cal.nb	191
Appendix C Other Attempted Projects	193
C.1 Carbon Nano Tube samples	193
C.2 Field-Effect CMR sample	198
C.3 Variable thickness sample prepared by the Focused Ion Beam technique ...	201
C.4 The $\text{CaCu}_3\text{Ti}_4\text{O}_{12}$ (CCTO) thin film sample	206
C.5 Superconducting thin films	208
Appendix D Fourier Transform of Surface Magnetic Field	210
Glossary	213
Bibliography	215

LIST OF TABLES

Table 1.1: Summary of key accomplishments in near-field microwave microscopy.	3
Table 1.2: Summary of key accomplishments of the University of Maryland group in near-field microwave microscopy.	11
Table 2.1: Summary of STM tip study (Δf contrast).	68
Table 2.2: Summary of STM tip study (geometry).	69
Table 5.1: Fit parameters for FIB Boron-doped Silicon sample.	157

LIST OF FIGURES

Fig. 1.1: Schematic of a Fourier optics calculation geometry.	6
Fig. 1.2: Sample as a boundary condition to the resonator.	13
Fig. 1.3: A sharp STM tip as a tool to confine the electric field.	14
Fig. 1.4: Transmission line and STM tip shown as a Fourier Optics source plane.	15
Fig. 1.5: Overview of the integrated STM-assisted near-field microwave microscope.	16
Fig. 1.6: The schematic for the ac-STM technique in transmission measurement.	18
Fig. 1.7: The schematic of ac-STM with resonant cavity.	19
Fig.1.8: Schematic for laser driven ac-STM.	21
Fig. 2.1: Schematic of tunnel barrier between tip and sample.	28
Fig. 2.2: A typical STM tunnel junction with tip and sample.	29
Fig. 2.3: Schematic of a Scanning Tunneling Microscope.	31
Fig. 2.4: Schematic of the STM head.	32
Fig. 2.5: Pictures of the STM head assembly.	32
Fig. 2.6: Picture of the blue head of the cryo-SXM probe.	33
Fig. 2.7: Sample puck.	35

Fig. 2.8: The schematic of STM data acquisition and control.	37
Fig. 2.9: Photographs of the TOPS3 box.	38
Fig. 2.10: Screen shot of the TOPS3 software.	40
Fig. 2.11: Schematic for the cross section of the Oxford cryostat.	42
Fig. 2.12: The Oxford cryostat shown covered with acoustic isolation.	43
Fig. 2.13: The new cooling cryostat from Kadel.	45
Fig. 2.14: Picture of experimental setup with the Kadel cryostat.	46
Fig. 2.15: The schematic (cross-sectional view) of the vibration isolation setups.	47
Fig. 2.16: The experimental setup (NSMM).	49, 50
Fig. 2.17: Schematic of NSMM amplifying all key components.	53
Fig. 2.18: Calculated $ S_{11} $ versus frequency.	55
Fig. 2.19: The concept of Δf and Q measurement.	57
Fig. 2.20: Schematic diagram of the integrated STM/NSMM.	61
Fig. 2.21: Schematic of tip-to-sample interaction.	63
Fig. 2.22: Tips investigated for use in NSMM/STM microscope (x 10).	65
Fig. 2.23: Tips investigated for use in NSMM/STM microscope (x 40).	66
Fig. 2.24: The SEM pictures for the tips.	67

Fig. 2.25: The embedded sphere illustration for two particular tips.	70
Fig. 2.26: A small feature sticking off of a tip.	71
Fig. 3.1: The circuit diagram of the lumped element model.	74
Fig. 3.2: Behavior of Q and Δf based on lumped element model.	77
Fig. 3.3: The circuit diagram of the transmission line model.	80
Fig. 3.4: The details of the resonator part of transmission line model.	81
Fig. 3.5: Behavior of Q and Δf based on transmission line model.	85
Fig. 3.6: Schematic for the multi-layered structure used in measurement.	87
Fig. 3.7: The measured impedance Z'_{film} versus R_x for thin resistive film.	90
Fig. 3.8: Schematic of the air-conductor boundary for evanescent wave model.	92
Fig. 3.9: The sphere above the plane geometry for evanescent wave model.	95
Fig. 3.10: Image charge method for calculating static electric field.	96
Fig. 3.11: Schematic of electric and magnetic fields due to sphere above infinite plane.	98
Fig. 3.12: Plot of surface electric field magnitude versus radial distance.	99
Fig. 3.13: Plot of surface magnetic field magnitude versus radial distance.	100
Fig. 3.14: Plot of absolute value of the surface magnetic field as a function k_{0r} .	103
Fig. 3.15: Plot of dissipated power in a metallic sample as a function of height.	105

Fig. 3.16: Plot of stored energy in the sample as a function of height.	106
Fig. 3.17: Plot of calculated Q as a function of height.	107
Fig. 3.18: Plot of the calculated magnitude of $\Delta f/f_0$ as a function of height.	109
Fig. 3.19: Plot of the calculated frequency shift as a function of height.	110
Fig.3.20: Logarithmic behavior of the capacitance from the image charge method.	111
Fig. 3.21: Schematic for the calculation of reflection and transmission of plane waves from stratified media.	113
Fig.3.22: CAD drawing of a sphere above a conducting plane in M2D.	117
Fig. 3.23: Numerical calculation of the sphere-to-plane capacitance as a function of height from M2D.	118
Fig. 3.24: Comparison of analytical to numerical models for capacitance of sphere above the plane model.	119
Fig. 3.25: Calculation of the sphere-to-sample capacitance vs. inverse box size in the M2D calculation.	120
Fig. 3.26: Capacitance versus height for the conical tip.	122
Fig. 4.1: Frequency shift contrast above a gold on mica thin film measured with the NSMM.	127
Fig. 4.2: Δf signal over bulk copper at room temperature.	128

Fig.4.3: Magnitude of the Δf signal with different tips over bulk copper as a function of embedded sphere radius r_{sphere} .	130
Fig. 4.4: Q versus height above the bulk copper sample for selected tips.	131
Fig. 4.5: Measured frequency shift versus height $\Delta f(h)$ ramps for a 200 nm thick gold on glass thin film sample.	132
Fig. 4.6: Schematic of the Neocera doped Silicon sample.	134
Fig. 4.7: AFM step data between the un-doped Silicon and the doped Silicon.	135
Fig. 4.8: Unloaded Q versus height for a Boron doped Silicon sample at 7.67 GHz.	136
Fig. 4.9: Measured $\Delta f(h)$ for the Boron-doped Silicon sample.	138
Fig. 4.10: Saturation of the Δf signal in last 100nm.	139
Fig. 4.11: Simultaneous imaging of a thin gold film on mica substrate.	141
Fig. 4.12: Schematic of the changes in capacitance for tip-sample interaction.	142
Fig. 4.13: Simultaneously acquired images of STM, Q and Δf for Boron-doped Silicon sample.	143
Fig. 4.14: Topography due to the p-n junction effect versus sample bias.	144
Fig. 5.1: Room temperature resistivity versus concentration for Phosphorous and Boron dopants in Silicon.	148
Fig. 5.2: Schematic of the variably Boron doped Silicon sample, based on the “write” file for FIB setup.	149

Fig. 5.3: Nominal room temperature sheet resistance (R_x) versus position for variable R_x Boron-doped Silicon sample.	151
Fig. 5.4: STM topography image of variable R_x Boron-doped Silicon sample at room temperature and 7.47 GHz.	153
Fig. 5.5: NSMM V_{2f} (proportional to Q) and Δf images of FIB Boron doped sample.	154
Fig. 5.6: Lumped element model for the Boron-doped Silicon sample.	155
Fig. 5.7: Fit of the lumped element model to the data at different frequencies for the Boron-doped Silicon sample.	157
Fig. 5.8: Fit to the Q'/Q_0 data from the lumped element model for Boron-doped Silicon sample.	159
Fig. 6.1: Resistance versus temperature of a thin $\text{La}_{0.67}\text{Ca}_{0.33}\text{MnO}_3$ thin film.	162
Fig. 6.2: Schematic atomic positions for the lattice mismatch at the interface between the LCMO film and the LAO substrate.	163
Fig. 6.3: Schematic of thin $\text{La}_{0.67}\text{Ca}_{0.33}\text{MnO}_3$ thin film.	164
Fig. 6.4: Simultaneous image data for the thin $\text{La}_{0.67}\text{Ca}_{0.33}\text{MnO}_3$ film above T_C .	165
Fig. 6.5: Simultaneously acquired data below T_C .	166
Fig. 6.6: Calculated R_x map from the $\text{La}_{0.67}\text{Ca}_{0.33}\text{MnO}_3$ film data.	167
Fig. 6.7: Simultaneous images on a single grain of thin $\text{La}_{0.67}\text{Ca}_{0.33}\text{MnO}_3$ film.	169
Fig. 6.8: Line cuts of the three data sets taken from the data shown in Fig. 6.7.	170

Fig. 6.9: STM image and calculated R_x map based of an interesting feature.	171
Fig. 7.1: Small Hertzian dipole near the interface of two materials.	175
Fig. A.1: Tunnel current ($\text{Ln}(I_{\text{tunnel}}(\text{nA}))$) versus Z position for an STM tunnel junction between a Pt/Ir tip and Au/mica thin film sample.	178
Fig. A.2: AFM image of the HD-750 Ni calibration sample.	180
Fig.A.3: STM topography images taken with three different tips on the Ni calibration standard sample.	181
Fig. B.1: Circuit diagram for the parallel RLC circuit and the measurement port.	183
Fig. B.2: Measured $ S_{11} $ versus frequency for a single resonance around 7.625 GHz.	187
Fig. B.3: Diode output voltage V_{diode} versus input microwave power measured for an HP8473C diode detector.	189
Fig. B.4: Polynomial fit to microwave source power versus V_{diode} for 7.67 GHz.	190
Fig. B.5: Raw data measured for the background and a single resonance.	191
Fig. B.6: Mathematica code to show an example calculation.	192
Fig. C.1: AFM image and the STM image of a CNT sample on Silicon.	195
Fig. C.2: STM of an interesting bundle that I found after scanning many different areas of a CNT sample spun on to a Au/glass substrate.	196
Fig. C.3: Simultaneous imaging of a CNT bundle on Au/glass substrate in the square region shown in Fig. C.2.	196

Fig. C.4: Simultaneous imaging of topography and frequency shift in a CNT bundle on Au/glass substrate.	197
Fig. C.5: Schematic of the electric field effect on the CMR sample.	199
Fig. C.6: Resistivity versus Temperature for a 1 mm x 1 mm LCMO/PZT/Nb:STO layer to see the electro-resistance effect.	200
Fig. C.7: Schematic of the variable thickness Cr/Silicon film sample.	202
Fig.C.8: AFM images of two of the features to show corrugation and damage on the surface.	203
Fig. C.9: STM of the Cr/Silicon sample prepared by FIB.	204
Fig.C.10: Scaled NSMM images of the Cr/Silicon FIB-modified sample.	205
Fig. C.11: STM of the $\text{CaCu}_3\text{Ti}_4\text{O}_{12}$ (CCTO) thin film.	207
Fig. C.12: Simultaneous imaging on top of one of the grains.	207
Fig. C.13: Room temperature STM and Δf images of MoGe.	209
Fig. C.14: Room temperature STM and Δf images of NbN.	209
Fig. D.1: Coordinate system used for the Fourier Transform calculation.	210

Chapter 1

Introduction to Near-Field Microwave Microscopy

Measurements of materials at microwave frequencies are important for both fundamental and applied physics. These measured quantities include the complex conductivity σ (measurement of σ is important for studying vortex dynamics and quasi-particle excitations in superconductors), dielectric permittivity ϵ (measurement of ϵ gives insight into polarization dynamics of insulators and ferroelectrics) and magnetic permeability μ (measurement of μ is needed to study ferromagnetic resonance and anti-resonance)¹. All these quantities are useful to know as a function of frequency. However, such materials properties of interest are rarely homogeneous, and the length scales of inhomogeneity can be on the millimeter to nano-meter length scale. These length scales are one to six orders of magnitude smaller than the free space wavelength of microwaves. Near-field experimental techniques have to be developed to probe materials with micron and sub-micron spatial resolution.

Near-field microwave microscopy has proven to be useful for extracting materials properties from a wide variety of condensed matter systems¹. For example, for answering questions from fundamental physics, such techniques have been useful for quantitative

imaging of dielectric permittivity, tunability, and ferroelectric polarization of thin dielectric films¹³. Other examples include measurement of the Hall Effect²¹ and dielectric constants of crystals^{19,20} and thin films^{22,23}. On the applications side, they have been used to study electromagnetic fields in the vicinity of active microwave devices⁴ and to perform dielectric metrology in semiconductor integrated circuits¹⁵. Table 1.1 shows recent key accomplishments from different groups working in the field of near-field microwave microscopy. The spatial resolution for the microscopes is at the micro-meter length scales, with some success towards sub-micron spatial resolution in dielectric thin films¹³.

Despite about a decade of research into the modern microwave microscope, there still remains a need to increase the spatial resolution and sensitivity to different materials parameters. One of the motivating factors for this need is the increasing activity at the nano-meter scale, both for basic physics and technology. Such activity involves the study of surfaces where quantities like ϵ , μ and σ (or equivalently resistivity ρ) need to be measured with nano-meter spatial resolution. For example, mixed phases in Colossal Magneto-Resistive (CMR) materials have charged ordered insulating and ferromagnetic metallic phases on nano-meter length scales⁷¹⁻⁷⁹. Such phases can be identified for a sample, by measuring its sheet resistance.

The novel microscope that I built for this thesis is an important development in response to these needs. Sections 1.1 and 1.2 discuss the motivation and construction of this novel

microscope in more detail. In section 1.1 I discuss the idea and importance of near-field measurements. In section 1.2, I discuss the idea behind the Maryland microwave microscope and the novel microwave microscope, which is the subject of this thesis.

Table 1.1: A few key accomplishments of near-field microwave microscopy from different groups around the world to show the breadth of its utility.

<u>Institution</u>	<u>Selected work</u>
Case Western Reserve University ¹⁶⁻¹⁸	Biological samples for local metabolism; expansion/contraction of p-n junction depletion region; imaging of defects in different materials
George Washington University ^{19,20}	Measured dielectric constant, loss tangent and topography in PbTiO ₃ crystal; dielectric anisotropy in Ba _{0.5} Sr _{0.5} TiO ₃ films
Hebrew University of Jerusalem ²¹	Local measurement of ordinary Hall effect in semiconducting wafers; extraordinary Hall effect in thin ferromagnetic Ni films.
Lawrence Berkeley National Laboratory ^{22,23}	Measured dielectric constant and loss tangent of library of doped thin films of (Ba _x Sr _{1-x})TiO ₃ and (Ba _{1-x-y} Sr _x Ca _y)TiO ₃ on LaAlO ₃ substrate
Neocera ¹⁵	Non-contact, non-destructive measurement of low-k (low ϵ_r) materials
Seoul National University ²⁴	Local electrical properties of epitaxial CaRuO ₃ thin films to study metal-insulator transition depending on growth and temperature.
Tohoku University ²⁵	Measurement of ferroelectric polarization parallel to the surface for LiNbO ₃
University of Maryland ¹⁻¹⁴	Details in Table 1.2

1.1 Basic idea of near-field measurement

To understand the basic idea of near-field measurements, I begin by briefly discussing a problem in scalar diffraction theory, otherwise known as Fourier Optics^{27,28}. The schematic of the problem is shown in Fig. 1.1. Ignoring the thin lens for now, the amplitude of the field (which can be electric field or magnetic field) is known and it is represented by $U(x, y, z = 0)$ in the source plane. The electro-magnetic fields can be represented by a scalar function if the problem at hand is two-dimensional (2D)³⁰ and can be expressed in terms of single dependent variables. In free space Maxwell's equations are:

$$\nabla \times \vec{E} = -\frac{\partial \vec{B}}{\partial t} \quad (1.1)$$

$$\nabla \times \vec{B} = -\frac{1}{c^2} \frac{\partial \vec{E}}{\partial t} \quad (1.2)$$

I will assume that the time dependence of two fields is $e^{-i\omega t}$. Then these equations become:

$$\nabla \times \vec{B} = -i \frac{\omega}{c^2} \vec{E} \quad (1.3a)$$

and
$$\nabla \times \vec{E} = i\omega \vec{B} \quad (1.3b)$$

In 2D, independent sets of two equations are obtained:

$$\frac{\partial E_z}{\partial y} = i\omega B_x \quad (1.4a)$$

$$\frac{\partial E_z}{\partial x} = -i\omega B_y \quad (1.4b)$$

$$\frac{\partial B_y}{\partial x} - \frac{\partial B_x}{\partial y} = -i\frac{\omega}{c^2} E_z \quad (1.4c)$$

$$\frac{\partial B_z}{\partial y} = -i\frac{\omega}{c^2} E_x \quad (1.5a)$$

$$\frac{\partial B_z}{\partial x} = i\frac{\omega}{c^2} E_y \quad (1.5b)$$

$$\frac{\partial E_y}{\partial x} - \frac{\partial E_x}{\partial y} = i\omega B_z \quad (1.5c)$$

It is important that equation (1.4) involves only B_x , B_y and E_z (called E-polarization³⁰) and equation (1.5) involves only E_x , E_y and B_z (called H-polarization³⁰).

For the case of H-polarization the complete field can be specified in terms of B_z and for the E-polarization case the complete field can be specified in terms of E_z . In both cases a 2D wave equation is satisfied. For example, in the case of E-polarization substituting for B_x and B_y in equation (1.4c) yields

$$\frac{\partial^2 E_z}{\partial x^2} + \frac{\partial^2 E_z}{\partial y^2} + k^2 E_z = 0 \quad (1.6)$$

where $k = \frac{\omega}{c}$. Notice that equation (1.6) only involves the component E_z . This allows us to represent an electromagnetic field as a scalar quantity U . To find the amplitude of the field $U(x, y, z)$ at a field point P , I note that U satisfies the wave equation $\nabla^2 U + k^2 U = 0$.

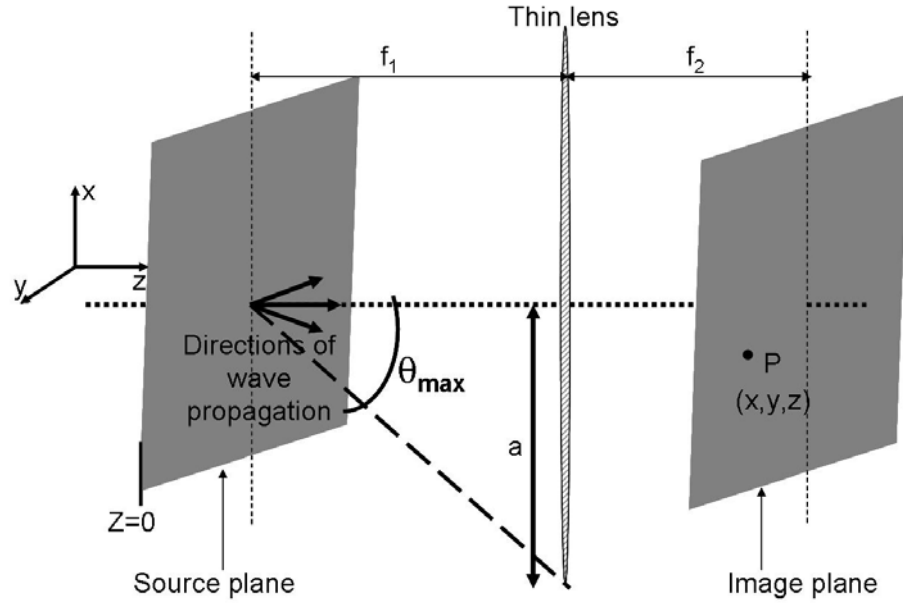


Fig.1.1: Schematic of a Fourier optics calculation geometry. In the source plane $z=0$, the amplitude of a scalar field $U(x,y,z=0)$ is known. The point P is located on the image plane. Fourier Optics allows us to find $U(x,y,z)$ at point P . The coordinate system is given to the left of plane $z=0$. Arrows with different directions are schematically showing different directions of wave propagation²⁸. The thin lens (radius a) should be considered when talking about image plane with point P is in the far-field.

To proceed, I use the concept of the Fourier Transform and assume that any arbitrary wavefront $U(x,y)$ can be written as an expansion of plane wave terms of varying amplitudes and

angles given by the angular spectrum, $A(k_x, k_y)$. Across the x-y plane the function U has a two-dimensional Fourier Transform given by,

$$A(k_x, k_y) = \int_{-\infty}^{+\infty} \int_{-\infty}^{+\infty} dx dy U(x, y, z=0) e^{-i(k_x x + k_y y)} \quad (1.7)$$

where $U(x, y, z=0)$ is the inverse Fourier Transform of $A(k_x, k_y)$:

$$U(x, y, z=0) = \frac{1}{(2\pi)^2} \int_{-\infty}^{+\infty} \int_{-\infty}^{+\infty} dk_x dk_y A(k_x, k_y) e^{i(k_x x + k_y y)} \quad (1.8)$$

where k_x and k_y are wave-vectors $2\pi/\lambda$ also called spatial frequency components in the language of Fourier Optics, and

$$k_x x + k_y y = \text{constant} \quad (1.9)$$

Notice that equation (1.9) is just a straight line for a given k_x and k_y . Physically equation (1.9) is just representing the condition of constant phase for a given wave front. As k_x and k_y vary, the slopes of these lines vary, and thus $A(k_x, k_y)$ involves plane waves that vary in direction. This is why $A(k_x, k_y)$ is called the angular spectrum²⁸.

When the wave equation $\nabla^2 U + k^2 U = 0$ is solved to find U at point P (where $z \neq 0$), the angular spectrum $A(k_x, k_y)$ comes out to be²⁸

$$A(k_x, k_y : z) = A(k_x, k_y) e^{ik_z z} \quad (1.10)$$

where

$$k_z = \sqrt{k^2 - k_x^2 - k_y^2} \quad (1.11)$$

When k_z is real, i.e. $k_x^2 + k_y^2 < k^2$, the solutions are propagating waves, and when k_z is pure imaginary, i.e. $k_x^2 + k_y^2 > k^2$, the solutions are decaying waves or evanescent waves. The latter condition is true when the contribution due to high spatial wave vectors (k_x , k_y) cannot be ignored, and these waves decay significantly within a distance equal to the free-space wavelength λ . In the far-field, contributions from these evanescent waves can be safely ignored. However, there are important contributions from evanescent waves in the near-field, especially when considering image formation.

It is worth remarking that the most well-known results about optical resolution are only valid in the far-field limit. For example, the famous Abbe's limit applies to far field imaging. In the far-field limit the image is only constructed from the propagating waves from the source, and this gives rise to a spatial resolution limit of about one half of a wavelength ($\lambda/2$). A simple way to understand why this limit exists, is to consider a thin lens (with radius a) placed between the source and the image plane (see Fig. 1.1). Here the distance between the thin lens and the source plane is f_1 . The largest angle which can be intercepted by the lens is $\sin(\theta_{\max}) = a/f_1$ and for paraxial angles it is simply $\theta_{\max} \approx a/f_1$. In the language of the Fourier Optics the largest spatial frequency component that can be imaged is θ_{\max}/λ or $a/(\lambda f_1)$. This corresponds to the smallest length $l_{\min} = (\lambda f_1)/a$ resolvable

at the image plane. For simplicity, let's choose f_1 such that it is equal to the focal length of the lens. In optics, the quantity $f/2a$ is called f-number²⁷ and for an ideal lens it is 1²⁹. For this ideal lens, we thus find $l_{\min} \approx \lambda/2$, which is Abbe's limit for the smallest object that can be resolved.

In the near-field limit, a spatial resolution much better than $\lambda/2$ can be achieved¹. The idea is that image is at least partly formed from evanescent (decaying) waves in the near-field of the source. In principle, in the near-field, a complex vector approach is needed to completely describe the fields²⁸. Still, the scalar diffraction theory gives the correct intuitive picture, yielding results which are adequate for many purposes²⁹.

Experimentally, utilizing evanescent waves for image construction requires several key steps. First, the probe must be brought close to the sample, in particular to a distance $h \ll \lambda$ (the free space wavelength). Second, the measurement probe must localize the fields on a small region of the sample, on the order of much less the wavelength λ of the incident radiation. For example, the earliest work on near-field microwave microscopy employed a small hole in the wall of a resonant cavity and then the sample was scanned underneath it³². A small amount of evanescent electromagnetic signal exits the cavity and locally interacts with the sample. The near-field approach does involve some trade-offs; the spatial resolution comes at the expense of having to scan point-by-point in order to construct an image.

1.2 A novel microwave microscopy technique

1.2.1 Transmission line resonator based microscopy

The original microwave microscope developed in our laboratory was an outgrowth of the Corbino reflectometry technique developed by James C. Booth²⁶. C. P. Vlahacos discovered that an open-ended transmission line resonator could be scanned (out of contact) over a sample and develop very interesting microwave contrast³. In the case of transmission line resonators, the center conductor acts as the field localizing feature. Such a microscope was invented and developed here in the CSR³. The schematic of the experiment will be discussed in detail in chapter 2.

Different versions of this microscope had been developed by different groups at different times to achieve specific goals. The key accomplishments of the Maryland group up to the turn of the century are summarized in Table 1.2. As is clear from the table, the microscopes have been used to examine a wide range of materials. Most of the measurement were done to answer questions of fundamental physics¹²⁻¹⁴, applied physics^{7,8,10,11} or to investigate the behavior of the microwave microscope itself^{2,3,5,6,9}.

Table 1.2: Key accomplishments of the University of Maryland group in near-field microscopy at the time of development of the novel STM-assisted microwave microscope, the subject of this thesis.

<u>Reference</u>	<u>Representative sample</u>	<u>Frequency (GHz)</u>	<u>Avg. Height of probe (μm)</u>	<u>Probe size (inner conduc- tor diameter in μm)</u>	<u>Spat- ial reso- lution (μm)</u>
Vlahacos ^{2,3} (1996)	Starrett 100-threads/in. steel rule	12	20	100	100
Anlage ⁴ (1997), Steinhauer ⁵ (1997)	Chromium thin film lines on glass	11.7 ⁴ , 10.7 ⁵	5	200	200
Steinhauer ⁶ (1998), Anlage ⁹ (1999)	Room Temperature R_x measurement of $\text{YBa}_2\text{Cu}_3\text{O}_{7-\delta}$ on 5cm sapphire wafer	7.5	50	500	500
Vlahacos ⁷ (1998)	US quarter dollar resolving 55nm in topography	9.5	30	480	480
Thanawalla ⁸ (1998); Hu ¹⁰ (1999)	77K measurement of normal component of electric field above $\text{Tl}_2\text{Ba}_2\text{CaCu}_2\text{O}_8$ (MgO substrate) micro-strip at fundamental tone, 2 nd harmonic and inter-modulation distortion	9.95 ⁸ and 8.2 ¹⁰	~250	200	200
Dutta ¹¹ (1999)	Vertical component of electric field for Cu micro-strip with vertical probe and horizontal component of electric field for Cu micro-strip with horizontal probe	8	25 vertical; 455 horizontal	200	200
Steinhauer ¹² (1999), Steinhauer ¹³ (2000)	Measurement and imaging of local (linear and non-linear) permittivity and tunability of 370nm $\text{Ba}_{0.6}\text{Sr}_{0.4}\text{TiO}_3$ on 70nm of $\text{La}_{0.95}\text{Sr}_{0.05}\text{CoO}_3$ on 500 μm LaAlO_3 substrate	7.2	touch	1 (STM tip)	1
Lee ¹⁴ (2000)	Local measurement (imaging) of magnetic permeability with loop probe of $\text{La}_{0.8}\text{Sr}_{0.2}\text{MnO}_3$ single crystal	6	10	200	200

The basic idea behind the design of the Maryland microscopes is to couple a coaxial cable through some impedance mismatch (typically a series decoupling capacitor) to a microwave source. The other end of the coaxial cable (the probe end) is left open, and this makes a half-wave resonator as shown in Fig. 1.2. The presence of a conducting sample in the near field of the open end changes the boundary condition at the probe end of the resonator (cable). The boundary condition changes from open to short circuit as the probe approaches the sample, and the resonator becomes a quarter-wave resonator, if shorted by the sample (see Fig 1.2). If one monitors the resonant frequency of the microscope, this change in boundary condition can be measured as the frequency shift (Δf) signal. Apart from the resonant frequency, the quality factor Q of the resonator can also be monitored as a function of probe height and position. The quality factor is given by

$$Q = \frac{\omega U_{stored}}{P_{dissipated}}, \quad (1.12)$$

where U_{stored} is the stored energy inside the resonator, $P_{dissipated}$ is the dissipated power inside the resonator and ω is 2π times the driving frequency. The presence of the sample will also affect the stored and dissipated energy inside the resonator. These changes can be measured by monitoring the quality factor (Q) of the resonator.

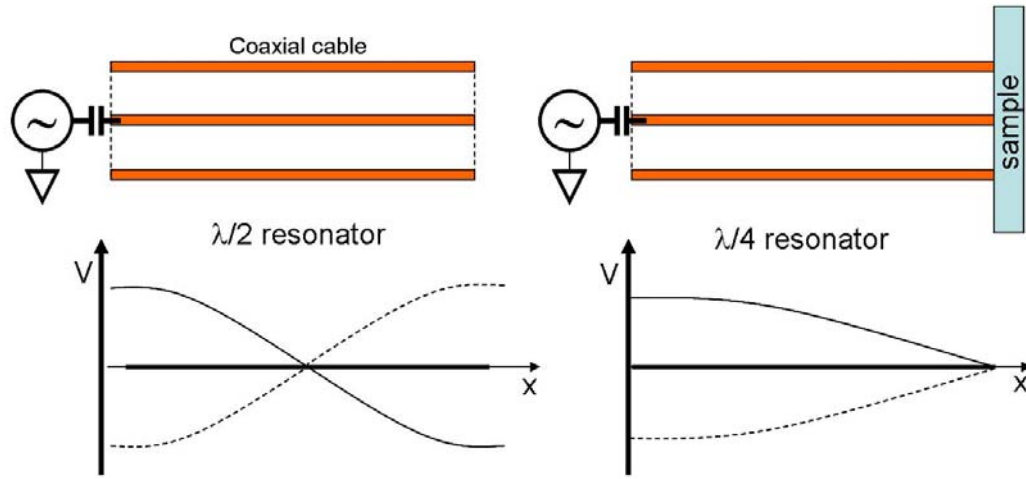


Fig 1.2: In the absence of a sample the resonator has open circuit boundary conditions on both ends and is a $\lambda/2$ resonator. The conducting sample shorts it on one end to produce a $\lambda/4$ resonator.

A similar situation occurs if an inductor is used as the impedance mismatch defining the transmission line resonator, or with an inductive probe (closed loop) at the end of the transmission line. As I mentioned earlier, I am interested in achieving contrast on micro-meter and nano-meter length scales. The size of the inner conductor of the transmission line resonator is one of the main factors that defines the spatial extent of the fields. A sharp object sticking out of the center conductor (like a sharp metal tip) can further reduce the spatial extent of the fields (This is schematically demonstrated in Fig.1.3). In particular, I used a sharp Scanning Tunneling Microscope (STM) tip to replace a small part of the inner conductor as shown in Fig. 1.3b.

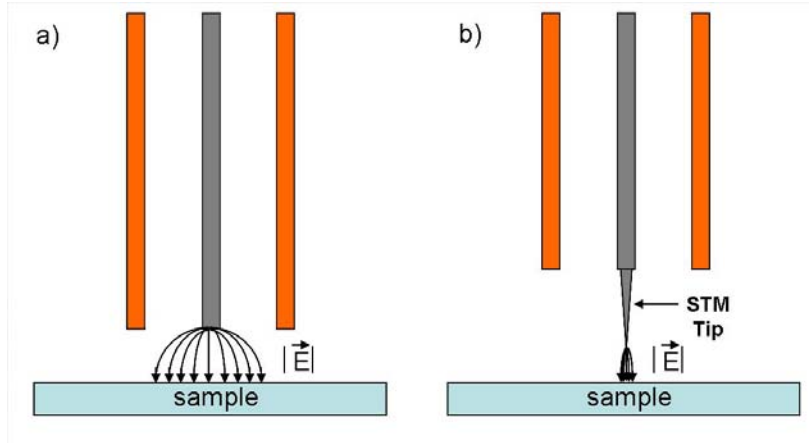


Fig 1.3: A sharp STM tip is added to the inner conductor of a coaxial cable resonator. a) shows the magnitude of Electric field spread between blunt inner conductor and metallic sample; b) shows improved field confinement due to the STM tip compared to a blunt inner conductor. In both cases the inner to outer conductor field lines, as well as the outer conductor to sample field lines, are ignored to make the point clear.

The second main factor in achieving nm scale spatial resolution is to reduce the height of the tip above the sample. In this way, it is possible to couple to high spatial frequency wave vectors due to evanescent waves. As the height of the tip above the sample is reduced, the contribution of evanescent waves increases (see Fig. 1.4). In order to increase the spatial resolution of the microscope over dielectric crystals and thin films, the STM tip could be made to touch the sample for measurement (no STM feedback circuit needs to be present for these experiments). However, touching the sample will make the sharp end blunt on the scale of $\sim 1\text{-}5\text{ }\mu\text{m}^3$. An improvement I made was to add an STM feedback circuit so that the tip can maintain a nominal height of 1 nm above the surface without getting damaged (see Appendix A).

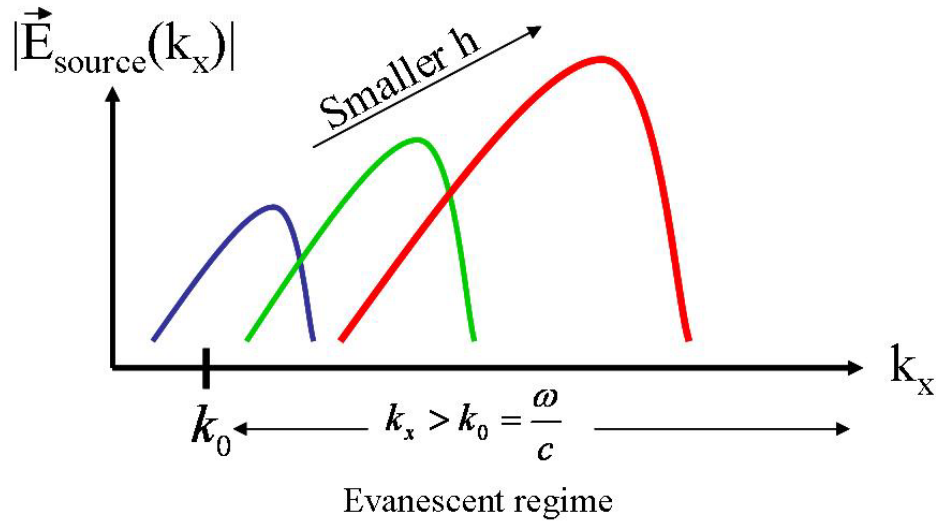
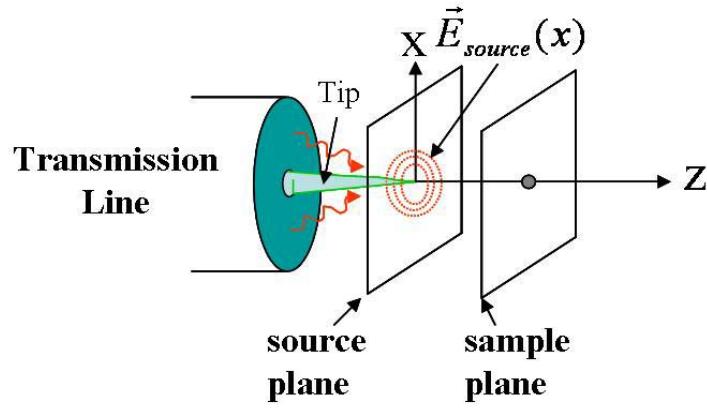


Fig. 1.4: Transmission line and STM tip shown as a Fourier Optics source plane. The graph shows schematically how the magnitude of the electric field Fourier component increases as the height h of the tip above the sample is reduced.

1.2.2 Integration of STM with the microwave microscope

In order to achieve nano-meter spatial resolution, it was necessary to bring the probe closer to the sample than ever accomplished before, and at the same time avoid damage to the tip. The step to take was to integrate the STM with the Near-Field Scanning Microwave Microscope (NSMM). On the one hand, the STM will maintain a very small height of nominally ~ 1 nm and on the other hand the sharp tip will not get damaged. I integrated the STM with the coaxial transmission line resonator based NSMM in order to build the novel microscope, as shown in the schematic in Fig. 1.5 (a more detailed schematic will be discussed in Chapter 2).

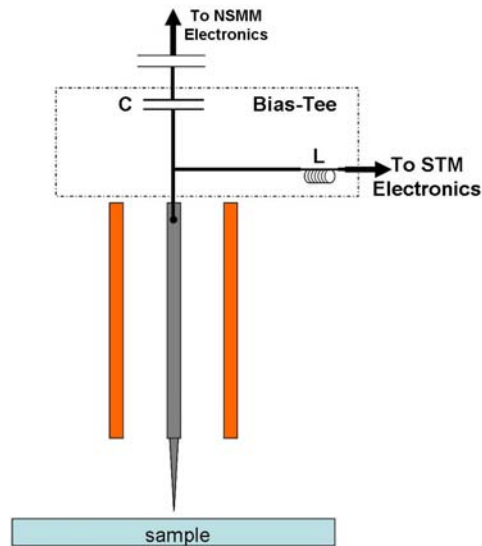


Fig. 1.5: General overview of the integrated STM-assisted near-field microwave microscope. A bias-Tee is added to the coaxial resonator to integrate the two microscopes. The inductor allows low frequency signals to pass to the STM electronics and damps out high frequency signals. The capacitor in the bias-Tee stops low frequency signals from interfering with NSMM electronics.

I used a bias-Tee to integrate the two microscopes. A bias-Tee has an inductor on one side to filter out high frequency signals and allow low frequency signals to pass (low-pass filter). There is a second port with a series capacitor which acts as a high pass filter. The inductor was connected on one side to the inner conductor of the coaxial transmission line resonator and on the other to the STM electronics. In this way a DC connection is established to perform STM. However the inductor will damp the ac microwave signal so that it doesn't interfere with STM operation. The capacitor of the bias-Tee just changes the effective decoupling capacitor since it is added in series with the decoupling capacitor, as shown in Fig. 1.5. In this way the sharp tip can be DC biased for performing STM and can simultaneously act as the field enhancing feature for the ac microwave signal.

1.3 Other ac-STM microscopes

The high spatial resolution and precise atomic scale height control of STM provides an excellent platform for doing ac measurements. Many attempts have been made to integrate STM with different ac measurement techniques. There have been many successes and some short-comings with these different attempts. First, many of these attempts lacked quantitative extraction of materials contrast and second they did not provide physical models to understand tip-sample interactions. There are three main categories in which I would divide the existing ac-STM techniques.

The first class integrates STM with near-field transmission measurements³⁴⁻³⁹. The concept of the experiment is shown in Fig. 1.5. In this case the substrate is illuminated with electromagnetic waves and a tip on the surface of the sample acts as the antenna and picks up and transmits the signal for measurement. The same tip is used to perform STM as well.

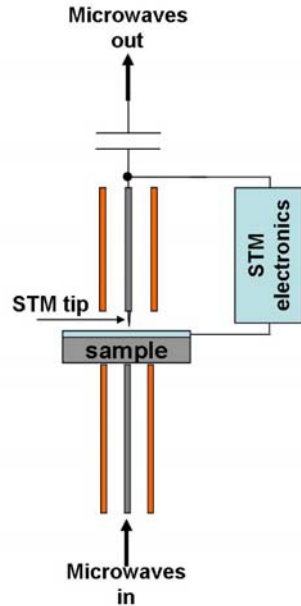


Fig 1.6: The schematic for the ac-STM technique in transmission measurement. The schematic is simplified for clarity (see references 31-39).

The major accomplishment here was in understanding the effect of surface topography on the complex transmission coefficient³⁹. The experiment was performed on a 7 nm thick Pt/Carbon film on a Si/SiO₂ substrate. There was a 2 nm deep depression in the Pt/C film and as the STM scanned across the depression, the frequency shift signal showed the same qualitative response as the topography. To show high resolution of such a microscope,

contrast due to mono-atomic steps on Cu(111) surface were imaged³⁷. This is a general problem in ac-STM microscopy techniques, that the materials contrast gets convolved with the topography of the sample. This requires that in order to understand the materials contrast due to microwave microscopy, samples should be prepared where materials contrast is topography independent, and I discuss one such sample in this thesis.

The second class integrates the STM with a resonant cavity⁴⁰⁻⁴⁴. The schematic is shown in Fig. 1.7. The sample is generally inside the resonant cavity and the tip (to perform STM) is brought into the cavity through a hole made on one of the cavity walls.

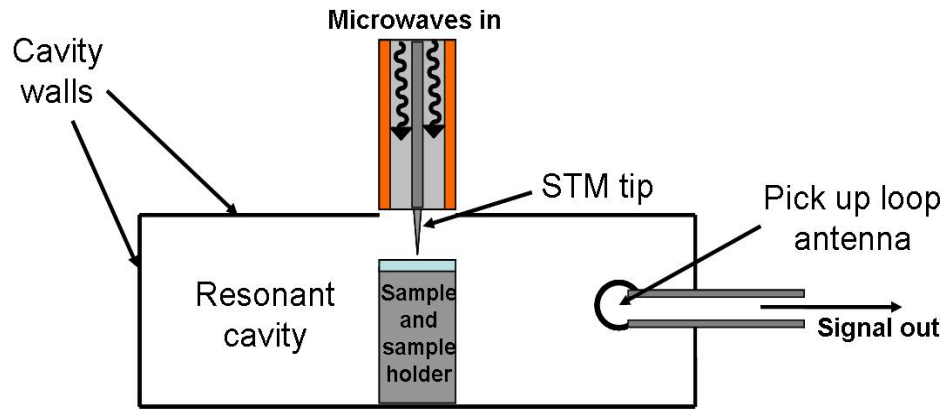


Fig. 1.7: The schematic of ac-STM with resonant cavity (the figure is not to scale). The pick-up loop antenna is placed at a location where the ac magnetic signal from a resonant mode of the cavity is maximum. The hole in the cavity for STM tip is generally much smaller compared to wavelength of incident microwaves.

Microwaves are injected locally in to the sample at a frequency that is resonant with the cavity. One can also send in microwave signals at a frequency that is exactly one half or one third of the resonant frequency of the cavity⁴³. Harmonics produced locally by the sample will then excite the cavity resonance. A loop antenna is set some where in the cavity where the magnetic field of the resonant mode is a maximum. Notable accomplishments are studies of different metal surfaces to show high resolution images of third harmonic signal. In one case self assembled mono-layers (made from a mixture of chemicals perflouroanonanoyl-2-mercahptoethylamide) on a gold surface were studied to show high z-resolution⁴¹ and in another a WSe₂ surface was studied to show high spatial resolution⁴⁴ in the third harmonic signal while simultaneously an STM topography image was also acquired.

The third class couples an STM tunnel junction with laser light⁴⁵⁻⁴⁹. The schematic is shown in Fig. 1.8. The tunnel junction is illuminated with two fine tuned frequencies. The non-linear IV characteristic of the tunnel junction is used to detect the rectification signal, the sum and difference frequencies. This technique can be used to detect higher harmonics as well.

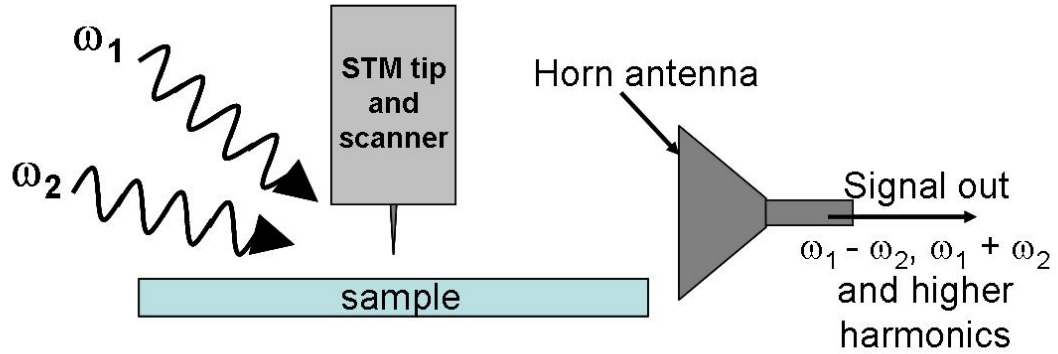


Fig.1.8: Schematic for laser driven ac-STM. The non-linear IV curve due to the tunnel junction between the tip and sample is used to generate the difference and sum frequencies. Higher harmonics can also be detected.

One notable experiment performed with such a setup is to simultaneously acquire the tunneling current and $\Delta\omega = \omega_1 - \omega_2$ signal over a graphite surface.⁴⁷ The $\Delta\omega$ signal was also used for distance control over the surface to construct a topography image. Another notable experiment (in which Scanning Force Microscope (SFM) was used) measured $\Delta\omega = \omega_1 - \omega_2$ on a pattern of small metal islands (gold) which was on top of a non-conducting BaF_2 substrate⁴⁸. A qualitative map of conductivity was made to distinguish between conducting and non-conducting regions.

In comparison to the above mentioned experiments, the main novel feature of my experiment lies in the fact that a transmission line resonator based microwave microscope is integrated with STM.

1.4 Outline of the dissertation

This dissertation presents quantitative measurements that I obtained with an STM-assisted transmission line resonator based near-field scanning microwave microscope. This discussion will be illuminated by models of the system.

In Chapter 2, I describe briefly the STM and NSMM as independent microscopes. Then I discuss the integration of the two microscopes, and the different components that constitute them. This chapter includes discussions of the electronics, the assembly of two microscopes, the cryogenic apparatus, and details on the metal tips that are used to detect both STM and NSMM signals.

In Chapter 3, I describe the different models that I used to understand the data from different samples. This chapter contains key ideas and predictions of these models. I note that earlier ac-STM techniques apparently did not make serious attempts to model to the data, rather they were generally satisfied with demonstrating the implementation of the technique. My experience suggests that more than one model is often needed to understand the STM-based NSMM. I also discuss future work needed to remove shortcomings in the current models.

Chapter 4 is geared towards understanding the height dependence of the Δf and Q data. The height dependent contrast in the last 2 μm before tunneling is the key quantity behind

materials contrast with high spatial resolution. In this chapter, I show that Δf and Q are both sensitive to the capacitance (C_x) between the tip and sample and the materials contrast (e.g. sheet resistance R_x) in the sample. However, within certain limits, we can make approximations that Δf is proportional to ΔC_x , and Q in this case is a measure of R_x .

In Chapter 5, the sheet resistance (R_x) contrast over a variably Boron doped Silicon sample is discussed. I designed this sample to achieve topography-free microwave contrast due to R_x . This sample helps us to understand the frequency dependence and R_x dependence of the Δf and Q data.

In Chapter 6, I discuss imaging of local resistance contrast in colossal magneto-resistive (CMR) thin films. In light of this data I draw conclusions regarding the high spatial resolution of my microscope. The spatial resolution is discussed in imaging of both C_x and R_x . In order to understand the data, the physics and microstructure of CMR materials is important, so these will be discussed as well. In chapter 7, I conclude and briefly discuss the future work needed both in relation to experiments and modeling.

Because I performed STM-assisted microwave microscopy on many new materials, there were many experiments that did not yield useful results. I learned much about the microscope from these measurements. Appendix C presents some of the projects that did not work out fully. I will mention a few samples and discuss the challenges that they posed

towards either STM or NSMM. The Appendix A discussed some of the issues in relation to STM. The Appendix B includes also includes the calibration procedure for the microscope as reference. The Appendix D contains details of calculations in relation to the Fourier Transformation performed in Chapter 3.

Chapter 2

Development of the Integrated STM and Microwave Microscope

2.1 Introduction

As mentioned in chapter 1, a unique feature of my experiment, compared to other Scanning Tunneling Microscope (STM)-assisted Near-Field Scanning Microwave Microscopes (NSMM), lies in the fact that a transmission line resonator based microwave microscope is used.

In order to build this novel microscope, the easiest way was to buy a commercially available STM and then make appropriate changes to integrate an NSMM. The major advantage of following this approach is saving the time required to design and build a cryogenic STM. The disadvantage is that I had to work around the design of an existing STM probe and electronics, and there were serious limitations to what I could build. Another challenge was the need to make repairs to the system, since Oxford Instruments stopped supporting this technology less than a year after I got the system.

2.2 Description of Scanning Tunneling Microscope (STM)

The commercially available STM that I used was a cryoSXM manufactured by Oxford Instruments. Their commercial package included an STM head assembly, electronics, software and a cryostat (see Fig. 2.4 and Fig. 2.5). The STM head assembly, probe arm, electronics and software combined together are called TOPSystem3 (TOPS3 for short). The Oxford cryostat has the ability to reach liquid Helium temperatures. The upper temperature limit of this cryostat is 300 K, limited by the windows of the cryostat had Indium seals, which could not sustain temperatures much above 300 K (see Fig 2.11). In this section, I give a description of the key features of the different components of the microscope after first briefly discussing the fundamental physics behind the STM.

2.2.1 The concept of a tunnel junction

Fundamental to STM operation is the tunneling of electrons through a vacuum barrier between two metals. For STM, the tunnel junction consists of a vacuum barrier between a conducting, geometrically sharp, probe tip and a conducting sample of interest. The geometrical sharpness of the probe tip is needed to achieve atomic resolution, the most celebrated feature of this microscope.

A simple way of looking at a tunnel junction would be to picture two metal electrodes brought in close vicinity to each other without touching⁵¹. If the electrodes were far apart,

then no DC current flows between them, even when small voltage is applied. However, when the separation between the electrodes is made small enough that the decaying wave function of free electrons in each metal can overlap, then electrons can tunnel from one electrode to the next. Under these conditions, applying a DC voltage bias across the electrodes establishes a constant and stable tunnel current between the two electrodes. The electrons will tunnel from one electrode to the other electrode⁵¹.

In the case of STM, one electrode is a sharp metal tip while the other is the sample. The sharp tip is what allows for high atomic resolution in scanning, since ideally the sharpest end of the tip has a single atom, which gets sufficiently close to the surface to establish tunneling and this tunnel current drops exponentially as a function of height above the sample (see Fig. 2.2). This sharp tip is scanned over the sample, and point by point the tunnel current can be measured. An alternative and popular way to run the microscope, is to add a feedback loop which maintains constant tunnel current during scanning (Fig. 2.3). The data is plotted as a 2D image, which is (in approximation) the topography of the surface as I explain below⁵².

In general, calculation of the tunnel current I_{tunnel} , with complete knowledge of 3D wave-functions for both tip and sample is a very formidable problem⁵². An elegant calculation and discussion (in 1D) was put forth by John Bardeen⁵³, in which time-dependent perturbation theory is used to calculate the current density j_{tunnel} , through the junction

between two electrodes. This formalism is used by Tersoff and Hamann to calculate I_{tunnel} between a conical tip (with spherical end and effective radius r_0) of a real solid surface (Au(110) surface)⁵⁴. The strength of this calculation is that it keeps essential elements of the physics

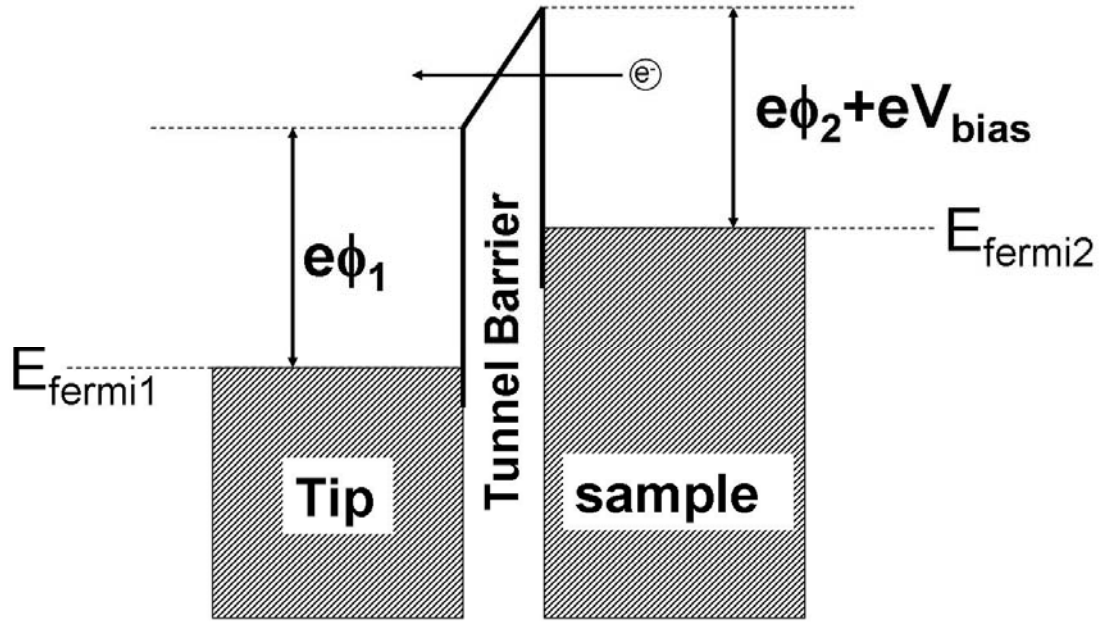


Figure 2.1: A tunnel barrier between a tip and sample from the energy perspective. The sample is one electrode and the tip is the other electrode. The $e\phi_1$ and $e\phi_2$ are the respective work functions for each metal electrode. In the convention of this diagram, electrons tunnel from sample to tip, which is depicted by an electron with an arrow.

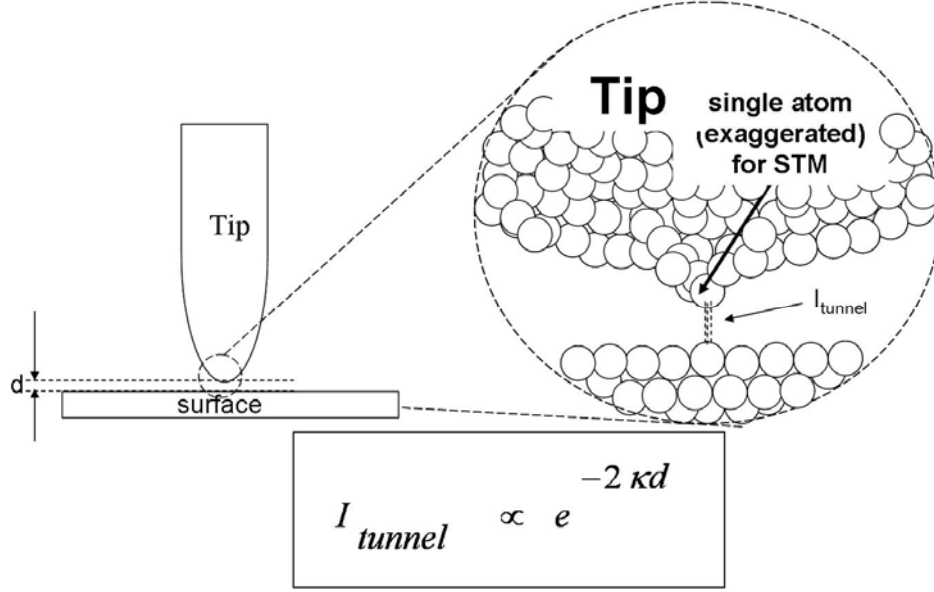


Fig. 2.2: Tip and surface are shown for a typical STM tunnel junction. The exaggerated single atom is responsible for tunneling, since this is the closest atom and the electron wave function falls off on the atomic length scale. The rest of the atoms are too far to tunnel due to the nature of exponentially decaying wave function in the barrier. The κ is material dependent (work function of metal) and is typically 1 \AA^{-1} (also see Appendix A).

of tunneling, while calculating the I_{tunnel} as a function of tip and sample properties⁵². The resulting equation for I_{tunnel} is:

$$I_{\text{tunnel}} \propto \int_{E_{\text{Fermi}}}^{E_{\text{Fermi}} + eV_{\text{bias}}} n_{\text{sample}}(E, r_0) dE \quad (2.1)$$

where $n_{\text{sample}}(E, r_0)$ is the density of states of the sample as a function of energy of the states evaluated at r_0 (center of curvature of the effective tip). The quantity n_{sample} evaluated at E_{Fermi} is called the Local Density of States (LDOS), and this quantity is what STM measures. I should remark that equation (2.1) is meaningful only in the low bias limit ($eV_{\text{bias}} \ll \phi$ (work function of electrodes used)). Under this approximation, in the case of a

sample with uniform LDOS (a metal is a good example), the scanned image under constant tunnel current can be viewed as a topography image, since I_{tunnel} is now being kept constant to maintain a constant gap between the tip and sample. This is assumed all throughout the thesis, for metals and semiconductors as well. The tunneling in semiconductors is quite complex⁵¹, and this makes the above assumption look very naïve. Since my goal is not atomic scale resolution with STM in semiconductors (my goal is understanding materials contrast with the NSMM), I can make this assumption safely to the first order⁵¹. However, pushing for very high (atomic) resolution with this setup requires that the details of energy band structure of semiconductors be kept to calculate n_{sample} .

The concept of an STM experiment is to bias one of the electrodes (say sample) and then monitor the tunnel current in series, as shown in Fig. 2.3. The same signal is sent to the STM electronics (which consists of data acquisition cards and feedback circuit). The feedback circuit helps maintain a constant tunnel current, even when the Piezo is being used to scan the sample in the plane perpendicular to the tip. The error signal (voltage applied to Piezo for z-motion) generated while maintaining a constant tunnel current is recorded as surface topography.

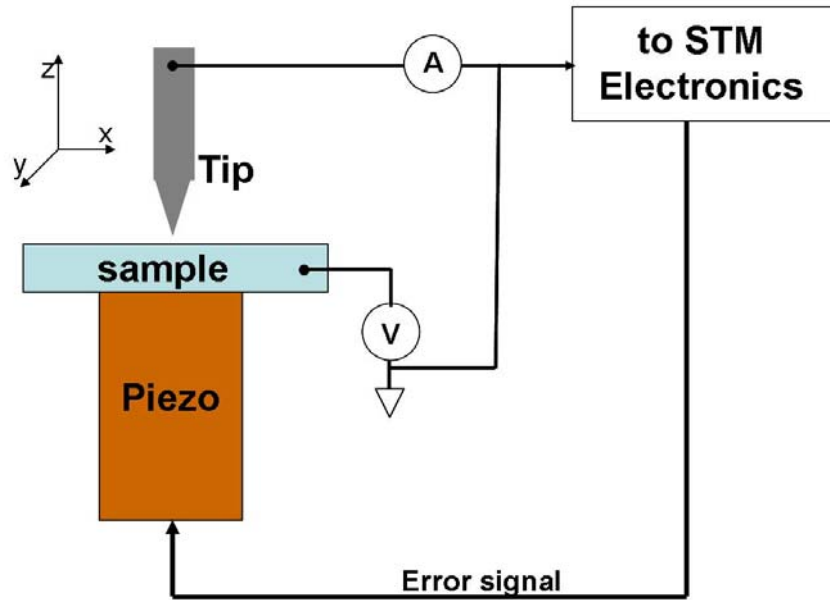


Fig 2.3: Simple schematic of a Scanning Tunneling Microscope. I have lumped the scanning electronics, data acquisition electronics and feedback circuit under the title “STM electronics” to keep the figure simple. The error signal contains the information from which surface topography is constructed after the scan is complete.

2.2.2 The STM probe arm and experimental stage

The experimental stage (head) of the STM is located at the end of a 36” probe arm, attached via what Oxford Instruments calls the ‘SXM mounting point’ (see Figs. 2.4 and 2.5). The other end of the arm has a “blue” head which serves two purposes (see Fig 2.6). The lower end of the “blue” head vacuum seals the whole probe with the help of a rubber O ring and metal clamp on top of the Variable Temperature Insert (VTI). The upper end of the “blue” head has another vacuum sealed plate (the connector plate or ‘CryoSXM top flange’) which accommodates all of the electronics connectors for both the STM experiment and the NSMM experiment, as shown in Fig. 2.6.

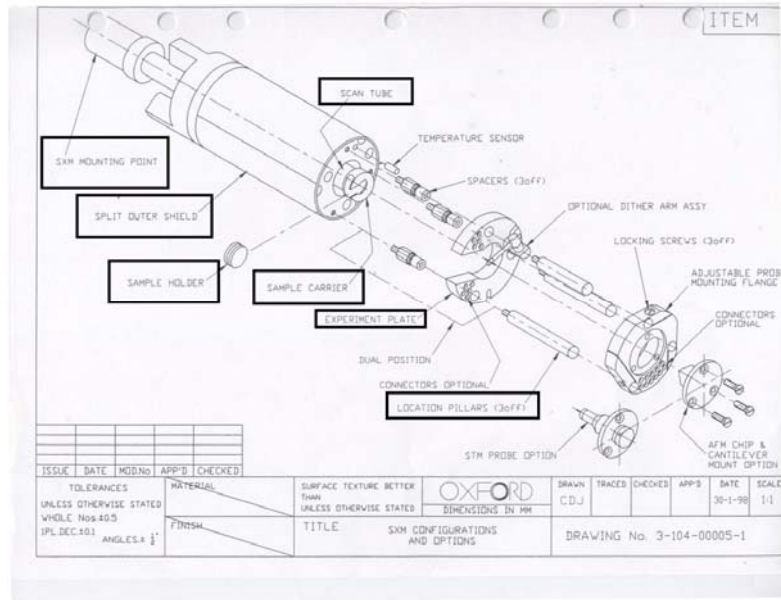


Figure 2.4: The schematic of the end of the STM head beyond the SXM mounting point. The names of important features are boxed for clarification.

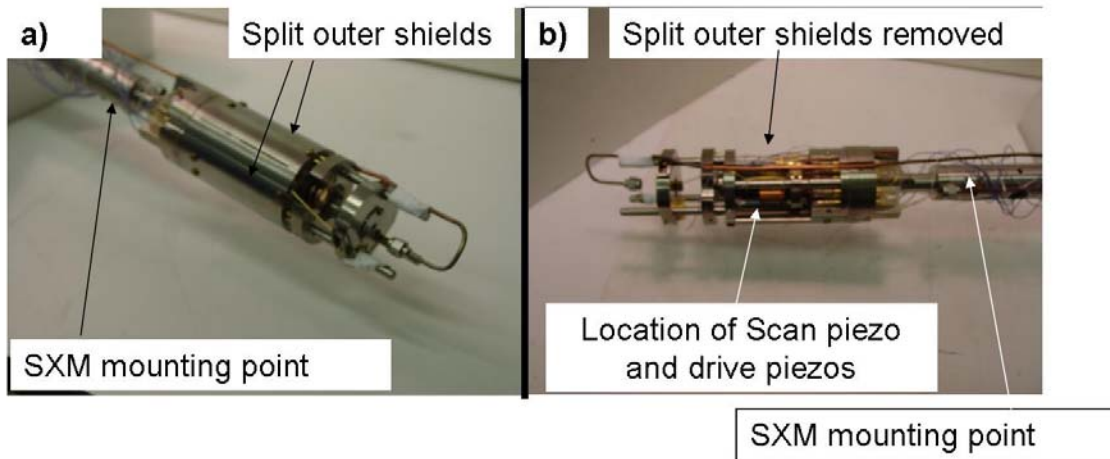


Fig 2.5: Pictures of the STM head assembly a) with the split outer shields, b) without the outer split shield to show location of piezos.

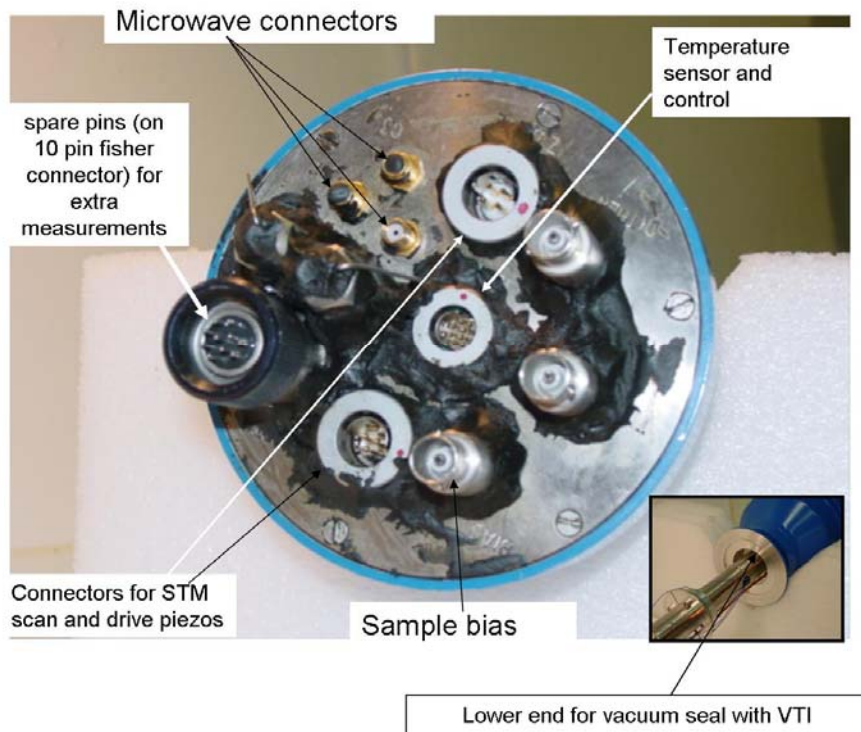


Fig 2.6: Picture of the blue head with the connectors on it. The inset shows the side which vacuum seals with the VTI. The black material is Apiezon high vacuum grease and is used to seal vacuum leaks.

The head of the STM has a hollowed cylindrical body, 49 mm in diameter and (4") ~100 mm long. The drive and scan piezos are inside this hollowed cylinder, which is covered with the help of two 'split outer shields' (Fig 2.5). The scan piezo has the 'sample carrier' attached to it, and this sample carrier holds the sample puck on which the sample sits during an experiment. During scanning it is the sample which moves and the tip remains stationary in this set up. There are three drive piezos which can move the scan stage (scan piezo and sample) forward and reverse. These are also located inside the hollowed cylinder,

behind the ‘split outer shields’. The DC bias for STM purposes is applied to the sample. The scan piezo has a maximum range of about 5 μm in the Z (direction along the length of the probe) and 50 μm in X and Y (all at room temperature). The range available for the scan stage to move is about 1.5 cm. From the 4” long cylindrical body, three metal rods (‘location pillars’) stick out and these rods support a base plate which contains the assembly to hold the STM tip (Fig. 2.4).

The sample carrier holds a spring-loaded copper piece, which is called a sample puck. The puck is a cylindrical copper piece which has a collar (a region of smaller cylindrical diameter) in the middle. One of the surfaces of the cylindrical puck has copper leaves attached to it and the sample is attached to the other surface (see Fig. 2.7). The collar and leaves together hold the puck with the sample in place in the puck holder. The leaves basically are there to provide an effective spring constant k_{spring} between the puck and the sample carrier.

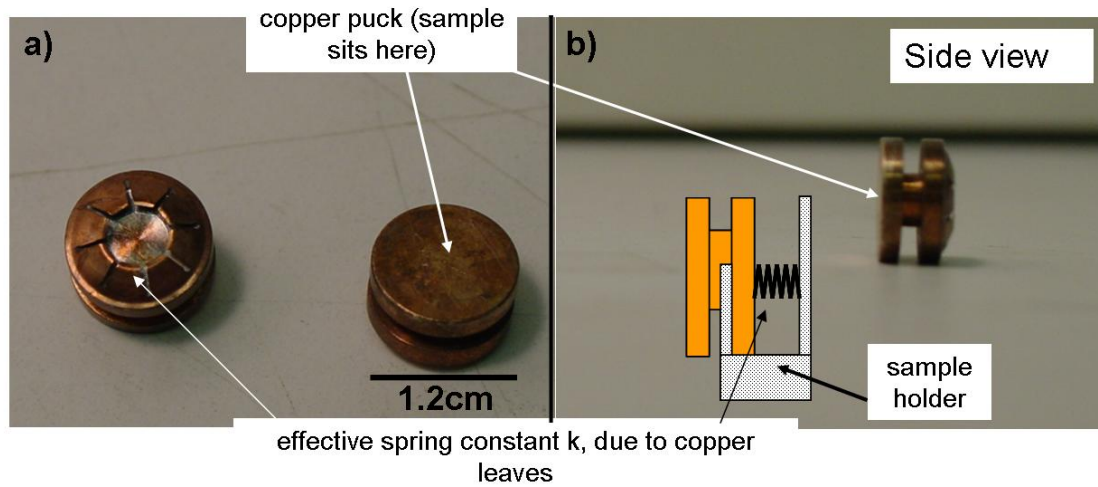


Figure 2.7: sample puck for mounting the sample a) the top view of spring side and the sample side b) side view of the puck and the schematic to clarify the spring effect for mounting the puck on the Oxford probe arm.

2.2.3 STM electronics and software

In the TOPS3, the hardware and software provide an interface to read the measured values and set different parameters for the STM experiment. For example, setting the tunnel current set point and monitoring the tunnel current can be done through the software. Similarly, setting the scan parameters (range, direction, speed, scan offset in X or Y direction), feedback parameters for constant tunnel current scanning, Z position of the scan piezo, data acquisition parameters (number of pixels/scan line, DC bias, external ac modulation) can be achieved using the software. Let me just remark here, that in the convention of the Oxford Instruments literature, Z is the direction perpendicular to the sample surface and X and Y are the directions in plane of the sample.

The software also allows data acquisition from other external experiment. This feature has been a major help, as it allowed me to acquire data from NSMM simultaneously with the STM-related data. The data is shown on the computer screen in real time from both STM and external sources. However, the software does not have any data processing ability. External software has to be used in order to process data, which included removing any underlying slopes due to systematic drift, making histograms out of image data, etc.

The key elements of TOPS3 include control electronics, data acquisition electronics and communication electronics. The control electronics contains approach electronics, feedback electronics and scanning electronics. (Fig 2.8 and Fig 2.9)

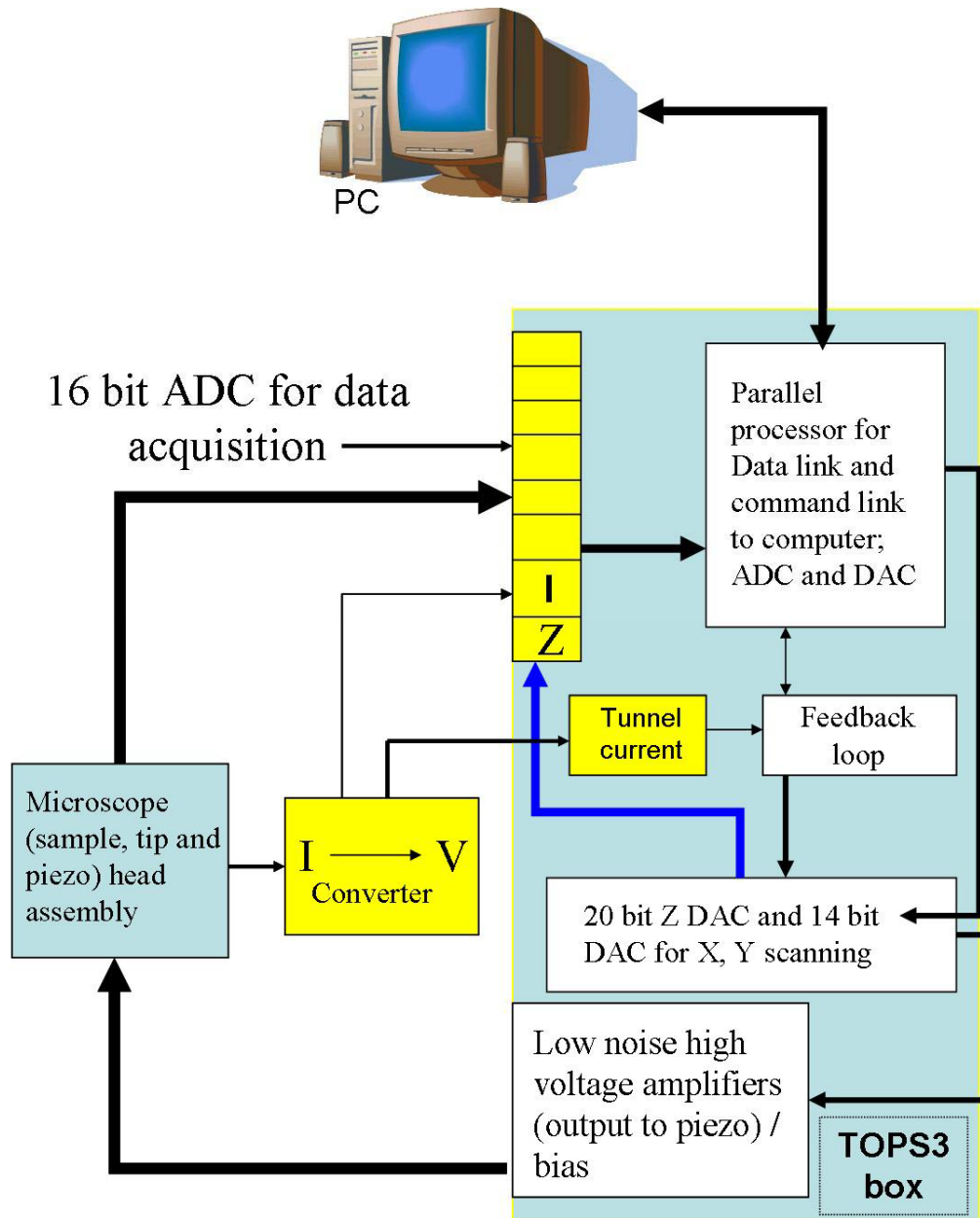


Fig 2.8: The schematic of STM data acquisition and control. The probe and TOPS3 box are light blue. The shaded-color is the data acquisition electronics and white is control and communication electronics.

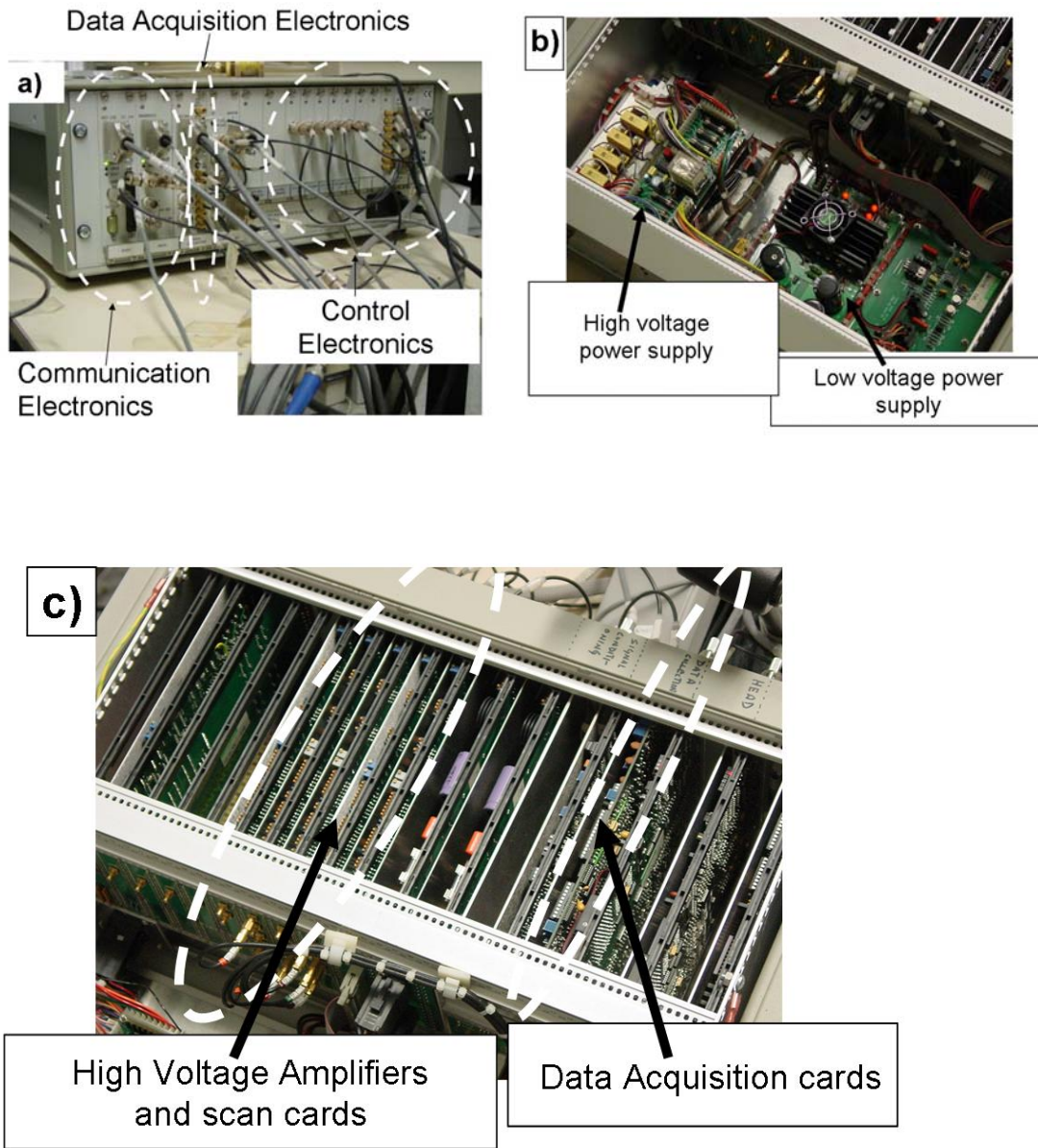


Fig 2.9: Photographs of the TOPS3 box. a) back (connector) panel of TOPS3; b) inside view of TOPS3 power-supply; c) inside view of the TOPS3 box to clarify HV amplifiers and Data Acquisition cards (external A/D 16 bit).

The purpose of the approach electronics is to bring the tip and sample close together on sub-micron length scales. The mechanism of motion is called the “slip stick mechanism” and it consists of three drive piezos, which move the scan stage, which are behind the ‘split outer shields’ as mentioned earlier (Fig 2.5). In general a single saw tooth pulse is provided to the three drive piezos which moves the scan stage forward $1\text{ }\mu\text{m}$ and then the scan piezo checks for tunnel current through its whole range ($\sim 5\text{ }\mu\text{m}$ in the ‘stick’ part of the motion). If tunnel current is established between the tip and sample then the approach electronics stops approaching. Otherwise the rapid drop in the saw tooth voltage pulse leaves the scan stage at its location (the ‘slip’ part of the motion), and it repeats the above procedure until a tunnel current is detected. If the tunnel current is detected, then the feedback electronics starts its function.

The purpose of the feedback electronics is to maintain a constant tunnel current between the tip and sample. As a default, the feedback circuit monitors tunnel current all the time and tries to control and maintain at the set value of the current. The feedback loop can be suspended manually (either using software or hardware switches). This suspension of the feedback loop is needed many times to perform experiments where an STM tunnel junction is not desirable. There are three parameters which characterize the feedback loop, called the PID parameters (P=Proportional, I=Integrator, D=Derivative). These parameters are coefficients in the equation

$$V_{out} = P(error + I \int (error)dt + D \frac{d(error)}{dt}) \quad (2.2)$$

where in this case *error* is the measured tunnel current value minus the set tunnel current value; and V_{out} is the voltage provided to the piezo for Z correction, and t is time. In light of this equation, the job of the feedback circuit is to keep the error equal to zero during scanning, and PID parameters are chosen by the user to help perform the task as efficiently as possible. There are three radio buttons on the software window of TOPS3 for the user to adjust these parameter values. In principle, for each new experiment these parameters have to be determined by trial and error. (Fig 2.10 shows the screen shot of TOPS3 software)

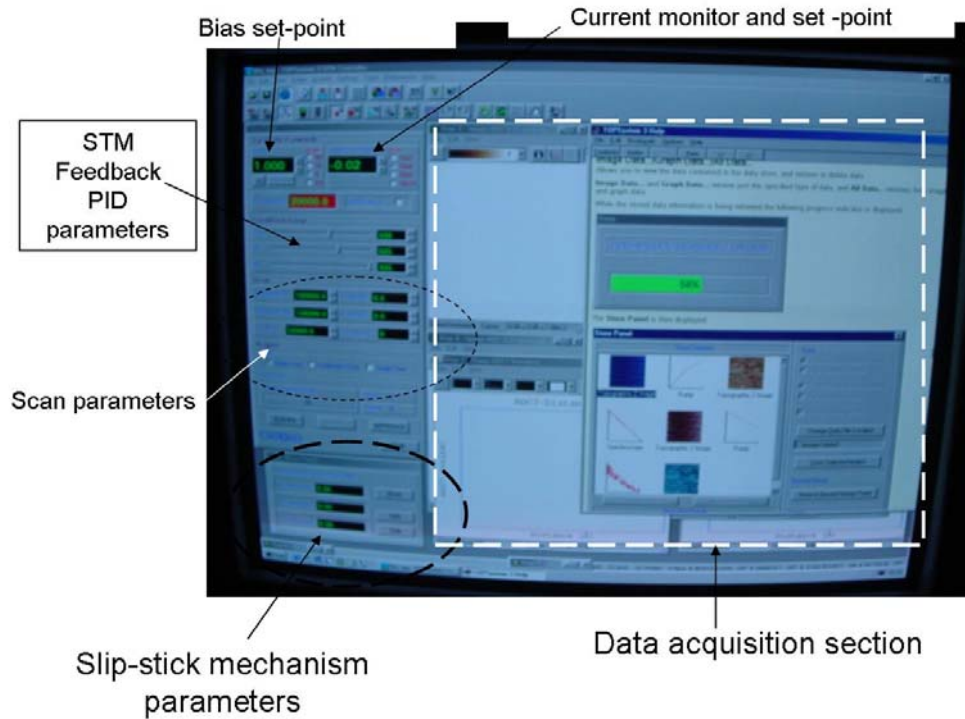


Fig 2.10: Screen shot of the TOPS3 software. All the key regions of user interface and labeled in the figure.

The scanning electronics contains high voltage amplifiers for +/- X, +/- Y scan directions and +/-Z for error corrections during the scanning. During scanning, as the roughness of the sample changes, the error signal in Z becomes the topography image. Generally, the scanning is done in the X direction, where scanning electronics applies voltage on +X and -X piezos (forward direction) and then -X to +X direction (reverse direction). The voltage steps are divided into the number of points (called pixels of an image) requested for each line during scanning. After finishing the scan line the STM rasters one point in the +Y direction and then repeats the same procedure to scan a line in X as mentioned earlier. The software allows scan directions to be changed anywhere between 0° and 90°.

2.2.4 The cryostat

Oxford Instruments provided us with a cryostat (Fig 2.11 and 2.12) which housed the STM probe mentioned above for cooling down to cryogenic temperatures. The inner-most hollow cylindrical cavity of the cryostat is called Variable Temperature Insert (VTI) as shown in schematic in Fig 2.11. The STM probe is placed in this VTI, where the temperature can be varied from room temperature to 4.2 K in flowing Helium gas. The VTI had a mechanical pump attached at its outlet (upper part of VTI in schematic in Fig 2.11), to allow for cool gas to flow over the sample and probe. A reservoir for cryogenics was also part of this cryostat, which had two vacuum jackets attached to its outer wall. The inner jacket system separated the reservoir and the outer jacket, the outer jacket separated

cryogen reservoir from the Outer Vacuum Chamber (OVC). It is OVC which isolated the VTI and cryogen reservoir with its jackets from the environment.

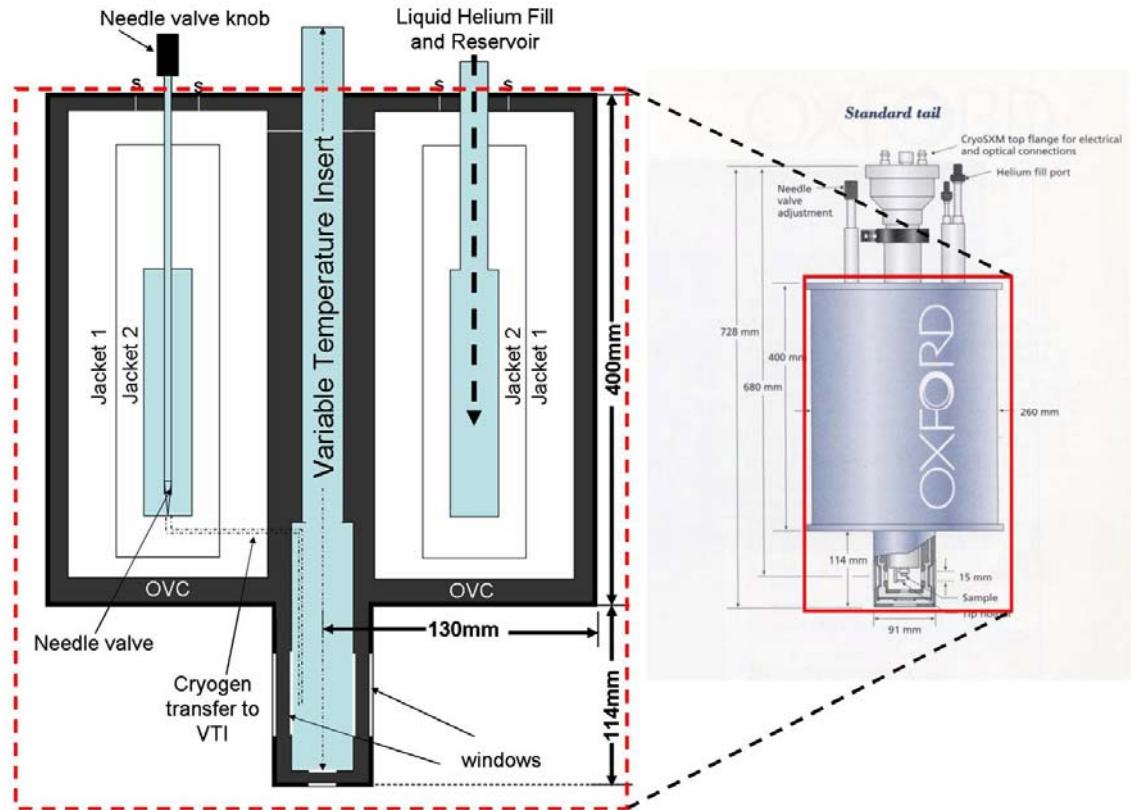


Fig 2.11: Schematic for the cross section of the Oxford cryostat (the solid-box is cross-sectioned for clarity to the left of figure). In the cross-section the light blue area gets cold for experiments. As can be seen in the solid red box, the sample is visible through windows, as it sits exposed to the cryogen flow. The amplified inset is not to scale, for the sake of clarity.

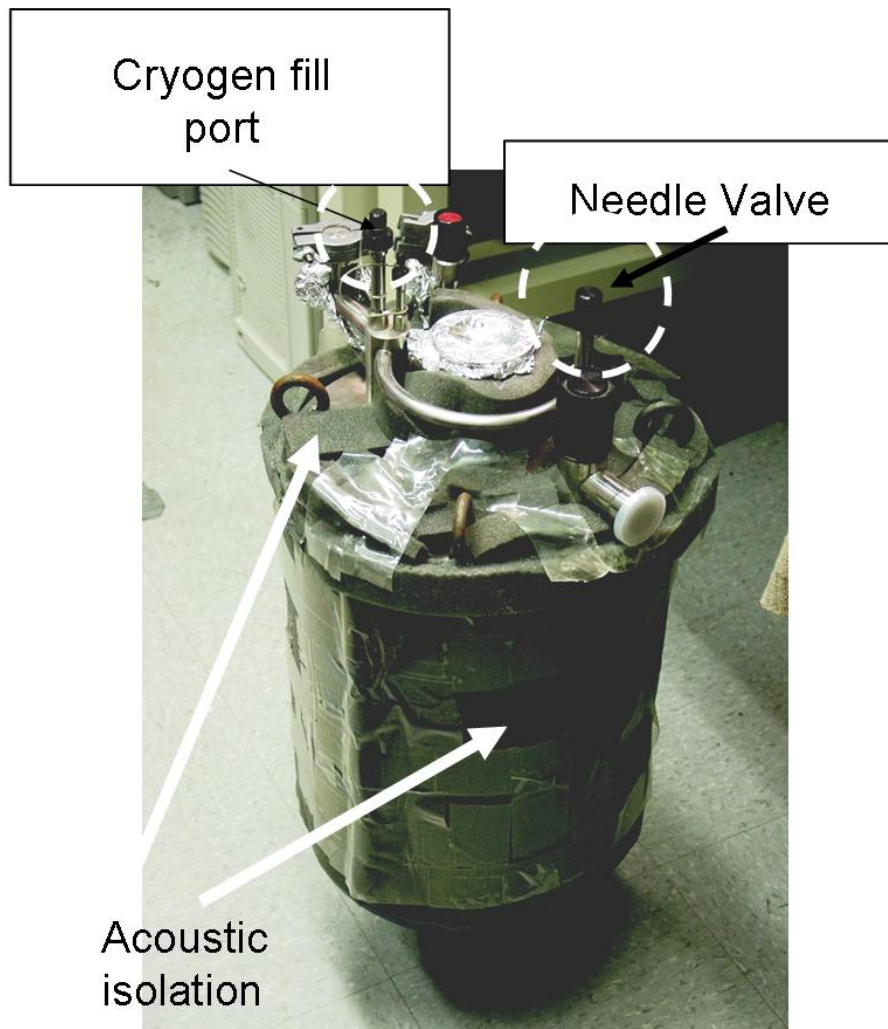


Fig 2.12: The Oxford cryostat shown covered with acoustic isolation foam. This was required for isolating STM from external acoustic noise.

This cryostat used flowing helium vapor to cool down the sample. The cryogen reservoir and VTI were connected via a needle valve (Figs 2.11 and 2.12) which allowed a controlled amount of the liquid helium (or liquid nitrogen) on the bottom surface of the VTI to flow into the sample space. The liquid evaporated and took away heat from the sample as it

passed through the VTI. There was a temperature and heater assembly in the vicinity of the needle valve to control the temperature of the inlet vapor.

The sample, STM tip, and piezos all sit in the flow of the cryogen vapor in this cryostat. As a result, the sample and tip surfaces will be contaminated; and this problem grew worse as I went to lower temperatures. I found out that below about 220 K, it was very difficult to find a clean and reliable spot on the surface to perform an STM experiment. Another problem was that the cryogen reservoir held liquid only for about 4 hours with the heat load (probe) present. This demanded stopping experiments and transferring cryogens every 4 hours. The experiments had to be stopped for transfer, since STM is very sensitive to mechanical vibrations. To avoid thermal shock to the piezos, I could not cool them down faster than about 5 K/minute. Hence going from 300 K to 4 K meant more than 1 hour of cooling time. This led to a very limited amount of time to perform experiments at low temperatures.

I circumvented the problems of surface contamination and limited scan time by designing a new cooling system. The Oxford Instruments cryostat was replaced by a Kadel cryostat which held enough cryogen for several days of experiments. I designed a new VTI for this cryostat, and it was built by our local physics machine shop (see Fig. 2.13 for schematic), and in this design sample does not sit in the flow of cryogens. I show the Kadel cryostat sitting in reference to the NSMM electronics (subject of section 2.3) and STM probe in Fig.

2.14. I generally fill the VTI with room temperature helium gas and then pump down to achieve a pressure of 10^{-4} to 10^{-5} Torr. The VTI was in thermal contact with the cryogen reservoir in the Kadel cryostat. Even low pressures of helium gas in the VTI coupled the STM probe with the reservoir enough for cooling purposes. A thermometer and heater on the probe arm is not sufficient any more for controlling the temperature set point. It is necessary to locate a heater and thermometer behind the sample puck to control the temperature of the sample. The temperature control electronics used is also from Oxford Instruments (ITC503). It has the capability to provide 80 W of power to a $20\ \Omega$ heater load.

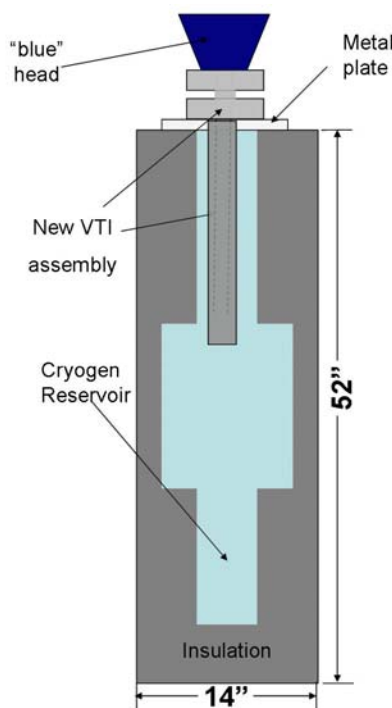


Fig. 2.13: The new cooling cryostat from Kadel. The “blue” head and new VTI assembly is shown for reference. In this design the cryogens cool down the external wall of VTI, and sample does not sit in the flow of cryogenes.

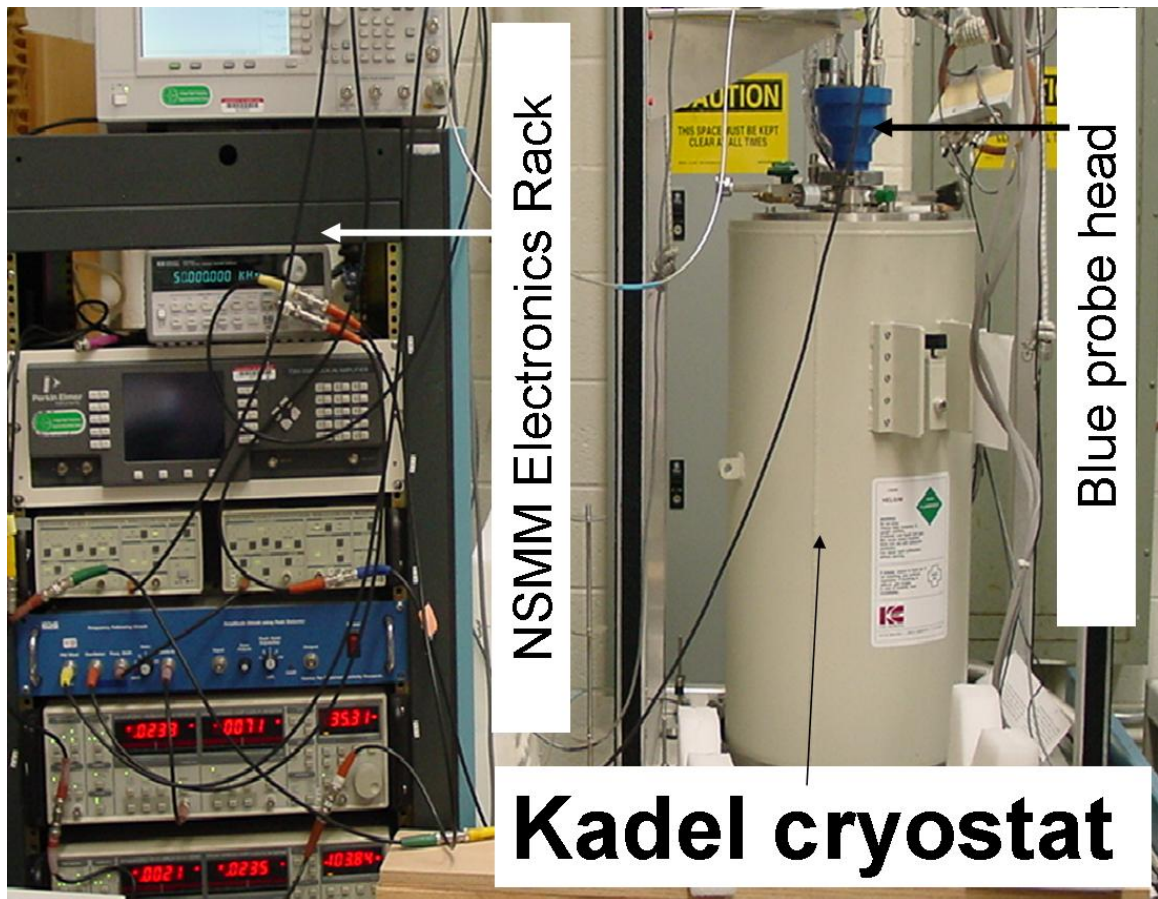


Fig 2.14: Picture of experimental setup with the Kadel cryostat in reference to NSMM electronics.

2.2.5 The acoustic noise and floor vibration isolation

The STM is very sensitive to the acoustic noise and vibrations of the support structure. Hence, it is important to have isolation from these two sources of mechanical noise. The Oxford cryostat (Fig 2.15a) was hung from an Aluminum cage with the help of four bungee cords. The Aluminum cage was sitting on top of the vibration isolation air table which damped out the floor vibrations. The cryostat itself was covered with lead acoustic isolator

layer (Fig. 2.12) to reduce vibrations due to acoustic noise. In the new cryostat, it was hard to hang it from the Aluminum cage (since it is ~ 4 times longer than Oxford cryostat and much heavier) so I placed it on top of heavy Aluminum metal plate which sits on top of an air-filled tire inner tube to isolate it from floor vibrations (see Fig 2.15b for schematic).

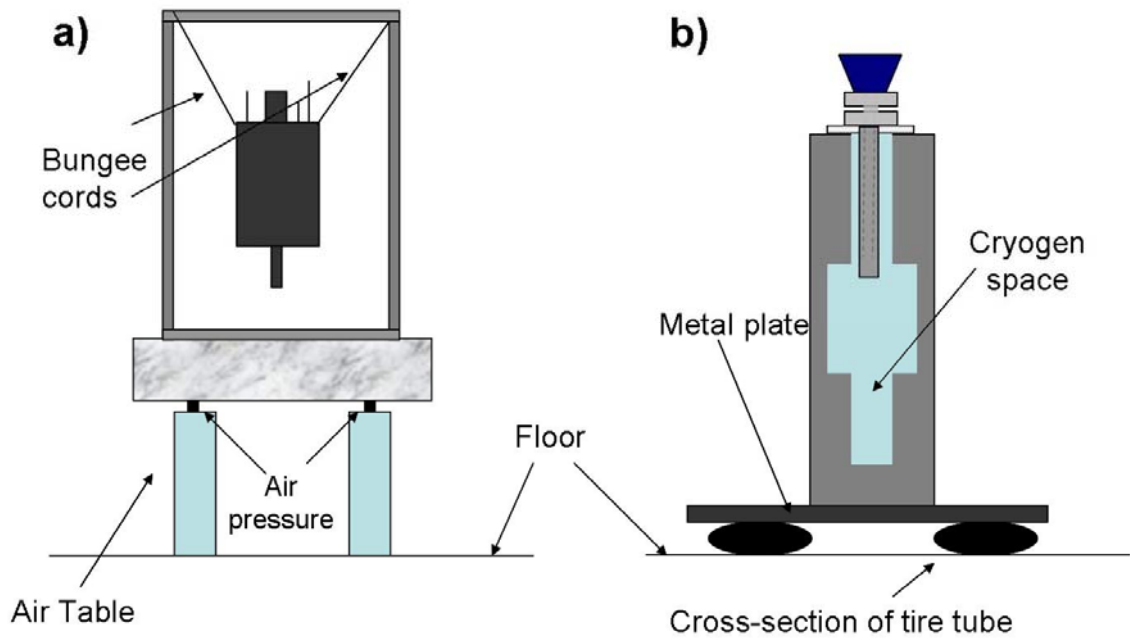
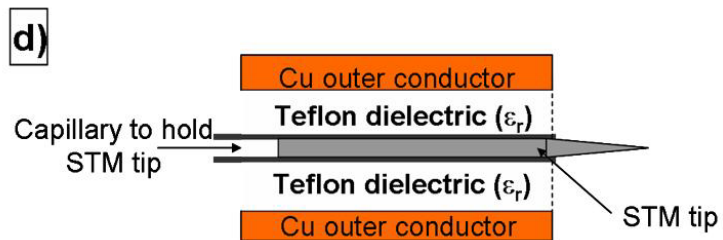
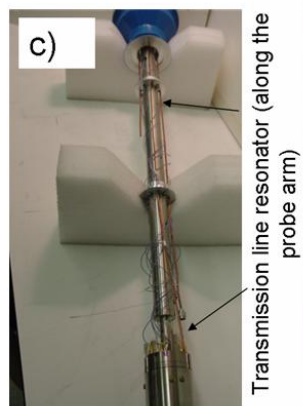
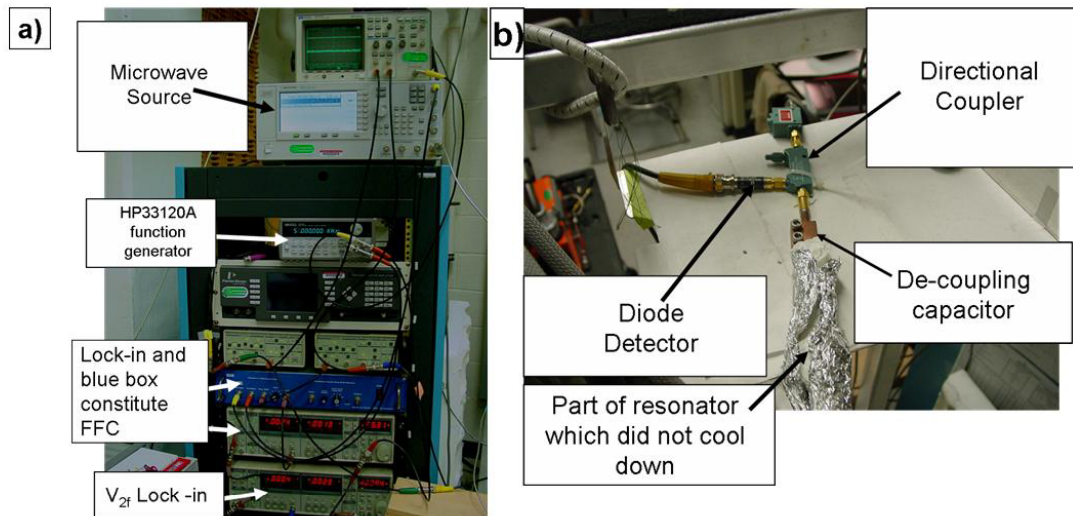


Fig 2.15: The schematic (cross-sectional view) of the vibration isolation setups for the STM. a) is the old Oxford cryostat set-up where an air table were used for floor vibration isolation b) is the new Kadel cryostat set-up, where a tire inner tube is used for floor vibration isolation.

2.3 Description of the Near-Field Scanning Microwave Microscope (NSMM)

The essential elements of the NSMM consist of a microwave source, a coaxial resonator coupled to the source (in my case via a decoupling capacitor), a detector to detect the reflected signal from the resonator, and a frequency following (feedback) circuit (FFC) or the NSMM feedback circuit (explained later in this chapter). This coaxial resonator is the transmission line resonator discussed in chapter 1. In this section, I go into the essential details regarding the Near-Field Scanning Microwave Microscope (NSMM). The pictures of the experimental setup are in Fig 2.16.



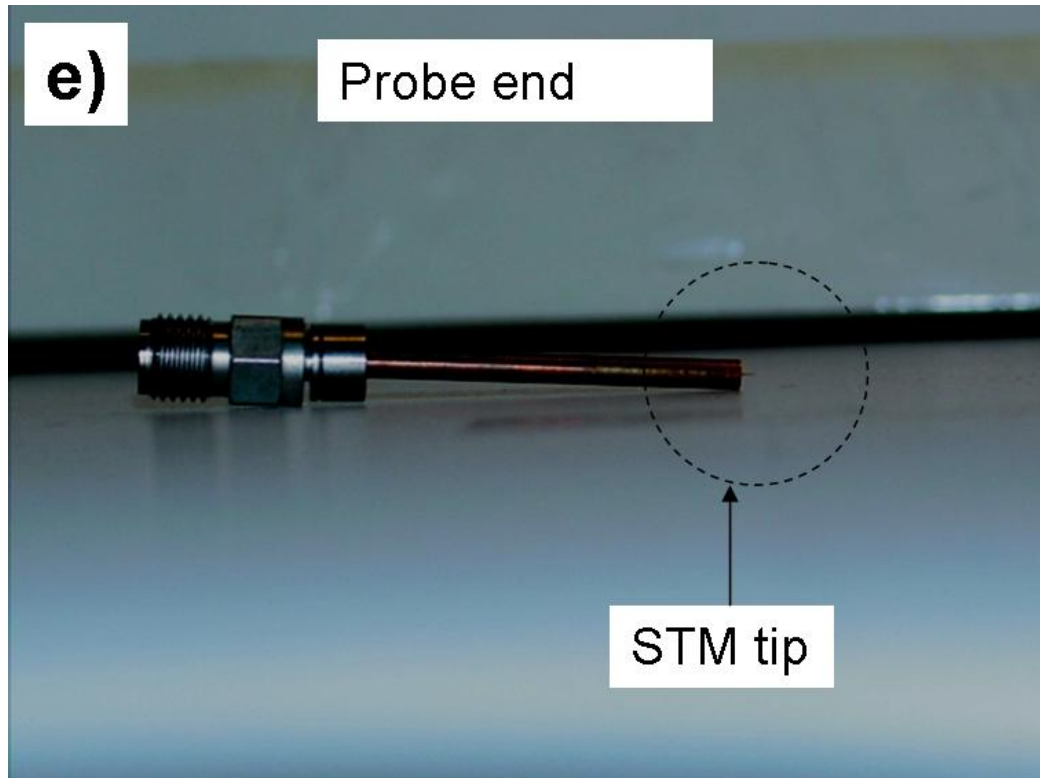


Fig 2.16: The experimental setup. a) The key elements of NSMM electronics in the electronics rack, b) the devices (Al sheet covering the resonator and bias-Tee is needed for isolation from 60 Hz electrical signals), c) the transmission line resonator shown in reference to the STM probe-arm, d) schematic of probe end for STM tip to clarify the stainless steel capillary tube used in the probe, e) picture of probe end for STM tip.

2.3.1 The experimental setup

Fig. 2.17 shows the circuit diagram of the NSMM. Here I briefly explain the NSMM in the light of Figs. 2.16 and 2.17. The resonator used is a coaxial transmission line which is coupled via a decoupling capacitor to the microwave source on one side and couples to a sample on the other side, with effective capacitance C_x between the probe and the sample. The microwave source is generally operating on one of the resonant frequencies of this resonator. The sample affects this resonator in two ways; one is to change the resonant frequency of the resonator and second is to increase the losses in the resonator.

In order to be able to measure these two effects, a directional coupler is used which plays two roles. First it allows the signal from the source to reach the resonator and second it allows the reflected signal from the resonator to be directed to the diode detector. The diode detector converts the measured power at microwave frequency into a voltage signal (this output (V_{diode}) is proportional to the input microwave power in the range of power of interest).

This voltage signal (V_{diode}) is sent to two lock-in amplifiers which phase-sensitively detects at the modulation frequency f_{mod} and twice the modulation frequency $2f_{\text{mod}}$ (labeled as f_{mod} in Fig. 2.17). This modulation frequency comes from an external HP33210A oscillator, shown in Fig. 2.16. The lock-in which is phase sensitively detecting at f_{mod} (f lock-in) is part of the FFC. The primary job of the FFC is to keep the microwave source locked onto

the resonant frequency of the resonator. The lock-in (which phase sensitively detects at $2f_{\text{mod}}$) measures a signal proportional to Q , and important details for the functioning of the NSMM are the subject of discussion in section 2.3.2. Together the f_{mod} oscillator, FFC and $2f$ lock-in are called NSMM feedback circuit, and this feedback circuit was designed to measure both Δf and Q simultaneously³³. The Δf is added with the f_{mod} signal and is sent to the source to keep it locked at the resonant frequency of the resonator. The inner and outer conductors are copper and the dielectric material used is Teflon. The inset of Fig. 2.17 clarifies the simple model of tip to sample interaction (in a classical lumped element model discussed in chapter 3).

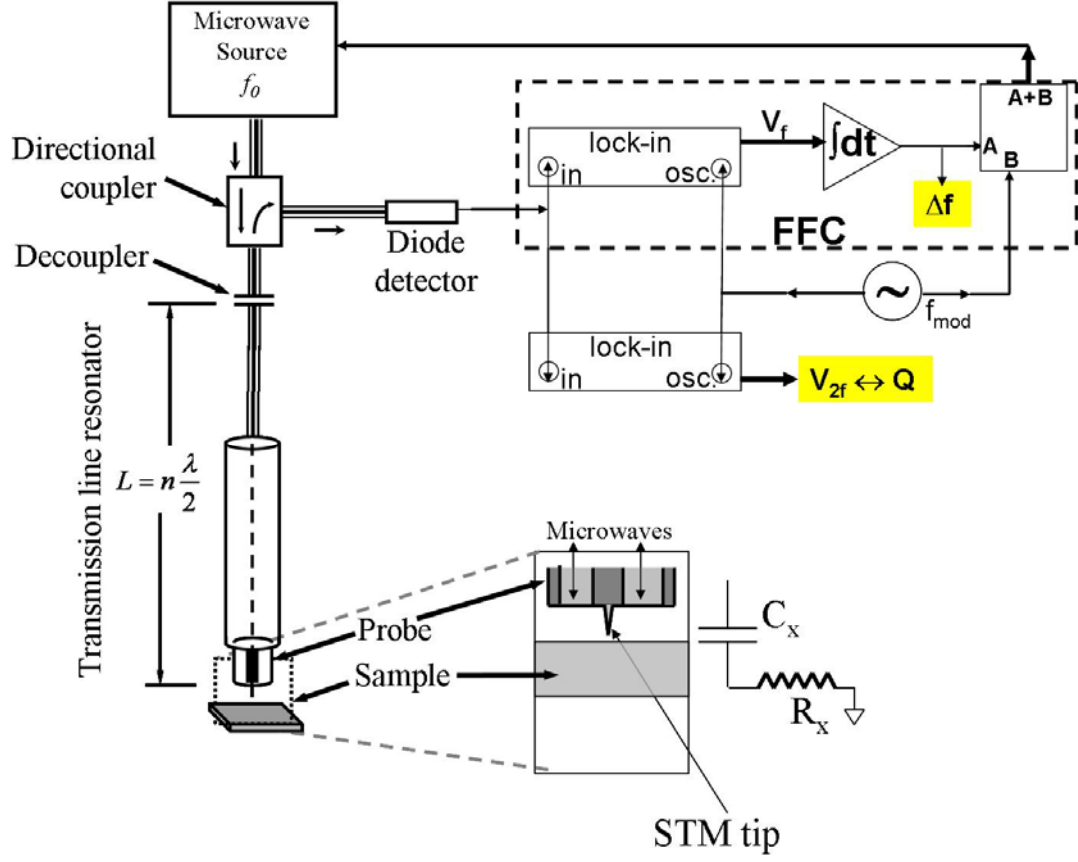


Figure 2.17: All the key components of the NSMM are shown in this schematic. FFC stands for “Frequency Following Circuit”, and one of its functions is to keep the source locked onto the resonant frequency of transmission line resonator. The resonant frequency and Q change continuously as the probe is scanned over the sample. The NSMM feedback circuit consists of a V_{2f} lock-in, f_{mod} source and FFC. The shaded-tags show output signals of the NSMM feedback circuit. The directional coupler is required to channel the reflection signal to the diode detector.

This resonator was integrated on the probe arm of the Oxford STM probe (shown in Figs. 2.5 and 2.6). The same mechanism which cools down the Oxford STM probe also cools down the transmission line resonator. However, only part of the transmission line resonator

is cooled down. The decoupling capacitor and part of the transmission line resonator that were outside of the probe arm (Fig 2.16b) did not cool down.

This microscope properties are monitored through a microwave reflection measurement. In Figs 2.18 and 2.19 I explain the idea behind the functioning of the NSMM. Later in this section I will discuss the function of the microscope in light of the instrumentation.

2.3.2 The functioning of NSMM (idea)

The magnitude of the reflection coefficient S_{11} versus frequency is a minimum at the resonant frequency of the resonator (see Fig. 2.18). The complex quantity S_{11} is the ratio of the reflected voltage to the incident voltage (Appendix B discusses how S_{11} relates to experimentally measured V_{diode} . Let me remark here that V_{diode} behaves qualitatively the same way as the magnitude of S_{11} behaves as a function of frequency). Since the resonator has nominally an open-circuit boundary condition on both sides, it is a $\lambda/2$ resonator at the fundamental tone. The increments to next higher modes are in steps of $\lambda/2$. The minima in S_{11} versus frequency occur at separations of about 120 MHz as shown in Fig 2.18 (the

spacing between minima = $\frac{c}{2L_{\text{res}}\sqrt{\epsilon_r}}$ where the length L_{res} of resonator is 1.06 m, c is the speed of light in vacuum and ϵ_r is the dielectric constant of the dielectric inside the coaxial cable).

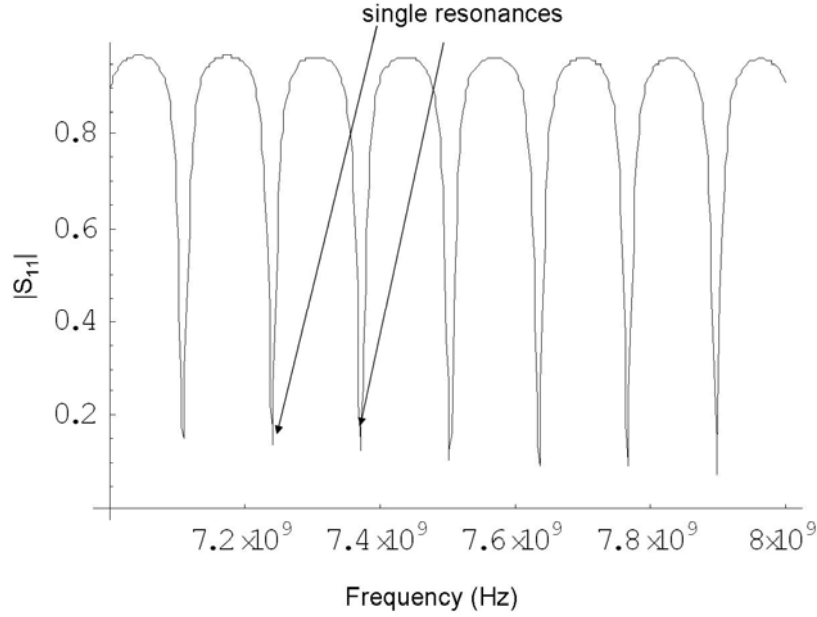


Figure 2.18: Calculated $|S_{11}|$ versus frequency from 7 GHz to 8 GHz, based on the transmission line model of the microscope discussed in chapter 3. With the help of arrows I point to two resonances. The frequency of the experiment, in principle, can be at any one of these minima. In general, not all resonances are sharp and deep enough for good signal to noise measurements.

One effect that the presence of the sample has on $|S_{11}|$ versus frequency is to shift the resonant frequency to lower values. From the point of view of the resonator, the coupling of the sample to the resonator effectively increases the length of the resonator, and an increase in length reduces the resonant frequency as shown schematically in Fig. 2.19 for one resonance. The second way the sample affects the resonance is that it changes the curvature of the minimum in $|S_{11}|$ versus frequency (shown exaggerated in Fig 2.19a). The modulation signal at frequency f measures the curvature of $|S_{11}(f)|$ at frequency $2f_{\text{mod}}$, as shown schematically in Fig. 2.19b. I have placed a ‘ball’ on the figure to clarify the origin

of the output signal at $2f_{\text{mod}}$. Over first half of the cycle of f_{mod} , the ball will reach one of the extreme ends (shown by a dashed ball) and then return, making a complete cycle of output for $|S_{11}|$. On the second half of the cycle of f_{mod} it will do the same on the other side of the curve. Hence, over one cycle of f_{mod} , the output of $|S_{11}|$ as a function of time will be at $2f_{\text{mod}}$ (or $2f$ signal). As the materials property on the surface changes, say due to some variable resistive losses in the sample, then this curvature changes from point to point on the sample. The change in curvature will show up as change in the amplitude of the voltage (output signal in Fig 2.19b) at twice the modulation frequency ($2f_{\text{mod}}$). Let me now get into some details in relation to the functioning of the instruments.

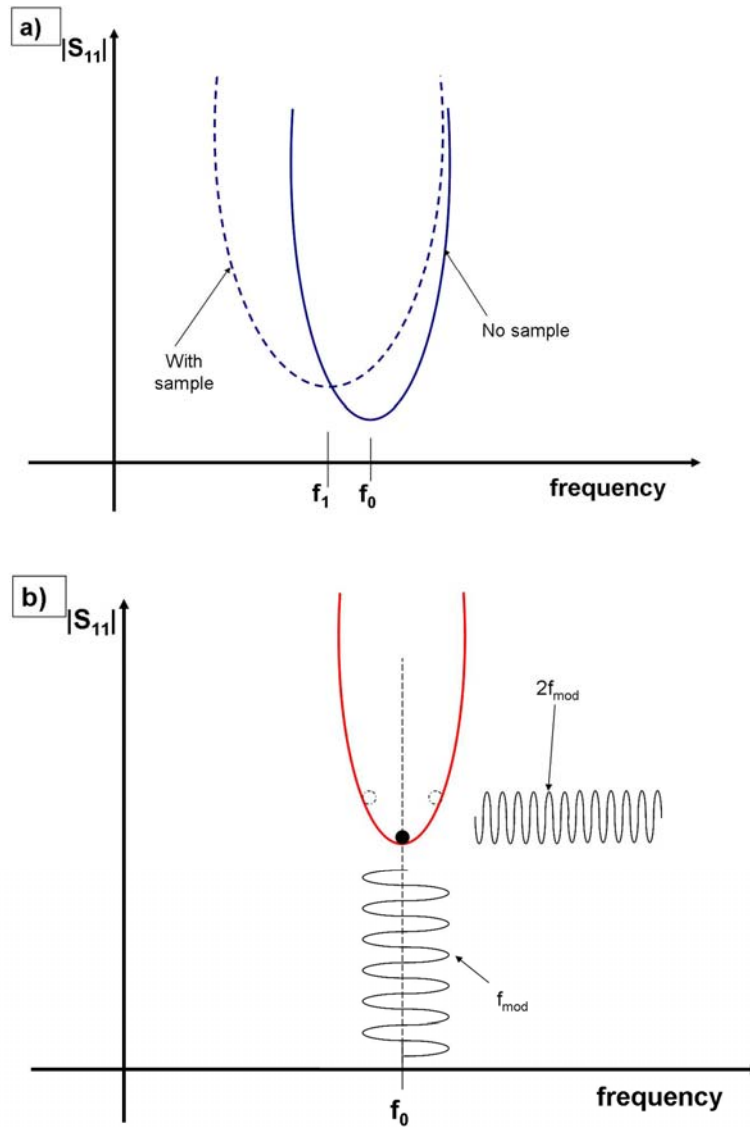


Fig 2.19: a) The concept of shift of resonance due to the presence of the sample. f_0 is the resonant frequency of the resonator (no sample) and f_1 is the new resonant frequency with the sample present. The sample effectively increases the length of the resonator and hence the resonant frequency goes down. The dashed curve is a bit exaggerated to clarify that there is also a slight change in curvature due to the losses inside the sample. b) The concept of measurement of curvature (needed for quantitative Quality Factor measurements). The 'ball' is just there for clarity: over one cycle the ball (shown by dashed ball positions) sees the two extrema positions and overall response is $2f_{\text{mod}}$ as explained in the text.

2.3.3 Functioning of the NSMM (experimental)

In a typical experiment when scanning over a sample with NSMM, the changes in the signal are very small compared to the noise, and hence lock-in signal recovery techniques have to be used. This means that the microwave source has to be modulated at the frequency f_{mod} , and then the output has to be phase sensitively detected at the modulation frequency. The first lock-in (with output V_f which is part of the FFC⁵⁵) is the phase sensitive detection at the modulation frequency f_{mod} . The lock-in amplifier simply time-averages the product of two signals (in this case V_{diode} and the f_{mod} signal) and this output is what I labeled as V_f (Fig 2.17). The V_f is 0 at resonance, negative above resonance and positive below resonance³³. The output of this lock-in is integrated over time and the resulting signal is called the frequency shift signal or Δf signal. This signal is recorded on one hand and added to the modulation signal (f_{mod}) on the other. The latter signal is sent to the microwave source FM input (such inputs are available on sophisticated sources for a variety of receiver related applications⁶⁰) and completes the feedback loop. The result is that the source is locked at the resonant frequency of the resonator, and the Δf error signal is recorded, which quantifies the degree to which the frequency shifted from the resonant frequency with no sample present. I should remark here that in the measurement Δf is to be regarded as a change in resonant frequency with respect the situation when no sample is present³³ and this is how it was done in earlier NSMM measurements. However, with the scan Piezo, I only have 2 μm of distance to go away from the sample. If the drive Piezos are used then I lose the region of interest (in the x-y plane), and it is quite a hassle to find it

again. Hence, I always report the Δf signal relative to 2 μm away. In other words, when the tip is 2 μm , I treat the situation as no sample present and this is assumed through out the thesis, unless stated otherwise.

The output of the V_{2f} lock-in measures the curvature of the resonance at which the source is locked, and it is related to Q . In transmission, if δf is the FWHM of the maximum of $|S_{12}|$ versus frequency and f_0 is the resonant frequency, then $Q = f_0/\delta f$. In this situation the expression for Q is simple since at resonance the transmitted power is a maximum. In reflection, complexity arises, since the transmitted power is a minimum at resonance, and there is a large background signal, hence measurement of Q is not trivial (as one needs to worry about the coupling). An approach⁸⁰ is used to calculate the loaded and unloaded Q , as discussed in Appendix B. The unloaded Q measures just the losses in the resonator and the loaded Q includes the losses in the coupling

Earlier in the NSMM experiment in the absence of the STM feedback, a microwave absorber (to simulate a radiating boundary condition) was used to determine Q from the V_{2f} signal³³ (since touching the absorber was not a problem and the height above the sample could be easily varied on micron length scales with a mechanical stage). The non-conducting nature of the microwave absorber made it useless for tunneling and hence measuring the nature of the V_{2f} signal in the last 2 μm above the sample. I chose a gold/mica thin film for purposes of calibration (since the losses were minimal and no

change in Q is observed, as will be discussed in chapter 4). The loaded Q was measured at various heights above the sample (within $2\text{ }\mu\text{m}$) using the method described in Appendix B. The resulting equation which relates the loaded Q to V_{2f} was fitted to a linear equation ($Q_L=A(V_{2f}/V'_{2f})+B$) to find the fit parameters A and B . The resulting equation is given by (2.3) where V'_{2f} is voltage $2\text{ }\mu\text{m}$ away from sample.

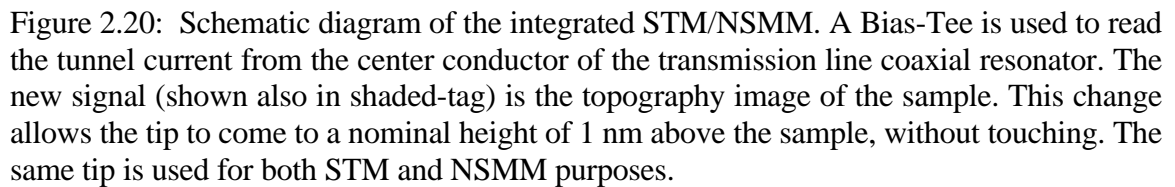
$$Q_L = 1553.97 \frac{V_{2f}}{V'_{2f}} - 1170.12 \quad (2.3)$$

To summarize at this stage, in order to have very high and spatially confined electric field above the sample, a sharp conical object (like an STM tip) can be used to concentrate the field. This helps to increase the spatial resolution for NSMM, as discussed in chapter 1. The presence of the sample will alter both the Δf and Q of the resonator (the measurement of these signals is non-trivial as discussed above). As a result the two signals will contain the physical information of the sample. This was done with dielectric thin films earlier³³ (no STM feedback was present in that case, it was just a tip in contact with the sample). I add the STM feedback circuit to the microwave resonator so the tip remains at a nominal height of 1 nm .

2.3.4 Integration of microwave resonator to STM

The changes made to the NSMM in order to integrate STM are shown schematically in Fig. 2.20. As mentioned in Chapter 1, with the help of a bias-Tee, the DC signal from the center

The sample now sits on top of an XYZ piezo as shown in Fig. 2.20.



61

I chose one of these coaxial cables and shaped it appropriately to replace the STM tip assembly (Fig 2.16e). The probe end of this coaxial cable has a small piece of coax with a hollowed stainless steel inner conductor (Fig. 2.16d). This becomes the new assembly for the STM probe as shown in Fig. 2.16(e). In order to make a DC connection to the STM circuit, an inductor is used (part of the bias Tee) between the inner conductor and STM electronics. The inductor filters out the ac signal from the microwave source so that it does not interfere with the STM operation. The same tip is used to perform both STM and NSMM. The Δf and Q signals were collected via the TOPS3 external A/D cards (see Fig. 2.8 & 2.9). A typical scan time for an image with 128 X 128 pixels is about 30 minutes. This slow scan rate is due to large time constants on the V_{2f} lock-in amplifier. Large time constants are needed to get good signal to noise ratio, and a typical value of time constant is 10 ms for the V_{2f} lock-in. It is the NSMM (and not STM) which requires such slow scan rates.

2.4 The geometry of the tips

As mentioned in the previous section, both STM and NSMM utilize the same tip. In general the two microscopes require rather different features in the tip geometry. A single atom at the apex of the tip will be sufficient for the purpose of establishing a tunnel junction for STM, as discussed earlier in this chapter. However, the geometry of the whole tip affects the signals of NSMM, since the capacitance (C_x) between tip and sample

depends on the details of the surface structure, particularly near the tip. This is shown schematically in Fig. 2.21.

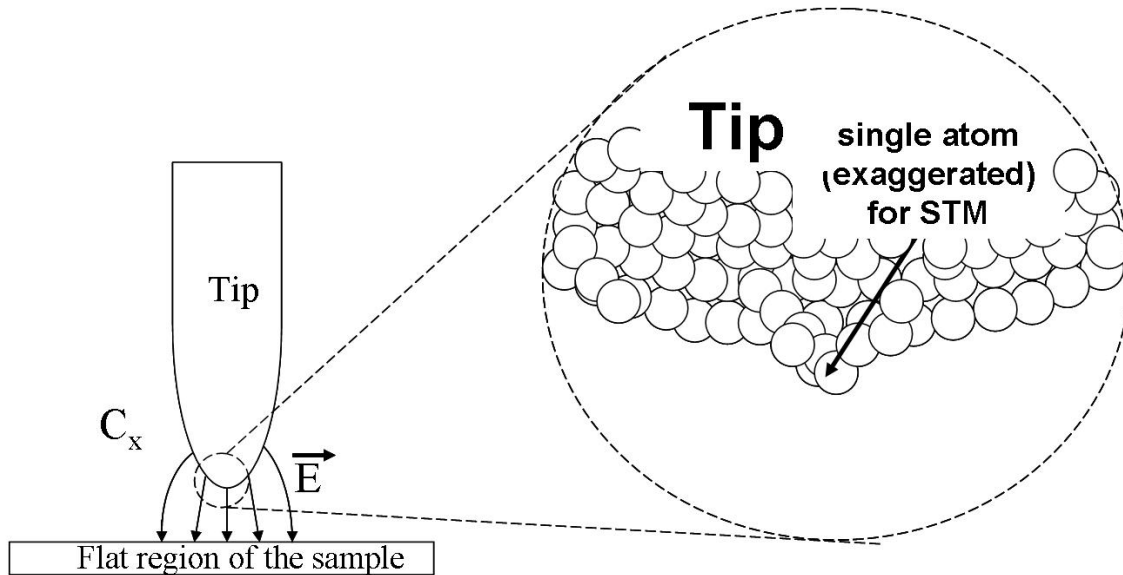


Figure 2.21: Schematic of tip to sample interaction. The capacitance (depicted by Electric Field lines) is what the NSMM is most sensitive to. The single atom (shown in magnification) at the end of the tip is what STM cares for.

Most of the tips that we used are (or were) commercially available. The companies chemically etch metal wires to produce nice conical tips with rounded ends (like a sphere embedded inside a cone). Since STM only cares for a single atom (ideally) at the very end of the tip, a piece of cut wire (Pt-Ir) is good enough for its purposes. However, the cut tips are generally poor for NSMM purposes since an irregularly shaped tip has a very pointy end (almost triangular with the lowest point like a vertex pointing towards the sample as in Fig. 2.24), compared to a nice embedded sphere in the case of etched tips (for example WRAP30R in Fig. 2.24). The cut tip as a result has a small C_x value for the tip to sample

capacitance. I have found the commercially available tips to be the best for NSMM signal due to the large value of C_x .

The etched tips that I used have been made of Tungsten (W), Platinum-Iridium (Pt-Ir) and Silver (Ag) coated Tungsten tips. An oxide layer grows on the surface of the W tip, which has to be either chemically etched away with a 1% HF solution, or removed by ion-beam erosion⁵⁶. The erosion has to be done *in situ* and in UHV; otherwise the oxide layer grows back on top of it. A coating of Ag on W circumvents this problem and makes it useful for ambient STM as well⁵⁸. A more systematic study of tip preparation can be found in the literature, where hazardous solutions (like HF) are replaced with more benign solutions for etching (NaCl, KCl, CaCl₂, NaBr)⁵⁷. Such tips are available from commercial sources⁵⁹.

Figs. 2.22 and 2.23 show pictures of a wide variety of investigated tips taken under the optical microscope with magnifications 10 and 40, respectively. Under the optical microscope all of the tips look conical, with the exception of the Pt-Ir cut tip, which has a rather irregular geometry, as I mentioned for tips made by cutting soft wires. The Fig. 2.24 presents Scanning Electron Microscopy (SEM) on these tips. Tables 2.1 and 2.2 summarizes the key results from this study. The end of the chapter draws key conclusions based upon the data presented in these tables.

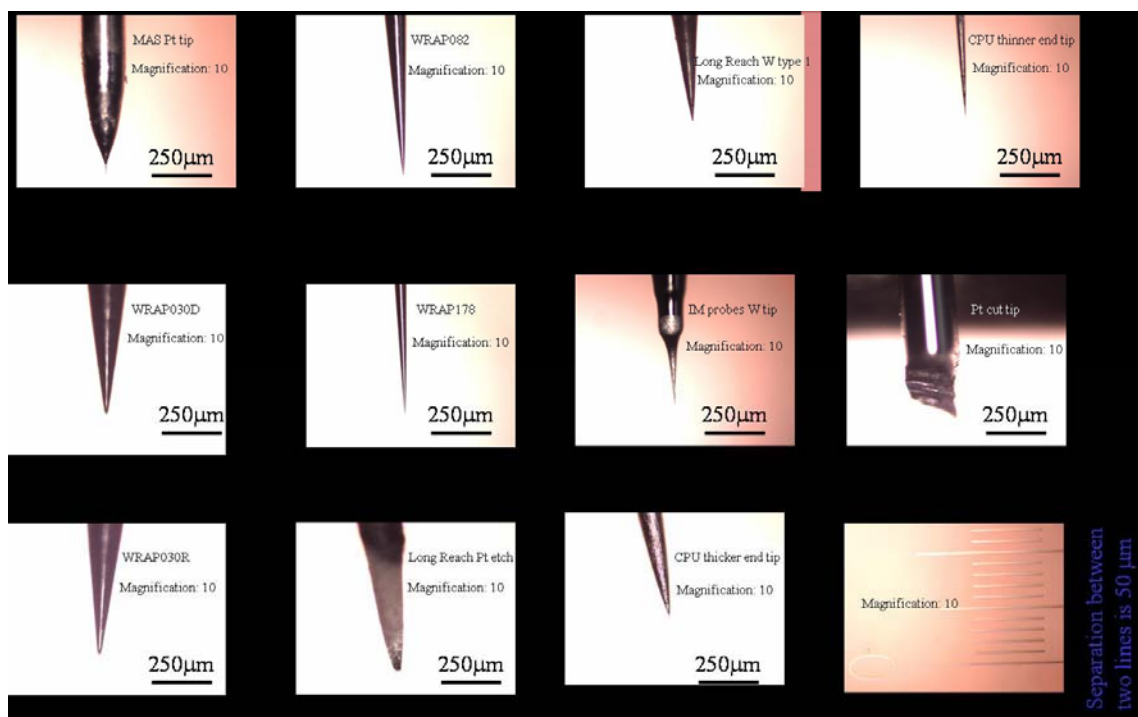


Fig. 2.22: All of the tips investigated for use in the combined NSMM/STM microscope, imaged in an optical microscope with magnification 10 for the objective lens.



Fig. 2.23: All of the tips investigated for use in the combined NSMM/STM microscope, imaged in an optical microscope with magnification 40 for the objective lens.

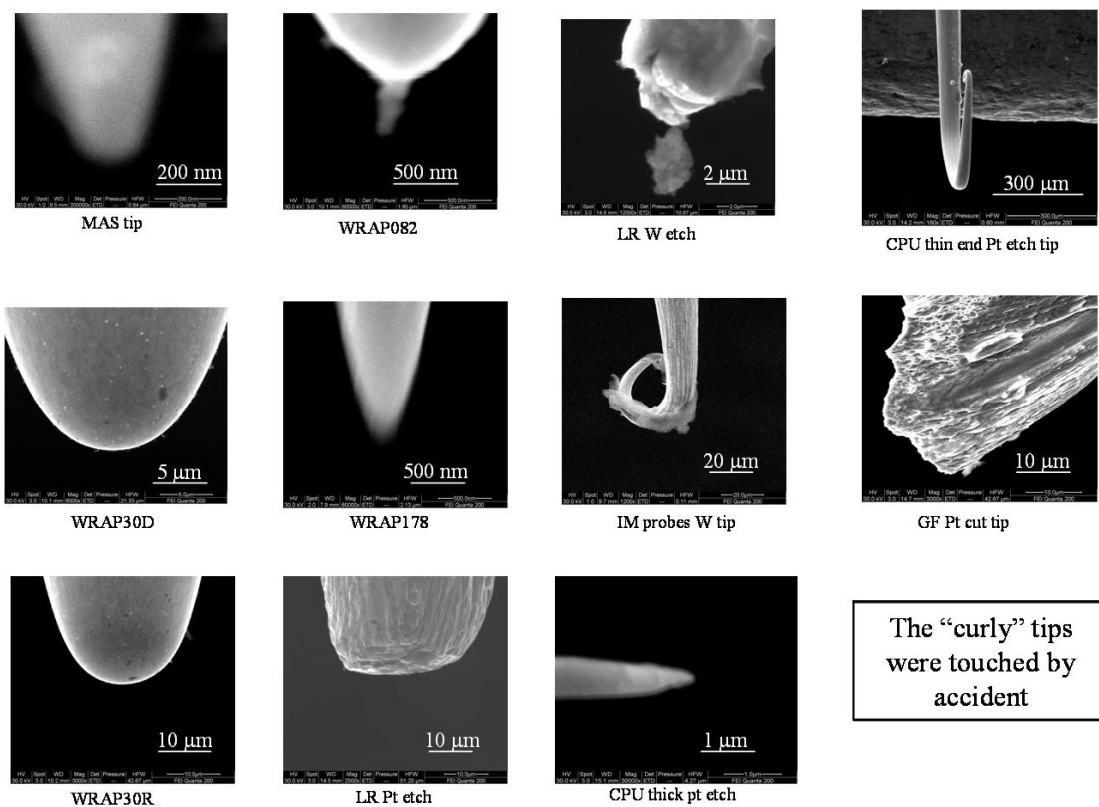


Fig.2.24: The SEM pictures for the same tips as shown in Fig. 2.23 and 2.24. This data makes the embedded sphere at the end of the conical tip clearer in many cases.

Table 2.1: Summary of key results from the STM tip study. The contrast here is defined as the Δf signal from 2 μm away. Some of the tips used were damaged as mentioned. The numbers shown represent the correct order of magnitude.

<u>Company Name</u>	<u>Brief Description of tip</u>	<u>Δf contrast over bulk copper</u>	<u>Δf contrast above gold on glass film</u>	<u>Δf contrast above gold on mica film</u>	<u>Δf contrast over 1% Nb:STO sample</u>
<i>Materials Analytic Services (MAS)</i>	<i>Platinum-Iridium etched tip</i>	-65 kHz	-35 kHz	-21 kHz	-80 kHz
<i>Advance Probing Systems (APS)</i>	<i>Ag coated W etched tip WRAP178</i>	-45 kHz	-40 kHz	-55 kHz	-60 kHz
<i>Advance Probing Systems (APS)</i>	<i>Ag coated W etched tip WRAP082</i>	-85 kHz	-135 kHz	-40 kHz	-160 kHz
<i>Advance Probing Systems (APS)</i>	<i>Ag coated W etched tip WRAP30D</i>	-300 kHz	-1150 kHz	-300 kHz	-1750 kHz
<i>Advance Probing Systems (APS)</i>	<i>Ag coated W etched tip WRAP30R</i>	-1000 kHz	-1275 kHz	-1100 kHz	-2500 kHz
<i>IM probes</i>	<i>W etched tip</i>	-30 kHz	-20 kHz	-25 kHz	-35 kHz
<i>Long Reach Scientific (LR)</i>	<i>W etched tip (small diameter)</i>	-	-	-80 kHz	-
<i>Long Reach Scientific (LR)</i>	<i>Platinum-Iridium (80:20) etched tip</i>	-	-	-500 kHz, not damaged; -1100kHz, damaged	-
<i>Custom Probes Unlimited (CPU) A</i>	<i>Platinum-Iridium (90:10) etched tip</i>	-	-	-80 kHz	-
<i>Custom Probes Unlimited (CPU) B</i>	<i>Platinum-Iridium (90:10) etched tip</i>	-	-	0 kHz	-
<i>Good Fellow (GF)</i>	<i>Platinum-Iridium (90:10) cut tip</i>	-	-	-40 kHz	-

Table 2.2: Summary of geometrical structure of tips with STM quality.

<u>Company Name</u>	<u>Brief Description of tip</u>	<u>Radius Curvature (r)</u>	<u>Aspect Ratio (α)</u>	<u>STM Quality</u>
<i>Materials Analytic Services (MAS)</i>	<i>Platinum-Iridium etched tip</i>	100 nm	Cone 1: 7°; cone 2: 43°; cone 3: 18°	Good (gold on mica)
<i>Advance Probing Systems (APS)</i>	<i>Ag coated W etched tip WRAP178</i>	130 nm	5°	Underestimates the feature size (Ni sample)
<i>Advance Probing Systems (APS)</i>	<i>Ag coated W etched tip WRAP082</i>	550 nm	8°	Good (many samples)
<i>Advance Probing Systems (APS)</i>	<i>Ag coated W etched tip WRAP30D</i>	5 μ m	17°	Doubles feature size (Ni sample)
<i>Advance Probing Systems (APS)</i>	<i>Ag coated W etched tip WRAP30R</i>	8 μ m	15°	Doubles feature size (Ni sample)
<i>IM probes</i>	<i>W etched tip</i>	? tip damaged	12°	Poor (oxide layer)
<i>Long Reach Scientific (LR)</i>	<i>W etched tip (small diameter)</i>	3.3 μ m	13°	Poor (oxide layer)
<i>Long Reach Scientific (LR)</i>	<i>Platinum-Iridium (80:20) etched tip</i>	12.6 μ m (projected estimate)	Cone 1: 14°; Cone 2: 29°	Good (many samples)
<i>Custom Probes Unlimited (CPU) A</i>	<i>Platinum-Iridium (90:10) etched tip</i>	≥ 100 nm	Cone 1: 10°; Cone 2: 17°	Good (gold on mica)
<i>Custom Probes Unlimited (CPU) B</i>	<i>Platinum-Iridium (90:10) etched tip</i>	Thin: damaged	Thin: 4°	Poor (too thin for successful insertion into probe)
<i>Good Fellow (GF)</i>	<i>Platinum-Iridium (90:10) cut tip</i>	NA	NA	Good (many samples)

Most of the tips appear to be conical, with an embedded sphere at the end. I call the radius of the embedded sphere ‘ r ’, as shown in Fig 2.25 for WRAP30D and WRAP30R. Here the ‘ r ’ values are on the order of $6\ \mu\text{m}$ and $8\ \mu\text{m}$, respectively. However, in practice I cannot choose a tip with arbitrarily large r value since large r tips do not resolve small features in STM topography on the surface of the sample (see Appendix A). For example, WRAP30R (with $r = \sim 8\ \mu\text{m}$) doubles the size of the features in the X and Y scan directions. I find WRAP082 (with $r = \sim 0.5\ \mu\text{m}$) to be the best compromise between good STM imaging and large enough C_x for NSMM.

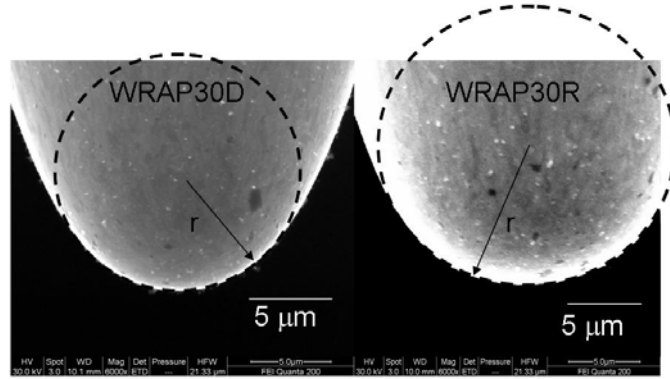


Fig. 2.25: The embedded sphere is illustrated for two particular tips. Here the r values are $\sim 8\ \mu\text{m}$ for WRAP30R and $\sim 6\ \mu\text{m}$ for WRAP30D.

I shall draw upon the observation of an embedded sphere at the tip later in this thesis when I construct a quantitative model of tip-sample interaction. However, the apex of the tip is not always an ideal sphere. Some times a tiny perturbation may be sticking out from the apex, and this can affect the capacitance C_x for the NSMM signal. Such a small cone is

shown in Fig. 2.26 sticking out from the WRAP082 Ag- coated W tip. Such features can affect the signal in an interesting way, as discussed in detail in chapter 4.

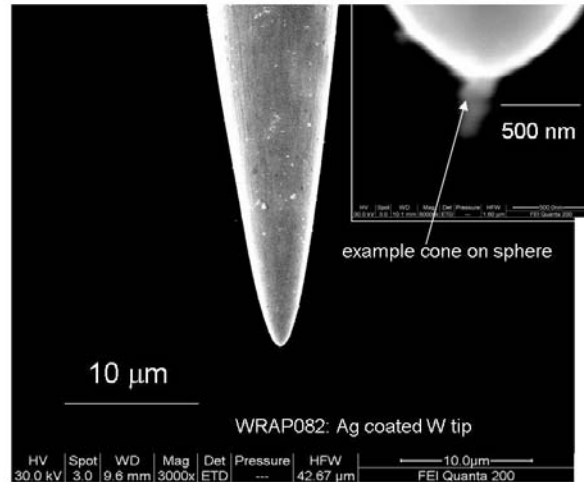


Fig. 2.26: A small feature sticking off of a WRAP082 Ag-coated W tip. The feature is only visible under high magnification (80000) in a scanning electron microscope and is about 200 nm in size

Some major conclusions which can be reached from the data in Table 2.1 are: measuring with NSMM at small height, the geometry of the very end of the probe tip is the most important for signal contrast. The large-scale conical structure does not play as significant a role as compared to the sphere near the end. A large C_x (large r) tip is best suited for high signal to noise in NSMM, however such large tips are not good for resolving nano-meter length scale features for STM topography. In general, a tip with a nicely shaped spherical end (via etching) with $r \sim 0.5 \mu\text{m}$ to $1 \mu\text{m}$ is good enough for both NSMM and STM.

Chapter 3

Modeling of the novel Near-Field Microwave Microscope

3.1 Introduction

In order to quantitatively understand the behavior of the frequency shift (Δf) and quality factor (Q) signals, I need to model the microscope, and include both propagating and evanescent (non-propagating) waves. Propagating wave models are important to understand the behavior of the entire microscope, including the resonator and its interaction with the sample. However, such models soon become inadequate as the tip to sample separation reaches nano-meter length scales. On these length scales the role of decaying (evanescent waves) cannot be ignored any more, as was discussed in chapter 1. On these scales, contributions from high spatial frequency wave vectors of the non-propagating waves become important to the Δf and Q signals.

3.2 Propagating waves or circuit models

3.2.1 Lumped Element Model

In the case of the lumped element model, any resonator is modeled as having a resistive element (denoted by R), a capacitive element (C), and an inductive element (L). Together it can be called an RLC circuit. When dealing with long resonators (1.06 m in my case) at

microwave frequencies, in general a complete transmission line theory (the subject of section 3.2.2) should be employed to calculate Q and Δf of the resonator (since λ is small compared to length of resonator). However, within a limited bandwidth of interest (which is usually true near a single resonance) one can use lumped element models⁶⁴, even at microwave frequencies. The strength of the lumped element model is that it provides quick qualitative insight into the behavior of the microscope as the sample properties change. These insights are important when working towards newer microscope designs for studying different samples. For example, study of dielectric samples requires a microscope with a certain set of lumped element parameter, while study of metallic or superconducting samples requires a completely different set of lumped element parameters to optimize sensitivity to relevant quantities.

In the lumped element model of the microscope, the resonator is modeled as a parallel capacitor C_0 , inductor L_0 and resistor R_0 which is driven by a microwave source as shown in Fig.3.1. In most cases I look at conducting samples because of the need to establish an STM tunnel junction. The sample is added in parallel to the resonator, as a series combination of capacitance C_x and resistance R_x (shown in Fig. 3.1). The reason why the sample is modeled this way goes back to the tip-to-sample interaction that was shown in Fig. 2.17. Since there is gap between the probe and the sample, this gap between two electrodes (tip and sample) is a capacitor C_x , and the losses in the sample are represented by the resistance R_x . In principle, some inductance L_x should also be added in parallel with

the R_x , however I ignore it here since this term only becomes relevant in the case of superconductors (due to kinetic inductance related to super-current⁸⁶ flow) which is not the subject of this thesis. The sample is assumed to present primarily a resistive channel to the microscope.

The series RLC circuit model of the resonator has been used successfully earlier for a strip line resonator⁸⁵. In that case the sample (a series combination of C_x and R_x) is added in parallel to the capacitor of the series RLC circuit. In principle, this model and the parallel RLC models are equivalent and give the same qualitative behavior for both, Δf and Q of the resonator. In this thesis I mainly concentrate on the parallel RLC circuit.

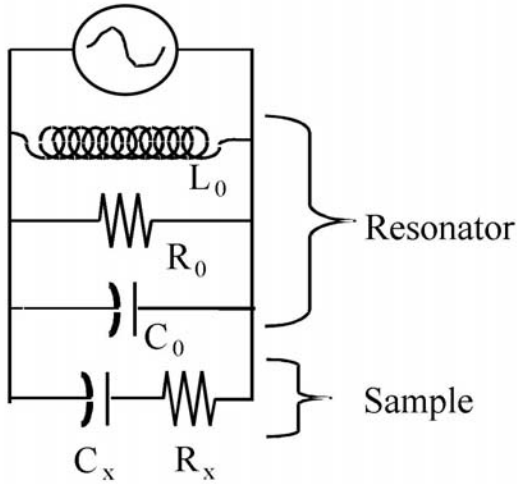


Figure 3.1: The circuit diagram of the lumped element model where L_0 , R_0 and C_0 are in parallel, and represent a single resonance of the resonator. The sample is added as a series R_x and C_x in parallel to the resonator RLC circuit.

For a parallel RLC circuit the Quality Factor Q_0 is given by⁶⁴ $Q_0 = R_0 \sqrt{\frac{C_0}{L_0}}$ and the resonant frequency of the resonator is given by $f_0 = \frac{1}{2\pi \sqrt{L_0 C_0}}$. In the presence of the sample (modeled as a series capacitance C_x and resistance R_x) the new Quality Factor Q' is given by

$$Q' = R \sqrt{\frac{C}{L}}, \quad (3.1)$$

and the new resonant frequency is given by

$$f' = \frac{1}{2\pi \sqrt{LC}}, \quad (3.2)$$

where the frequency shift is given by the equation

$$\Delta f = f' - f_0. \quad (3.3)$$

The total impedance Z_T (seen by the voltage source) for this parallel circuit is:

$$Z_T = \frac{1}{\frac{1}{i\omega L_0} + \frac{1}{R_0} + i\omega C_0 + \frac{1}{Z_{sample}}}. \quad (3.4)$$

Here $Z_{sample} = R_x + \frac{1}{i\omega C_x}$, and after lumping the circuit elements of the sample and

resonator together, I get the following equations,

$$\begin{aligned}
L &= L_0 \\
C &= C_0 + \frac{1}{1 + (\omega C_x R_x)^2} \\
R &= R_0 \frac{1 + (\omega C_x R_x)^2}{(1 + (\omega C_x R_x)^2) + \frac{R_0}{R_x} (\omega C_x R_x)^2}
\end{aligned} \tag{3.5}$$

and these new parameters are used to get the Δf and Q' given by equations (3.1 and 3.3).

I have found that working with this model is easier if a few dimensionless parameters are introduced. These parameters are: $x \equiv \omega C_x R_x$, $y \equiv \omega C_x R_0$ (a typical experimental value is close to 0.13 at 7.5GHz) and $c = C_x/C_0$ (a typical experimental value is $c \cong 2.51 \times 10^{-4}$ at a height of 1 nm). With these parameters the equations for quality factor and frequency shift Δf are as follows for the lumped element model:

$$\frac{Q'}{Q_0} = \frac{(1 + x^2)}{(1 + xy + x^2)} \sqrt{\frac{1 + x^2 + c}{1 + x^2}} \tag{3.6}$$

$$\frac{\Delta f}{f_0} = \sqrt{\frac{1 + x^2}{1 + x^2 + c}} - 1 \tag{3.7}$$

It is important to note here that in the limit $x \ll 1$, Δf can be approximated as

$$\frac{\Delta f}{f_0} \cong -\frac{C_x}{2C_0} \tag{3.8}$$

so it is just dependent on c , and quality factor as

$$\frac{Q'}{Q_0} \cong 1 - (R_0)\omega^2 C_x^2 R_x \tag{3.9}$$

The strength of these relationships in this limit is that for $x \ll 1$, I can interpret Δf as a function of capacitance C_x only and then the R_x information can be extracted from equation (3.9) by substituting equation (3.8) into it. Fig. 3.2 shows the plots of Q'/Q_0 and $\Delta f/f$ based on these equations.

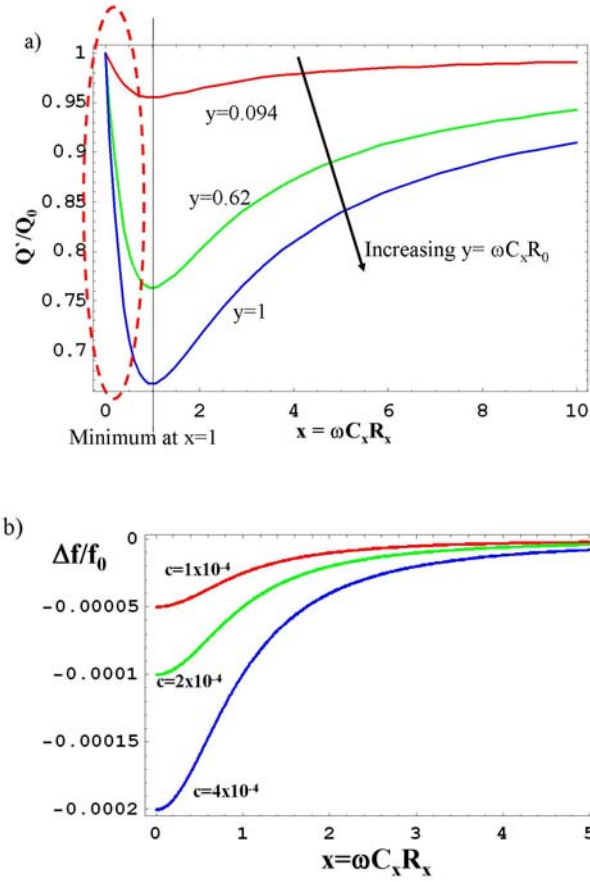


Fig. 3.2: a) The behavior of Q/Q_0 versus $x = \omega C_x R_x$. Different curves are for different $y = \omega R_0 C_x$ values. The minimum in each case is at $x=1$. For $x < 1$ (broken ellipse) the Q contrast of the microscope is predicted to be the largest; b) $\Delta f/f_0$ versus $x = \omega C_x R_x$ which is plotted for different c values. Here $x=1$ represents the point of inflection.

The dimensionless parameter x physically characterizes the interaction of the microscope with the sample, and it contains the source frequency $\omega = 2\pi f$, the tip to sample capacitance C_x , and the materials property of the sample R_x . It is essentially the normalized sample RC-time constant. The knowledge that x is the relevant parameter is helpful in the design of an experiment. For example, if it is assumed that the materials property of the sample cannot be tuned, the model still predicts that by changing the tip geometry (section 2.4) or frequency of the source, I can operate the microscope in the region where contrast can be maximized (shown by dashed red ellipse in Fig. 3.2a). On top of that, $y = \omega R_0 C_x$ (where R_0 is the resonator resistance) can be tuned to change the curvature of Q/Q_0 versus x curve (experimentally this task is a bit more challenging in my setup since the STM design restricts me to a certain length of resonator). An earlier microscope³³ explored the region of x from ~ 0.1 to 4, and with this STM-assisted microscope I explored values of x from 0.01 to 70, and that sample will be discussed in chapter 5.

For my purposes, the sample is assumed to present primarily a resistive channel to the microscope. However, the model can be modified depending on the sample. For highly resistive thin films on a substrate (for example a Boron-doped semiconductor sample), there could be a dielectric component to the response (modeled as a capacitor). In this case, a parallel capacitor (called C_{sub}) can be added to the R_x of the sample, and such a model will be discussed in chapter 5.

3.2.2 Transmission line model of the NSMM

The transmission line model for the microscope is based on standard microwave transmission line theory. This model has been used successfully to model earlier versions of this microscope and to calculate Δf and Q as a function of changing impedance provided by the sample³³. I use this model to calculate these quantities as a function of sample properties as well. Note that we also treat the sample just like in the lumped element model using capacitance C_x and resistance R_x . The main strength of this model is that Δf and Q are calculated by modeling all the microwave devices used in the microscope. This includes the attenuation of the signals due to ohmic losses (inside the resonator and transmission lines) as part of the calculation.

Unlike the lumped element model, the transmission line model does not provide me with nice and simple equations, which are insightful. However, for purposes of calculations, the transmission line model provides a reliable way to calculate the measurable quantities. The circuit diagrams of the transmission line model are shown in Figs. 3.3 and 3.4. By following the standard transmission line model analysis^{64,88}, the time varying source voltage V_s and current I_s are given by the equations:

$$\begin{aligned} V_s &= e^{i\omega t} (V_s^+ + V_s^-) \\ I_s &= \frac{e^{i\omega t}}{Z_0} (V_s^+ - V_s^-) \end{aligned} \quad (3.10)$$

where V_s^+ is the amplitude of the outgoing wave, and V_s^- is the amplitude of the wave moving to the left.

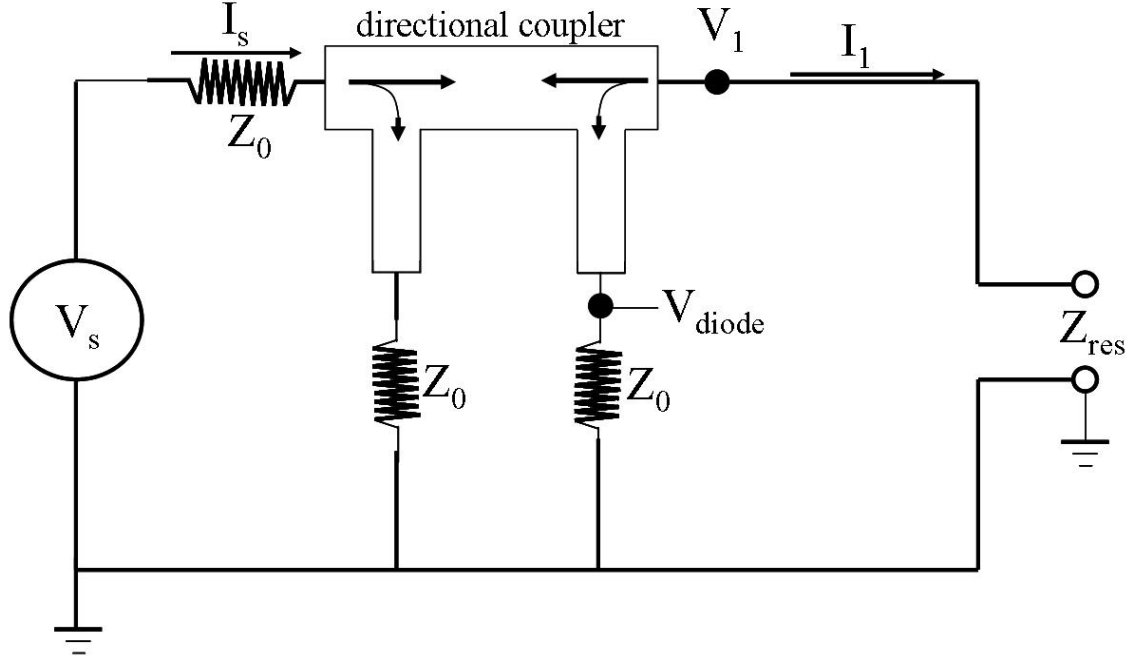


Figure 3.3: The circuit diagram of the transmission line model without details of the resonator. The source V_s drives the circuit. The voltage across the resonator is V_1 and current through the resonator is I_1 . A directional coupler sends part of the signal to the diode detector which is detected as voltage (V_{diode}).

The frequency of the driving signal is denoted by ω and Z_0 is the characteristic impedance of the coaxial wave guide and the internal impedance of the source. The time varying voltage and current at the resonator input are denoted by V_1 and I_1 respectively, where V_1^+

and V_1^- denote the amplitude of the wave traveling right and amplitude of the wave traveling left, respectively.

$$\begin{aligned} V_1 &= e^{i\omega t} (V_1^+ + V_1^-) \\ I_1 &= \frac{e^{i\omega t}}{Z_0} (V_1^+ - V_1^-) \end{aligned} \quad (3.11)$$

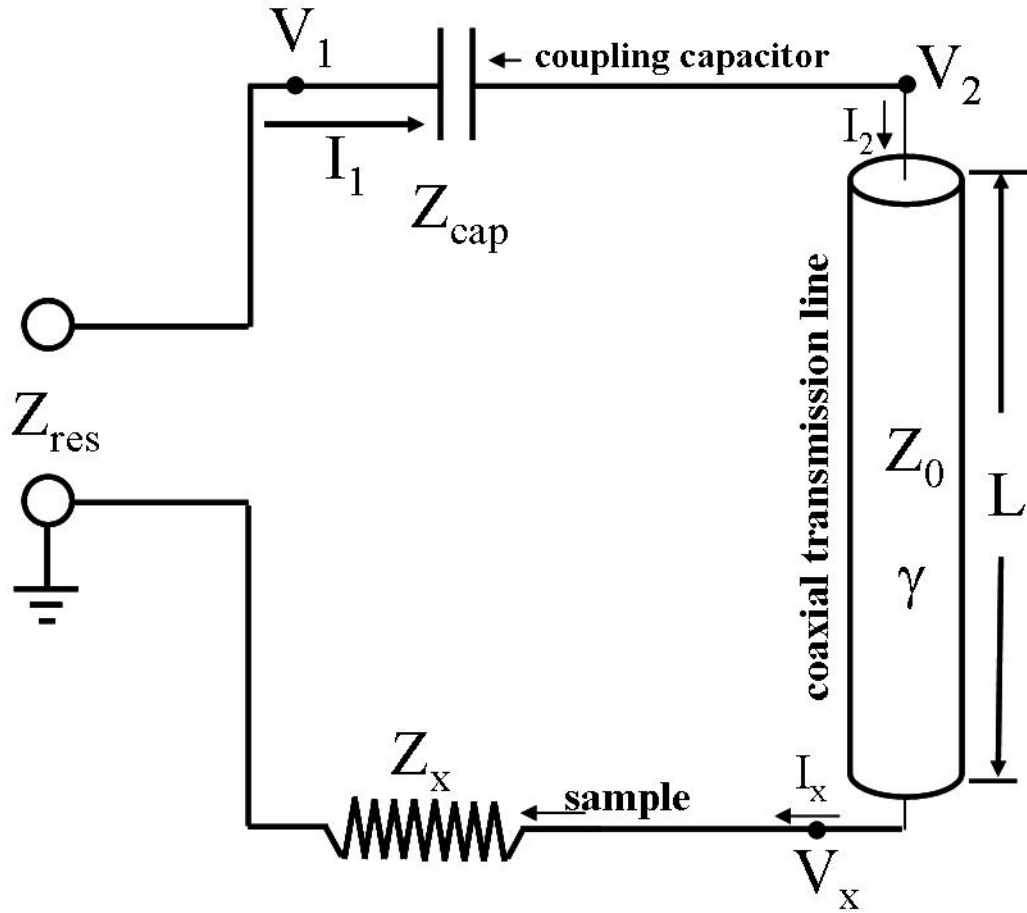


Figure 3.4: The details of the resonator part and the sample. The sample is shown as complex impedance $Z_{\text{sample}} = R_x + \frac{1}{i\omega C_x}$. The parameter γ is the complex propagation constant of the transmission line. The coupling capacitor is shown with impedance Z_{cap} .

In order to measure the signals from the resonator, the source and resonator are connected via a directional coupler as shown in the Fig. 3.3. The directional coupler sends part of the signal to the diode and the coupling voltage fraction is denoted by $\eta_{voltage} = 10^{\xi/20}$ where ξ is the specified coupling in dB. With this the voltages V_1^+, V_s^- and V_{diode} are given by:

$$\begin{aligned} V_1^+ &= V_s^+ - \eta_{voltage} V_s^+ = V_s^+ (1 - \eta_{voltage}) \\ V_s^- &= V_1^- - \eta_{voltage} V_1^- = V_1^- (1 - \eta_{voltage}) \\ V_{diode} &= V_1^- - (V_1^- - \eta_{voltage} V_1^-) = \eta_{voltage} V_1^- \end{aligned} \quad (3.12)$$

The voltage drop across the resonator is given by $V_1 = I_1 Z_{res}$. From this and equation

(3.11), I get the ratio of $\frac{V_1^-}{V_1^+}$ to be:

$$\frac{V_1^-}{V_1^+} = \frac{Z_{res} - Z_0}{Z_{res} + Z_0} \quad (3.13)$$

which gives us the expression for the measured diode voltage V_{diode} from 3.12 as:

$$V_{diode} = \frac{(Z_{res} - Z_0)}{(Z_{res} + Z_0)} \eta_{voltage} (1 - \eta_{voltage}) V_s^+ \quad (3.14)$$

The circuit diagram for the resonator section is drawn in Fig. 3.4. The impedance of the

coupling capacitor (de-coupler) is given by $Z_{cap} = \frac{1}{i\omega C_{cap}}$ and beyond the de-coupler the

voltage and current are given by:

$$\begin{aligned} V_2 &= e^{i\omega t} (V_{coax}^+ + V_{coax}^-) \\ I_2 &= \frac{e^{i\omega t}}{Z_0} (V_{coax}^+ - V_{coax}^-) \end{aligned} \quad (3.15)$$

Here V_{coax}^+ and V_{coax}^- are amplitudes of the wave traveling through the coax, right and left, respectively. The voltage and current across the sample are denoted by V_x and I_x

$$\begin{aligned} V_x &= e^{i\omega t} (V_{coax}^+ e^{-\gamma L} + V_{coax}^- e^{\gamma L}) \\ I_x &= \frac{e^{i\omega t}}{Z_0} (V_{coax}^+ e^{-\gamma L} - V_{coax}^- e^{\gamma L}) \end{aligned} \quad (3.16)$$

where γ is the complex propagation constant on the coaxial transmission line of length L .

The propagation constant $\gamma = \alpha_{trans} + i\beta_{trans}$ where α_{trans} is the attenuation constant (0.15

nepers/meter at 5 GHz for UT-085 coaxial cable) and $\beta_{trans} = \frac{\omega\sqrt{\epsilon_r}}{c} = \frac{2\pi}{\lambda}$ is the

propagation factor. Note that the sample is still modeled as a series capacitor C_x and

resistance R_x with complex impedance $Z_x = R_x + \frac{1}{i\omega C_x}$. At the coupling capacitor we have

$I_1 = I_2$ and $V_1 - V_2 = I_1 Z_{cap}$. From this equation and the equation for voltage $V_1 = I_1 Z_{res}$, I

get $Z_{res} = \frac{V_1}{I_1} = Z_{cap} + \frac{V_2}{I_2}$ and $\frac{V_2}{I_2} = Z_2 = Z_0 \frac{(V_{coax}^+ + V_{coax}^-)}{(V_{coax}^+ - V_{coax}^-)}$. From this equation and

equation (3.16) I get

$$Z_x = Z_0 \frac{(V_{coax}^+ e^{-\gamma L} + V_{coax}^- e^{\gamma L})}{(V_{coax}^+ e^{-\gamma L} - V_{coax}^- e^{\gamma L})} \quad (3.17)$$

Combining equations (3.16) and (3.17) I get a final equation for Z_{res} and this equation can be put back into the equation for calculation of V_{diode} (given by equation (3.14)). The resonator impedance Z_{res} is given by:

$$Z_{res} = Z_{cap} + Z_0 \left[\frac{(Z_x + Z_0)e^{\gamma L} + (Z_x - Z_0)e^{-\gamma L}}{(Z_x + Z_0)e^{\gamma L} - (Z_x - Z_0)e^{-\gamma L}} \right] \quad (3.18)$$

Fig. 3.5 shows the behavior of Q and Δf signals as the R_x (sheet resistance of the sample) is varied. Different curves represent different C_x values used to calculate these results. The key parameters that can be varied are the source power (V_S and I_S), temperature dependent attenuation constant α (the curves in Figure 3.5 assume $T=300$ K). The Q versus R_x curve in Fig. 3.5a, still satisfies the condition that the minimum occurs where $\omega C_x R_x = 1$, and qualitatively it shows the same behavior as the lumped element model (Fig. 3.2a). The Δf versus R_x from the transmission line model (Fig. 3.5b) shows very similar behavior to the lumped element model (Fig. 3.2b). The different C_x values show different Δf contrast; higher the C_x value, higher is the Δf contrast.

The strength of the transmission line model lies in giving quantitative results, since experiment can be modeled to great precision by including frequency dependent effects, dielectric losses in cables (which I ignored here), and the effect of all the microwave

devices used in building the circuit. However, the lumped element model is much simpler and more insightful compared to the transmission line model.

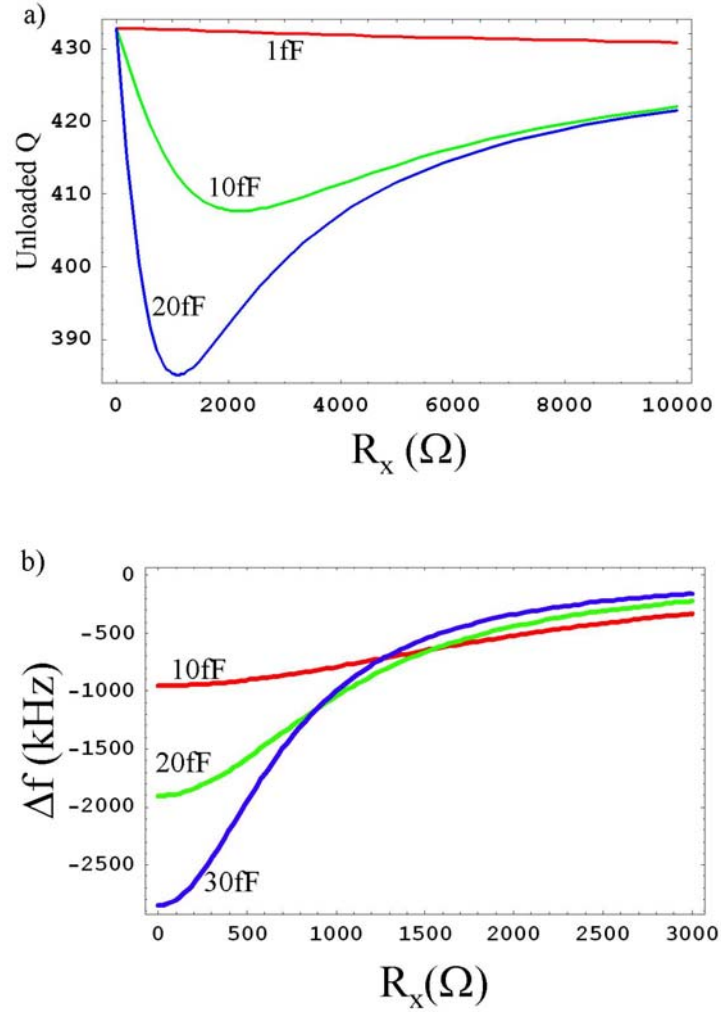


Fig. 3.5: a) The unloaded Q versus R_x calculated from the transmission line model for different C_x . The minimum again occurs at $\omega C_x R_x = 1$; b) Δf versus R_x calculated from transmission line model (the point of inflection occurs at $\omega C_x R_x = 1$).

3.2.3 Propagating Wave model of Impedance of a Thin Film over a Substrate

In general, the measurements by NSMM are conducted over a thin film on a substrate. To understand the signal response, the multilayer structure of the sample has to be considered. In this section I discuss the effect of a tri-layer structure (film/dielectric/metal) which is a typical geometry of the sample used in measurements with the NSMM.

When a plane propagating wave is incident on a substrate, the impedance Z of the surface (on which the wave is incident) is given by the ratio of tangential electric and tangential magnetic field at the interface, for example $Z = \frac{|\vec{E}_x|}{|\vec{H}_y|}$ (see Fig. 3.6a for axes). The problem

is very simple when the medium beyond the interface is infinite (marked semi-infinite medium in Fig. 3.6a). In such cases the surface impedance of a semi-infinite good conductor ($\sigma \gg \omega\epsilon$) in the local limit is given by

$$Z_{surface} = \frac{1}{\sigma\delta}(1+i) \quad (3.19)$$

where δ is the skin depth, σ is the conductivity, and the quantity $1/(\sigma\delta)$ is known as the surface resistance⁶⁵ R_s . In the case of a semi-infinite lossy dielectric the surface impedance is given by

$$Z_{surface} = \frac{Z_0}{\sqrt{\epsilon_r}}(1 + \frac{i}{2} \tan \Theta) \quad (3.20)$$

and the above equation is true in the limit when $\sigma \ll \omega\epsilon$. The quantity

$$\tan \Theta = \frac{\omega \varepsilon'' + \sigma}{\omega \varepsilon'} \quad (3.21)$$

is called the loss tangent of the dielectric⁶⁴.

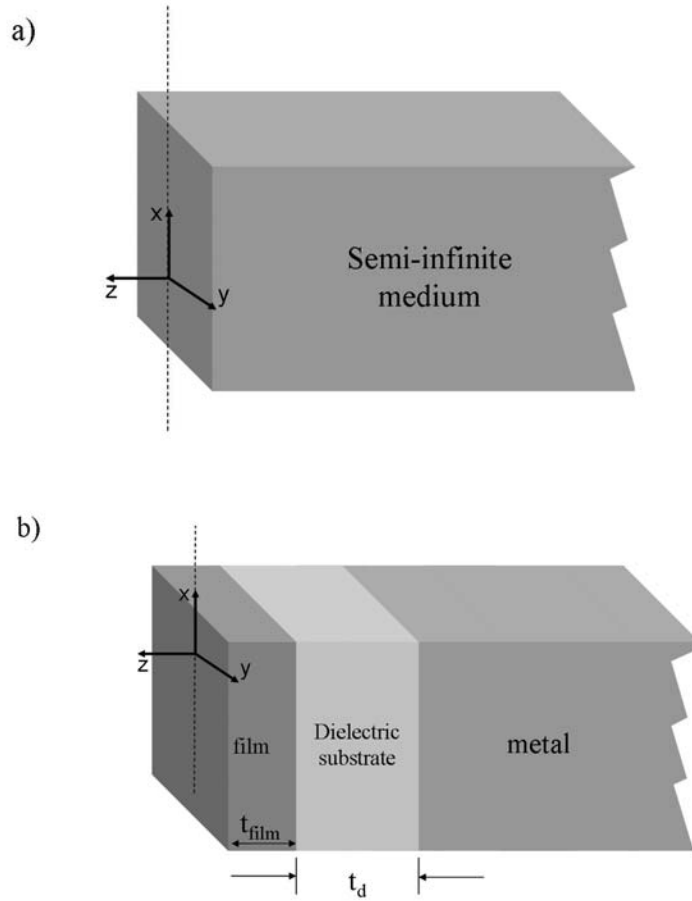


Fig. 3.6: a) Diagram of a semi-infinite medium showing the coordinate axes, where $Z = \frac{|\vec{E}_x|}{|\vec{H}_y|}$; b) Diagram of the tri-layer structure to clarify the typical geometry of a thin film

measurement. The film is on top of a dielectric substrate which sits on top of an infinite metal (which is the copper puck as discussed in chapter 2). The model keeps the complex dielectric constant of the dielectric and the resistivity of the film and metal.

However, when dealing with multi-layered structures (for example a thin film/dielectric substrate/metal trilayer structure in Fig. 3.6b) then the impedance is not that simple. The reflections from each interface complicate the problem, as there can be standing waves set up inside the substrate or film due to these reflections. The general equation for the effective impedance looking into the l^{th} layer is given by⁶⁶:

$$Z'_l = Z_l \frac{Z'_{(l-1)} + iZ_l \tan(k_l t_l)}{Z_l + iZ'_{(l-1)} \tan(k_l t_l)}, \quad (3.22)$$

where the primed quantities are effective quantities and the unprimed ones are bulk quantities, where t_l is the thickness of the l^{th} layer and k_l is the wave number in the l^{th} layer. The quantity Z'_l is measured during an experiment, in the case of an infinite plane wave excitation. This shows that even for thin film/substrate/metal structure, the equations are very complex and in an experiment one measures the effect of substrate and metal behind it. The effective impedance Z'_{film} for such a film/substrate/metal structure is written as (Fig. 3.6b)

$$Z'_{\text{film}} = Z_{\text{film}} \frac{Z'_d + iZ_{\text{film}} \tan(k_{\text{film}} t_{\text{film}})}{Z_{\text{film}} + iZ'_d \tan(k_{\text{film}} t_{\text{film}})}, \quad (3.23)$$

where the effective impedance of the dielectric is given by

$$Z'_d = Z_d \frac{Z'_{\text{metal}} + iZ_d \tan(k_d t_d)}{Z_d + iZ'_{\text{metal}} \tan(k_d t_d)}, \quad (3.24)$$

where $Z'_{metal} = \sqrt{\frac{i\mu_0\omega}{\sigma_{metal}}}$, which is the surface impedance for a bulk metal. In the limit (called the thin film approximation⁶⁶) where, $|k_{film}t_{film}| \ll 1$ (physically it means that the thickness of the film much smaller than the wavelength) and $|Z'_d| \gg \omega\mu_0 t_{film}$ (physically it means that the penetration depth is much longer than the film thickness) then the complicated equations above simplify to⁶⁶

$$\frac{1}{Z'_{film}} = \frac{t_{film}}{\rho_{film}} + \frac{1}{Z'_d} - \frac{i\mu_0\omega t_{film}}{(Z'_d)^2}. \quad (3.25)$$

In this situation the effective impedance that one measures is just a parallel combination of the sheet resistance of the film, i.e. $R_x = \frac{\rho_{film}}{t_{film}}$, the effective impedance of the substrate

Z'_d , and a correction term $\frac{iZ_d'^2}{\mu_0\omega t_{film}}$. This equation justifies our treatment of thin film

samples in the lumped element model discussed below. It is possible to create a situation where only the first term on the RHS of Eq. (3.25) dominates, in which case the effective impedance is simply the sheet resistance of the film, R_x , and I illustrate this with a plot shown in Fig. 3.7. The figure illustrates how an ideal measurement should have a one-to-one relationship with the materials property R_x (straight line in Fig. 3.7). However, due to the tri-layer structure (film/dielectric/metal) the measured values are a convolution of materials property and geometry of the sample (the curve which saturates in Fig. 3.7).

This thin film approximation was achieved, for example, in the Corbino reflectometry measurements of resistive and superconducting thin films by James C. Booth^{26,89}. However, the thin film approximation is not easy to achieve in every experimental situation. As can be seen from equations (3.21) and (3.23), getting the materials information of the film (when dealing with propagating wave models) is not an easy task and is still work in progress for the NSMM measurement

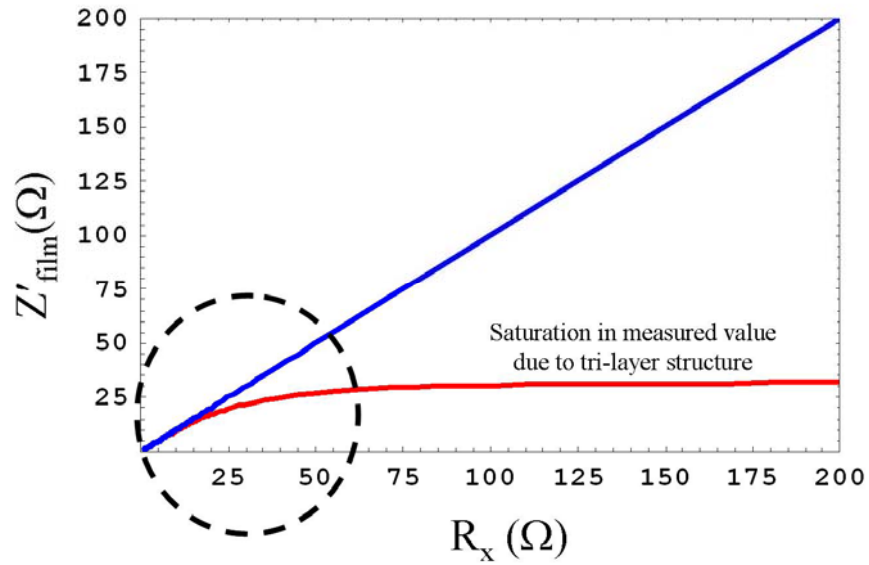


Fig. 3.7: The measured impedance Z'_{film} versus R_x for thin resistive film on LaAlO_3 substrate on top of bulk copper metal. The straight line is the ideal curve that the NSMM should measure if the multi-layer structure effect was not there. The saturated-curve is what is measured due to the tri-layer structure, at least in the propagating mode model. The dashed circle is where the thin film approximation can hold.

3.3 Evanescent (non-propagating) waves

As I discussed at the end of the last section, in the context of near-field measurements, the propagating wave models are insufficient to fully extract physical information (materials property) of the sample. This means that when the tip-to-sample separation with the NSMM is nominally 1 nm (with the help of STM feedback), evanescent wave contributions cannot be ignored (as mentioned in chapter 1), and this is what motivates this section.

The particular physical model that I studied for the source fields is one of a conducting sphere above an infinite conducting plane^{62, 63}. In section 2.4, I showed clearly embedded spheres at the end of many STM tips which are used in the microscope, and this model gets its initial motivation from there. The idea is that the source (conducting sphere in the model of radius R_0 shown in Fig. 3.9) is brought near the sample (initially the sample is modeled as a semi-infinite conductor^{62, 63}) a distance much smaller than R_0 , and the fields are calculated. The ultimate goal of the model is to calculate the dissipated power and stored energy in the sample, since that will help me calculate the Q and the Δf of the microscope. Let me explain the model and calculation in some detail, since getting to the point of calculating the dissipated power and stored energy in the sample is not trivial.

3.3.1 Spatial wave vectors on the air-conductor boundary:

In order to calculate the above mentioned quantities, as a first step, let me link this sphere-above-the-plane problem with the language of Fourier Optics, which was developed in chapter 1. Let me start with equation (1.6), which allows me to write the field as a scalar quantity in the Helmholtz equation or the wave equation, as was discussed in section 1.1 for the near-field. For now, ignore the sphere and just consider the air-conductor boundary. The following two equations are the wave equations for the air and conductor (schematically shown in Fig.3.8), for a scalar field represented by U , as shown by equation (3.26) and (3.27),

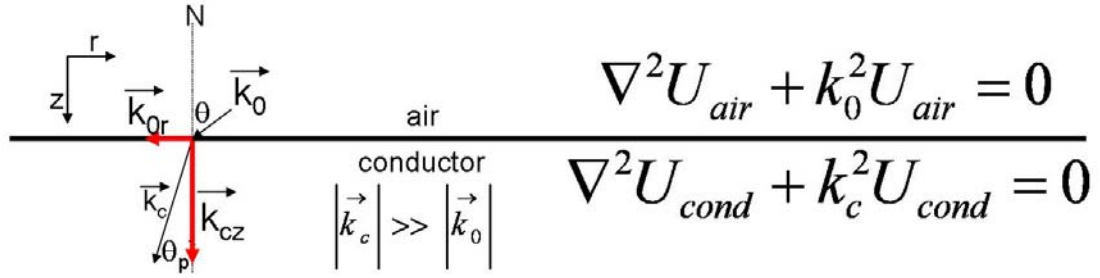


Fig.3.8: The schematic showing the wave vector decomposition for an incident wave vector k_0 at the air-conductor boundary. The two equations in each region show the relation of the wave vectors to the scalar fields in the region. The r and z mark the coordinate system and N labels the normal.

$$\nabla^2 U_{air} + k_0^2 U_{air} = 0 \quad (3.26)$$

$$\nabla^2 U_{cond} + k_c^2 U_{cond} = 0 \quad (3.27)$$

where k_0 is the wave vector in air, and k_c is the wave vector in the conductor. At the interface between the two media (and this is true for both propagating and non-propagating waves), the boundary condition requires that the lateral component of the wave vector crosses the interface continuously i.e.,

$$\vec{k}_0 \times \vec{n} = \vec{k}_c \times \vec{n} \text{ or } |k_0| \sin \theta = |k_c| \sin \theta_p \Rightarrow \theta_p = \sin^{-1} \left[\frac{|k_0|}{|k_c|} \sin \theta \right] \quad (3.28)$$

where k_0 and k_c are the complex for air and conducting space, respectively (equations 3.26 and 3.27), and θ_p and θ are shown in Fig. 3.8. The red vectors in Fig. 3.8 are marking the components of the vector k_c , where $k_c^2 = k_{cz}^2 + k_{0r}^2$ and hence k_{cz} can be written as

$$k_{cz} = \sqrt{k_c^2 - k_{0r}^2} ; \quad (3.29)$$

This k_{0r}^2 is the same as $k_x^2 + k_y^2$ in equation (1.11). Just like in section 1.1, the solutions are propagating waves when $k_{0r}^2 < k_c^2$ and the solutions are non-propagating when $k_{0r}^2 > k_c^2$ where the k_c for the conductor is given by the equation

$$k_c^2 = \omega^2 \epsilon \mu \left(1 - \frac{i\sigma}{\omega \epsilon} \right) \quad (3.30)$$

For propagating waves, k_{0r} is nearly negligible compared to k_c (which follows straight from the geometry of wave vectors at the interface via the equation $\vec{k}_0 \times \vec{n} = \vec{k}_c \times \vec{n}$ and the good conductor limit $\sigma \gg \omega \epsilon$) so one can easily make the following approximation in the near-field:

$$k_{cz} \approx k_c \quad (3.31)$$

In the near-field limit, for the non-propagating waves (evanescent waves) k_{0r} can be comparable or even larger than k_c and we don't have the liberty to use equation (3.31). This means that in order to find the dissipated power and stored energy in the sample the contribution due to these high spatial wave-vectors (high valued k_{0r}) are important. Hence, I need to integrate the Poynting vector over all possible values of k_{0r} . This means that I should find the fields as a function of k_{0r} in order to find the angular spectrum similar to equation (1.10). What follows next is the process to get there and the first step is to get the fields in free space.

3.3.2 Calculation of Capacitance and Fields between a sphere and infinite conductor

In the case of the NSMM, the probe is acting like a source, and it is modeled as a sphere of radius R_0 , and the sample is represented as an infinite conducting plane (in the radial direction), as shown in Fig. 3.9. As a starting point, the potential on the sphere is set to a constant V_0 . The infinite conducting plane is left at zero potential. In the image charge method, the potential on the sphere can be thought of as arising from a charge q given by $q = 4\pi\epsilon_0 R_0 V_0$, which is taken (for the purposes of electrostatics calculations) to be at the origin of the sphere. At this stage the whole problem is just one charge q a distance $h+R_0$ away from the infinite conducting plane. In the method of images, the conducting plane is

removed by putting an image charge $-q$ which re-establishes the original zero potential on the infinite plane.

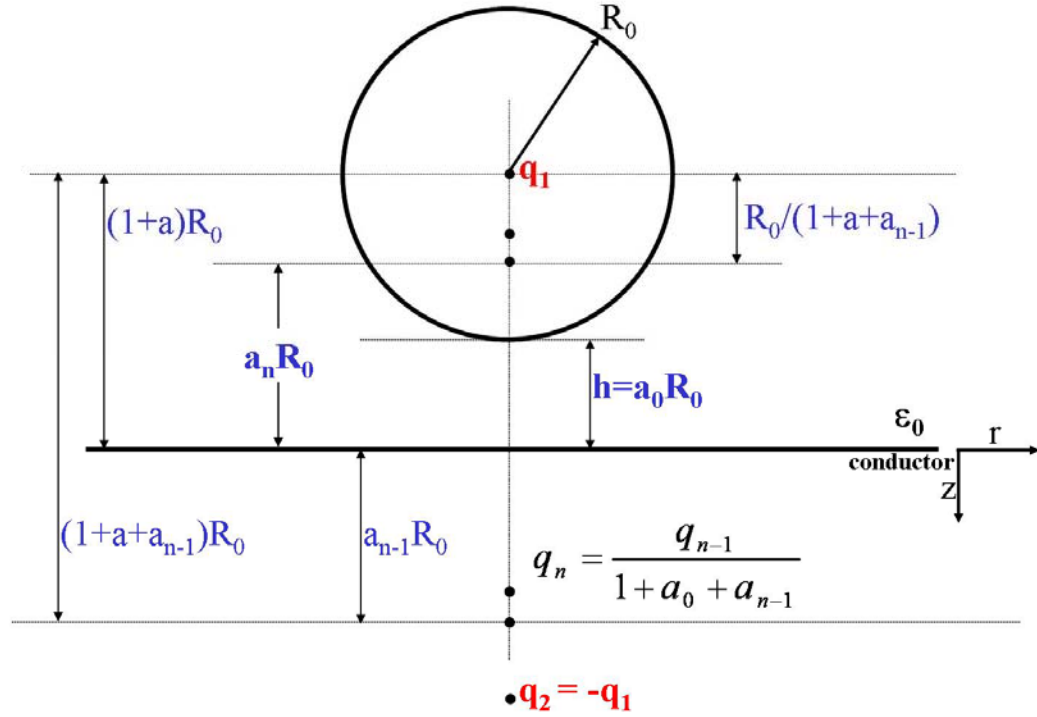


Figure 3.9: The sphere above the plane model. The dark lines represent the border of the sphere and infinite plane. The quantities close to double arrows are representing different important length scales in the problem used in order to calculate the fields. The r and z are marking the coordinate system (please note that positive z is downwards the page). The n in subscripts are marking the iteration count.

At the second step, the image charge $-q$ now disrupts the equipotential surface on the conducting sphere (with the conducting infinite plane removed) and this in turn calls for another image charge to restore that surface to an equipotential. At this stage, the image charge q' is placed inside the sphere due to this $-q$ (again establishing the potential V_0 at the spherical boundary). Then given these charges q and q' inside the sphere, the image

charge method is repeated to make the infinite conducting plane an equipotential. Only the first two steps of the process are shown schematically in Fig. 3.10.

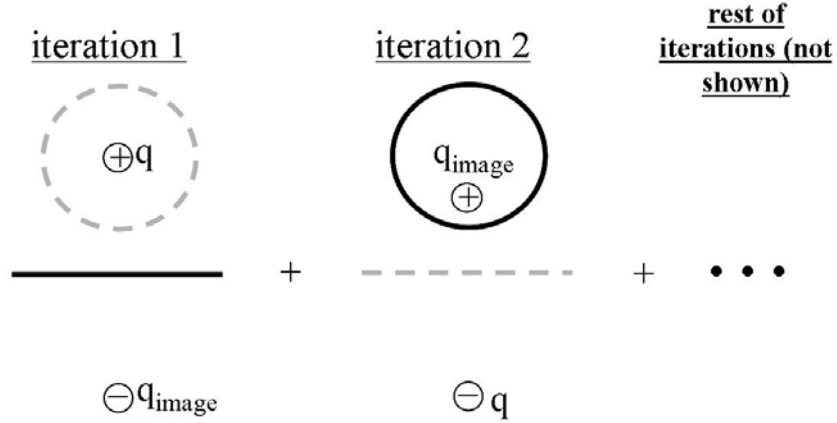


Figure 3.10: First two iterations of the image charge method. In iteration 1, the minus charge q_{image} is the same distance away from the plane as the positive charge q . As the process goes on, charges change in magnitude and position, getting smaller in magnitude and closer to the bottom surface of the sphere and to the metal surface. I have found that after about 200 iterations the value of capacitance quickly starts to converge. To save time, I kept the number of terms between 200 and 300 for most of the calculations.

In principle, one should keep an infinite number of terms to get the real physical fields between the sphere and the plane. However, I have found that beyond 200 iterations the value of physical quantities derived from the model remain within 1% of the value at the 200th iteration. In order to save time, I generally truncate the series around 300. The capacitance and the static electric field in the region between the sphere and infinite plane is given by the following equations, where n is counting the number of iterations:

$$C = \left(\sum_{n=1}^{\infty} q_n \right) / V_0 \quad (3.32)$$

$$\vec{E} = \frac{1}{4\pi\epsilon_0} \sum_{n=1}^{\infty} q_n \left\{ \frac{r\hat{r} + (z + a_n R_0)\hat{z}}{(r^2 + (z + a_n R_0)^2)^{\frac{3}{2}}} - \frac{r\hat{r} + (z - a_n R_0)\hat{z}}{(r^2 + (z - a_n R_0)^2)^{\frac{3}{2}}} \right\} \quad (3.33)$$

where the cylindrical coordinate system of r and z is defined in Fig. 3.9. The n^{th} image

charge value q_n and position a_n are given by $q_n = \frac{q_{n-1}}{1 + a_0 + a_{n-1}}$ and

$a_n = 1 + a_0 - \frac{1}{1 + a_0 + a_{n-1}}$ respectively and $a_0 = \frac{h}{R_0}$, where h is height of sphere above

infinite plane. I can get the electric field at the surface of the sample, by putting $z=0$ in equation (3.33):

$$E_s = \frac{2}{4\pi\epsilon_0} \sum_{n=1}^{\infty} \frac{a_n q_n R_0}{(r^2 + (a_n R_0)^2)^{\frac{3}{2}}} \hat{z} \quad (3.34)$$

Now comes the question of getting the magnetic field at the surface of the sample. We assume that the potential of the sphere oscillates harmonically in time as $e^{-i\omega t}$. We then assume that the structure of the electric field does not change from its static value, at least for length scales near the sphere much smaller than the wavelength. The oscillating electric field gives rise to a magnetic field by induction. Let me first write the expression for the surface magnetic field (at $z=0$, denoted as H_s) given by⁶² (calculated from

$\oint \vec{H} \cdot d\vec{l} = \int_{\text{Surface}} -i\omega\epsilon_0 \vec{E} \cdot d\vec{a}$ where the electric field is from equation (3.34)):

$$H_s = -\frac{i\omega}{2\pi r} \sum_{n=1}^{\infty} q_n \left\{ \frac{[r^2 + (a_n R_0)^2]^{\frac{1}{2}} - a_n R_0}{[r^2 + (a_n R_0)^2]^{\frac{1}{2}}} \right\} \hat{\phi} \quad (3.35)$$

The magnetic field comes from displacement currents between the sphere and the sample, as well as induced currents in the sample. For now, I am going to move forward with these equations. However there are a few issues with the fields calculated in this model, which I will discuss later. Fig. 3.11 shows the schematic of how the electric and magnetic fields look like for the sphere-above-the-plane model. The electric field (Fig. 3.11a) is in the \hat{z} direction at the surface, and the magnetic field (Fig. 3.11b) is in the $\hat{\phi}$ direction. Before I move on to calculate fields as a function of spatial wave-vectors, let me point out a few key features of the fields as a function of position.

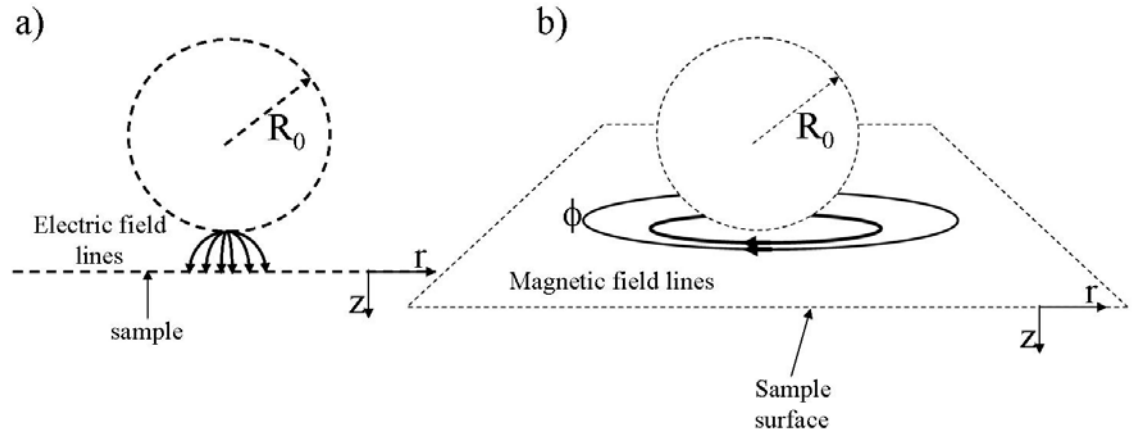


Fig. 3.11: a) The schematic to show the electric field (in \hat{z} direction) due to sphere above the infinite plane model (only the region of strongest field is shown); b) the schematic to show magnetic field in the same model (in $\hat{\phi}$ direction). The plane with dashed lines just marks the position of the infinite conductor.

Fig (3.12) and Fig. (3.13) show the electric and magnetic fields as calculated using equations (3.34) and (3.35) for different values of the sphere height above the plane, h .

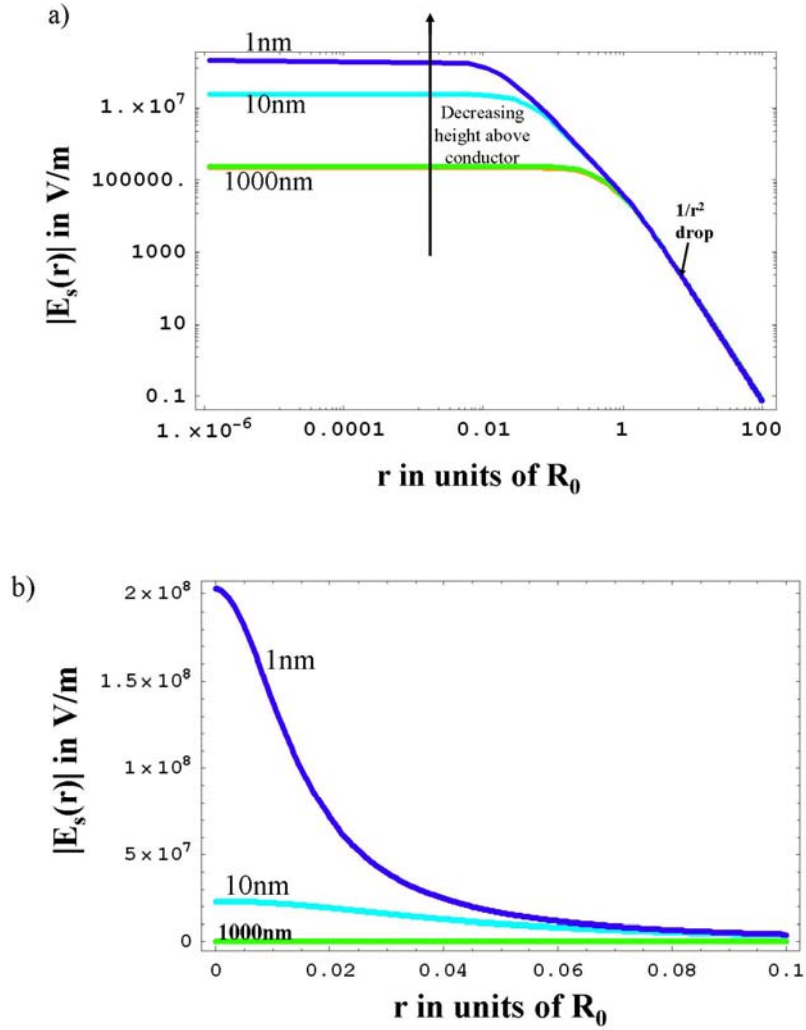


Fig. 3.12: Plot of surface electric field magnitude versus radial distance for the sphere-above-the-plane model. Different curves represent different heights of the sphere above the sample a) The behavior of the magnitude of electric field as a function of r (in units of R_0) on log-log scale; b) the behavior of electric field as a function of r (in units of R_0) on linear scale. An important point to notice is the significant increase in the magnitude of electric field as the sphere is brought closer to the sample. At large r , the $1/r^2$ drop in magnitude of electric field is consistent with equation (3.34). Plot b) clarifies the quick drop of the field as a function of r more clearly compared to a). The value of R_0 used is $10 \mu\text{m}$ and the frequency used is 7.67 GHz with 1 mW of input power.

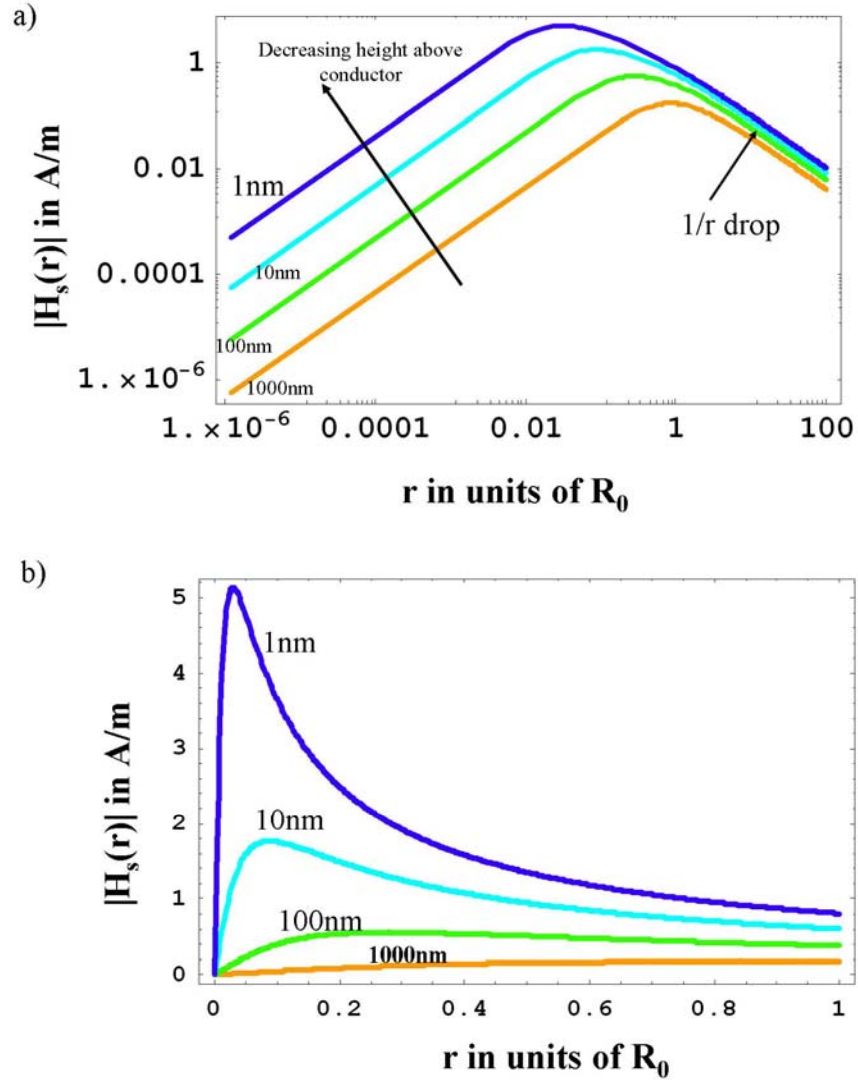


Fig. 3.13: Plot of surface magnetic field magnitude versus radial distance for the sphere-above-the-plane model. Different curves represent different heights of the sphere above the conductor a) the magnitude of magnetic field as a function of r (in units of R_0) on log-log scale; b) the magnitude of magnetic field as a function of r (in units of R_0) on a linear scale. Just like the magnitude of the electric field, the magnitude of magnetic field also shows a significant increase as the sphere comes closer to the sample. Plot b) clarifies better the changing shape of the magnitude of magnetic field as the sphere comes closer to the sample. The value of R_0 used is $10\text{ }\mu\text{m}$, frequency is 7.67 GHz , and input power is 1 mW .

The important point to note regarding both fields (Fig. 3.12a and Fig. 3.13a) is the significant rise in magnitude as the sphere is brought closer to the plane. As can be seen from Fig. 3.12a, the magnitude of electric field rises by one order of magnitude (from 10^7 V/m range to 10^8 V/m range) for a decrease of height from 10 nm to 1 nm. In a similar fashion the magnitude of magnetic field doubles for an order of magnitude drop in height (Fig. 3.13a). At the same time the magnitude of both fields drop in r very fast compared to the characteristic radius of the sphere, R_0 . For example, the electric field (Fig. 3.12b) drops to 10% of its maximum value at $r = 0.05 R_0$. The magnetic field (Fig. 3.13b) drops to 20% of the maximum value within R_0 . It is encouraging that the model predicts strong spatial confinement of the fields and this spatial confinement improves as the sphere comes closer to the sample, just like the STM tip should do (this was shown in Fig. 1.3 earlier). Now I am going to find out the fields as a function of k_{0r} (spatial wave-vectors), which is required before I am ready to calculate the dissipated power and stored energy in the sample.

3.3.3 Calculation of fields as a function of spatial wave vectors over an infinite conductor

Now I want to calculate the contribution to the fields due to high spatial wave vectors. It is useful to express the fields using the approach of Fourier optics (from chapter 1). The way I begin, is to find the magnetic field as a function of these wave vectors by taking the Fourier Transform (FT) of the magnetic field⁶³ at the surface of the infinite conductor as follows

$$\vec{H}_s(\vec{k}_{0r}) = \frac{1}{2} \int \vec{H}_s(\vec{r}) \text{Exp}[i\vec{k}_{0r} \cdot \vec{r}] d^2r \quad (3.36)$$

The final result for the magnetic field is (calculation shown in appendix D):

$$\vec{H}_s(k_{0r}) = \hat{\phi} \left\{ \frac{-i\omega}{2} \sum_{n=1}^{\infty} q_n \left\{ \frac{1}{k_{0r}} - a_n R_0 I_0 \left(\frac{k_{0r} a_n R_0}{2} \right) K_0 \left(\frac{k_{0r} a_n R_0}{2} \right) \right\} \right\} \quad (3.37)$$

where I_0 and K_0 are the modified Bessel functions^{61,90}. The plot of the magnitude of the magnetic field Fourier components as a function of these spatial wave-vectors is shown in Fig. 3.14. The different curves are for different heights of the sphere above the plane, h/R_0 . The calculation is for $\omega/2\pi = 7.5$ GHz, and sphere radius R_0 is 10 μm . The important feature in this figure is the rise in the magnitude of the high spatial frequency magnetic fields (large k_{0r}), as the sphere gets closer to the sample (both axes are logarithmic). This rise argues that at 1 nm height ($h/R_0 = 0.0001$, the pink curve in Fig. 3.14) the contribution to fields from high spatial wave vectors is significant. The magnetic field in the high k_{0r} limit drops as $1/k^3$, and in the low k_{0r} limit, it shows a negative logarithmic divergence (alternatively expanding equation (3.37) in the limit of large k_{0r} and small k_{0r} justifies these results as can be seen in equations (D.4) and (D.5) of appendix D). The dips in the magnetic field (Fig. 3.14) are due to the zero crossings between the two limits. This negative logarithmic divergence comes from the $1/r$ dependence (shown in Fig. 3.13a) of the magnetic field at large r (which is one inherent weakness in this model which needs a remedy, and I will discuss it shortly). When calculating dissipated power or stored energy in the sample, I set the location of these zero crossings as the lower limit of integration on k_{0r} .

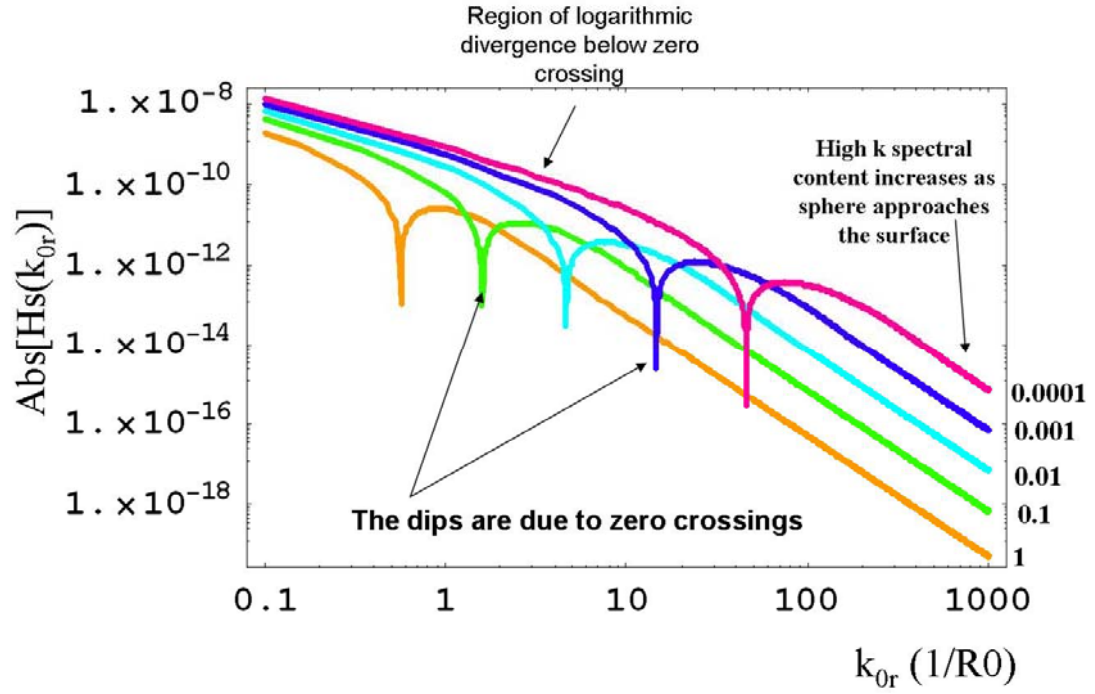


Figure 3.14: Absolute value of surface magnetic field Fourier component plotted as a function of spatial wave-vector (radial wave-number) k_{0r} . The changing parameter is h/R_0 (the values are on the right hand side of the graph). Note the significant rise in high frequency (large k_{0r}) spectral content as the sphere gets closer to the sample. The radius of the sphere is $10 \mu\text{m}$. The dips are zero crossings between the two limits discussed in Appendix D. The region below the zero crossing cannot be trusted due to a built-in weakness of the model.

Below the sphere, the other half of space is filled with an infinite conductor (sample) and I assume a propagating solution to the field⁶³ in this conducting space again given by the following equation from Fourier Optics for the surface field inside the conductor:

$$\vec{H}_c(k_{0r}) = \hat{\phi} H_s(k_{0r}) \text{Exp}[i(k_{cz}z + k_{0r}r)], \quad (3.38)$$

where H_c denotes the magnetic field inside the conductor (sample). Then using Maxwell's equations, the associated electric field is given by:

$$\vec{E}_c(k_{0r}) = \frac{\vec{\nabla} \times \vec{H}_c}{\sigma - i\omega\epsilon}, \quad (3.39)$$

$$\vec{E}_c(k_{0r}) = \frac{H_s(k_{0r})}{\sigma - i\omega\epsilon} \left[\hat{r} \left(\frac{e^{i(k_{cz}z + k_{0r}r)}}{r} + ik_{0r} e^{i(k_{cz}z + k_{0r}r)} \right) - \hat{z} i(k_{cz}) e^{i(k_{cz}z + k_{0r}r)} \right]$$

Where $\hat{n} \cdot \hat{z} = 1$ and $\hat{n} \cdot \hat{r} = 0$; (these are the unit vectors in the above equation after the cross product operation).

3.3.3 Calculation of dissipated power in infinite conducting space

In order to calculate the power dissipated in the sample, the Poynting vector $\vec{S} = \frac{1}{2} \vec{E} \times \vec{H}^*$ has to be evaluated and integrated over all spatial wave vectors k_{0r} . The real part of \vec{S} gives the dissipated power $P_{\text{dissipated}}$ in the sample (plot shown in Fig. 3.15 as a function of height),

$$P_{\text{dissipated}} = \frac{1}{2} \int \text{Re} \{ \vec{n} \cdot (\vec{E}_c \times \vec{H}_c^*) \} d^2 k_{0r} \quad (3.40)$$

The energy stored in the sample (U_{sample}) is given by (plotted as function of height in Fig. 3.16)

$$\omega U_{\text{sample}} = \frac{1}{2} \int \text{Im} \{ \vec{n} \cdot (\vec{E}_c \times \vec{H}_c^*) \} d^2 k_{0r} \quad (3.41)$$

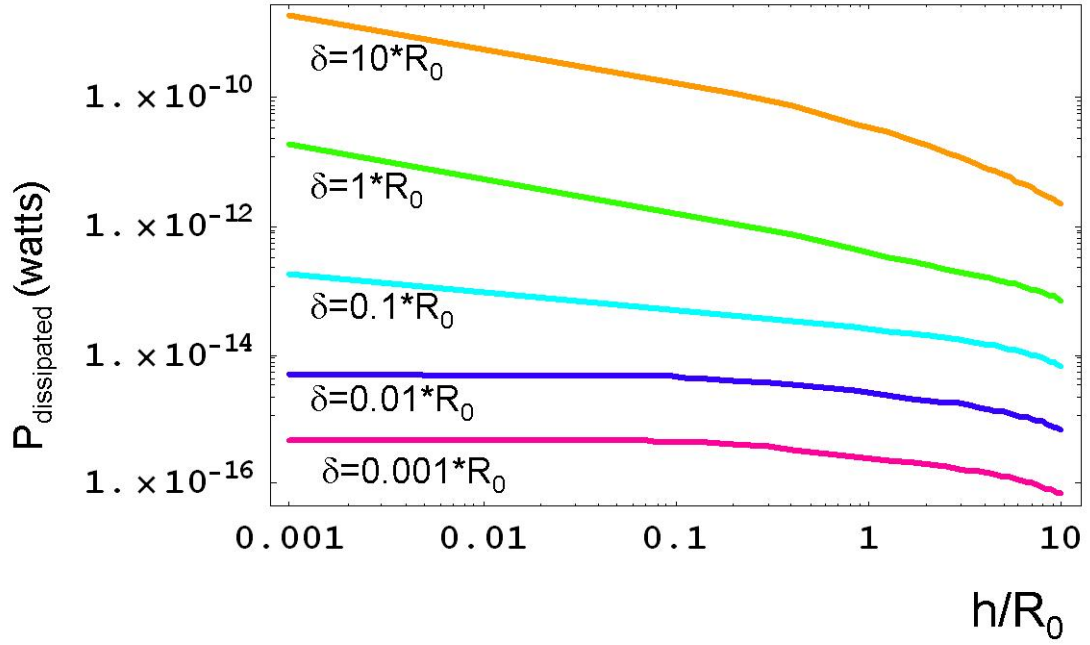


Fig.3.15: The dissipated power in the metallic sample for different skin depths δ . One sees that the higher the skin depth δ , the greater the dissipated power, for a given probe height. As the tip is brought closer to the sample, the dissipated power increases significantly due to the inclusion of more fields with high spatial wave vectors. The calculation is performed at 7.67 GHz with the power level of the source 1 mW.

An important feature to note is that for each given skin depth, the dissipated power in the sample increases as the sphere is brought closer to the sample, due to the inclusion of more fields and currents due to high spatial wave vectors. I also expect the dissipated power to increase as I increase resistivity, which is consistent with the model (increasing skin depth, δ). As far as stored energy is concerned, I expect that the stored energy in the sample will increase as the sphere comes closer to the sample. This is contrary to the results seen from

the calculation (see in Fig. 3.16). In any case, according to the model calculation, the contribution to stored energy due to evanescent waves is very small. This calculated stored energy is roughly eleven orders of magnitude smaller compared to the stored energy in the resonator (the ωU_{stored} in the resonator is estimated to be 28.3×10^{-3} Watts at 7.67 GHz). Hence this contribution to the frequency shift is almost certainly too small to measure, since experimentally the measurement resolution⁹¹ is $\delta f/f \sim 0.1 \times 10^{-6}$. There is a peak in ωU_{stored} versus h/R_0 at the point where skin depth δ , equals the height of sphere above the sample. This could be due to the enhanced fields when the skin depth δ , is comparable to the decay length of evanescent waves (the $H_s(r)$ in Fig. 3.13a shows this enhancement).

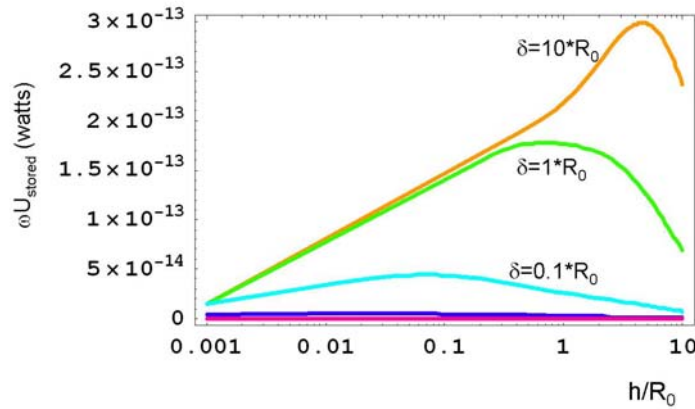


Fig. 3.16: The energy stored in the sample times the angular frequency ω versus the height of the sphere above the plane for different values of the skin depth in the sample. Interesting features are, 1) very little energy is stored in the sample when the sphere is near the conductor (the ωU_{stored} in the sample is 28.3×10^{-3} W, which is 11 orders of magnitude higher), 2) the energy stored is maximum when the height is equal to the skin depth δ . This could be due to enhanced field strengths when the skin depth is comparable to the decay length of evanescent fields from the sphere. The calculation is performed at 7.67 GHz, with a source power of 1 mW.

3.3.4 Calculation of Δf and Quality Factor for infinite conductor sample

The next important step to take with this model is calculation of the measured quantities, namely Δf and Q . The Q is related to the dissipated power and stored energy is as follows:

$$\Delta\left(\frac{1}{Q}\right) = \frac{P_{\text{dissipated}}}{\omega U} \quad (3.42)$$

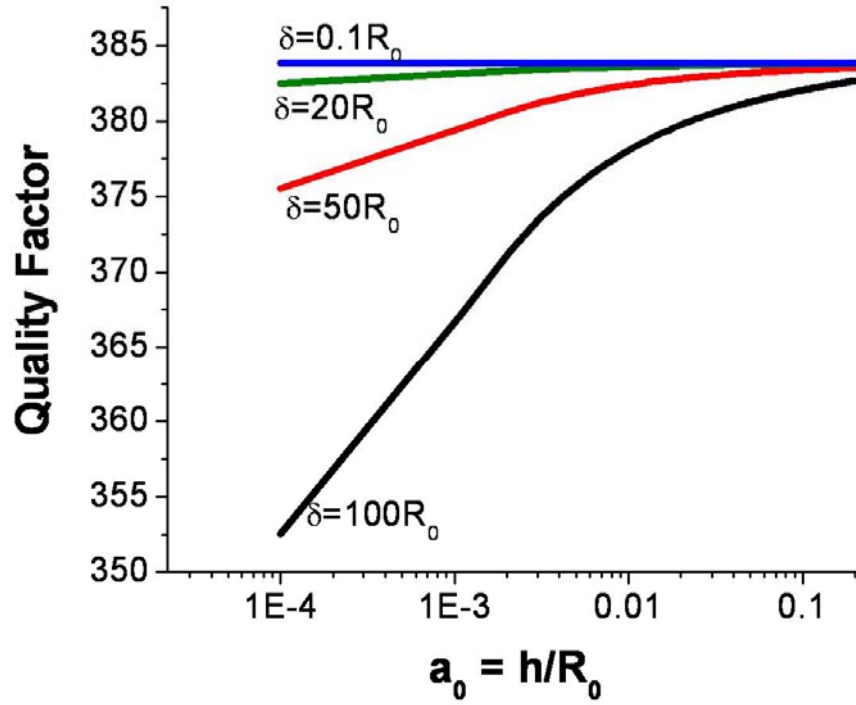


Figure 3.17: The Q calculated from the evanescent wave model as a function of sphere to sample distance h/R_0 for different skin depths of an infinite conductor sample. The R_0 used is 10 μm . The result predicts that the higher the resistivity (higher skin depth), the greater the drop in Q . The frequency of calculation is 7.67 GHz with 1 mWatts of input power.

Here U is the energy stored in the resonator and sample, ω is the frequency of the driving signal, and Δ refers to a change in the reciprocal of the quality factor due to the presence vs. absence of the sample. I would expect the Quality factor to be lower (the drop in Q to be higher) when the resistivity is increased, which is consistent with the results shown in Fig. 3.17. The drop in Q is higher for more resistive materials compared to good metals. A good metal (like Cu) has a skin depth δ on the order of $1\text{ }\mu\text{m}$ at 7.5 GHz , which shows no drop at all in Fig. 3.17 (blue curve). This result is consistent with our data on gold thin films, shown in Fig. 4.4. The R_0 used for the calculation is $10\text{ }\mu\text{m}$. Since I am using good metal tips (Silver coated Tungsten), I assume that the drop in Q due to the tip is negligible, hence the tip is well represented by a perfectly conducting sphere. The next step is to calculate the Δf versus height of sphere above the sample.

The frequency shift Δf can be calculated as the ratio of stored energy in the sample and between the tip and the sample, compared to the total energy stored in the microscope (approximated by just the energy in the resonator) as follows:

$$\frac{\Delta f}{f} = -\frac{U_{\text{sample}} + \frac{1}{2}C_x V^2}{U_{\text{resonator}}} \quad (3.43)$$

where C_x is the capacitance between the sphere and the infinite conductor (assuming that both are perfect conductors) and V is the potential of the sphere, and here Δf refers to change in resonant frequency between a height of 1 nm compared to $2\text{ }\mu\text{m}$ away. The

second term in the numerator of Eq. (3.43) accounts for the capacitive energy stored in electric fields between the tip and sample. The contribution from each term is shown in Fig. 3.18. The major contribution comes from the capacitance, calculated from the image charge method for the sphere-above-the-plane model. The stored energy in the metal due to high-spatial frequency wave vectors are not making a significant contribution to Δf . The capacitance model makes the prediction that Δf contrast gets larger as the height of the probe above the infinite plane is reduced, as shown in Fig. 3.19.

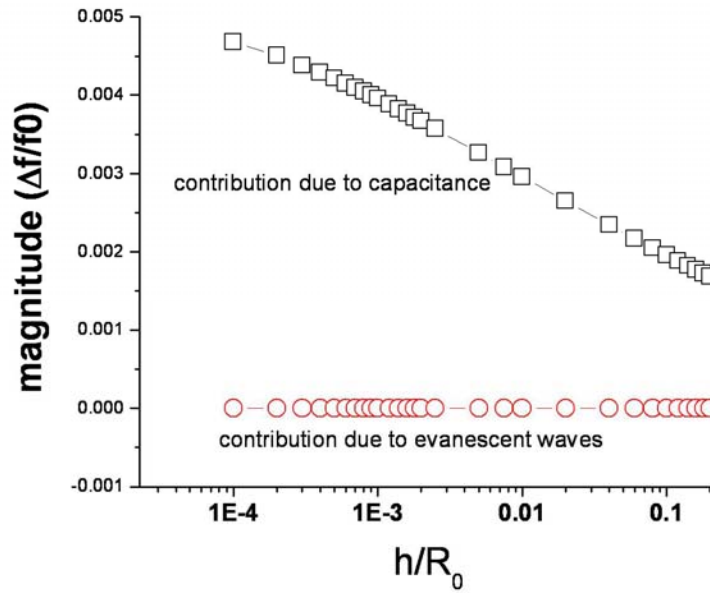


Fig. 3.18: Plot of contributions to $\Delta f/f_0$ from external capacitance (open-squares) and internal stored energy (open-circles) versus probe-sample separation. Most of the contribution to the Δf comes from the capacitance, where the capacitance is calculated from the image charge method of sphere above the plane model

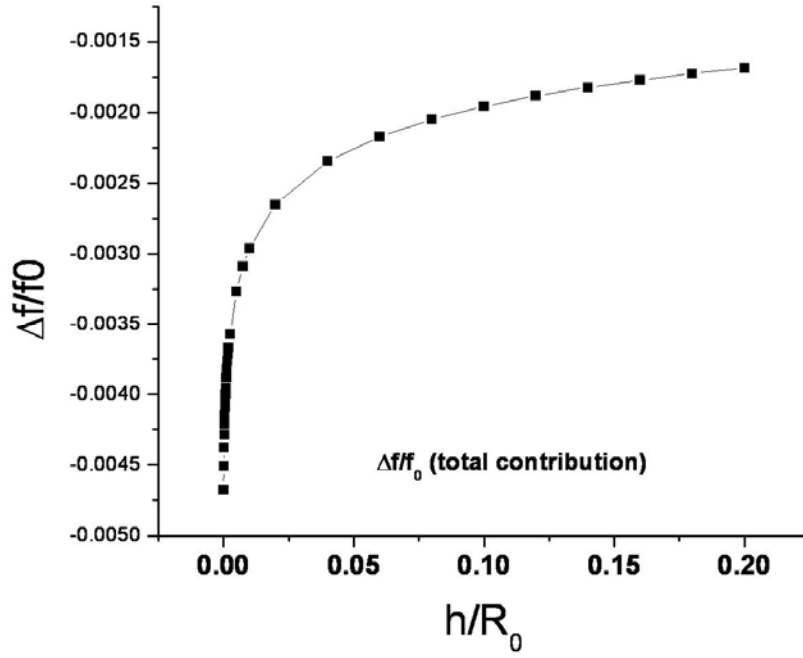


Fig. 3.19: Predicted frequency shift as a function of height from the evanescent wave sphere-above-the-plane model with sphere radius of 10 μm . Most contribution to the Δf signal comes from the $\frac{1}{2}(CV^2)$ external capacitance term.

3.3.5 Logarithmic behavior of capacitance as a function of height above sample

The capacitance expression from the image charge for the sphere-above-infinite-plane method converges to⁶²

$$C = 4\pi\epsilon_0 R_0 \sinh(\alpha) \sum_{n=1}^{\infty} \frac{1}{\sinh(n\alpha)} \quad (3.44)$$

where $\alpha = \cosh^{-1}(1 + \frac{h}{R_0})$, where R_0 is the sphere radius and h is the height of the sphere

above the infinite plane. The capacitance calculated from this expression shows a logarithmic drop as the sphere height above the sample increases as shown in Fig. 3.13.

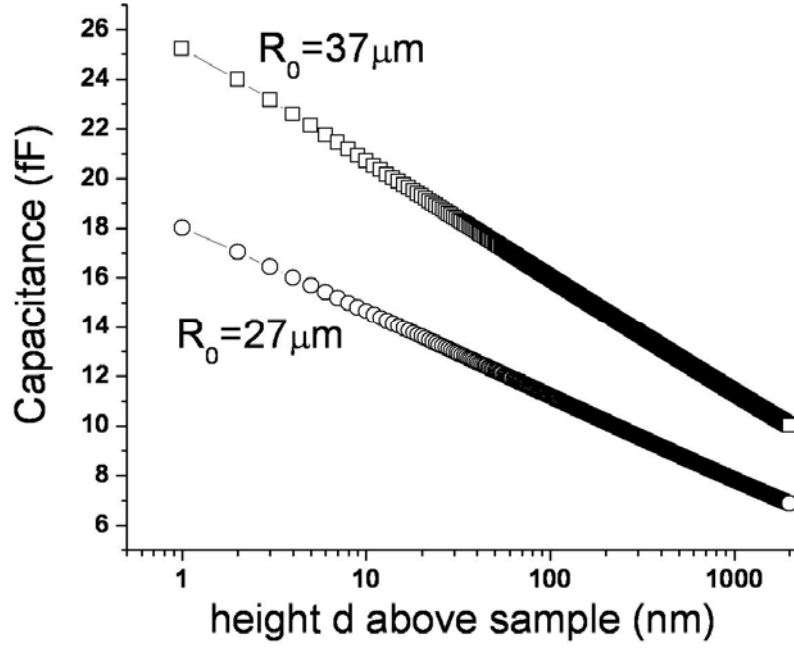


Fig.3.20: The logarithmic behavior for the capacitance from the image charge method. The data from *Mathematica* evaluation of Eq. (3.44) is shown here for two different R_0 values. The slope change is expected from equation 3.44.

To see where the logarithmic dependence comes from, one can approximate the sum in Eq. (3.35) as an integral. The indefinite integral can be evaluated exactly as

$\int \frac{dx}{\sinh(ax)} = \frac{1}{a} \ln(\tanh(\frac{ax}{2}))$ and the integral becomes

$C = 4\pi\epsilon_0 R_0 (\sinh \alpha) \left[\frac{1}{\alpha} \ln(\tanh(\frac{n\alpha}{2})) \right] \Big|_1^\infty$. Once substituting for the limits, the

capacitance goes as $\frac{1}{\alpha} \ln(\tanh(\frac{\alpha}{2}))$, i.e. $C = 4\pi\epsilon_0 R_0 (\sinh \alpha) \left[\frac{1}{\alpha} \ln(\tanh(\frac{\alpha}{2})) \right]$. The first term

in the Taylor series of $\tanh(\alpha/2)$ is $\alpha/2$, if $|\alpha/2| < \pi/2$ ⁶¹. The first term in the Taylor expansion for $\alpha = \cosh^{-1}(1+h/R_0)$ is $\ln(2(1+h/R_0))$ ⁶¹. The leading term for the Taylor expansion of $\ln(1+h/R_0)$ is just h/R_0 (for $h/R_0 \ll 1$)⁶¹ which shows that in the limit of small h/R_0 the capacitance is proportional to $\ln(h/R_0)$, hence the final expression for C (when $h/R_0 \ll 1$) is

$$C = 4\pi\epsilon_0 R_0 \left[\frac{1}{\alpha} \ln\left(\frac{0.693}{2} + \frac{h}{2R_0}\right) \right] (\sinh \alpha). \quad (3.45)$$

This result is consistent with the numerical simulations of a sphere above a plane as well (section 3.4). The Δf data (which can be interpreted as purely dependant on capacitance as seen in equation (3.8)), also shows this logarithmic trend as a function of height⁹¹, and I have seen this above all the samples for all the tips, as will be discussed in Chapter 4.

3.3.6 Weaknesses in the sphere-above-an-infinite-plane model and proposed corrections

There are several problems with the model discussed in section 3.3. One problem with this model is that it performs the calculation for bulk metal, rather than the multilayered

structure which is measured in a typical NSMM experiment. I think the best way to fix this is to follow the recipe of plane wave reflection and transmission calculation for stratified media⁹⁴. Under this recipe the schematic of my problem is shown in Fig. 3.21 (the problem is solved for a general case allowing N layers). Each horizontal line represents the boundary between the two media, where each region is labeled (air is 0, film is 1, dielectric is 2 and metal is 3, and it is assumed the metal is semi-infinite in z and such that a plane wave just transmits into the metal, never to return). The r and z show the coordinate system and k_{0z} represents the wave-vector incident on the film.

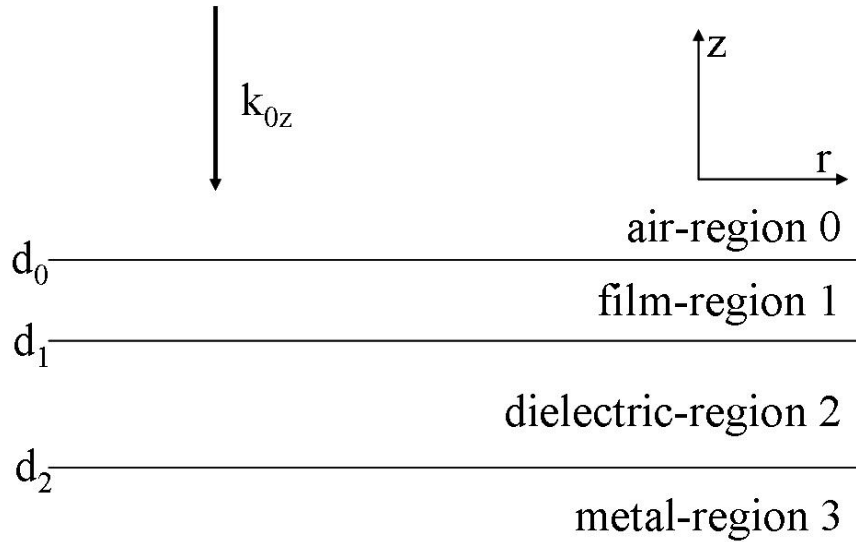


Fig. 3.21: The schematic for the calculation of reflection and transmission of plane waves from stratified media (multilayered structures). The horizontal lines represent the boundaries of the media and the d represents the position of the interface in space. The coordinate system is defined by r and z . The k_{0z} is a representative vector drawn for clarity and in general k_{jz} is the wave-vector in each region where j represents the region number of the medium.

The equation for the reflection coefficient η at the top surface is given by:

$$\eta = \frac{e^{i2k_{0z}d_0}}{\eta_{01}} + \frac{(1 - \frac{1}{\eta_{01}^2})e^{i2(k_{1z}+k_{0z})d_0}}{(\frac{1}{\eta_{01}})e^{i2k_{1z}d_0}} + \frac{e^{i2k_{1z}d_1}}{\eta_{12}} + \frac{(1 - \frac{1}{\eta_{12}^2})e^{i2(k_{2z}+k_{1z})d_1}}{(\frac{1}{\eta_{12}})e^{i2k_{2z}d_1}} + \eta_{23}e^{i2k_{2z}d_2} \quad (3.46)$$

where $\eta_{j(j+1)} = \frac{1 - \frac{\epsilon_j k_{(j+1)z}}{\epsilon_{j+1} k_{jz}}}{1 + \frac{\epsilon_j k_{(j+1)z}}{\epsilon_{j+1} k_{jz}}}$, and ϵ_j denotes the permittivity of j^{th} layer (j denotes the

region number), and k_{jz} represents the wave-vector in the j^{th} layer. This will make the calculation time cumbersome, however, it will take away the first weakness of the model by modifying the field equations given by equations (3.38) and (3.39).

A second problem with this model is that the electric and magnetic fields are not determined from Maxwell's equations self-consistently. The correct way will be to calculate the magnetic field using Maxwell's equations where the electric field is taken from equation (3.33). However, the magnetic field calculated this way diverges as r goes to 0 ($H(r) \sim 1/r$ for small r). Since, the purpose here is to get information on small length scales, it is essential to have fields which behave well as r goes to 0. The other option is to use the equation (3.35), where the magnetic field is well behaved (it goes as r as r goes to 0). The equation (3.35) is calculated from the electric field equation (3.34), where artificially the z dependence is ignored⁶². The equation (3.35) for surface magnetic field shows a $\sim 1/r$ drop in magnetic field at large r , but I fix that problem by introducing an

arbitrary cut-off at large r (as I discussed earlier in section 3.3.3). The way I intend to fix this is to seek an alternative problem to consider besides a sphere-above-the-sample. In this context, the problem of a radiating electrically small dipole antenna located near an interface between two media⁹⁵ is promising. The problem is also solved for a three layer structure⁹⁶. One advantage that this problem offers is that it is a full-wave self-consistent solution to Maxwell's equations in both media (it includes evanescent wave contributions as well). The second advantage is that it includes the reflection coefficients η , as part of the calculation, so I will not need to make any corrections of the type as seen in equation (3.46). However, this model still is far from trivial, for example, there are disagreements in the literature on significant details of calculations related to high spatial wavevectors⁹⁷.

3.4 Numerical Simulations

For many electromagnetic problems, it is very difficult to get analytical solutions. For such problems it is very essential to resort to numerical techniques, and for such cases I used numerical techniques as well to model the NSMM. The software used is Ansoft Maxwell 2D (M2D), which is an interactive package for analyzing electric and magnetic structures for static cases. Here I use the approximation that in the near-field limit ($h \ll \lambda$), the fields have quasi-static structure¹⁰⁶, hence static calculations are justified. The numerical simulations were done in collaboration with undergraduates Greg Ruchti, Marc Pollak, and most recently Akshat Prasad.

One particular situation where analytical models are not helpful is shown in Fig. 3.23. Here we consider the effects on the electric fields and capacitance of adding a conical protrusion at the end of a sphere. Such protrusions can be there if the tip picks up a particle during scanning, or there can be one left from the manufacturing process of the tip (see Fig. 2.26 for an example of such cone at the end of WRAP082 tip)⁹². Adding a protrusion to the numerical model of the sphere is easier than adding it to the analytical model.

In the M2D model we drew a sphere (and because of azimuthal symmetry only a 2D cut is needed, which reduced the calculation time significantly), within a given box with the boundary condition of the electric field vector being tangent to the boundary. With other types of boundary conditions (called balloon boundary where either total charge is zero at infinity or voltage is zero at infinity) I found most of the field lines to terminate at infinity as well. As a result the capacitance values were ridiculously small. The CAD drawing of the model is shown in Fig. 3.22. The software basically calculates the capacitance between the sphere and plane (labeled sample in Fig. 3.22).

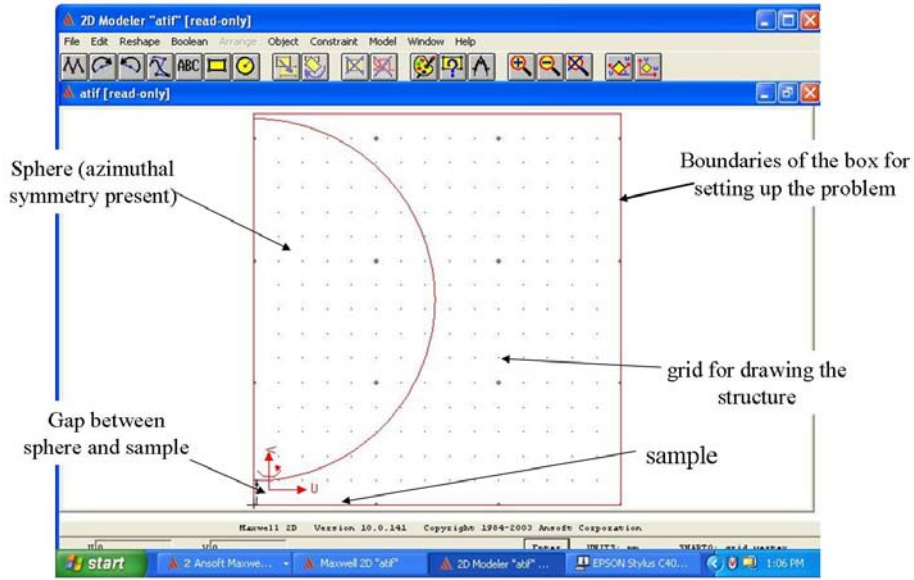


Fig.3.22: CAD drawing of a sphere above a conducting plane in M2D. This program calculates the electric potential, electric fields, and capacitance between the sphere and the sample. The sphere, grid, and the box of drawing is labeled here from the M2D user interface. The lower boundary of the box is the sample, and the rest of the boundaries have conditions imposed on them (for example, the tangential electric field condition discussed in the text).

Once we added the perturbation (a tiny cone at the end of the sphere) we found that for the sphere above the plane model, we get a deviation of the capacitance from the logarithmic dependence on height (see Fig. 3.23). This logarithmic dependence of capacitance on height is consistent with the analytical model, as was discussed in 3.3.6. The deviation is coming from the added cone (with height d_{pert}), which causes the capacitance to saturate to a lower value compared to the case of no cone being present. The larger the d_{pert} , the smaller the value of saturation capacitance, which is what I would expect, since a larger d_{pert} is effectively increasing the distance of the sphere from the sample.

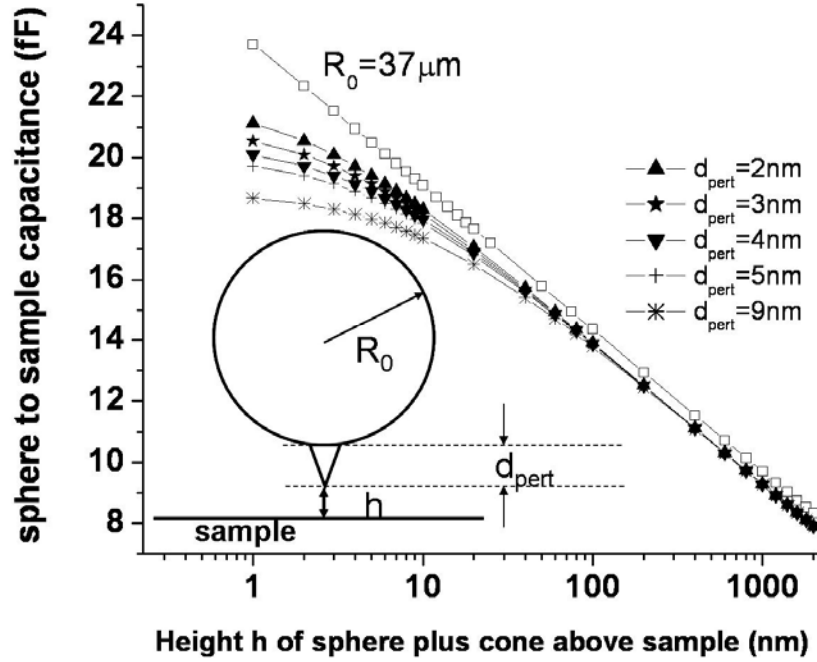


Fig. 3.23: Numerical calculation of the sphere-to-plane capacitance as a function of height from M2D. A deviation from the logarithmic behavior of capacitance as a function of height is seen after adding the cone perturbation to the sphere. The open squares represent values without the perturbation cone. The rest of the curves correspond to different d_{pert} values as shown in the legend.

The results of the software matched with the analytical results except for a certain offset (see Fig. 3.24) in the absolute value of the capacitance, which was caused by the limited size of the box (this will be discussed in Fig. 3.25). The solid line is the result from the image charge method of the sphere above the infinite plane (Eq. (3.32)), and the open squares are the data from M2D calculations. The slopes from the two calculations (-4.62

fF/nm from analytical versus -4.68 fF/nm from numerical) are very similar, as can be seen in the Fig. 3.24.

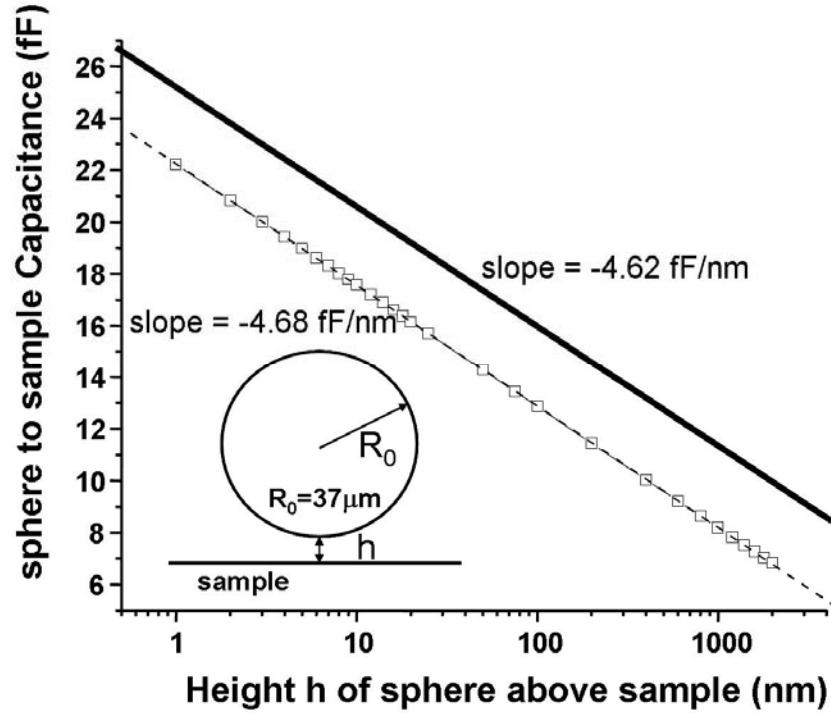


Fig.3.24: The comparison of analytical to numerical models for capacitance of sphere above the plane model. The offset is due to limited box size used in numerical simulations. The solid curve is the analytical model, and the open squares are the M2D simulations.

We did a systematic study to confirm that the offset is due to the finite box size of the calculation (Fig. 3.25). We changed the size of the box systematically and calculated the capacitance as a function of height for a given radius R_0 of the sphere. It is found that all of the points for a given height fall very close to a single straight line when plotted as

capacitance vs. the inverse of the box area. In the limit of infinite box size, the capacitance values became very similar to the numerical values within 1.5%, as shown in Fig. 3.25.

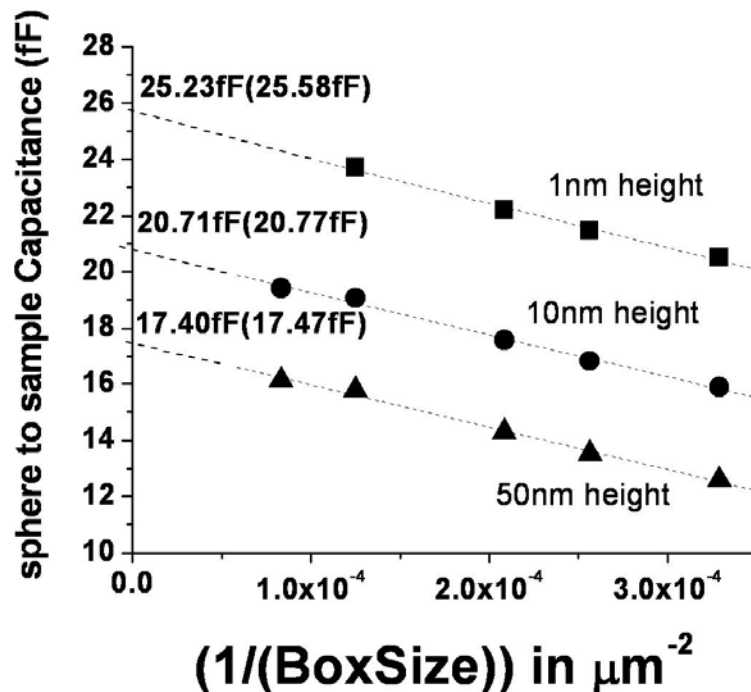


Fig. 3.25: Calculation of the sphere-to-sample capacitance vs inverse box size in the M2D calculation. The points at a given height are extrapolated to infinite box size (dashed lines) and the intercept value is given in units of fF. The values in parentheses are from the analytical image charge method. The figure shows that in the limit of infinite box size (0 on the horizontal axis), the analytical and numerical results agree within 1.5%.

The major strength of the numerical models for NSMM are their ability to solve problems for which seeking analytical solutions would have been very time consuming and challenging. For example, adding the cone would have made calculating the fields and capacitance from the analytical model very challenging. The other significant strength is to

be able to plot the field lines (as well as magnitude) for situations of interest (electric field for the sphere above the infinite plane model) in free space or inside a material of interest. However, one major shortcoming of numerical models is the aspect ratio issue. Aspect ratio is defined as the ratio of the largest length scale in the drawing to the smallest length scale. This effectively means that we cannot solve problems numerically that have both wavelength scale (mm to cm) and nm scale features simultaneously present in the problem. For example, I cannot draw the whole coaxial cable and STM tip (objects on millimeter and micrometer size) and then get the information on vector fields, magnitude of fields and currents on the surface of the sample on nanometer length scales (which naturally means that evanescent wave calculations containing high spatial frequency information cannot be made). According to the user manual for Ansoft M2D, the maximum aspect ratio is 10000, however sometimes it is possible to push it to values twice as great. The user can come up with smart ways to circumvent certain problems in the drawing to gain qualitative understandings. For example, the inset of Fig. 3.26 shows the drawing of a conical tip and coaxial cable, in which only 2100 μm of the coaxial cable was kept in the problem. I needed this to develop more trust in the logarithmic dependence of the capacitance with height. As Fig. 3.26 suggests, down to a tip-sample distance of 100 nm, the capacitance does show the logarithmic dependence with height.

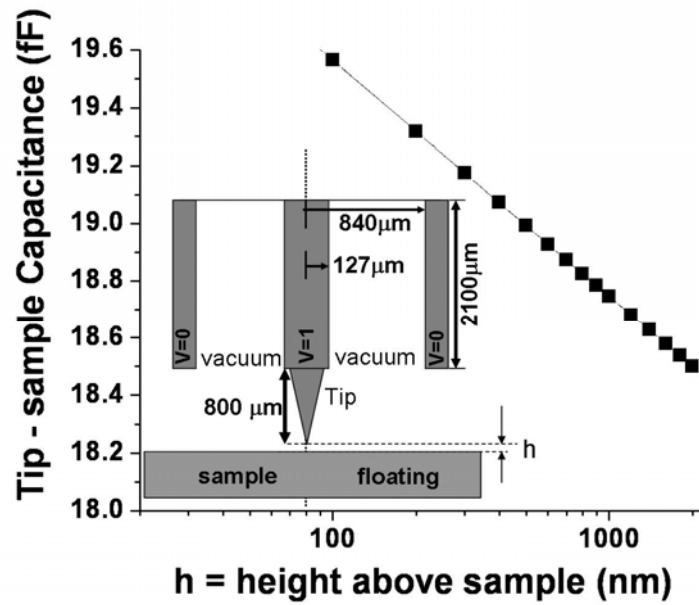


Fig. 3.26: The capacitance versus height for the conical tip and small piece of coaxial cable. The numerical results even for this more realistic geometry show logarithmic dependence of capacitance as a function of height. The calculation runs into aspect ratio limitations for heights h less than 100 nm.

3.5 Conclusions from different models of NSMM

The modeling of NSMM is a complex and challenging problem of electrodynamics. As can be seen in this chapter, no single tool was sufficient to understand the behavior of the microscope, and the models are still evolving.

Chronologically, I started with transmission line model, which was good from a practical computation point of view, however, it did not leave me with simple equations to think

about. This becomes an impediment in thinking about the data and designing new microscopes. I moved to the lumped element models to remove this weakness, because the equations were much simpler. However, both these models were insufficient when it came to visualizing the fields and developing a microscopic understanding of how the microscope worked. I was resorting to numerical techniques in parallel to understand the field structure and learning by trial and error (with the help of undergraduates mentioned earlier) what works and what doesn't work. As far as static calculations were concerned results were in general satisfying, specifically for calculation of capacitance and static fields. However, numerical techniques could only go so far due to the limitations that I discussed in section 3.4. In search for a good analytical model I came across the sphere above the plane model. It had the electro-dynamic aspect to it apart from the static aspect, and initially I felt that all the problems are resolved. However, as I discussed in section 3.3.6, this model has its shortcomings, although it was good to be able to analytically calculate the dissipated power in a material and study it as a function of materials property. In order to remove the short comings of this model, now I have come across the new models of lateral electromagnetic waves⁹⁵⁻⁹⁷ of a radiating dipole above a conducting plane, which looks like a very promising direction. I am looking forward to grinding through the equations to see what improvements are made and what else is needed to understand the results from different samples of interest.

Chapter 4

Contrast of Near-Field Microwave Signals

4.1 Introduction

In this chapter, my main goal is to understand the tip-sample interaction, especially in the region where that separation is 2 μm or less (the 2 μm restriction is due to limited range of STM piezo in the Z-direction).

As the height of the tip above the sample is decreased, the tip to sample coupling increases via the capacitance between the probe and the sample. Roughly the last 100 nm above the sample are very interesting for this novel NSMM. First, the capacitance with height may show deviations from the logarithmic behavior (which is discussed in section 3.4) in the last 100 nm above the sample. Second, contributions to physical quantities of interest increase significantly due to high spatial frequency wave vectors (Fig. 3.14). In this chapter, I discuss first the height-dependent contrast of frequency shift (Δf) of the resonator and the Quality factor (Q) of resonator. After that I will discuss the spatial dependent contrast in Δf and Q . This spatial dependent contrast is basically the map constructed point by point (during scanning) at the nominal height of 1 nm of the tip above the sample.

4.2 Height Dependent Contrast of Δf and Q

When the tip is brought closer to the sample, the resonant frequency of the resonator goes down, since coupling to the sample increases the effective length of the resonator. As a result the frequency shift of the resonator goes more negative relative to no sample present (or 2 μm away in case of the STM assisted microscope). Note that I arbitrarily define the frequency shift Δf at 2 μm height to be 0, since this is the maximum height above the sample that tip can go to without using slip stick mechanism, as was mentioned in chapter 2. Ideally, the Δf should be defined as 0 with no sample present, however, with my set-up achieving a no sample situation is very time consuming and difficult. However, the contrast in the NSMM signal is the largest below heights of 100 nm (see Fig. 4.1), so I think, this definition is justified.

Representative data is shown in Fig. 4.1 for a conducting gold on mica thin film for two different tips. The solid lines are calculations from the sphere above the infinite plane model with appropriate values chosen for the sphere radius R_0 to fit the data. I used equation (3.8) from the lumped element model to relate the calculated capacitance to the measured frequency shift. The frequency shift signal is directly proportional to the change in capacitance C_x , as can be seen by the good agreement between the solid lines and the data points for two different tips. The Δf data (just like the capacitance due to the sphere above an infinite plane model presented in chapter 3) follows a logarithmic behavior as a

function of height. To show the dramatic drop clearly in the last 100 nm, I plot the data on a linear height scale.

One of the tips is the Pt-Ir etched tip (shown in chapter 2) from Long Reach Scientific and the other one is a W etched tip from the same company (not shown in chapter 2 since this type of W-tip was not available at the time of the tip study). However the IM probes W tip in Fig. 2.22 has a similar geometry to the Long Reach Scientific W etched tip. The multi-cone structure (see IM probes tip in Fig. 2.22) of the etched W tip is similar to the IM probes W-tip, however the dimensions are different for the two tips. The deviations from the model dependence seen for the W-tip in Fig. 4.1 are due to this multi-cone structure. The multi-cone structure makes the effective radius R_0 of the sphere in the model a function of height above the sample. In order to understand it, view the tip as an interceptor of the static electric field lines originating from the sample. If the tip equivalent capacitance geometry changes (which is happening when the tip is moved closer to the sample), the effective area of one of the electrodes of the capacitor changes, which in turn will change the capacitance. Here I am thinking in terms of parallel plate capacitor with area replaced by an effective area. Due to the multi-cone structure, the change in effective area occurs relatively abruptly at certain heights. The Pt-etch tip from Long Reach Scientific (see also Fig. 2.22) is more like a single cone and does not show any abrupt changes in its shape. The radius R_0 (for the sphere above the infinite plane model) for the W tip is 27 μm and for the Pt-Ir tip it is 10 μm , and these two different values for the R_0 are also due to the

geometry differences. I make a caveat here, that during the scanning the tip-to-sample interaction is very complex, and so tips are not always nice geometrically, the way Fig. 2.22 shows. For a soft metal Pt tip, it is very easy for it to get damaged during scanning. The reasons for damage can be many, for example, a dirt particle that the tip hits or the feedback loses control at some point. This leads to a change of geometry in an uncontrolled way, and this will be discussed further in section 4.2.4. On the same line of argument, a small feature on the surface of the sample may also cause such deviations in Δf versus height. The thin films in general have small nanometer sized grains or terraces, which locally can affect the signal, although this is harder to model.

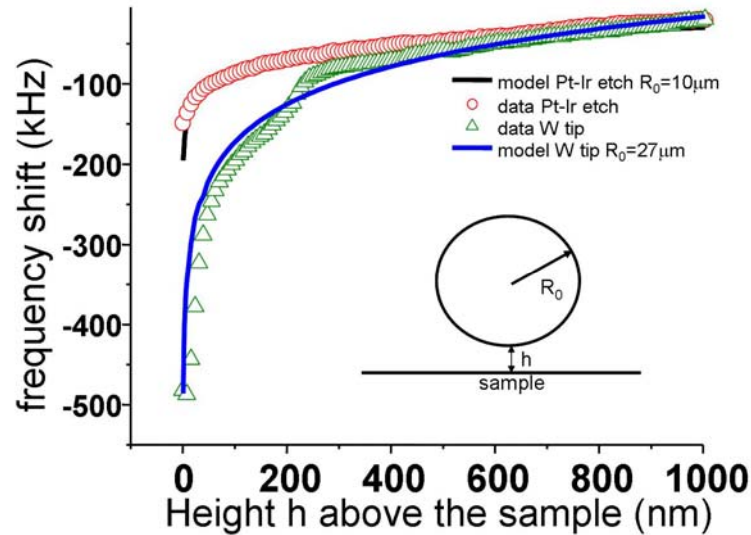


Fig. 4.1: The frequency shift contrast above a gold on mica thin film measured with the NSMM at room temperature and 7.37 GHz. The solid line is a fit to a capacitance result using the sphere above the infinite plane model with the radius of the sphere R_0 used as the only fitting parameter. The W tip is from LR (large diameter), not shown in chapter 2.

4.2.1 Contrast over bulk metal (thickness $t > \text{skin depth } (\delta)$)

In Fig. 4.2 I show contrast of Δf over bulk copper for different tips, and these tips were discussed in chapter 2. In this case the experiment was performed over the copper sample puck (also shown in chapter 2) which is 6 mm thick. The resistivity of copper at room temperature is $1.56 \mu\Omega\cdot\text{cm}^{83}$ and this gives the skin depth δ of $0.73 \mu\text{m}$ at 7.5 GHz (assuming that the bulk Cu is in the local limit). I used the low loss bulk copper for two reasons: one is to have thickness $t \gg \delta$, so I can understand the contrast over a sample which does not have the multi-layered structure; second, such a sample will bring forth the contrast of the Δf signal purely from capacitance (C_x) changes (since copper is low loss material).

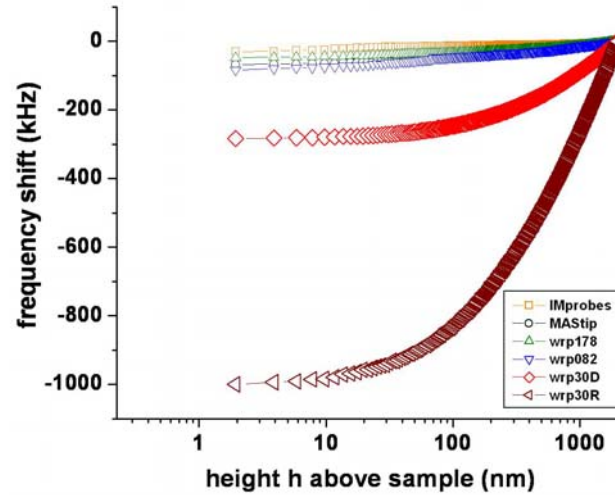


Fig 4.2: Δf signal over bulk copper at room temperature. The experiment is performed at 7.47 GHz. The different curves represent different tips that were discussed in Chapter 2. Δf is defined to be 0 at $2 \mu\text{m}$ height above the sample.

The contrast of the Δf signal is larger for tips with a larger embedded sphere radius (r_{sphere}), which is expected from the capacitance expression for the sphere above the infinite plane model. I find that R_0 is somewhat larger than the embedded sphere radius r_{sphere} , since the model sphere radius R_0 has to account for all the field lines terminating on the conical tip, rather than just the embedded sphere part. The magnitude of the frequency shift contrast between tunneling height and $2\text{ }\mu\text{m}$, defined as $\overline{\Delta f}$, is shown in Fig. 4.3. This contrast $\overline{\Delta f}$ rises roughly exponentially as a function of tip embedded sphere radius r_{sphere} , as indicated by the fit in Fig. 4.3. In general, the tips with higher embedded sphere radius (r_{sphere}) are not very good for the purposes of doing STM (discussed in Appendix A), and as a result the spatial resolution is poor. This means that I don't have the freedom to simply use high r_{sphere} tips to get maximum contrast in frequency shift.

In general, all of the tips show a logarithmic dependence of Δf on height, given by a straight line on Fig. 4.2, at least for heights above about 100 nm. The saturation that is seen in the last 10 nm (Fig. 4.2) is likely due to deviations from the sphere above infinite plane model, and will be discussed in detail in section 4.2.4. There was no drop seen in the quality factor (Q) of the microscope (Fig. 4.4) for bulk Copper. This is consistent with Fig. 3.17 for the evanescent wave model calculation, where the drop in Q gets smaller and smaller as the skin depth δ becomes smaller. For $\delta=0.73\mu\text{m}$, which is close to δ of $1\mu\text{m}$ ($0.1R_0$) in Fig. 3.17, there is no predicted drop. This behavior is also consistent with the

propagating wave models (see Fig. 3.2a and Fig. 3.5a) as well. In both figures, if the sample is low loss, the drop in Q should be zero, even if the capacitance C_x changes. It is for non-zero R_x values where the drop in Q starts to show a change due to capacitance C_x as well (different curves in Fig. 3.2a and Fig. 3.5a).

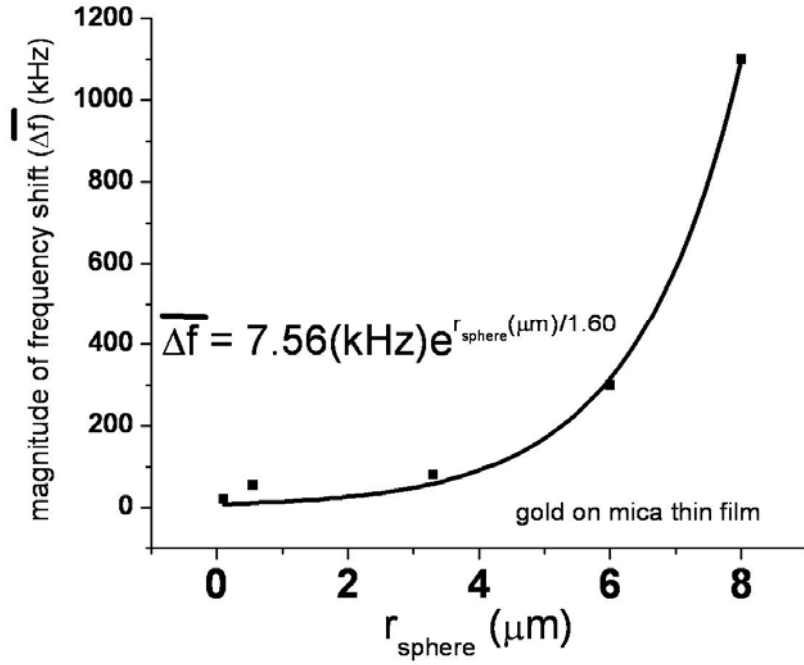


Fig.4.3: Magnitude of the Δf signal difference between tunneling height and $2 \mu\text{m}$ with different tips over bulk copper as a function of embedded sphere radius r_{sphere} . There is an approximate fit to the exponential of the data (solid line). Unfortunately, this strong contrast cannot be utilized effectively because of spatial resolution problems, as discussed in the text.

4.2.2 Contrast over thin metal (thickness (t) < skin-depth (δ))

A thin gold film on glass (nominal thickness about 2000 Å) is thinner than the skin depth, which at 7.5 GHz is about 0.83 μm in gold (resistivity at room temperature of 2.04 $\mu\Omega\cdot\text{cm}$). The Q versus height data for this thin gold film is plotted in the inset of Fig. 4.4 for many different tips, and it shows that the Quality Factor of the resonator does not change as the tip approaches the sample. This behavior is just like the behavior of bulk copper, since the gold thin film is also a very low loss sample, and based on the propagating wave model, the changes due to C_x do not show in Q for low R_x values.

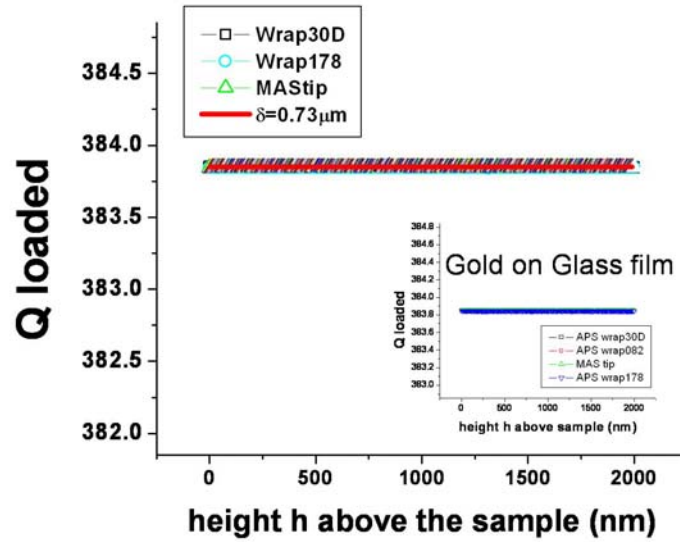


Fig 4.4: Q of the microscope versus height above the bulk copper sample for selected tips shown in Chapter 2. The solid-line (lies right on top of the data) is the fit for $\delta=0.73\mu\text{m}$ due to the evanescent wave model. The inset shows the Q versus height of the gold on glass thin film sample. The height scales are the same for both the graph and the inset.

The magnitude of the Δf signal due to different tips shows very similar behavior to that of the bulk copper. The qualitative behavior however is different for the gold on glass thin film. The slopes of the curves are smaller compared to the bulk copper case. Also, in comparison to the bulk copper case, this is a multi-layered structure with thin metal film (with thickness = 200 nm < δ = 830 nm), on top of glass substrate on top of bulk metal. The impedance seen by the microscope in this case will be the effective impedance (Fig. 3.7) which will have the effects of the dielectric substrate included in it (so the dielectric losses

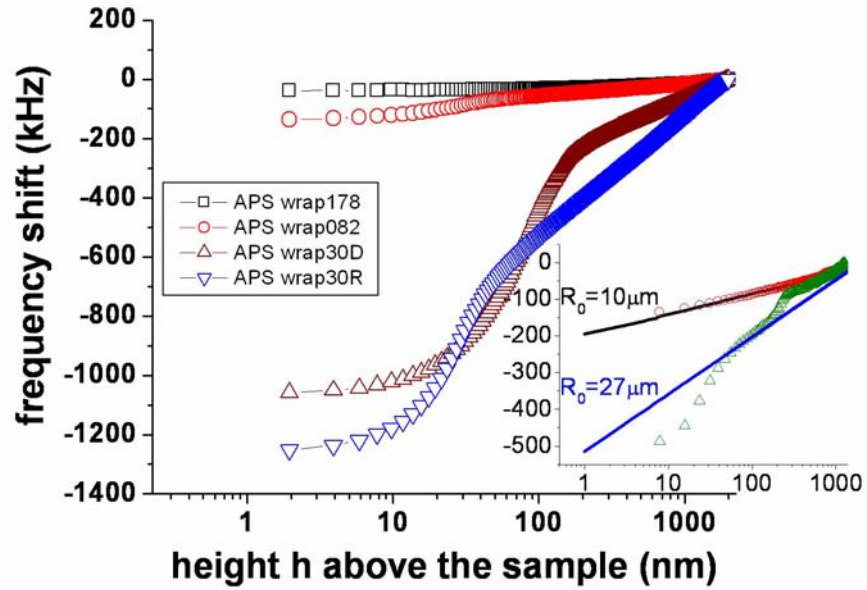


Fig. 4.5: Measured frequency shift versus height $\Delta f(h)$ ramps for a 200 nm thick gold on glass thin film sample. The shifts are measured with four different tips. The measurement is made at 7.47 GHz at room temperature. The inset shows the same data as in Fig. 4.1 on the log scale to clarify the capacitance fit based on the sphere above the plane model.

will change the qualitative behavior of the Δf versus height in comparison to the bulk copper). As was mentioned in chapter 3, it is a very challenging task to calculate the Δf and Q with propagating waves when the multi-layered structures are involved. I have plotted the Δf versus height data of Fig. 4.1 again as an inset of Fig. 4.5, to clarify the logarithmic drop of Δf versus height over thin metal sample (gold on mica), fitted to the capacitance of the sphere above the plane model. The deviations from the logarithmic behavior may be due to some local feature on the tip or sample. For a better understanding of this data, the evanescent wave contribution needs to be added to the model. In order to do so, a small dipole antenna based evanescent wave model has to be introduced⁹⁵⁻⁹⁸, where for small heights, the behavior of Δf can be calculated including the multi-layered structure⁹⁸.

4.2.3 Thin Film Materials contrast (Boron doped Silicon)

One of the samples that I studied in order to understand the response of the NSMM to the materials is a Boron doped Silicon sample. The sample was acquired through a collaboration with Neocera, Inc. A 3" diameter (n-type) Silicon wafer with resistivity $\rho > 20 \Omega \cdot \text{cm}$ at room temperature was doped with Boron at a concentration of $10^{14} \text{ ions/cm}^2$. This implant was done in a pattern on the wafer, and this pattern was in the form of stripes (of different widths) and squares (Fig. 4.6 shows the schematic of the striped section which I measured). The wafer was broken into pieces (I cannot load an entire wafer on my microscope) and the piece that I got had Boron-implanted stripes. The unit of stripe width

is 2 μm . Thus a doped stripe is 2 μm wide (almost 80 μm long but I did not measure in that direction) and it appears in between undoped regions of Silicon. The undoped region was in the form of a geometric series of 1, 2, 4...2 μm wide stripes (see Fig. 4.6 for clarity). As a result the sample only had either bare Silicon or Boron implanted Silicon.

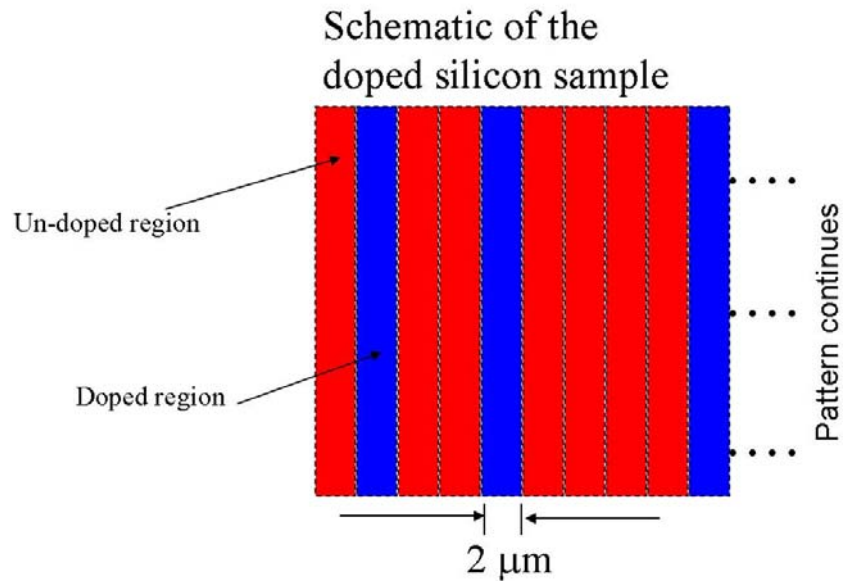


Fig.4.6: Schematic of the Neocera doped Silicon sample, showing doped regions in dark and un-doped regions in light. The undoped regions are in geometric series of 1, 2, 4...2 μm -wide stripes. The dashed lines are showing the separation between the regions.

The sample is interesting for two reasons. One is that it has almost no topography between the two materials (see the discussion in section 4.3 for the definition of ‘almost’), creating a sharp step in materials property (under AFM, the topography was just 7.5 \AA peak-to-peak across the edge as shown in Fig. 4.7). However, away from the edge the topographic level of the two regions is the same. Second, an STM tunnel junction could be easily established with this sample.

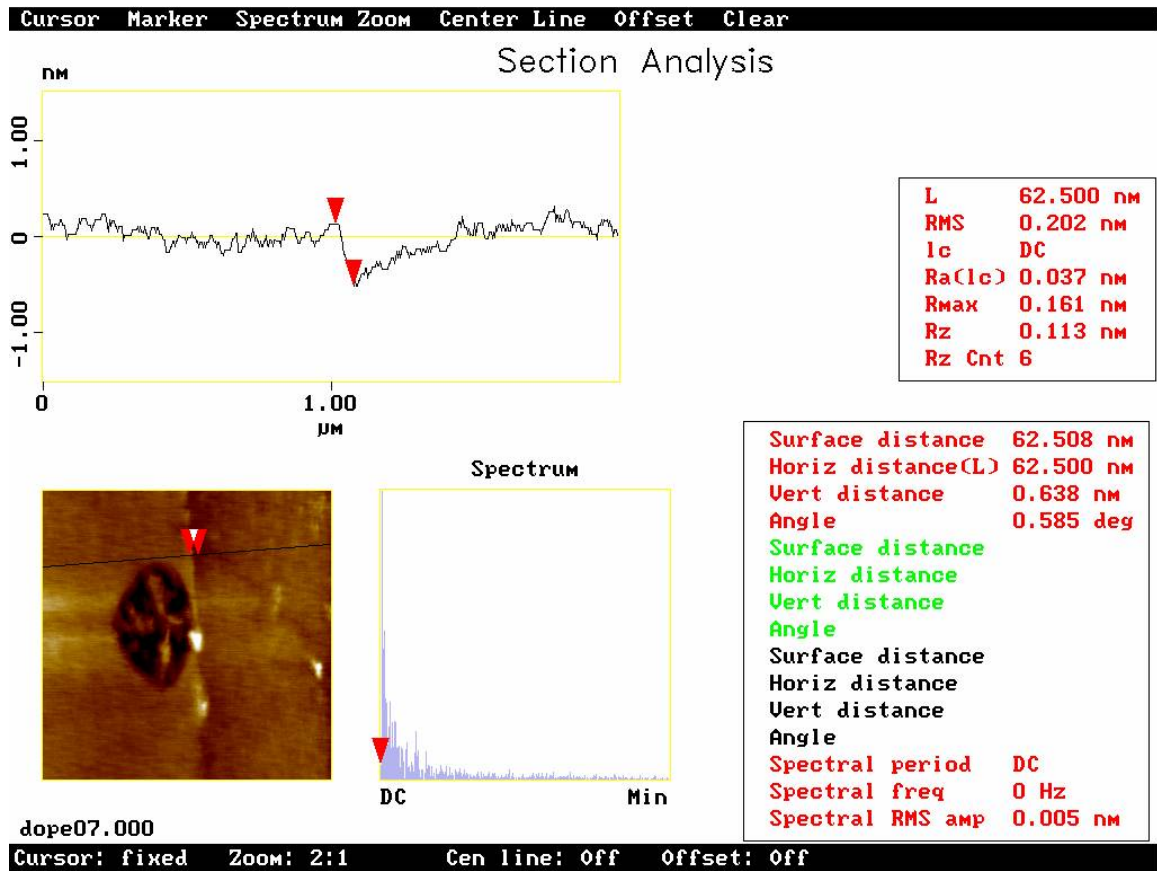


Fig. 4.7: The AFM step data between the un-doped Silicon (left) and the doped Silicon (right). The step is about 7.5 \AA high at the border of the two regions (the red triangles with vertex pointing down). The big crater is damage caused by the long term high bias that I applied on the sample during some of the experiments.

The height dependent data for the Q and Δf of the NSMM is shown in the Fig. 4.8 and Fig. 4.9 respectively. In this case the Q shows a significant drop for both the Silicon and Boron doped regions, in contrast to the data on bulk or thin film metals such as Cu and Au. The reason is that the NSMM is now measuring a lossy semiconductor with or without a thin film with non-zero R_x . The Δf also shows different contrast for the two regions. The Δf is

higher for the doped, compared to the un-doped region. This shows qualitatively the sensitivity of the NSMM to materials contrast.

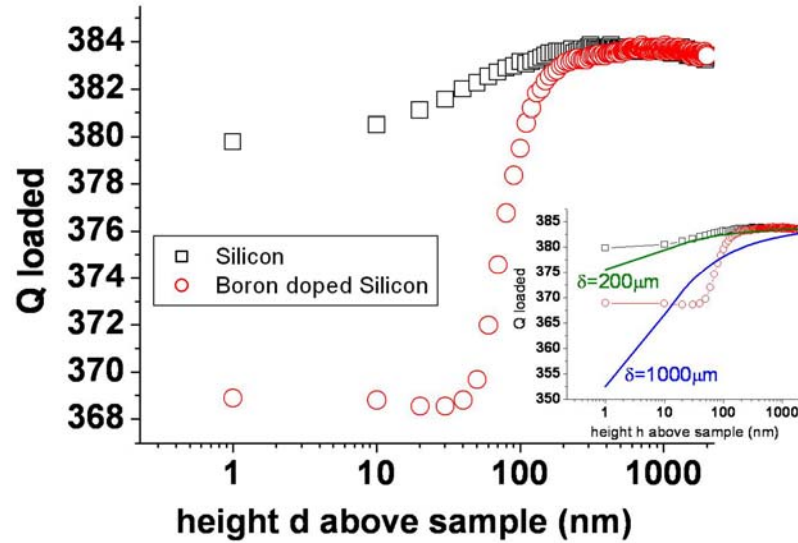


Fig.4.8: The unloaded Q versus height for a Boron doped Silicon sample at 7.67 GHz and room temperature. The red data is for the doped region, and the black for the un-doped region. In the inset, the solid lines are based on the evanescent wave model. The R_0 used for fitting the data is $10\ \mu\text{m}$.

The contrast for the Boron doped region is higher compared to the Silicon, even though the resistivity of the bare Silicon is higher than the doped region. In the model of the plane wave incident upon the sample, there are two different conditions provided by the sample. The boron doped region is a thin doped layer on top of silicon substrate, which is on top of bulk metal, again making the tri-layer structure. On the other hand, the bulk silicon is a

system of thin film on top of the infinite metal (thickness t ($550\text{ }\mu\text{m}$) $< \delta$ ($4500\text{ }\mu\text{m}$) at 7.5 GHz). So from the perspective of propagating waves, the two regions pose two different problems. For this chapter, the main purpose is to show the sensitivity of NSMM to materials contrast, where the contrast shows sharply in first 100 nm or so of the probe height above the sample. In chapter 5, I discuss the model for doped Silicon in more detail, which is based on the propagating wave model.

Even though neither the doped region of the sample, nor the un-doped region of the sample can be approximated as bulk conductors, I fit the data to the evanescent wave model to see what kind of skin depths values would fit the data (inset of Fig. 4.8). As can be seen in the inset of Fig. 4.8, I get the ridiculous result of higher δ for the low resistivity region (doped region) of the sample. The δ for the un-doped region is coming out wrong as well, as it is $200\text{ }\mu\text{m}$ (compared to the known value of $4500\text{ }\mu\text{m}$) for 7.5 GHz.

The higher contrast in the Δf data (Fig. 4.9) for the doped rather than the un-doped regions can be understood from the resistivity point of view of the two regions. As can be seen from Fig. 3.2a, the lower the R_x , the higher the Δf , which is consistent with the data in Fig. 4.9.

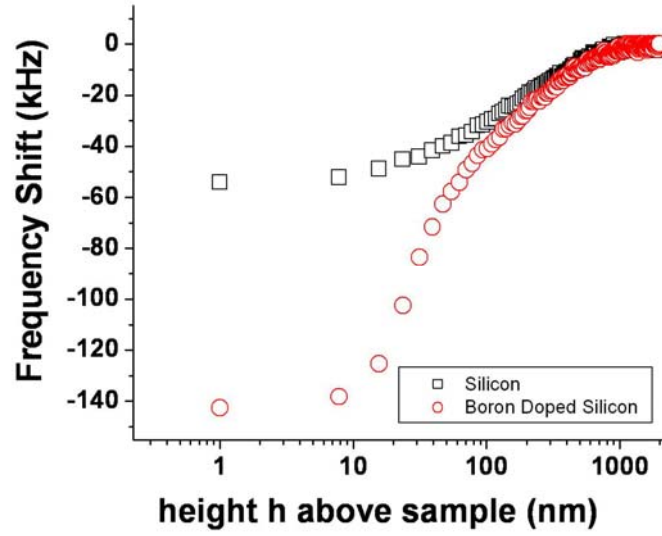


Fig. 4.9: Measured frequency shift versus height $\Delta f(h)$ for the Boron-doped Silicon sample. The measurement is done at two locations at 7.47 GHz and room temperature.

4.2.4 Behavior of Δf and Q signals in the last 100 nm above the Boron doped Silicon sample

In the last 100 nm, apart from a large signal, Δf shows another interesting feature. There is a saturation of the Δf signal, as can be seen in Fig. 4.7. I find that the origin of this saturation can be explained by a slight deviation from the sphere above the infinite plane model. This saturation can originate, for example, from a protrusion hanging off from the end of the tip, as was shown in Fig. 2.15. Fig. 4.10 shows the Δf versus height (on a similar B-doped Silicon sample) for the last 200 nm before tunneling.

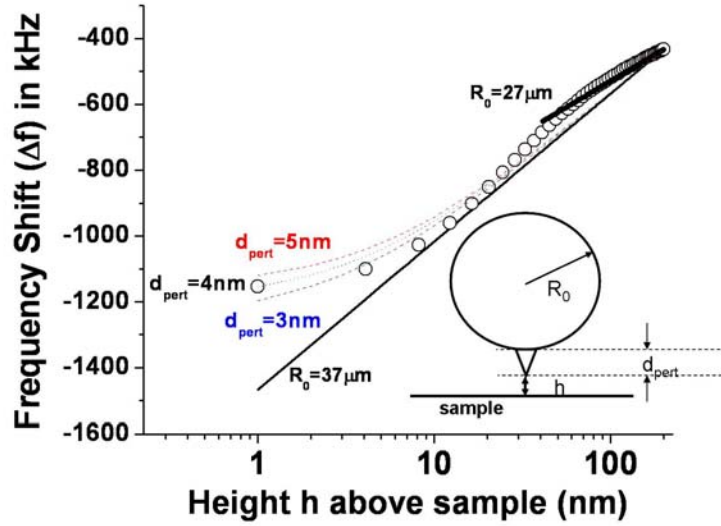


Fig. 4.10: The saturation of the Δf signal in last 100nm above a Boron doped Silicon sample. This sample was prepared with the Focus Ion Beam technique, and is discussed in detail in chapter 5. The region of the sample picked satisfies the $x = \omega C_x R_x \ll 1$ condition. The measurement is done at 7.47 GHz at room temperature. The parameter d_{pert} is the height of the cone on the sphere.

The solid lines in Fig. 4.10 are from the analytical sphere above infinite plane model, which was discussed in chapter 3. The analytical problem gets extremely complicated to solve with the image charge method if a small deviation is made from perfect sphere. So I resorted to numerical simulations with the help of Maxwell 2D (M2D), where it is easy to add small objects at the end of the sphere. The open circles are the data and the dotted lines show the calculated $\Delta f(h)$ behavior for a sphere with a conical feature added at the end of the sphere towards the sample. The larger the conical feature, the sooner the data saturates as the tip approaches the sample. I find that the saturation in Δf is explained well with the help of a cone of height d between 3 nm and 5 nm. Hence, one reason for this saturation of

$\Delta f(h)$ in NSMM signals (also seen in Q as can be seen in Fig. 4.8) is a protrusion at the end of the tip, which affects the capacitance C_x , when looking at the probe to sample interaction in the static limit. The R_x is non-zero for the Neocera B-doped Silicon sample, so I expect to see saturation there due to C_x sensitivity. However, the character of the two saturations (in Q and Δf) in Fig. 4.8 and Fig. 4.9 is quite different. However, the tip could have changed character (character of protrusion) between the two experiments.

Although the Boron doped Silicon sample was chosen for its flat topography, one can qualitatively imagine a similar saturation in $\Delta f(h)$ occurring in rough samples due to features on the surface, rather than the tip.

4.3 Spatial (lateral) contrast of Δf and Q

The STM feedback circuit helps keep the tip at a nominal height of 1 nm above the sample. While the STM is trying to maintain a constant tunnel current as it scans over the surface, I also collect the NSMM data simultaneously. As a result, for a given surface three images are obtained: STM topography, Δf and Q . The Δf and Q images will contain the microwave materials information of the sample. Because of the need to establish STM tunneling, I was confined to samples which are conducting enough to establish a tunnel junction in these experiments. I found in general that metals and lightly doped semiconductors are good samples.

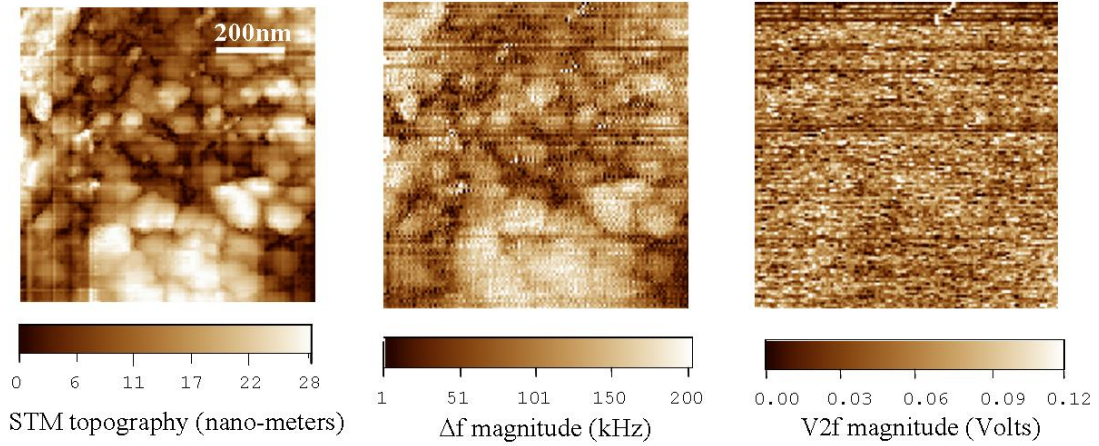


Fig.4.11: Simultaneous imaging of a thin gold film on mica substrate. Since the sample and substrate are not lossy, the V_{2f} shows no contrast, just noise. The sample bias is 100mV and current set point is 1 nA. The experiment is performed at 7.48 GHz at room temperature.

In Fig. 4.11, I show the images taken on a gold thin film on mica substrate. The sample is a low loss sample, as a result there is no contrast in the V_{2f} signal (see equation 2.3). As discussed in section 3.2.1, in the limit of $\omega C_x R_x \ll 1$, the Δf image can be regarded as changes in capacitance between tip and sample, as schematically shown in Fig. 4.12. During scanning the STM maintains a constant tunnel current over the surface, and the topography of the surface shows up as the error signal from the voltage applied to the piezo in order to maintain that constant tunnel current. However, as the tip moves into the surface valley, the capacitance C_x increases compared to the capacitance of a flat region of the sample. The capacitance decreases compared to the flat region of the sample if the tip moves onto a hill on the surface. The increase in capacitance is shown schematically through the number of field lines compared to the flat region of the sample in Fig. 4.12(b).

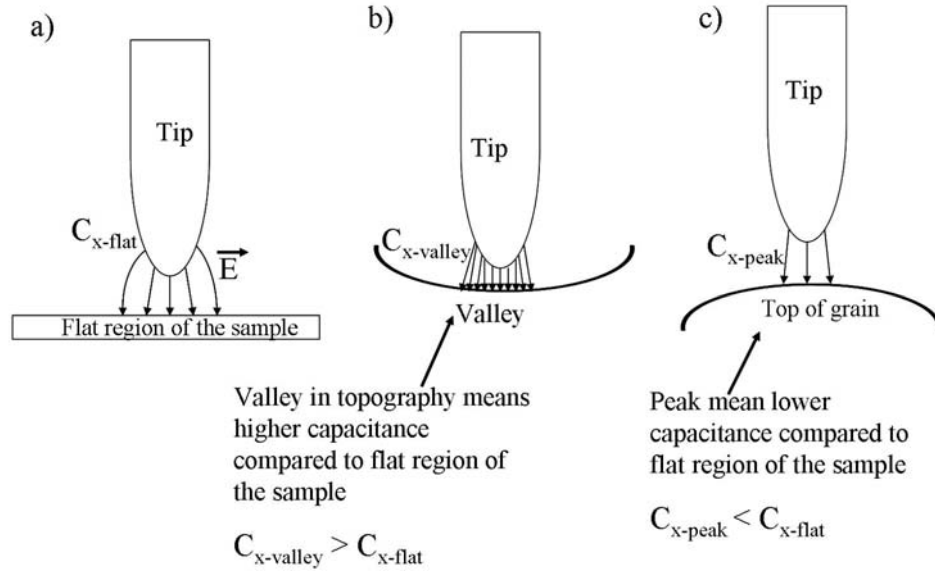


Fig. 4.12: Schematic illustration of the changes in capacitance for tip-sample interaction. The capacitance is higher in case b compared to case a. The capacitance is lower in case c compared to case a.

If the material has sufficiently large losses, then contrast can be seen both in the Δf and Q signals of the NSMM. This can be clearly seen in the Neocera-Boron-doped Silicon sample, as shown in Fig. 4.13. In this field of view, the sample has a 2 μm -wide stripe of un-doped Si surrounded by doped-Si. During scanning over the doped and the un-doped regions (the regions are marked with the dashed line) the STM topography does not show evidence of the stripe, while the NSMM signals clearly distinguish the two regions. The topography which is seen in the STM topography image are mostly due to the damage done to the surface at high bias scanning, which is needed to avoid “false” topography from the p-n junction effect between the doped layer and Silicon (Fig. 4.14). A constant drop of 0.7 volts is needed across the p-n junction, since it is acting like a diode⁸³.

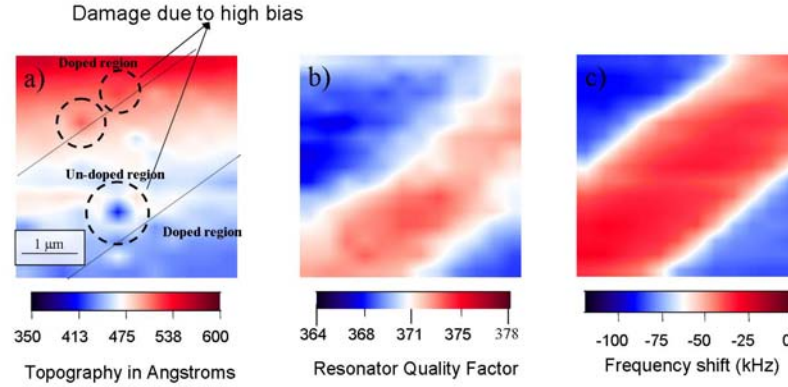


Fig 4.13: Simultaneously acquired images of STM, Q and Δf for Boron-doped Silicon sample. V_{bias} is 4 volts, and tunnel current set point is 1 nA. This is a room temperature measurement at 7.67 GHz. The Q lock-in for this experiment was slower than the Δf lock-in, and the scan was fast to perform experiment in reasonable time. This is the reason why the Q and Δf images do not line up. In general, the large time constants (to get good signal to noise ratio) on NSMM lock-ins slows down scanning.

When the STM tip went from the doped Silicon (shown as edge in Fig. 4.14a) to the un-doped Silicon, the 0.7 volts of drop across the p-n junction vanishes. This extra voltage drop across the p-n junction showed as topography (this is shown in Fig. 4.14b). The y-axis in Fig. 4.14b is this topography step between the doped and un-doped regions across the edge. Notice that higher bias reduces the topography between the two regions at the edge. To minimize the false topography, high bias on the sample was needed (to make it almost topography free). This high bias started to damage the surface of the sample (as can be seen in Fig. 4.13 STM topography). However, at high bias ($V_{\text{bias}} \sim 4 \text{ V}$), it is still fair to think of the sample as having effectively ‘no topography’ as far as the transition between the two regions is concerned, for I do not know of any other sample which can provide us with nice topography-free materials contrast.

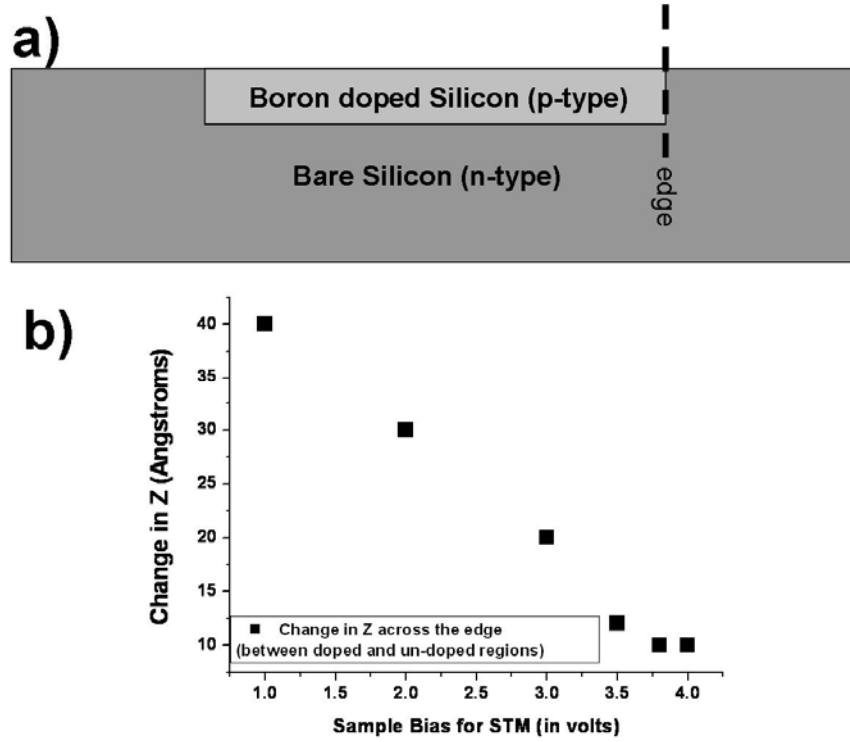


Fig. 4.14: The topography (across the edge) due to the p-n junction effect versus sample bias. a) The doped region with undoped region (bare Silicon) makes a p-n junction. Hence, the doped region required an extra 0.7 volts of voltage drop. b) This voltage drop caused false topography on the surface. At high bias the effect is minimized and the topography value is closer to the value measured by AFM, namely 7.5 Å.

4.4 Conclusion

In this chapter, I have shown data for Q and Δf over different samples, where the contrast is both height and spatial dependent. As can be seen from the discussion in sections 4.1 and 4.2, the range from tunneling height through the first couple of hundred nano-meters above the sample is very interesting for the NSMM signals. It is exactly the sharp drop seen in

this height range which makes possible the spatial contrast seen in section 4.3. I have shown in this chapter that the NSMM is sensitive to the materials contrast. The problem to solve now is the de-convolution of the sample properties from the geometry of the probe-to-sample interaction (this includes, for example, the probe geometry, features on the surface of the sample, multi-layer structure of the sample, etc.).

In the next two chapters, I will build on these results. In chapter 5, I discuss a Boron doped Silicon sample where the doping concentration is varied systematically. This will shed more light on the extraction of R_x information of the sample in the light of the models discussed in chapter 3. In chapter 6, I will show a Colossal Magneto-Resistive (CMR) thin film measured by the NSMM for local contrast, i.e., contrast on nano-meter length scale laterally. This chapter will bring forth more appreciation of the challenge regarding extracting materials information of interest from a sample measured by NSMM.

Chapter 5

Imaging of Sheet Resistance (R_x) contrast with the NSMM

5.1 Introduction

As we saw in chapter 4, the Boron-doped Silicon sample provided us with a surface where the probe-sample capacitance C_x was kept constant and the materials property (R_x) changed. On this particular sample we only had a binary contrast: undoped regions and certain regions of the sample doped with a particular concentration. Due to this, the sample surface is basically “digital” with the sample presenting either bare Si or Si with a dopant concentration of 10^{14} ions/cm². However, it is important to study the response of the microwave microscope to varying R_x while the C_x is kept constant. Such a sample can also be an important platform for calibrating the microscope for materials measurement.

One way to study this is to have a variably Boron-doped Silicon sample, where the doping concentration will be changed continuously. The way I went about it was to use the Focus Ion Beam (FIB) technique, to implant Boron in laterally-confined regions of the sample. This work was performed at the FIB facility here at the University of Maryland by John Melngailis and John Barry. John Barry is the chief operator of the FIB system. From the conception of the sample to its preparation and the experiment, the whole process took

more than one year, and this sample turned out to be a very challenging experiment. One of the main problems was the absence of good navigation marks to find the microscopic features. As a result, it took more than month of scanning to find the feature.

5.2 The preparation of sample with FIB (Focus Ion Beam) technique

In Fig. 5.1, I show the Resistivity (ρ) versus concentration (ions/cm³) of both Boron and Phosphorus doped into Silicon. Over a broad range of Boron concentration (10^{16} to 10^{21} ions/cm³) the room temperature resistivity changes by 4 orders of magnitude (10^{-4} to $1 \Omega\cdot\text{cm}$). This data also makes the Boron-doped Silicon an ideal sample to be prepared, since these resistivity values are good for establishment of an STM tunnel junction.

The idea of the sample is to have the sheet resistance vary on the surface of the Silicon over a distance that can be easily scanned by my piezo-positioning system. Hence, when I scan across it, within a reasonable scan range, the microscope will see many different values of R_x and I will understand the response of the microscope to materials contrast. I should remark here that this structure came out as a compromise between me and John Barry after many meetings. He did not want to spend more than one day preparing this sample, and as a result I had to give up on much more ambitious goals that I had in mind. For example, I was interested in obtaining sharp concentration steps to experimentally measure the spatial resolution with topography-independent regions.

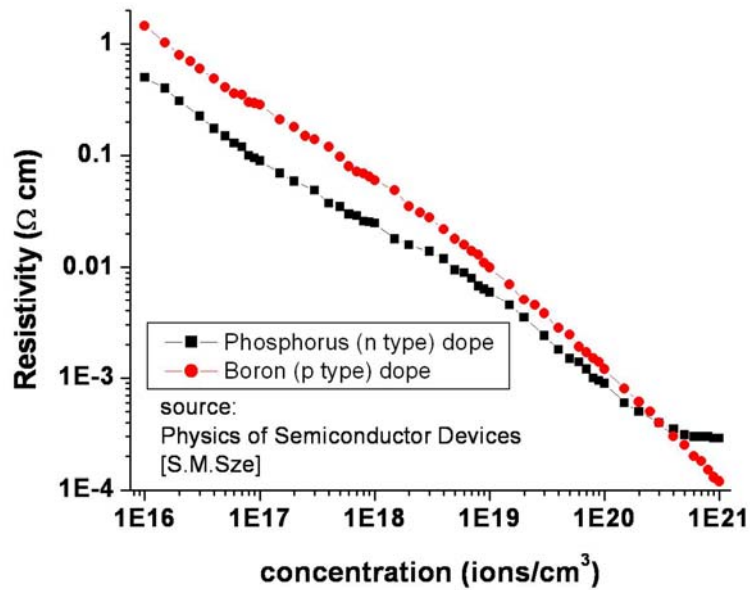


Fig. 5.1: Room temperature resistivity versus concentration of either Phosphorous or Boron dopants in Silicon. Notice the 4 orders of magnitude change in resistivity for 5 orders of magnitude change in dopant concentration. Also note that the resistivity values are all reasonable for STM tunneling. Boron was chosen since the FIB set up was easily available for this material. See reference 69.

The layout of the sample is shown schematically in Fig. 5.2, which is based on the “write” file used by the computer that controls the FIB instrument. This “write” file is input to the software (for running FIB) which then controls the position and dwell time of the beam over the sample. Different regions were given different doping concentrations.

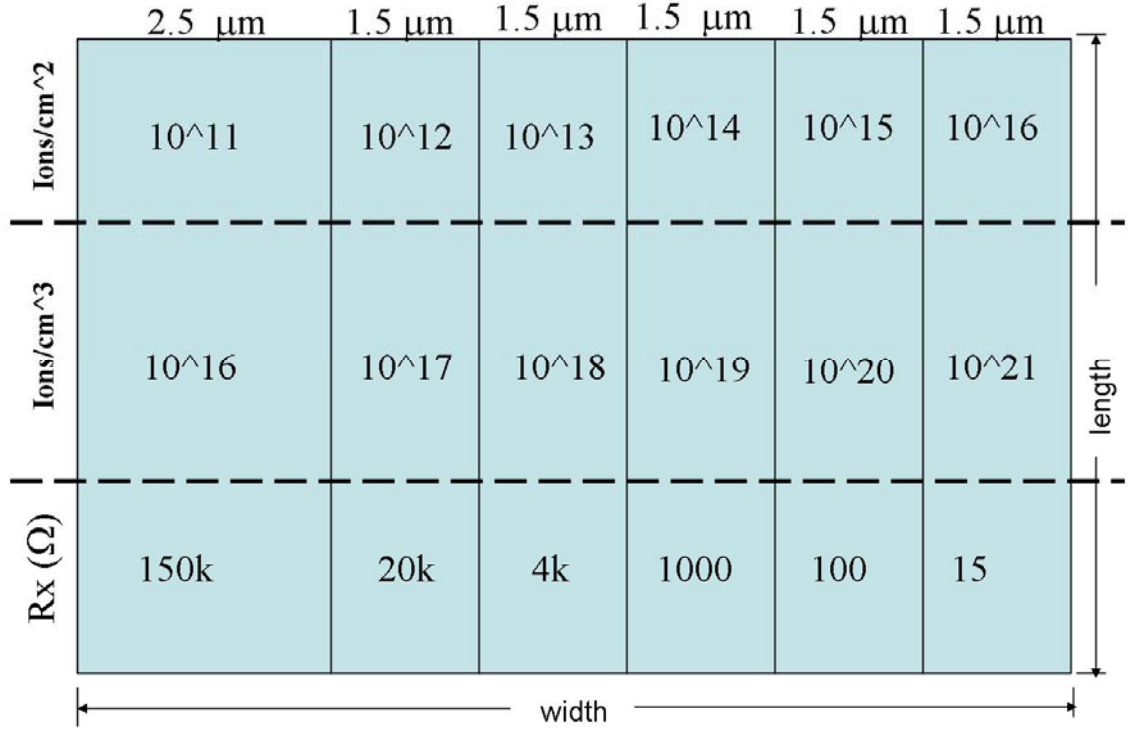


Fig.5.2: The schematic of the variably Boron doped Silicon sample, based on the “write” file for FIB setup. Dopant concentrations are given in terms of area dose, volume density, and nominal room temperature sheet resistance. The nominal width of each stripe is also shown. The length of the pattern is 10 μm . Due to the FWHM of 0.5 μm of the FIB Gaussian beam, a continuous variation is produced rather than the sharp steps implied by the drawing.

The Boron doping was performed on an n-type, 4” diameter Silicon wafer, which had a resistivity of 0.61 $\Omega\cdot\text{m}$ at room temperature. A beam energy of 30 keV was used to Boron dope the surface of Silicon in an area of 10 μm x 10 μm . At this beam energy the total depth of Boron implant into Silicon is approximately 100 nm⁷⁰. The geometry of the 10 μm x 10 μm region was such that along the length of the area the FIB beam wrote for a certain dwell time. The dwell time of the beam was adjusted so that one line along the

length is written with a given concentration of ions. After it finished the line along the length of the area, it rastered along the width to write the next line along the length, and the dwell time was changed to increase the concentration of ions. The raster step size was 45 nm and this process was repeated all across the 10 μm width, to get the region schematically shown in Fig. 5.2. However, I got a continuous variation of doping rather than the anticipated stepped regions of Fig. 5.2. The reason for getting the continuous variation is discussed below.

In order to know the resistivity as a function of position across the width of the sample, I need to know the concentration as a function of position across the width of the sample (Fig. 5.1). This requires that I calculate the concentration profile of implanted Boron ions across the width using the parameters of beam that went into writing this pattern. Knowing the Gaussian beam profile with exponential tails of the beam⁶⁷, I modeled the writing process in a program written in *Mathematica*. In the program, the concentration is modeled as

$$concentration(x_0, \sigma) = \int dx' \frac{[D_0 \Theta(x' - x_0)]}{\sqrt{2\pi\sigma^2}} e^{-\frac{(x' - x_0)^2}{2\sigma^2}} \quad (5.1)$$

where σ is the Full Width Half Maximum (FWHM) of the Gaussian beam used for FIB (FWHM is $0.5\mu\text{m}$ ⁶⁷). The D_0 is the number of ions calculated based on the beam current (10 pA) and the exposure time. In the equation $\Theta(x' - x_0)$ the step function, which represent

the width of each stripe shown in Fig. 5.2. For the calculation of equation (5.1), I used the information from the original write files of the FIB system. From the concentration, I calculated the R_x . The result of the calculation shows a four decade variation of R_x contrast over a 10 μm width, which actually is a continuous variation (Fig 5.3). This continuous variation in R_x is due to the Gaussian profile of the beam.

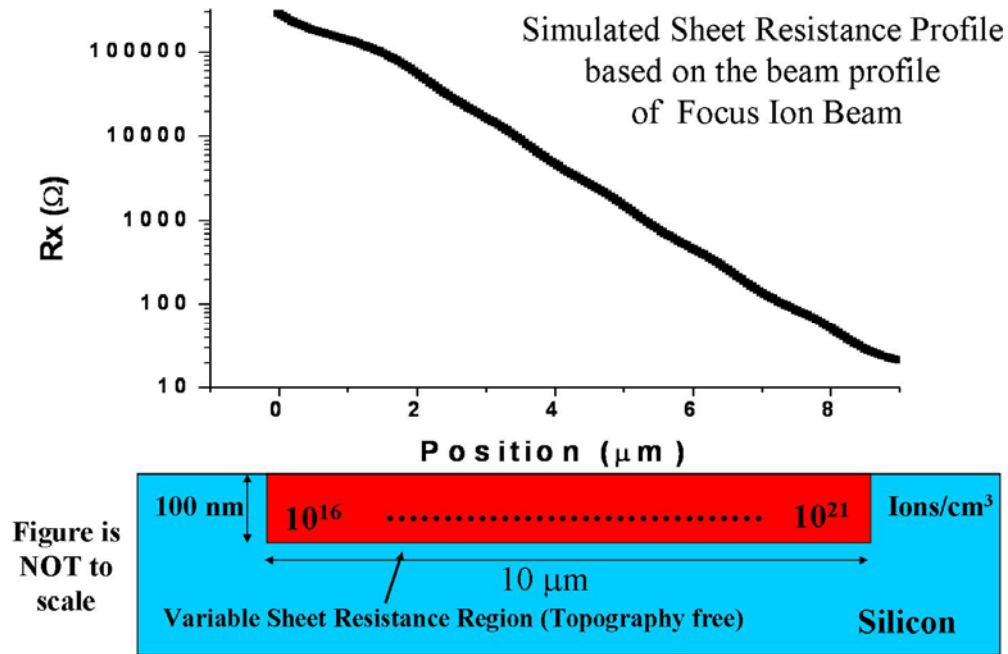


Fig 5.3: The nominal room temperature sheet resistance (R_x) versus position for variable R_x Boron-doped Silicon sample. The FWHM of the Gaussian focused ion beam used is 0.5 μm .

A 10 μm square size was chosen because above this range, the piezo hysteresis of my STM/NSMM affects the scan in the XY plane. There were 9 features like that in Fig. 5.2 prepared to check for reproducibility of our results. However, only 4 were good for

experimentation. Several of the features were not completed appropriately due to technical difficulties with the FIB instrument, and others were contaminated due to junk over the surface, and this showed as STM topography in the measurement. However, four of the features were good, and showed similar general results during simultaneous imaging of topography, Δf and Q . The data in this chapter is taken from the $10\text{ }\mu\text{m} \times 10\text{ }\mu\text{m}$ feature that was studied most thoroughly.

After the ion beam deposition the sample was rapid thermal annealed (RTA) to 900°C in Nitrogen for 20 seconds (5 seconds to ramp up the temperature, 10 seconds to anneal at 900°C and then 5 seconds to ramp down the temperature) to activate the carriers. At this point the sample is ready for the simultaneous STM and NSMM experiment.

5.3 Scanning Tunneling Microscopy of FIB Boron doped Silicon sample

The STM topograph image of the variable R_x region of the sample is shown in Fig. 5.4. The tunnel current set point for this image is 0.5 nA and the bias used was 1 volt. The region of high concentration (and low R_x) is on the left side of the sample. This part of the sample is damaged because the beam dwell time was very long on this region to dope with a high concentration. As a result there is roughly $50\text{ }\text{\AA}$ of topography present. The rest of the doped region is topography free, which is a good region for maintaining constant C_x for the NSMM. The NSMM contrast expected here is just due to the change in R_x .

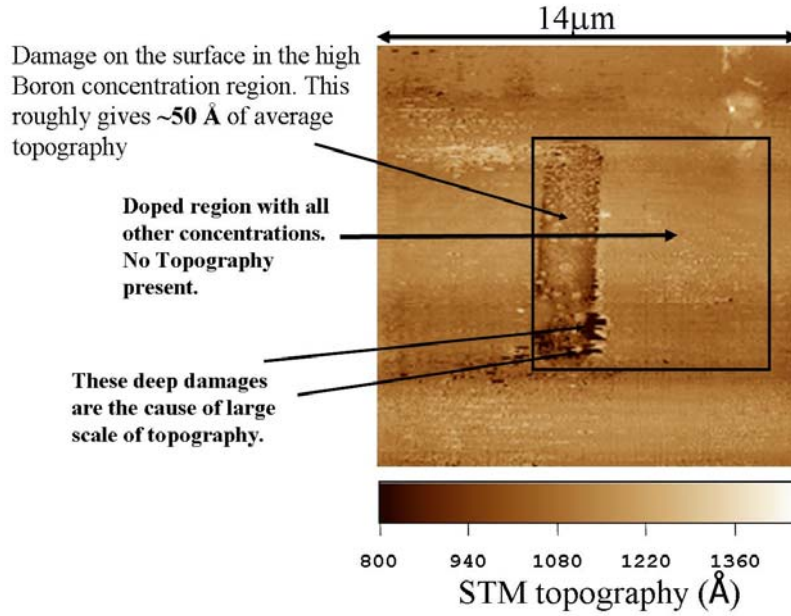


Fig. 5.4: STM topography image of variable R_x Boron-doped Silicon sample at room temperature and 7.47 GHz. The tip used is APS WRAP082. STM bias is 1 volt and tunnel current set point is 0.5 nA. The damages are due to FIB or high bias applied to the sample.

5.4 NSMM data on FIB Boron doped Silicon sample

When I performed STM on this sample, I simultaneously acquired the data to construct the Δf and Q images as shown in Fig 5.5. The doped region clearly shows contrast in regions where it had no topography. In this case, the experiment is now performed at fixed height above the sample. Here, it is clear that the NSMM signals respond to the variable R_x region of the sample. The NSMM signals also respond to the damaged (strong topography) area. I performed experiment on these features at many different frequencies. Since the image doesn't show any interesting change in the vertical direction, I take horizontal line segments at a fixed vertical position, and average them together to form line cuts (shown in

Fig 5.7 and Fig. 5.8), and the data over the region of damage (as seen on the left of images) and the data on bare Silicon (as seen on the right of the images) is removed.

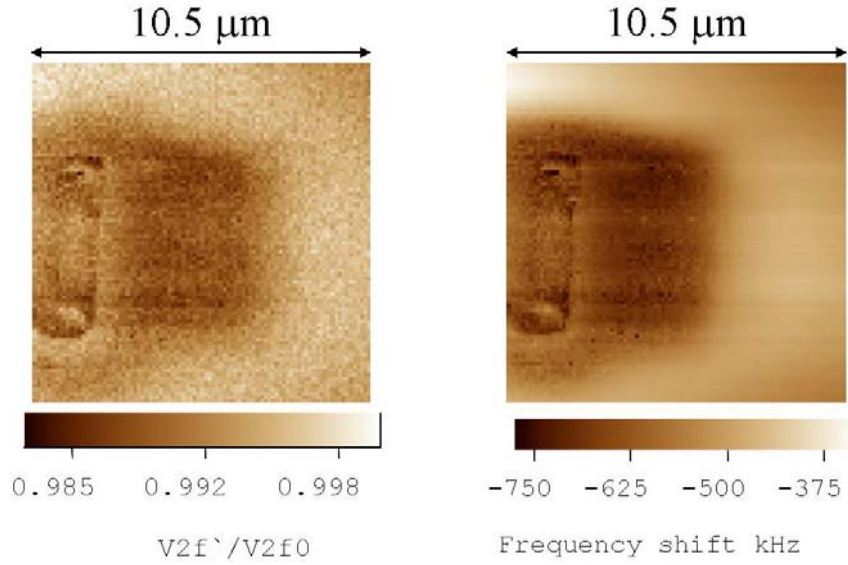


Fig 5.5: NSMM V_{2f} (proportional to Q) and Δf images of FIB Boron doped sample. The tip used is APS WRAP082. This is a room temperature measurement at $f = 7.47$ GHz. The STM bias is 1 volt with tunnel current set point of 0.5 nA.

I performed imaging experiments of the same feature at 1.058 GHz, 3.976 GHz, 7.472 GHz and 9.602 GHz. I have used the calculation presented in Fig. 5.2 to translate the position of the probe to the corresponding local sheet resistance value.

The schematic of the lumped element model^{102, 104}, used to understand the data is shown in Fig. 5.6. The sample in this case is a thin doped layer with impedance AR_x , on top of the Bulk Silicon, with impedance Z_{Si} . The R_x is the sheet resistance of the doped layer and A is the geometrical coefficient. The Z_{Si} includes the resistivity ρ_{sub} of the bulk Silicon (which

in this case is $60\Omega\cdot\text{cm}$) and the real dielectric constant ($\epsilon_{\text{Si}} = 11.9$). The capacitance between the inner-conductor of transmission line resonator and the sample is labeled as C_x , and the capacitance between the sample and outer conductor is labeled as C_{out} . The parameter C_{out} is in the range of pico-farads, which is much greater than C_x (in range of femto-farads). Since C_{out} is in series with C_x as well, this means that total capacitance will be dominated by C_x . Hence C_{out} can be safely ignored for purposes of this model.

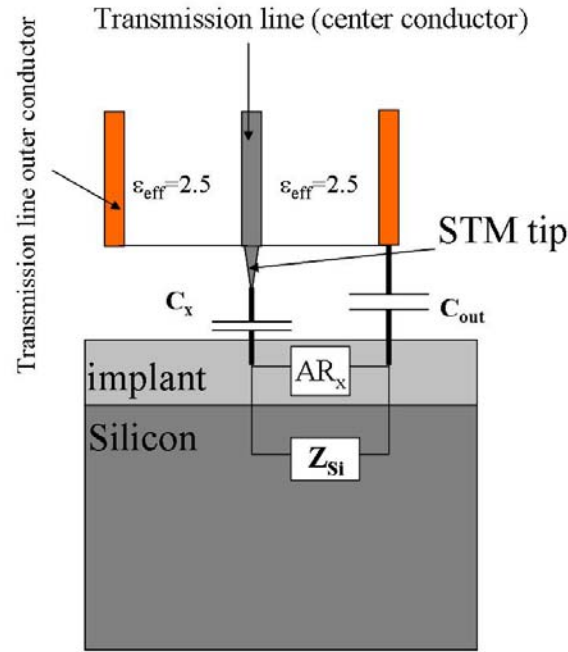


Fig. 5.6: The lumped element model for the Boron-doped Silicon sample based on the idea discussed in reference 104.

The recipe¹⁰⁴ to calculate the quality factor and frequency shift is as follows. The transmission line resonator (with characteristic impedance of $53.28\ \Omega$, attenuation constant α , the mode number n and the length L_{res}) is being terminated by the sample (Boron-doped

Silicon) and the STM tip (electrical tip), with characteristic size called D_t . The tip and sample together have impedance Z_{tE} which is sum of both resistive (R_{tE}) part and the reactive (X_{tE}) part to it. Assuming that $|Z_{tE}| \gg Z_0$, the complex reflection coefficient¹⁰⁴ is calculated (for the geometry shown in Fig. 5.6) for the resonant condition of the transmission line resonator. This yields Q' and $\Delta f/f_0$ for the resonator as:

$$Q' = \frac{\pi n + \frac{Z_0 X_{tE}}{R_{tE}^2 + X_{tE}^2}}{2\alpha L_{res} + \frac{Z_0 R_{tE}}{R_{tE}^2 + X_{tE}^2}} \quad (5.2)$$

and

$$\frac{\Delta f}{f_0} = \frac{Z_0}{2\pi f_0 L_{res} \sqrt{\epsilon_0 \mu_0 \epsilon_{eff}}} \frac{X_{tE}}{R_{tE}^2 + X_{tE}^2} \quad (5.3)$$

where

$$R_{tE} = \frac{\frac{1}{AR_x} + \frac{D_t}{\rho_{sub}}}{\left(\frac{1}{AR_x} + \frac{D_t}{\rho_{sub}}\right)^2 + (2\pi f_0 \epsilon_0 \epsilon_{Si} D_t)^2} \quad (5.4)$$

and

$$-X_{tE} = \frac{1}{2\pi f_0 C_x} + \frac{2\pi f_0 \epsilon_0 \epsilon_{Si} D_t}{\left(\frac{1}{AR_x} + \frac{D_t}{\rho_{sub}}\right)^2 + (2\pi f_0 \epsilon_0 \epsilon_{Si} D_t)^2} \quad (5.5)$$

The fitting parameters in this model are now the geometrical factor A , tip-to-sample capacitance C_x and the characteristic probe size D_t . In Fig. 5.7 I show the fit due to these

models to the $\Delta f/f_0$ data at different frequencies. The parameters of fit are shown in Table 5.1.

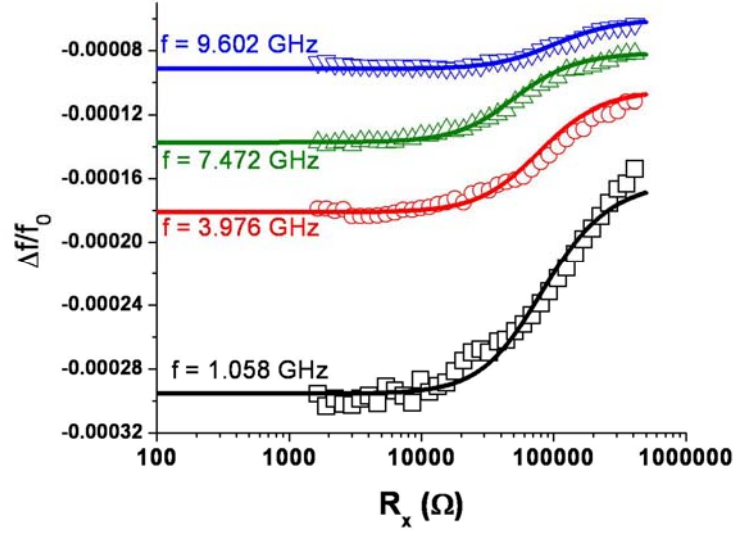


Fig. 5.7: The fit of the lumped element model to the data at different frequencies for the Boron-doped Silicon sample. All of the fits in general required that geometrical parameter A either be close to 0.1 or less than 0.1.

Table 5.1: The fit parameter values for the data and fit shown in Fig. 5.6. D_t is on the order of feature size and C_x values are close to values from sphere-above-the plane model discussed in Chapter 3.

Frequency (GHz)	D_t (μm)	A	C_x (fF)
1.058	10	0.12	15.5
3.976	15	0.05	9.5
7.472	15	0.05	7.2
9.602	20	0.025	4.8

The values for the D_t and C_x are in the range that I expect based on the data fitted for other samples. For example, the R_0 in chapter 4 earlier, for the sphere above the plane model was $10\text{ }\mu\text{m}$ and the C_x of about 10 fF . The value of the geometrical factor A was varied in order to fit the data.

I used these fitting parameters to fit the data for the quality factor from the same sample (Fig. 5.7), which is plotted as Q'/Q_0 , where Q_0 is quality factor with no sample present. In general for the high R_x values, the same parameters (given in Table 5.1) worked very well for the fit (solid line in Fig. 5.8), however for the low R_x the data shows different behavior from what the model predicts. In order to fit the low R_x data (dashed lines) I had to either increase D_t by an order of magnitude ($D_t=100\text{ }\mu\text{m}$ for $f=9.602\text{ GHz}$ data) or change the geometrical factor A considerably ($A = 3$ for $f=1.058\text{GHz}$ data). In case of the 3.976 and 7.472 GHz data I had to fiddle with both. For the case of 3.976 GHz data, $D_t=140\text{ }\mu\text{m}$ with $A = 0.3$, and for the 7.472 GHz data $D_t=100\text{ }\mu\text{m}$ and $A=0.28$).

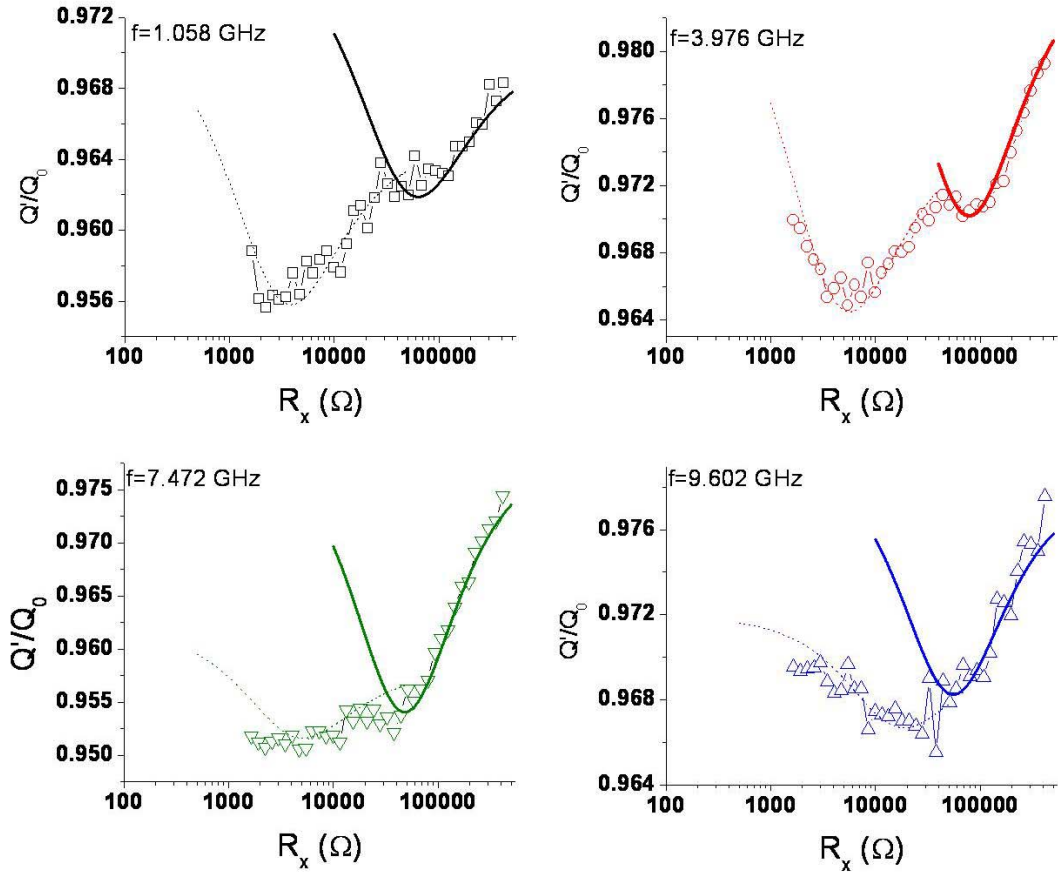


Fig. 5.8: Fit to the Q'/Q_0 data from the lumped element model. For the high R_x data the same parameters given in Table 5.1 worked, however for the low R_x data I had to change the parameters, as discussed in the text.

In order to understand the low R_x data, in the future I plan to understand the effect of the damaged region on the quality factor of microscope. The field structure could have changed dramatically over the damaged region, and that shows as change in D_t and A .

In conclusion, this variably Boron-doped FIB sample has been an interesting one to measure with the novel NSMM. It provides me with very interesting platform for understanding the behavior of microscope. The contrast in quality factor and frequency shift seen is on about 3 decades of R_x (after ignoring the damaged region), which is in the region of about 7.5 μm . This shows the sub-micron spatial resolution of the microscope in the materials property.

Chapter 6

Imaging of local contrast in a correlated electron system

6.1 Introduction

It had been a challenge to find samples which simultaneously have very interesting physics for the NSMM to measure and allow an STM tunnel junction to be established at the same time. The correlated electron Manganites in this sense have been important. These systems basically have “insulating” and “metallic” states mixed together on short length scales⁷⁴⁻⁷⁷. It has become clear that manganites all have non-trivial phase segregation on nano-meter, and larger length scales. These phases can have many different underlying physical causes, and in this chapter I discuss one such sample.

6.2 Colossal Magneto-Resistive (CMR) thin $\text{La}_{0.67}\text{Ca}_{0.33}\text{MnO}_3$ film

The Colossal Magneto-Resistive (CMR) sample that I had success in establishing an STM tunnel junction is a thin $\text{La}_{0.67}\text{Ca}_{0.33}\text{MnO}_3$ (LCMO) film on a LaAlO_3 (LAO) substrate. The average thickness of the film is 1000 Å (as measured with AFM). The resistance versus temperature of this sample is shown in Fig. 6.1. This particular material has the ferromagnetic Curie temperature (T_C) of 250 K. Above T_C the sample is paramagnetic and

insulating and below T_C it is ferromagnetic and metallic. The two transitions (metal/insulator and ferromagnetic/paramagnetic) take place at the same temperature.

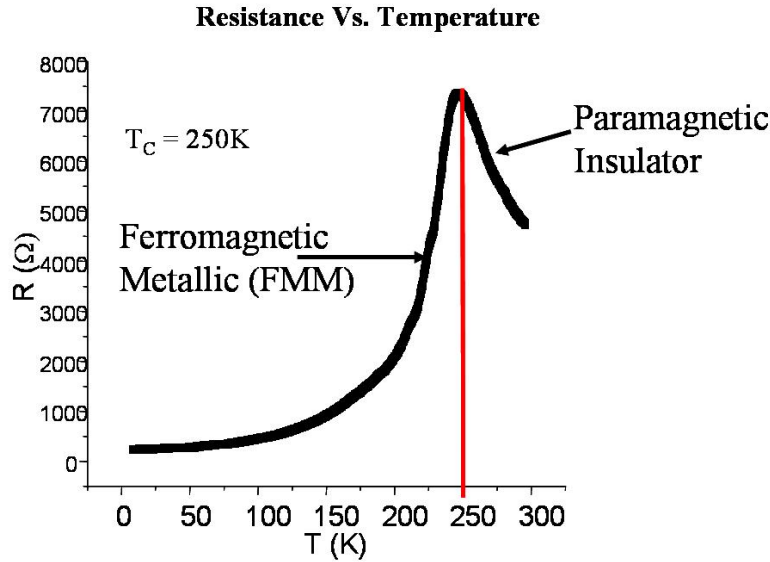


Fig. 6.1: The resistance versus temperature of a thin $\text{La}_{0.67}\text{Ca}_{0.33}\text{MnO}_3$ thin film. The Curie temperature T_C is 250 K (shown by the solid vertical line). Below this temperature the film is ferro-magnetic and metallic. Above that temperature it is paramagnetic and insulating.

The lattice constant of the $\text{La}_{0.67}\text{Ca}_{0.33}\text{MnO}_3$ thin film is 3.86 \AA and the lattice constant of the LaAlO_3 substrate is 3.79 \AA (shown schematically in Fig. 6.2). As a result of this lattice mismatch, there is biaxial strain in the film. For the thinner part of the film, or for parts of the film near the substrate, this biaxial strain causes charge ordering (electrons are “localized”) and as a result the thinner section of the film is expected to be more “insulating” compared to the bulk film⁷⁸. This thin film sample has an island-like (granular) growth structure on the surface, which is schematically shown in Fig. 6.3. The grains are thought to be ferromagnetic metallic (since they are thicker regions of the film) and the

behavior of the inter-granular region is thought to be charge ordered insulating, as I discussed earlier. This strain model is also backed by data from cross-sectional Transmission Electron Microscopy (TEM) where the thin part of the film is seen to have higher strain^{78,79}.

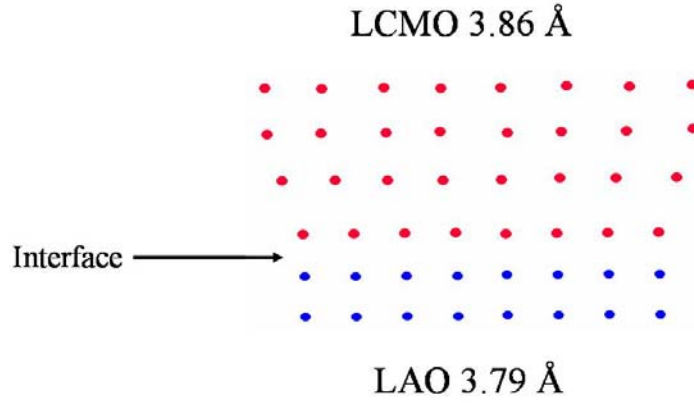


Fig. 6.2: Schematic atomic positions for the lattice mismatch at the interface between the LCMO film and the LAO substrate. The film has a larger unit cell by 0.07Å.

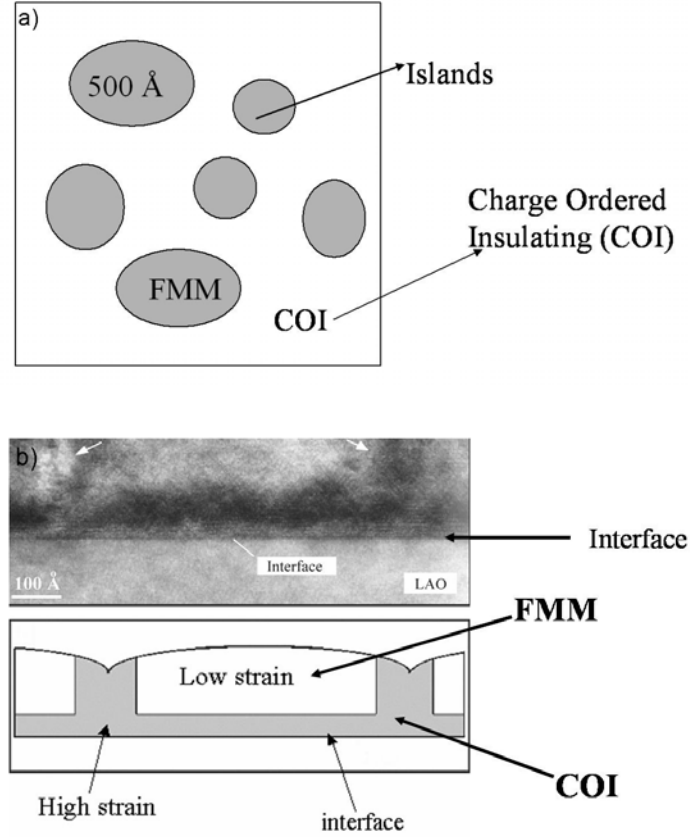


Fig. 6.3: a) shows a schematic of the surface of the film divided into thicker metallic grains separated by thinner insulating regions. b) Cross-sectional TEM image of an LCMO film on an LAO substrate suggesting that the inter-granular region of the film is a high strain region. The data is taken from Ref. [78].

6.3 Simultaneous STM and NSMM imaging

6.3.1 Experimental data above and below T_C

I performed a simultaneous experiment of STM and NSMM on the thin CMR $\text{La}_{0.67}\text{Ca}_{0.33}\text{MnO}_3$ film. Figure 6.4 shows the data for the above T_C experiment. Figure 6.4(a) shows the STM topography over a 600 nm X 600 nm area. It shows the granular structure of the film as was discussed in the previous section, where grains are $\sim 500 \text{ \AA}$ in

size laterally and ~ 175 Å in height. Figures 6.4(b) and (c) show the simultaneously acquired Q and Δf images from the NSMM. The streakiness in the Δf image is due to fluctuations in the output frequency of the Wave-Tek microwave source. The NSMM signals also clearly contain the granular structure of the surface, similar to the STM topography. The images are 6000 Å square.

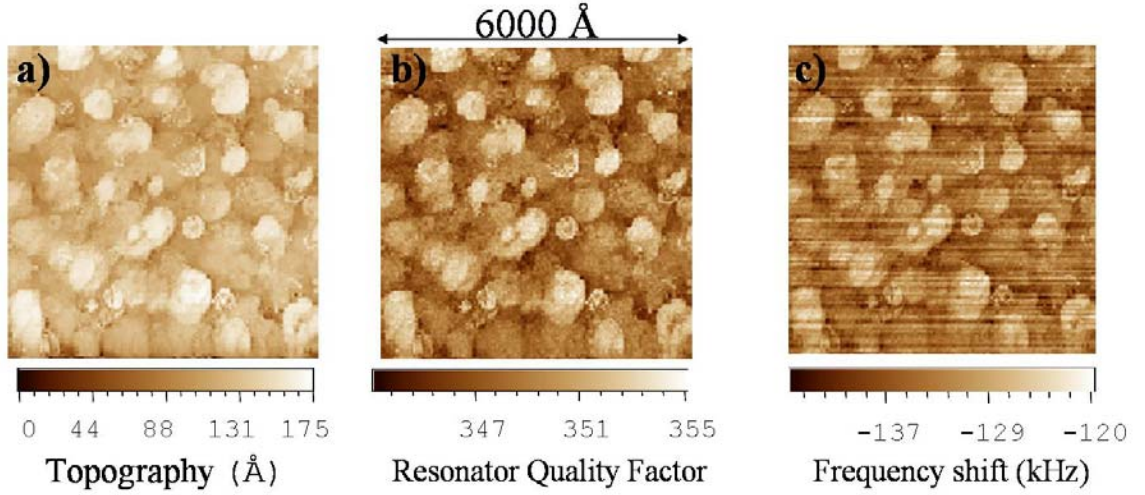


Fig. 6.4: Simultaneous image data for the thin $\text{La}_{0.67}\text{Ca}_{0.33}\text{MnO}_3$ film above T_C at temperature of 272K. a) STM topography of the grains. b) Quality factor of the resonator and c) Δf of the resonator where streakiness is due to the stability problems of the Wave-Tek source. $V_{\text{bias}} = 1$ volts, tunnel current set point is 1 nA and experiment was performed on 7.67 GHz.

Fig. 6.5 shows the data for a below T_C experiment. This region of the sample is not identical to that of the above T_C experiment because it is very hard to find the same region again after the sample is cooled down due to thermal drifts. The reason is that in order to cool down, the sample and the tip have to be separated to prevent the tip from crashing into

the sample as the whole system is going through thermal contraction. Fig. 6.5(a) shows the STM topography which shows the granular structure of the film and Fig. 6.5(b) and (c) show the Q and Δf images, respectively. Again the granular structure is clear in the NSMM signals. For both experiments, the loss information is contained in the NSMM data.

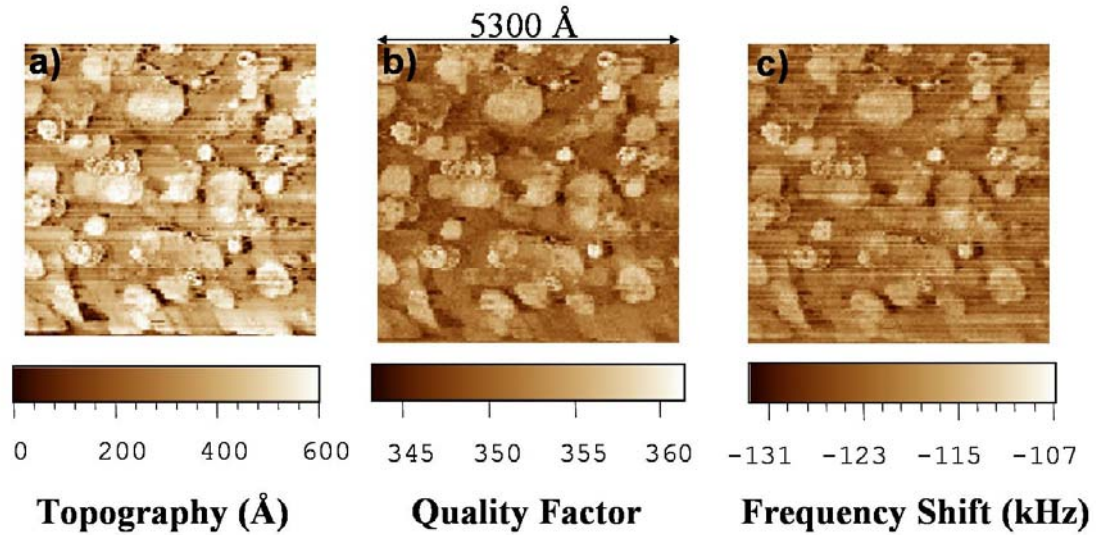


Fig. 6.5: Simultaneously acquired data below T_C at a temperature of 240K a) STM topography, b) Quality factor of the resonator and c) Δf of the resonator. $V_{\text{bias}} = 1$ volts, tunnel current set point is 1 nA and frequency of measurement is 7.67 GHz.

6.3.2 Calculation of R_x from the data

In order to extract the local losses it is essential to calculate the R_x map of the surface from the Q and Δf data. The problem at hand is that both NSMM signals are functions of the probe to sample capacitance C_x and a materials property R_x , i.e. $Q = Q(C_x, R_x)$ and $\Delta f = \Delta f(C_x, R_x)$ and the information of loss is in the materials property, R_x . I used the lumped

element model to calculate the R_x map which is shown for the above and below T_C data in Fig. 6.6.

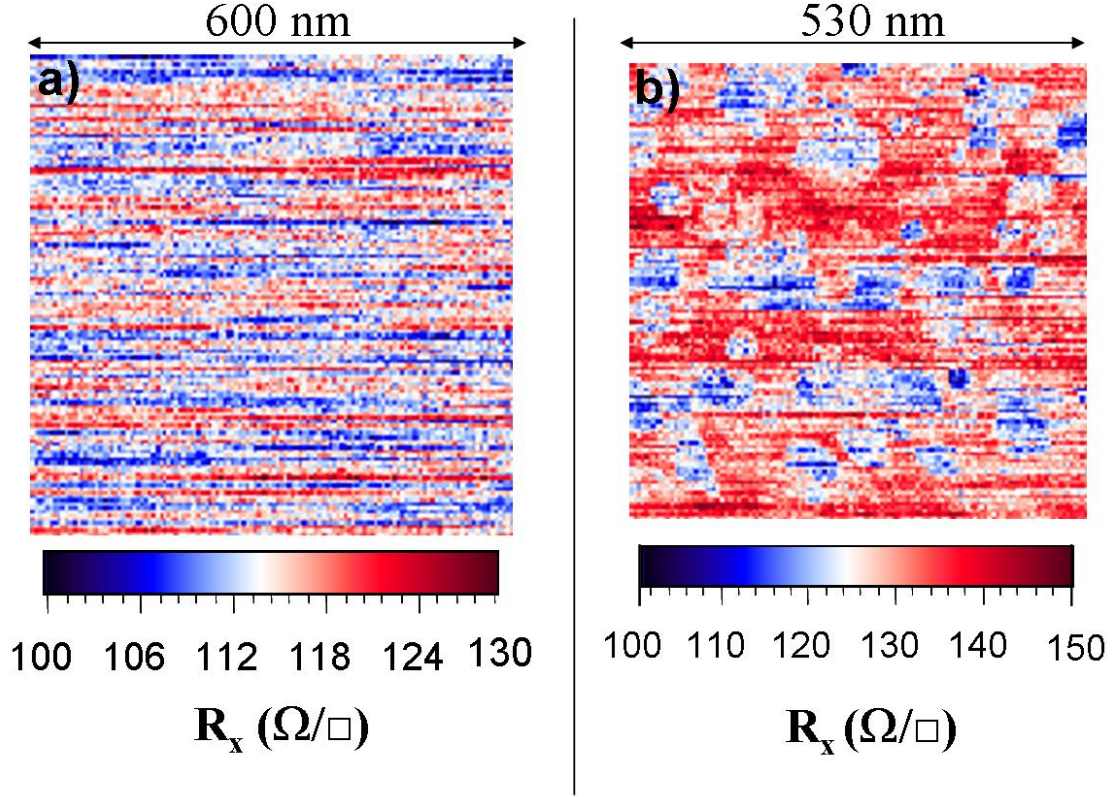


Fig.6.6: the calculated R_x map for the data shown in section 6.3.1.a) the R_x map for the data at $T=272$ K above T_C b) the R_x map for the data at $T=240$ K below T_C . The $T_C = 250$ K and the frequency of the experiment is 7.67 GHz.

The way the calculation is performed is as follows. I start with a plot similar to Fig. 3.2a. Using this plot, I can get find a linear expression (around $x=0$) to fit. The expression for R_x that I get is given in equation (6.1), using equations (3.8) and (3.9), since $x \ll 1$ condition is satisfied:

$$R_x = \frac{1}{(2\pi f)^2 R_0 \left(\frac{-2(\Delta f)C_0}{f}\right)^2} \left(1 - \frac{Q'}{Q_0}\right) \quad (6.1)$$

where f is the frequency of the experiment, Q_0 is the quality factor with no sample present, Q' is the quality factor (image) data, Δf is the frequency shift (image) data and R_x is the sheet resistance image. The value of C_0 used for the calculation is 100.8 pF and R_0 is 28 k Ω .

Fig. 6.6(a) shows the R_x map as calculated from the above- T_C data and Fig. 6.6(b) shows the below- T_C data. The R_x map below T_C shows a very interesting granular structure, while the data above T_C shows no clear interesting features. The R_x map below T_C shows granular structure similar to the original data in STM. The grains in the R_x map are regions of low R_x and the inter-granular region is of high R_x consistent with the proposed model for the film. The R_x values calculated, are roughly 50 times smaller compared to the expected R_x values that I would expect based on numbers in Fig. 6.1. The problem is again that for the lumped element model case, the tri-layer structure has been ignored, which can significantly affect the measured values of resistance.

6.3.3 Measurements on top of a single grain

Fig. 6.7 shows the simultaneously performed STM and NSMM experiment on a single grain below T_C . I show this data to comment on the spatial resolution of the microscope. As

I have discussed earlier, both NSMM signals are functions of both C_x and R_x , and in order to comment on the spatial resolution, I need to comment on both the C_x and R_x resolution based on the data. In fig. 6.7(a), the STM topography is shown for a single grain. Figs. 6.7(b) and (c) show the Q and Δf data in a 492\AA square. The dotted circle on the STM topography is pointing to an interesting feature on the grain. In Fig.6.8, I show a line cut through the region of the circle which is marked in Fig. 6.7(a) with a line.

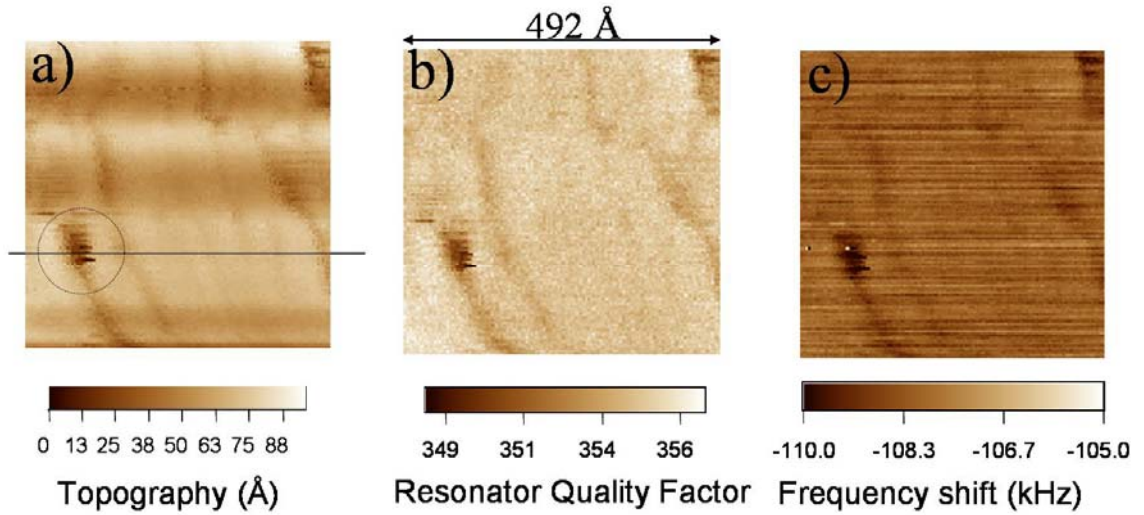


Fig.6.7: Simultaneous images on a single grain of thin $\text{La}_{0.67}\text{Ca}_{0.33}\text{MnO}_3$ film. a) STM topography, b) quality factor of the resonator and c) Δf of the resonator. The temperature of measurement is 240 K, $V_{\text{bias}} = 1$ volt, tunnel current set point is 1 nA and the frequency of experiment is 7.67 GHz.

In Fig.6.8, the line cut through the three data sets is shown. There is a feature roughly 55\AA deep and it shows the lateral resolution of 25\AA between its starting point (shown by the line on the left) and its deepest point (shown by line on the right). The variation in the

NSMM signals show similar response to this particular feature, and this suggests that the spatial resolution is also 25 Å, just as good as STM. However, this spatial resolution is the spatial resolution for C_x , since these variations are due to changes in the probe-sample capacitance as discussed in Fig. 4.12. In order to find out the spatial resolution in R_x , one needs to calculate the R_x map of this particular data, by following the procedures that I discussed earlier in this chapter. This calculated R_x map for the interesting feature is shown in Fig. 6.9.

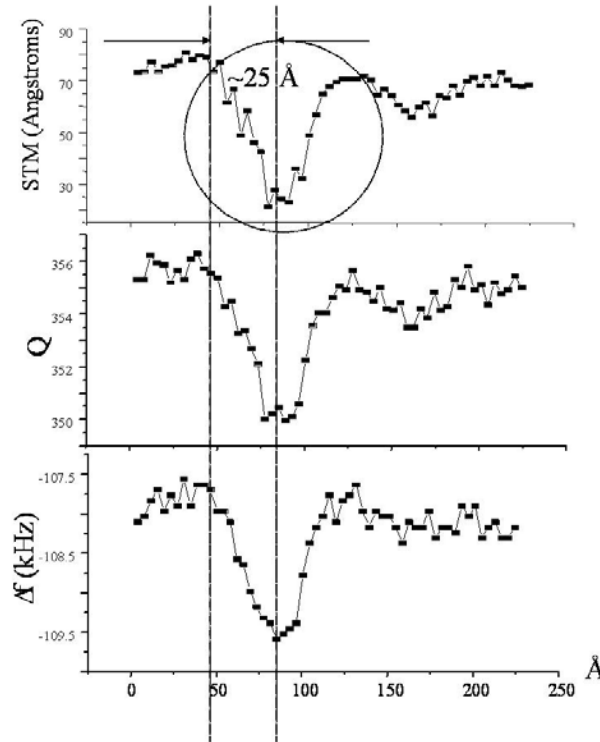


Fig 6.8: The line cuts of the three data sets taken from the data shown in Fig. 6.7. The region of the line cut is the feature in the dashed circle of fig. 6.7a. The Quality factor and the Δf , both have contribution from C_x and R_x . This line cut suggests that the STM assisted NSMM has a spatial resolution which is 2.5 nm in C_x .

Based on the calculated R_x map, the interesting feature seems to be more resistive compared to the rest of the region in the image. This region (the dip in topography) is the more strained part of the sample⁷¹, so it appears to be in charge ordered insulating state. Further experiments are required, which is discussed in the next section.

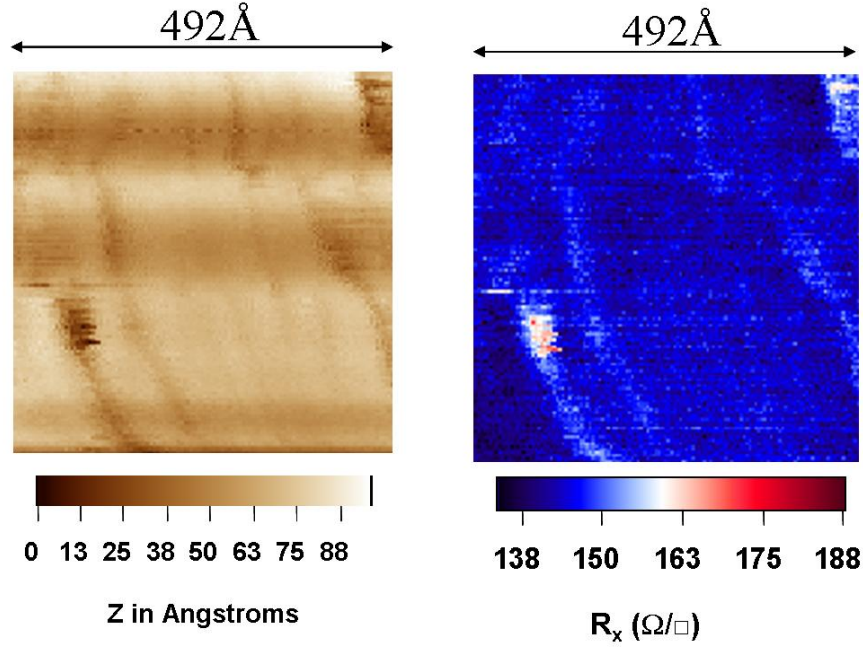


Fig. 6.9: The left image is the STM image of the interesting feature and the right image is the calculated R_x map based on the lumped element model. This dip in topography shows up as being more resistive in the R_x map. The temperature of experiment is 240 K performed at 7.67 GHz.

6.4 Conclusion

In this chapter I have shown the potential of NSMM to quantitatively measure local contrast in one of the CMR ($\text{La}_{0.67}\text{Ca}_{0.33}\text{MnO}_3$) thin films. Due to the significant contribution from the high spatial wave-vectors (Fig. 3.14), I expected small film features

to be resolved. The data presented in this chapter clearly shows this, and the spatial resolution of the microscope is 2.5 nm in C_x . I have used the lumped element model to calculate the R_x map from the same data. However, such a calculation gives confidence that there is sheet resistance (R_x) contrast present in the data, although it does not give any quantitative confidence.

In order to gain such quantitative confidence in the future, I am thinking of two new directions. One is to follow a more detailed calculation in which the contribution from both propagating and evanescent waves is kept as part of the calculation⁹⁸ (see section 3.3.6). From such a model the goal will be to again get an equation for R_x where the spatial data of Q and Δf ($Q(x,y)$ and $\Delta f(x,y)$) are used as an input. A second approach is to use single crystals of CMR materials, for several reasons. One reason is that crystals are much thicker than the skin-depth δ , at the frequencies and temperatures of interest. This helps avoid the multi-layered structure problem all together, and hence the formalism developed in section 3.3 will be directly applicable. The other good thing is that such crystals cleave to give clean surfaces with relatively flat terraces on length scales of hundreds of nano-meters^{99,101}. Such terraces mean topography-free surfaces (on the length scales of interesting physics), where the local contrast will show as R_x contrast, and then the lumped element model can be successfully used to calculate R_x (since the C_x is essentially fixed during scanning).

Chapter 7

Conclusions and Future Directions

7.1 Conclusions

In this thesis I have demonstrated a cryogenic STM-assisted NSMM, which is based on the transmission line resonator. I have demonstrated that this novel NSMM has sensitivity to the materials contrast (R_x). This makes the NSMM an important platform for measurements related to fundamental physics (chapter 6) and applied physics (chapter 5).

The strength of this NSMM comes from the presence of the STM feedback circuit, which allows the nominal tip-to-sample separation of 1 nm. From the point of view of propagating waves, the STM facilitates an increase in tip-to-sample coupling via the capacitance, C_x . From the point of view of non-propagating (evanescent) waves the contribution of high spatial wave-numbers increases significantly when the tip-to-sample separation reaches the height of 1 nm. As a result, very interesting contrast is seen in Δf and Q signals, as was discussed in chapter 4. However, at this stage it is important to briefly describe the next steps to be taken, both with theoretical models for the microscope and the experiments to be performed with this microscope. In the next two sections I am going to give a brief description for future directions.

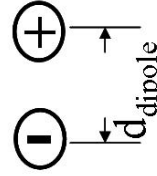
7.2 The future directions with NSMM models

The NSMM in general is a complex problem of electrodynamics. I performed extensive modeling (analytical and numerical) to understand the tip-to-sample interaction. The analytical model consists of propagating and non-propagating (evanescent) wave models. In chapter 3, I discussed the evanescent wave model that was developed for NSMM. I also discussed the shortcomings of the evanescent wave model developed for the sphere above the plane. One problem was the lack of self-consistency in the field equations. The second issue was that the problem was not solved for multi-layered structures with appropriate Fresnel coefficients.

The solution to these problems is to model the STM tip as an antenna. This antenna is a small Hertzian dipole antenna⁸⁸ near an interface between two media (shown in Fig. 7.1), with the dipole moment (denoted by \vec{p}) of $|\vec{p}| = |d_{dipole}| \left(\int I dt \right)$ where I is the current and d_{dipole} is the length of the dipole. The exact solution for both electric and magnetic fields in both media exists in the literature⁹⁵⁻⁹⁸ in the form of complicated integrals⁹⁵. The important thing is that the solutions contain the contribution of the evanescent waves explicitly for near-field cases. The literature contains recipes to extend the model to multi-layered structures^{96,98}.

small electrical radiating dipole

$$(d_{\text{dipole}} \ll \lambda_{\text{radiation}})$$



Medium 1

Medium 2

interface

Fig. 7.1: A small Hertzian dipole near the interface of two materials. Medium 1 and medium 2 have different electromagnetic properties.

7.3 The future direction with NSMM experiments

The geometry of the tip is very crucial to experiments with this novel microscope, as was shown in chapter 4. It is required that the tip which is picked, is good for both STM and NSMM experiments. My studies with the available tips so far show, that the WRAP082 tip (shown in Fig. 2.26) is simultaneously the best tip for both NSMM and STM experiments. The tip is commercially available and this is the tip which should be used for future experiments. This will fix the tip-to-sample capacitance C_x (assuming the sample is topography free) and then the signal changes will come due to the sheet resistance (R_x) contrast in the sample.

As far as the samples are concerned, the next interesting direction to take are the single crystals of layered CMR materials. These layered materials can be cleaved easily to expose fresh surfaces of the sample, where the surface cleaves with topography-free terraces which spatially are on length scales of hundreds of nanometers^{99, 101}. Since the material is single crystal, it will make it easier to model the experiment. Such materials are thought to have “insulating” and “metallic” states⁷⁴⁻⁷⁷ as was discussed in chapter 6. It will be very interesting to map these different phases by measuring sheet resistance. There are evidences that such phases coexist on atomic length scales⁷⁶. The Oxford STM can be easily modified for atomic resolution imaging, if the HV amplifiers (Fig. 2.9c) are bypassed. This will reduce the noise in the piezo system and then low voltage amplifiers can be used for scanning with atomic resolution.

Appendix A

Few Issues in Relation to the Scanning Tunneling Microscope (STM)

As was mentioned in chapter 1, this novel NSMM has STM feedback integrated on it to achieve the closest possible tip-sample separation without touching the sample. This requires addressing a few key issues regarding STM (tip-sample interaction) which affect the NSMM measurement. These issues are the subject of this appendix.

A.1 Nominal height of tip above sample during tunneling

All throughout the thesis it is assumed that the nominal height of tip above the sample is 1 nm during tunneling. Here I establish the validity of this claim in the light of data taken over the gold on mica thin film. The arguments are based upon the one-dimensional tunneling model which was discussed in chapter 2. Fig A.1 plots the tunnel current as a function of height as $\text{Ln}(I_{\text{tunnel}}(\text{nA}))$ versus $Z(\text{\AA})$ position of the Piezo.

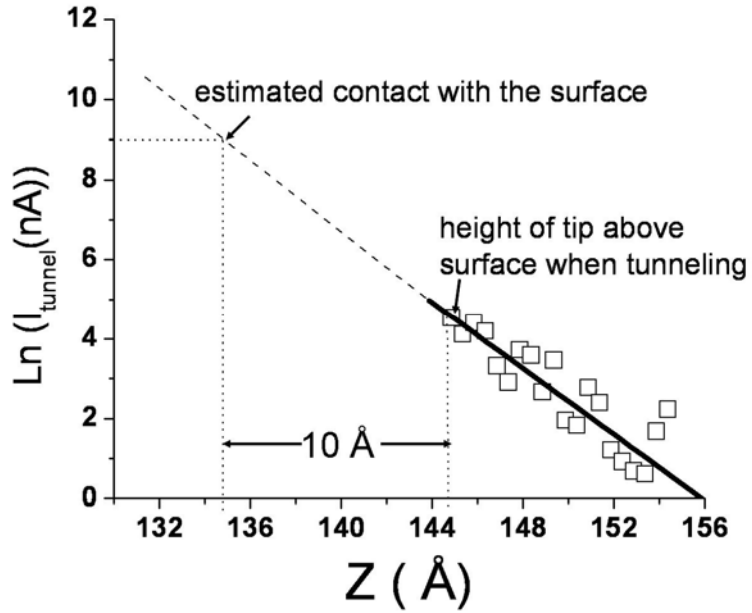


Fig A.1: Tunnel current ($\text{Ln}(I_{\text{tunnel}}(\text{nA}))$) versus Z position for an STM tunnel junction between a Pt/Ir tip and Au/mica thin film sample. The open squares are the data points and solid black line is the exponential fit with the slope of -0.41\AA^{-1} . The bias on the film was 100 mV. The contact point is estimated using $I_{\text{contact}} = V_{\text{bias}}/R_{\text{contact}}$ where R_{contact} is the expected point contact resistance of 12.9k Ω . This determines the height of the tip to be 1 nm above the sample.

For a one-dimensional tunnel barrier between two metal electrodes, the tunneling current I

decays exponentially with the barrier width d , as $I \propto e^{-2\kappa d}$, where $\kappa = \sqrt{\frac{2m\phi}{\hbar^2}}$, where ϕ is

the work function of the metal⁸³. For a typical metal the $\kappa \sim 1\text{\AA}^{-1}$, and the tunnel current data in Fig. A.1 shows clear exponential drop with probe-sample separation, having a slope of -0.4\AA^{-1} which is on the right order for κ . The z position of the surface is estimated from

the extrapolated point contact current which is calculated through $I_{\text{contact}} = V_{\text{bias}}/R_{\text{contact}}$ where $V_{\text{bias}}=100$ mV and R_{contact} is taken to be $12.9\text{k } \Omega^{82}$. This estimate yields a nominal probe-sample separation of 1 nm during STM scanning.

I also need to mention that I have observed it over many sample that STM topography does not change when the microwave signals are applied. This observation has been made for up to +5 dBm of microwave source power levels. I have performed most of the experiments at microwave source power level of +3 dBm or less. At height of 1nm and tip voltage of 0.23 volts (1 mW of power), the displacement current density ($|J_{\text{disp}}| = \epsilon_0 \omega |\vec{E}|$) at 10 GHz is $\sim 1.3 \times 10^4$ A/cm². Such current density can be a concern for local heating, for example, when dealing with superconducting samples, as locally film may go in the normal state.

A.2 Effects of tip geometry on topography

Based on Table 2.1 in chapter 2, I concluded that large r tips are not good for STM purposes, although such tips are important for increasing the signal to noise ratio for NSMM. Here I want to briefly discuss it in the light of some data taken on a Nickel (Ni) calibration sample. Such samples are commercially available and are used to calibrate the X, Y and Z scales of different Scanning Probe Microscopes (SPM). In my case I had a Ni disk, which was 0.3 mm thick, and about 0.63 cm in diameter. The pattern was a CD track pattern (HD-750) on it, and the surface topography was quantitatively known with the help

of Atomic Force Microscope (AFM) as shown in Fig. A.2 (AFM was performed by the supplier company⁸⁴).

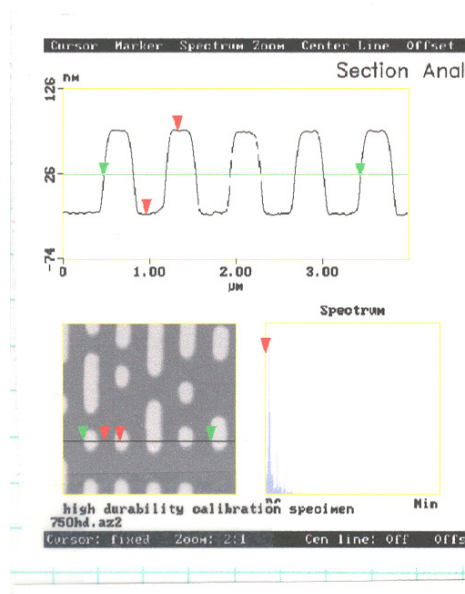


Fig. A.2: The AFM image of the HD-750 Ni calibration sample. The scan is 4 μm X 4 μm and the topography in z is about 100 nm and pitch of features in plane is 740 nm.

By scanning with the STM system, I can match the resulting image with the AFM image to calibrate. The results with three different tips (chosen from the ones mentioned in table 2.1) on this Ni sample are shown in Fig.A.3.

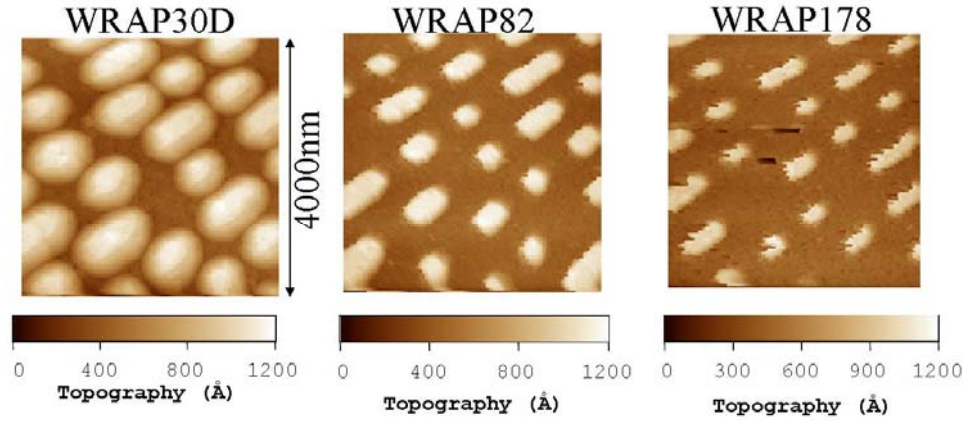


Fig.A.3: STM topography images taken with three different tips on the Ni calibration standard sample. The WRAP082 data matches the closest with expectations based on AFM data. The WRAP30D is a tip with large r , and the features are enlarged. The WRAP178 tip has very small r , and the island images have ragged borders.

The WRAP082 data matches the closest with the expectations based on the AFM image of Fig. A.2. The WRAP30D is a tip with a large embedded sphere radius r , and the features are enlarged. The reason is that multiple tunneling sites are produced with the surface (since the curvature of the tip is $\sim 6 \mu\text{m}$ compared to a $0.74 \mu\text{m}$ pitch in the features). On the other hand, the WRAP178 tip image has ragged borders. This tip has a very long (thin tapered) end which sticks out and I think it mechanically vibrates parallel to the plane of the sample surface. The effect of this vibration is more visible at borders. The data presented in this thesis is mostly from the WRAP082 tip (or tips with similar geometry but different materials). The WRAP082 had been the easiest compromise for both high quality STM and reasonable signal to noise ratio for NSMM.

Appendix B

Determination of Microscope Q

The microscope electronics do not directly measure the quality factor, or Q , of the microscope. Instead the electronics measures the output of a lock-in amplifier tuned to the second harmonic of the modulation frequency, as was discussed in chapter 2. This signal, V_{2f} , must be converted to Q using the procedure described in this appendix^{80, 81}.

.

B.1 Theory:

For a given resonator there are two types of quality factors defined: unloaded quality factor (Q_u) and loaded quality factor (Q_L). The unloaded Q takes into account only the losses in the resonator and excludes losses due to the coupling system (microwave source, cables linking the source to resonator and devices used). What is measured though is the loaded Q . Hence to find out the dissipation inside the resonator I need to know the relationship between Q_u and Q_L . An example calculation is shown from the *Mathematica* code in section C.

Let us start with the parallel lumped element circuit discussed in chapter 3. The parallel RLC is the resonator and external circuit has impedance Z_0 (Fig. B.1). For my microscope,

a 1.06 m transmission line coaxial cable is used as the resonator. It is capacitively coupled to the source and feedback circuit. The S_{11} versus frequency has a minimum at the resonant frequencies of the resonator and $|S_{11}|$ becomes 1 away from resonance. For an ideal resonator $|S_{11}|$ goes to 0 at the resonance frequency (called critical coupling). The reflection coefficient S_{11} is given by

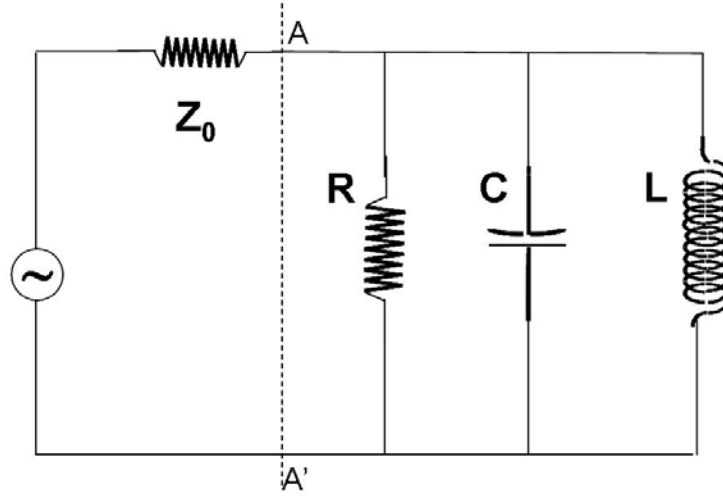


Fig. B.1: The circuit diagram for the parallel RLC circuit and the measurement port is denoted as AA'. The impedance of external circuit is Z_0 .

$$\rho = S_{11} = (Z_L - Z_0)/(Z_L + Z_0) \quad (\text{B.1})$$

where Z_L is the impedance of the load (resonator) and Z_0 is the impedance looking into the source. For the parallel circuit lumped element model case the total impedance of the circuit is given by:

$$\frac{1}{Z} = i\omega C + \frac{1}{i\omega L} + \frac{1}{R} \quad (\text{B.2})$$

where C is the capacitance, L is the inductance, R is the resistance and ω is the driving frequency. The losses in the circuit can be specified as Q where

$$Q = \frac{U_{\text{resonator}} \omega}{P_{\text{dissipated}}} \quad (\text{B.3})$$

and $U_{\text{resonator}}$ is the energy stored in the resonator and $P_{\text{dissipated}}/\omega$ is the power dissipated per unit cycle. For the parallel circuit the unloaded Q (Q_u) is given by⁶⁴

$$Q_u = \omega_0 RC \quad (\text{B.4})$$

where ω_0 is the resonant frequency of the lumped element circuit. For the parallel lumped

element circuit model, the loaded Q is $Q_L = \frac{\omega_0 C}{(\frac{1}{R} + \frac{1}{Z_0})}$ which can be written as

$$Q_L = \frac{\omega_0 RC}{(1 + \beta)}, \text{ where } \beta = \frac{R}{Z_0} \text{ is called the coupling parameter, and then using (B.4) I can}$$

write

$$Q_L = \frac{Q_u}{1 + \beta} \quad (\text{B.5})$$

Going back to the equation (B.2), the impedance of the resonator can be written as

$$Z = \frac{1}{\frac{1}{R} + i(\omega C - \frac{1}{\omega L})} \quad (\text{B.6})$$

Given that $\omega_0 = \frac{1}{\sqrt{LC}}$ the equation above can be written as

$$Z = \frac{1}{\frac{1}{R} + i(\omega_0 C(\frac{\omega}{\omega_0} - \frac{\omega_0}{\omega}))} = \frac{R}{1 + iQ_u(\frac{f}{f_0} - \frac{f_0}{f})} \quad (\text{B.7})$$

where I have substituted for Q_u from equation (B.4). If f is the frequency which deviates slightly from the resonant frequency f_0 of the resonator by amount v (that is $f = f_0 + v$ and v is considered small), then with the help of this equation (B.7) can be written as

$$Z = \frac{R}{1 + iQ_u[\frac{(f + f_0)(f - f_0)}{f_0 f}]} = \frac{R}{1 + iQ_u[\frac{2v}{(f_0 + v)} + \frac{v^2}{f_0(f_0 + v)}]} \quad (\text{B.8})$$

where terms on the order of v^2 can be ignored. Substituting this Z in equation (B.2 and B.1) yields

$$\rho = \frac{(R - Z_0) - i2Z_0Q_u \frac{v}{f}}{(R + Z_0) + i2Z_0Q_u \frac{v}{f_0}} \quad (\text{B.9})$$

and taking the magnitude of this equation yields

$$|\rho| = \sqrt{\frac{(R - Z_0)^2 + (2Z_0Q_u \frac{v}{f})^2}{(R + Z_0)^2 + (2Z_0Q_u \frac{v}{f_0})^2}} \quad (\text{B.10})$$

At the resonance frequency ν in equation (B.10) goes to zero and I get equation (B.1) back with $Z_L = R$. In order to find the loaded Q , consider the following condition satisfied at deviation frequency ν_1 ,

$$2Z_0Q_u \frac{\nu_1}{f_0} = \pm(Z_0 + R) \quad (\text{B.11})$$

This yields a corresponding reflection coefficient

$$|\rho_1| = \frac{\sqrt{1 + \left(\frac{R}{Z_0}\right)^2}}{1 + \frac{R}{Z_0}} = \frac{\sqrt{1 + \beta^2}}{1 + \beta} \quad (\text{B.12})$$

and we also get $\left| \frac{f_0}{2\nu_1} \right| = \frac{Q_u}{\frac{R}{Z_0} + 1} = \frac{Q_u}{\beta + 1} = Q_L$ which is just equation (B.5).

However, as shown in Fig. B.2, in the real resonator the S_{11} may not go to 1 away from resonance. It happens when the resonances are closely spaced and hence they may “interfere” with each other. It may happen that ν_1 is so large that it is in the next resonance curve. In order to find Q_L for such cases, we seek a smaller value of ν , such as ν_m , where $m > 1$. In this case, the condition (B.11) is modified as follows:

$$2Z_0Q_u \frac{\nu_m}{f_0} = \frac{\pm(Z_0 + R)}{m} \quad (\text{B.13})$$

and then equation (B.12) is modified as follows

$$|\rho_m| = \frac{\sqrt{1 + \beta^2 - 2\beta\left(\frac{m^2 - 1}{m^2 + 1}\right)}}{1 + \beta} \quad (\text{B.14})$$

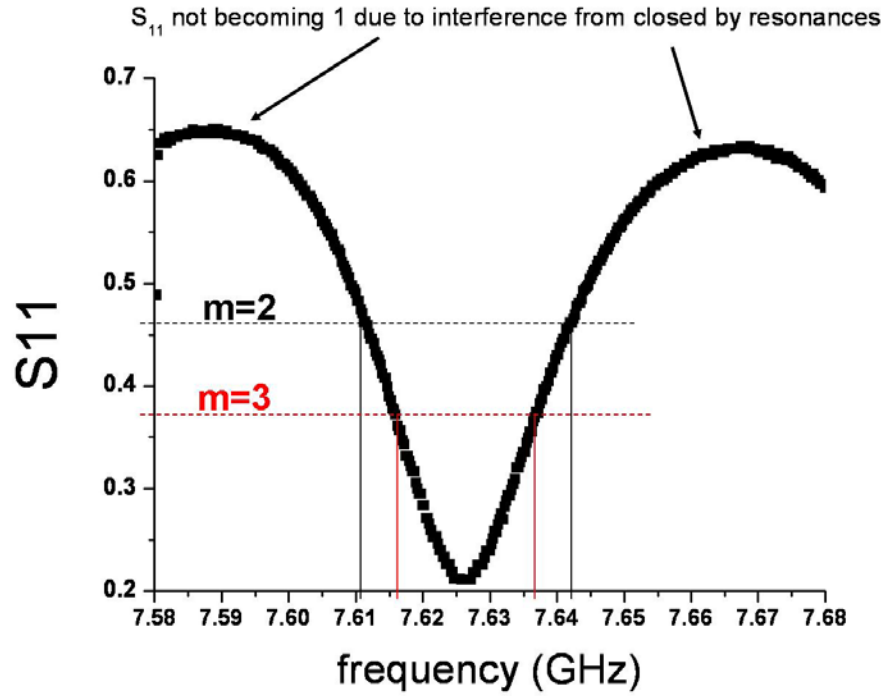


Fig.B.2: Measured $|S_{11}|$ versus frequency for a single resonance around 7.625 GHz. The arrows are pointing to the down turn of $|S_{11}|$ before it even reaches the value of 1. This is happening due to interference from nearby resonances. The $m=2$ and $m=3$ are shown to clarify the range used for calculation of Q . For any m , the Q_L is the same due to equation B.13.

B.2 Experimental Procedure:

The following describes the procedure to find the unloaded Q and loaded Q for the coaxial resonator used in the near-field microwave microscope. The *Mathematica* file used to calculate Q is called “Qcal.nb” (section C). The setup is basically to attach the diode

detector directly to an A/D board which communicates with a computer to collect data (the NSMM feedback, modulation and V_{2f} lock-in is removed). A background measurement is done without the resonator. The measurement is then done with the resonator and in both cases the V_{diode} is measured and recorded as a function of frequency.

1) The first step is to sweep the frequency (that is measure V_{diode} versus frequency). A LabVIEW program is used to communicate with the microwave source in order to sweep the frequency (the file is located C:\Atif\LabVIEW\...). The file name is “frequencysweep.vi.” The Computer 152 in Rm 0310A is currently connected via GPIB interface to the Agilent E8257C source. From the interface window of the “frequencysweep.vi,” one can choose the range of frequency sweep, frequency step size, time for each frequency step and power level of the source. The output of the HP 8473C diode detector (Fig. 2.16b) is fed into the ACH0 Channel of the National Instruments A/D board which sends the data to the Computer 152. The data can be saved as a *.txt file by giving the path and file name. The *.txt file is two column file, with frequency in GHz as the first column and the diode voltage in Volts in the second column.

2) Once the above setup is in place, sweep the frequency with the resonator present. Save this result as a text file. Disconnect the resonator and the decoupling capacitor (keep the resonator and decoupling capacitor connected together), and then sweep the frequency of the source again to get the background for the measurement. Save this background data as a separate text file.

3) At the frequency of resonance, the diode voltage (V_{diode}) dependence on the power level of the microwave source should be known (V_{diode} (volts) versus microwave source power level (mW)). It is sufficient to know this in the region of power values of interest for the experiment (see figure B.2). V_{diode} versus the microwave source power is not a strong function of frequency. However, for more precise measurements this curve should be measured in the vicinity of each resonance frequency at which experiment is performed. Figure B.2 shows that the V_{diode} versus source power data falls over each other for two different frequencies. The same is true for higher and lower power levels of the microwave source, which is not shown in the figure.

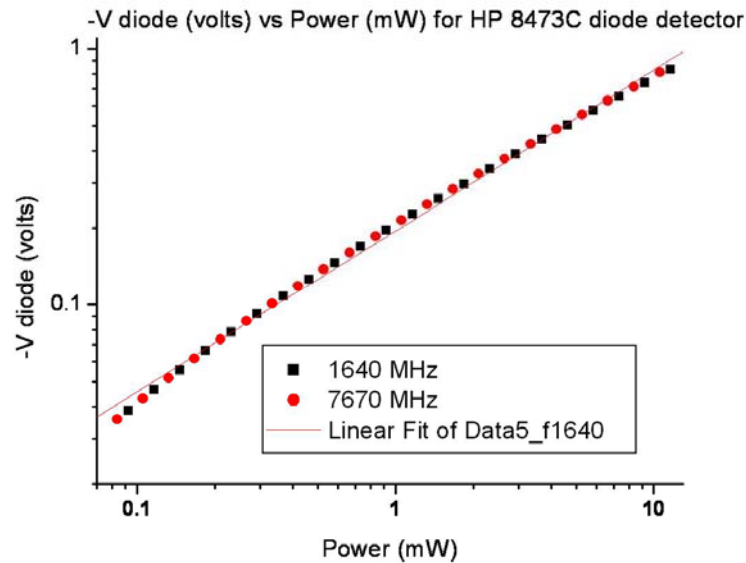


Fig.B.3: The diode output voltage V_{diode} versus input microwave power measured for an HP8473C diode detector. The source is an HP83260B microwave synthesizer. Most of the experiments I performed were in the vicinity of 1mW of input power. From the quality of

the linear fit (solid line) the dependence of V_{diode} on microwave source power is approximately linear.

4) Plot power versus V_{diode} , and then fit it to first order Polynomial (for the range of power level where behavior of V_{diode} versus power level is fairly linear). Get the coefficients of the fit. Generally, Origin can be used to achieve this. One such example fit is shown in Fig. B.2.

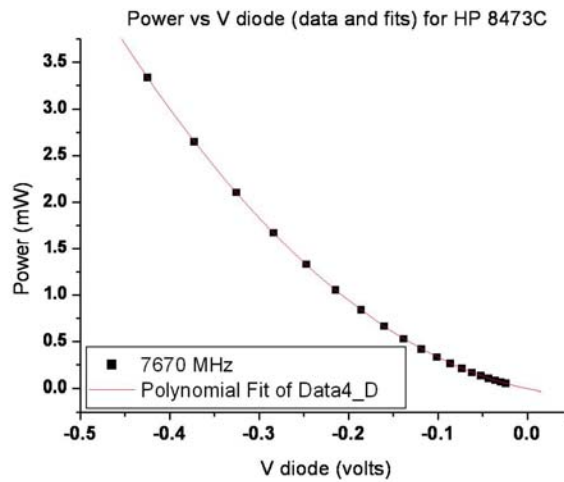


Fig. B.4: The polynomial fit to the microwave source power versus V_{diode} for a frequency of 7.67 GHz. The equation of the polynomial fit for this particular data set is $y = -0.0044437259 - 1.9480740139x + 13.924029069 x^2$.

5) As a next step, we need to convert the Voltage output of the diode (V_{diode}) to Power output of the diode (P_{diode}) using curves similar to the one shown in Fig. B.4. The magnitude of S_{11} is

$$S_{11} = \rho = \sqrt{(P_{diode\text{resonator}})/(P_{diode\text{background}})} \quad (\text{B.15})$$

This completes the process to convert the V_{diode} versus frequency to S_{11} versus frequency, which gives me the data similar to the one shown in Fig. B.2. The original data and background data in form of V_{diode} is shown in Fig. B.5.

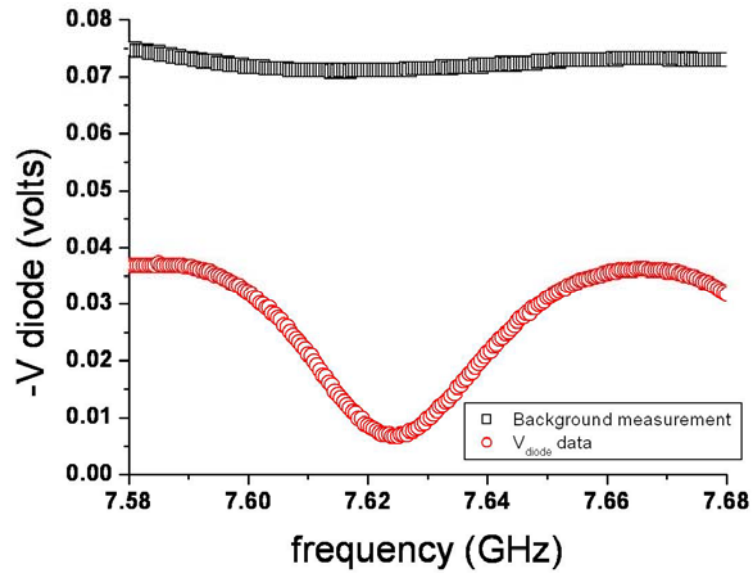


Fig. B.5: Raw data measured for the background and a single resonance. The frequency is done based on the code written in LabView.

B.3 An example of calculation from the file Qcal.nb

This section has an example of resonance data used to calculate loaded and unloaded Q from the data (Fig. B.6).

```

ClearAll["Global`*"];
Off[General::spell, General::spell1];
(* This section is just to read in data *)
SetDirectory["C:\\Atif\\S11sweeps\\Aug02\\Aug_23"];
listbg = ReadList["Background_oneResonance_50MHz_A.txt", {Number, Number}];
listdata = ReadList["Data_oneResonance_50MHz_A.txt", {Number, Number}];
(* The equations (as given in theory section) are being used here
   setting up the calculation *)

a0 = -0.0044437259;
a1 = -1.9480740139;
a2 = 13.924029069;
m = 2;
power[v_] := a0 + a1*v + a2*v^2;
beta[smin_] :=  $\frac{1 - smin}{1 + smin}$ ;

$$\rho[m_, smin_] := \frac{\sqrt{1 + \beta[smin]^2 - 2 \beta[smin] \frac{m^2 - 1}{m^2 + 1}}}{1 + \beta[smin]}$$
;

s11list = Table[{listbg[[n]][1],  $\sqrt{\frac{\text{power}[listdata[[n]][2]]}{\text{power}[listbg[[n]][2]]}}$ },
  {n, 1, Length[listbg]}];
(*ListPlot[s11list, PlotRange -> All]*)
s11 = Interpolation[s11list];
p1 = Plot[s11[x], {x, 7.61, 7.65}, PlotRange -> All, PlotStyle -> {RGBColor[1, 0, 0]},
  DisplayFunction -> Identity];
p2 = ListPlot[s11list, PlotRange -> All, PlotStyle -> {RGBColor[0, 0, 1]},
  DisplayFunction -> Identity];
Show[p1, p2, DisplayFunction -> $DisplayFunction]

```



```

- Graphics -
- Graphics -
(*Calculation is being performed *)
resonance[f_, fmin_, fmax_] := FindMinimum[s11[f0], {f0, f, fmin, fmax}];
result = resonance[7.63, 7.61, 7.65]
 $\beta$  = beta[result[[1]]]
 $\rho$ m =  $\rho$ [m, result[[1]]]
f1 = FindRoot[s11[f] - ( $\rho$ m) == 0, {f, 7.65}, MaxIterations -> 100][[1]][2]
f2 = FindRoot[s11[f] - ( $\rho$ m) == 0, {f, 7.61}, MaxIterations -> 100][[1]][2]
df = f1 - f2
 $Q_L = \frac{f_0}{df}$  /. result[[2]]
 $Q_{UL} = Q_L (1 + \beta)$ 

{0.226185, {f0 -> 7.6303}}
0.631076
0.490844
7.64645
7.61319
0.0332556
229.444
(* The upper value here is loaded Q *)
374.24
(* The upper value here is unloaded Q *)

```

Fig. B.6: The mathematica code to show an example calculation.

Appendix C

Other Attempted Projects

Many attempts were made to find samples that were simultaneously interesting to study with the NSMM and which we could successfully establish an STM tunnel junction. The samples picked had either interesting physics associated with them or could have been helpful in giving us insight regarding the operating principles of the NSMM. Some of the samples that were picked, but not entirely successful for one reason or another, are highlighted in this appendix.

C.1 Carbon Nano Tube samples

The goal of this study was to isolate a single carbon nano-tube (CNT) and measure its microwave properties with NSMM. Todd Brintlinger in Dr. Fuhrer's group collaborated directly with me and helped prepare samples for me. The major challenge to overcome was preparation of a surface clean enough for the STM to establish a tunnel junction.

We grew CNTs on top of three pieces of a Boron-doped Silicon sample. The (Boron-doped Silicon) substrate was dipped in $\text{Fe}(\text{NO}_3)_3/\text{IPA}$ solution for 10 seconds. As a next step (in order to precipitate out $\text{Fe}(\text{NO}_3)_3$), the Silicon was dipped in hexanes. Next it was heated to 900°C in oven, under H_2/Ar . In order to start the growth process, the methane (5L/min) was

turned on and then the H₂/Ar gases were turned off. After allowing 10 minutes for the CNTs to grow, the Argon was turned on, and methane was turned off. The samples were removed after the cool down.

From the AFM images (Fig. C.1a) of these samples, we could see in a 25 μm square area 10 – 12 distinct CNTs, with an average length of 4 μm. There were some scattered dirt particles in the AFM image as well. However, during STM the tunnel junction with this sample was very unstable. Many different areas were probed but all showed similar results. It appears that the whole surface is contaminated with some sort of 'junk' that has the CNT buried underneath. The AFM probably is not sensitive to it and was able to show the tubes, but STM works through tunneling and may be digging into the junk and then dragging it about while scanning the tip. Two tips were used to scan and they both ended up with a 'birds beak' deformation, similar to the ones seen in Fig. 2.23 and Fig. 2.24. A typical STM topography scan is shown in Fig. C.1.

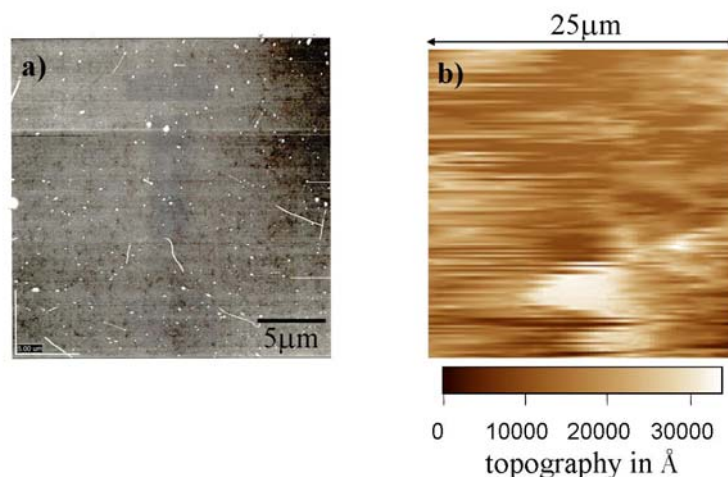


Fig. C.1: a) AFM image of a CNT sample on Silicon. b) The STM image from the Silicon sample with CNTs grown on top of it. It looks like the whole surface is contaminated with some sort of junk. The STM tips were damaged in the form of a ‘birds beak’ as if they were piercing through and scanning through some junk layer on the surface.

We tried to clean the film with Buffered oxide etch, then water, and then methanol. Todd and I were hoping that this process would clean the junk while leaving the CNTs intact. However, from the AFM images we found that we washed away the nano-tubes as well.

The second attempt we made was on 2000Å thick gold on glass film. Single wall/multi-wall nano tubes were spun onto this gold/glass sample. The process included 2 drops of CHCP₃ (100 μg/mL) spun on for 60 sec at 4000 rpm. The sample was annealed to 300°C. After scanning many regions, I only found one large bundle, which is shown in Fig. C.2 as imaged by STM.

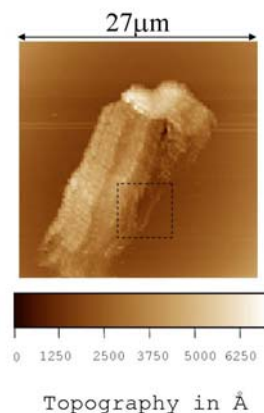


Fig. C.2: STM of an interesting bundle that I found after scanning many different areas of a CNT sample spun on to a Au/glass substrate. The dashed square represents a region where I thought I may find a single isolated CNT. The data from there is shown in Fig. C.3.

I picked the region (shown by the dashed square in Fig. C.2) where I was hoping there would be a single CNT available for imaging. However, I think the tip had been damaged when scanning over the bundle, as can be seen from the images in Fig. C.3.

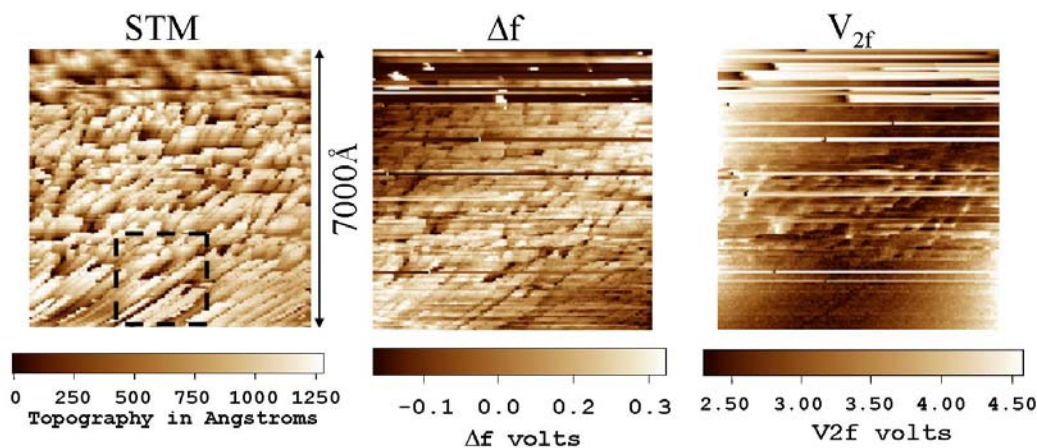


Fig. C.3: The simultaneous imaging of a CNT bundle on Au/glass substrate in the square region shown in Fig. C.2. Due to a damaged tip it was hard to conclude whether the square region of Fig. C.2 contained any CNTs. The square on the STM marks the approximate location of the image area of Fig. C.4.

I became interested in the lower part of the images in Fig. C.3 as these may be regions where I can find CNTs. However, narrowing down on these features (see the dashed box in Fig. C.3 for approximate position of area shown in Fig. C.4) just amplified the fact that tip was damaged, and this becomes clear in Fig. C.4.

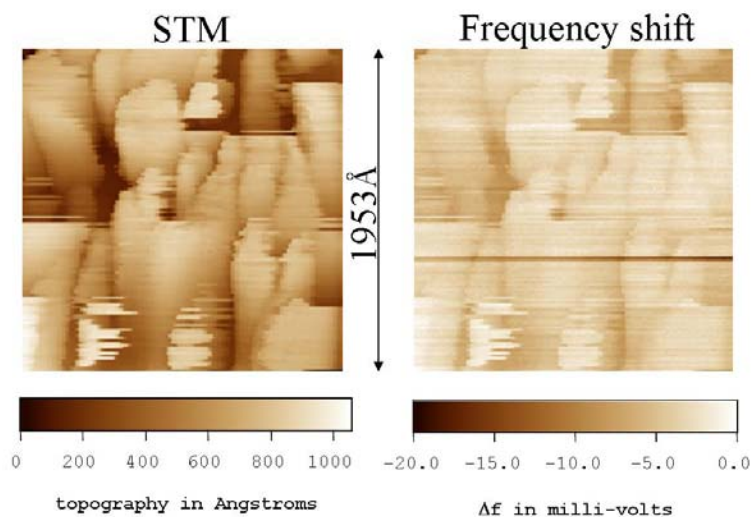


Fig. C.4: The simultaneous imaging of topography and frequency shift in a CNT bundle on Au/glass substrate. I think that due to the damage to the tip, these features are just tip artifacts. It is hard to conclude whether they are CNTs or just distorted gold grains on the gold on glass film.

At this stage I set a few goals for myself. One is to find a sample with a high yield of isolated CNTs, and the second is to have a surface clean enough for STM. After discussions with Todd, we decided to look into better evaporation techniques of CNTs, which is currently work in progress.

C.2 Field-Effect CMR sample

For this sample Dr. Eric Li (of Dr. Venkatesan's group) collaborated with me. It had been reported that certain CMR samples show a complimentary electroresistance effect (change of resistivity when electric field is applied to the material) to the CMR effect. Dr. Wu's paper⁷¹ mentions seeing this effect in an LCMO ($\text{La}_{0.7}\text{Ca}_{0.3}\text{MnO}_3$ and $\text{La}_{0.5}\text{Ca}_{0.5}\text{MnO}_3$) $\sim 500\text{\AA}$ thin films on 1500\AA of PZT ($\text{PbZr}_{1-x}\text{Ti}_x\text{O}_3$)⁷¹. The ferroelectric PZT was sandwiched between the LCMO thin film and a $500\text{ }\mu\text{m}$ thick 1% Nb:STO gate electrode (see Fig. C.5). The reason for this electroresistance effect is claimed to be the coexistence of insulating and metallic phases in the LCMO. The metal phase exists as small domains embedded in insulating material (as shown in the schematic in Fig. C.5). These domains are thought to be on nanometer to micron length scales. As the temperature is lowered or electric field is applied, the growth or shrinkage of these domains change the global resistivity of the material. In both cases, the metallic regions start to grow and they interconnect with each other (top view in Fig. C.5), reducing the resistance. Effectively the electric field can produce a percolating network of metallic domains in the LCMO.

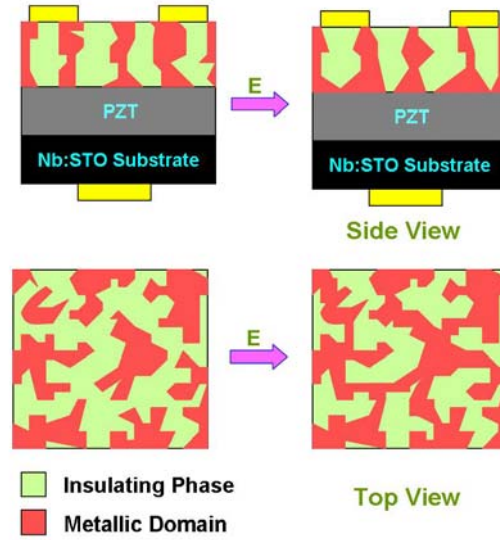


Fig. C.5: The schematic of the electric field effect on the CMR sample. The electric field is applied vertically between the yellow electrodes and the Nb:STO counterelectrode. The electric field causes PZT domains to flip and locally dope the LCMO film into the metallic state. This helps to interconnect the metallic domains, hence reducing resistivity.

Since I already had tunneled successfully in $\text{La}_{1-x}\text{Ca}_x\text{MnO}_3$ with composition $x = 0.33$ (very close to the reported $x = 0.3$) I decided to perform an experiment on this sample. The NSMM should have been sensitive to the interconnects between domains, as these are the regions where the sheet resistance changes. This change in sheet resistance will occur with the electric field due to voltage on gate electrode.

The main problem which plagued this project was the pin-holes which occur in the thin PZT layer during the growth process. The original samples prepared were $20\text{ }\mu\text{m} \times 200\text{ }\mu\text{m}$ bridges of LCMO sample on top of a 1% Nb:STO substrate (1mm^2), with PZT sandwiched in between. Such a device itself was not big enough for me to locate optically, and then

place the tip (via slip stick mechanism) on top of it to establish tunnel junction. So we tried to make the device a size which was 1 mm x 1 mm, and the results of the electro-resistance (ER) experiment are shown in Fig. C.6. With a gate voltage of 0 V, when the temperature was ramped down, the CMR effect was not as pronounced as we expected it to be (the expected peak value was 30 mΩ.cm). Applying -6V at the gate and ramping down the temperature did show the ER effect, however, ramping the temperature up, we did not see the ER effect. The subsequent temperature ramps to see the ER effect were not successful on this device.

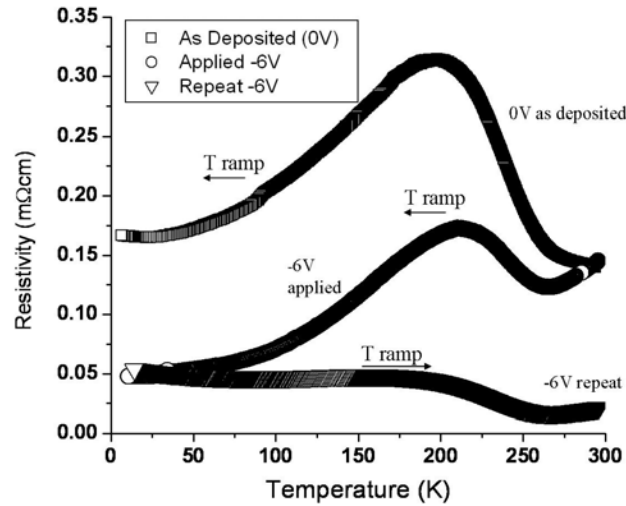


Fig. C.6: Resistivity versus Temperature for a 1 mm x 1 mm LCMO/PZT/Nb:STO layer to see the electroresistance effect. The device did not show reproducible behavior when the temperature was ramped.

We think, that we ended up shorting the LCMO thin film with the 1% Nb:STO layer via the pin-holes in the PZT layer (the LCMO film entered these pin-holes during deposition

and connected with the 1% Nb:STO). This problem of holes in the PZT layer was there even in the $20\text{ }\mu\text{m} \times 200\text{ }\mu\text{m}$ bridges as well. However out of 100 devices prepared and tested, there was a region which did not have the holes shorting the thin film and substrate, and the device worked. With a 1mm^2 sample the probability of shorting is very high, and that is what convinced me to discontinue the project.

C.3 Variable thickness sample prepared by the Focused Ion Beam technique

For this sample I collaborated with Dr. Andrei V. Stanishevsky, who operated the Focused Ion Beam (FIB) facility. This sample was a Chromium (Cr) thin film deposited on Silicon, and Cr was selectively removed from certain regions using the Focused Ion Beam technique. The idea of this sample was to make a topography-free variable sheet resistance (R_x) sample that could be examined with a single scan of the STM piezo head. The sheet resistance was defined by the thickness of the film. Hence for a fixed resistivity (ρ) but different thickness (t), the NSMM sees contrast in $R_x = \rho/t$, which for each thickness should be topography independent. Cr was picked as a material to avoid soft metals like gold, silver and copper. It was feared that soft metals may show corrugation and the material may not form sharp steps (as seen in Fig. C.8; it did not work out with Cr as well).

The average thickness of Cr deposited on the Silicon substrate was $500\text{ }\text{\AA}$. The layout of the sample is shown schematically in Fig. C.7. Each square represents a $5\text{ }\mu\text{m} \times 5\text{ }\mu\text{m}$ area, and all six plateaus together formed a $10\text{ }\mu\text{m} \times 15\text{ }\mu\text{m}$ feature. Even with the navigation

marks placed, it was quite challenging to find these features with the STM. The squares were supposed to be in steps of thickness 500Å, 400Å, 300Å, 200Å, 100Å and 50Å, respectively.

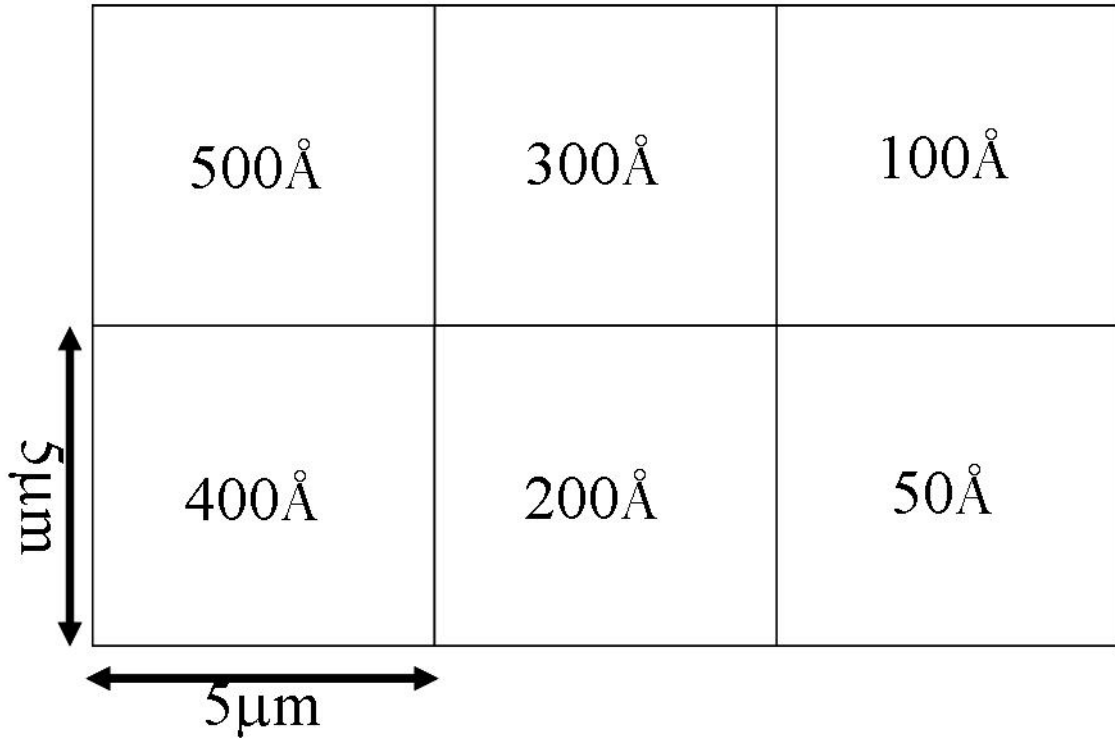


Fig. C.7: The schematic of the variable thickness Cr/Silicon film sample prepared by the Focused Ion Beam technique. The idea is to have uniform plateaus of variable sheet resistance. Three such features were made in one film.

However, the sample that I got fell short of fulfilling the goals that I had in mind. The plateaus did not come out free of topography, and there was much undesired corrugation and damage on the surface. The Atomic Force Microscope (AFM) images of two of the features are shown in Fig. C.8.

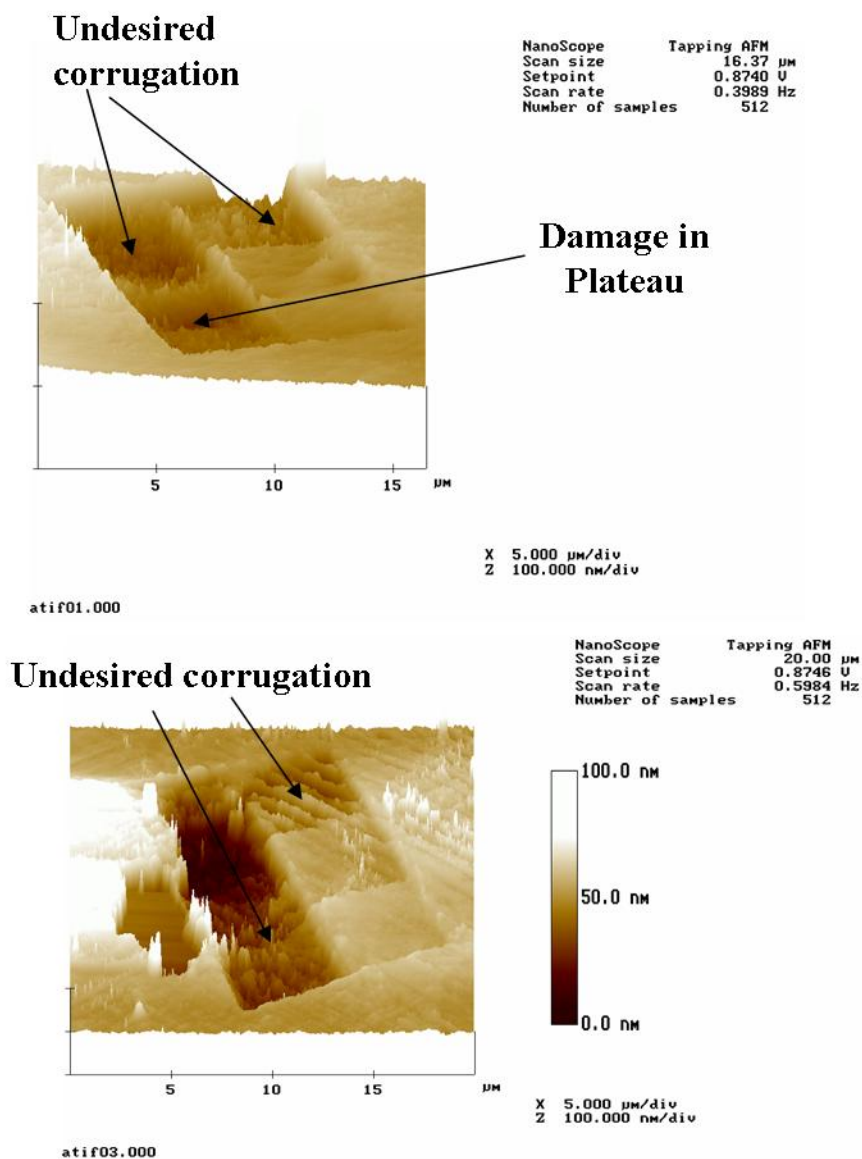


Fig.C.8: The AFM images of two of the features to show corrugation and damage on the surface. The Cr material was not removed smoothly by FIB.

The STM showed similar results as AFM (the STM is shown in Fig. C.9), where damage and non-uniformity of the plateaus is clear. The microwave microscopy signal just showed

topography contrast rather than reliable materials contrast (shown in scaled format in Fig. C.10).

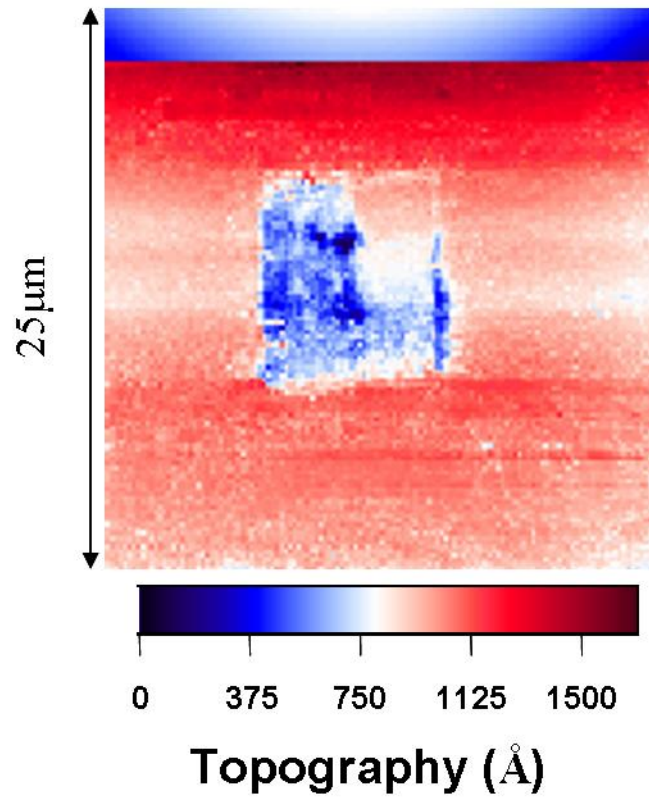


Fig. C.9: The STM of the Cr/Silicon sample prepared by FIB. All three plateaus on the left are damaged and acting like one big region with topography of about 1000Å.

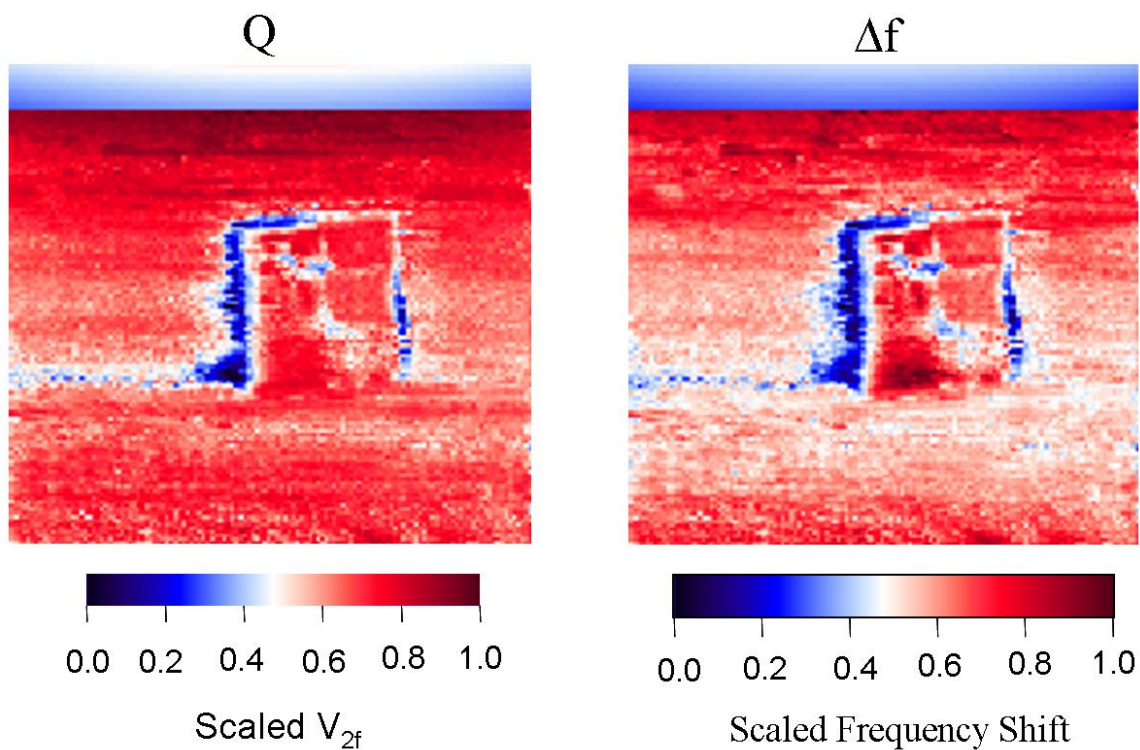


Fig.C.10: The scaled NSMM images of the Cr/Silicon FIB-modified sample. Due to damage to the surface no quantitative information could be extracted. The thick blue trailing response on the left may be due some damage beneath the surface, since the skin depth $\delta=2\mu\text{m}$ for this experiment at 7.5 GHz. The experiment was performed at room temperature.

I learned valuable lessons from this sample, and the result was the variably boron-doped Si discussed in Chapter 5.

C.4 The $\text{CaCu}_3\text{Ti}_4\text{O}_{12}$ (CCTO) thin film sample

Another material of interest in our group is the colossal dielectric constant oxide $\text{CaCu}_3\text{Ti}_4\text{O}_{12}$ (CCTO). I collaborated with Dr. Alexander Tselev in the measurements on these materials. He had already measured the dielectric response of his insulating CCTO films¹⁰⁰. He discovered that these materials could be made conducting by appropriate annealing in oxygen, thus enabling experiments with my microscope. Dr. Tselev was curious to see if any inhomogeneities in the properties of these films could be observed with my microscope. I went ahead and performed an experiment on one of the films, on which I was able to establish an STM tunnel junction. The results of STM are shown in Fig. C.11 and the simultaneous imaging (on top of grain) is shown in Fig. C.12.

The films that I was able to tunnel into still did not turn out to be very interesting samples for NSMM. The tips over-all were getting damaged during scanning (which I think is showing as scratches in the NSMM signals, and salt-like noise in the STM image in Fig. C.12). Later on the CCTO project in our group evolved into studying bulk dielectric properties as a function of frequency, and hence we terminated the studies for local contrast on CCTO.

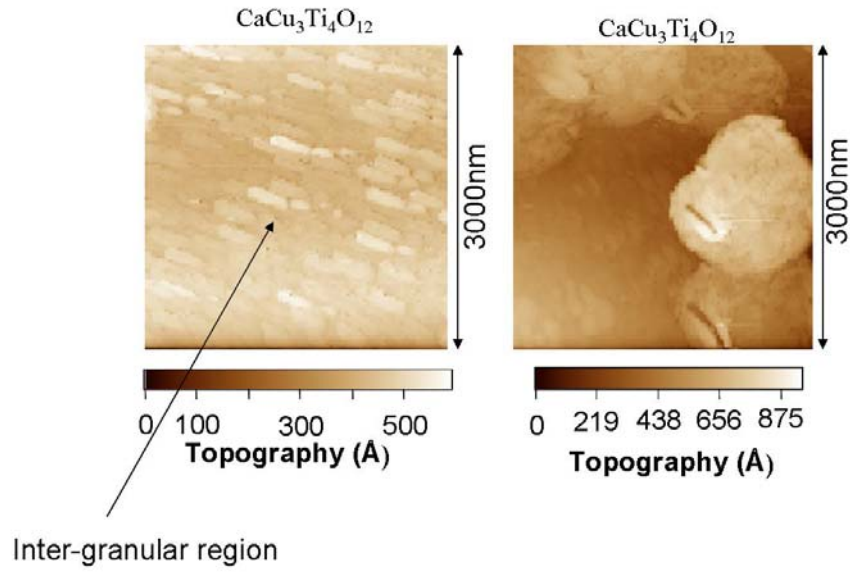


Fig. C.11: The STM of the granular region and the inter-granular region on top of the CaCu₃Ti₄O₁₂ (CCTO) thin film. This is just to show granular structure of the film.

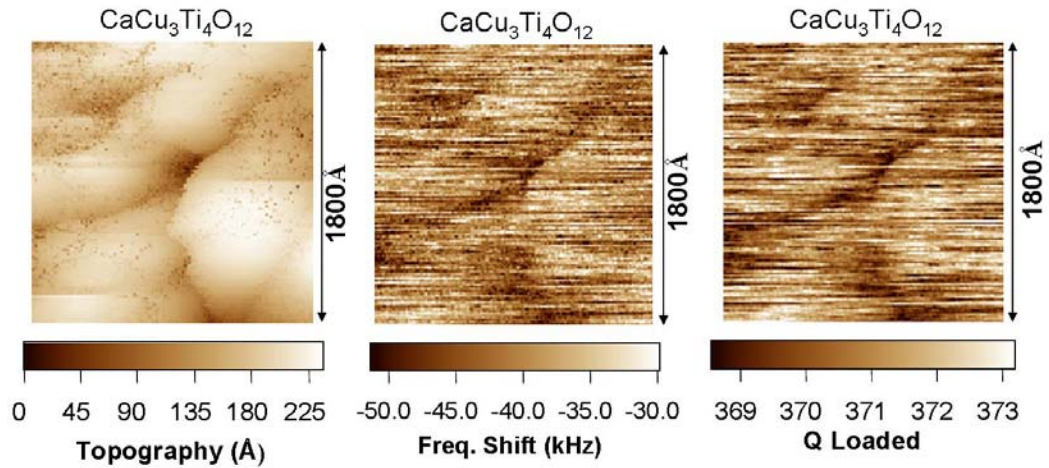


Fig. C.12: The simultaneous imaging on top of one of the grains. The Q and Δf data shows correlation with the topographic image. The tips were getting damaged during scanning.

C.5 Superconducting thin films samples

Superconductors provide a whole set of interesting experiments at microwave frequencies. At the time I started to build my experiment, there was quite an activity in superconductivity to understand the pairing symmetry¹⁰⁷ and to image vortices^{108,109} in high- T_c superconductors. This STM-assisted microscope provides a very good platform to study dynamics of vortices at microwave frequencies. It was also possible to distinguish between the coexisting semi-conducting and superconducting phases¹¹⁰. This motivated me to make an attempt for studying superconducting thin films.

The first goal here was to be able to see how the Q of the microscope behaves when a low microwave-loss superconducting thin film is measured. The two films which I studied were Molybdenum-Germanium (MoGe) with $T_c = 7$ K, and Niobium-Nitride (NbN) with $T_c = 15.84$ K. The room temperature images of the two films are shown in Fig. C.13 and Fig. C.14. The films are low loss even at room temperature, so the Q image (not shown in the figures) was just noise and the Δf image is just the capacitance image. At low temperatures the surface quality degraded due to immersion in flowing cryogens, as was discussed in chapter 2. As a result the low temperature experiments did not contain any valuable information about the samples. With the new cooling system in place, I think the problem of surface degradation can be overcome, and it may be good to perform experiments again on superconducting thin films.

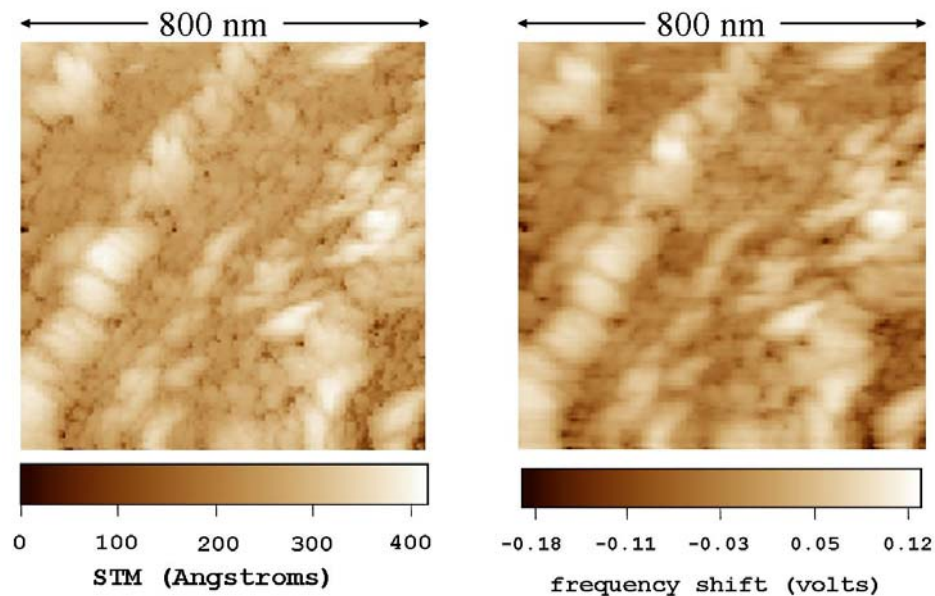


Fig. C.13: The room temperature STM and Δf images of an MoGe thin film. The images are 800 nm square and the frequency for the experiment is 8.24 GHz.

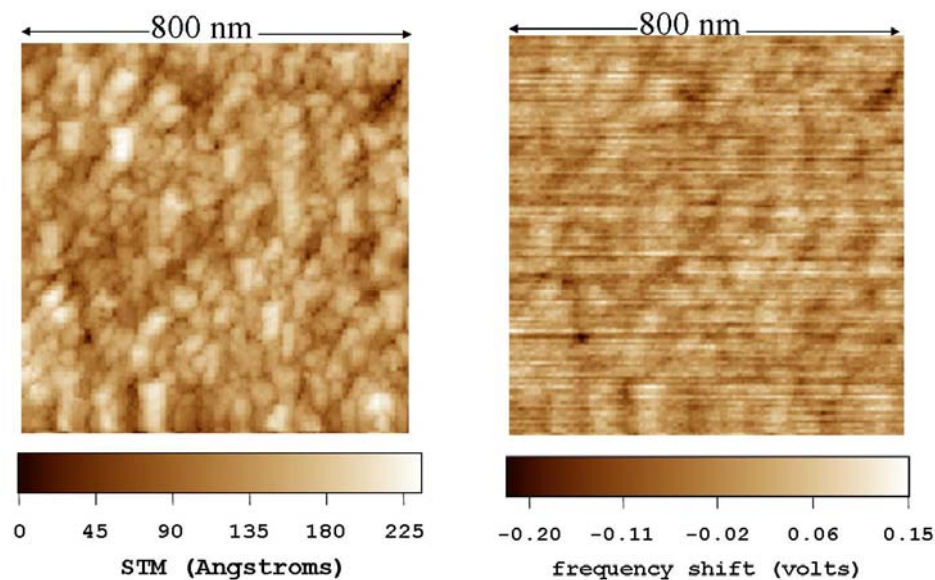


Fig. C.14: The room temperature STM and Δf images for a NbN thin film. The images are 800 nm square and the frequency for the experiment is 8.24 GHz.

Appendix D

Fourier Transform of Surface Magnetic Field

This appendix fills in some of the details in relation to the calculation of the Fourier Transform of the surface magnetic field in the sphere-above-the-plane model in section 3.3. In this calculation, I made use of references 61, 90 and 93 extensively. Fig. D.1 shows the coordinate system used during the calculation.

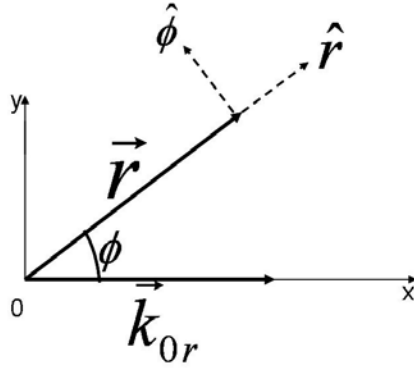


Fig. D.1: The coordinate system used for the calculation. The angle between \vec{k}_{0r} and \vec{r} is denoted by ϕ . The dashed vectors denote the unit vectors of the coordinate system. The unit vectors are shown at the end of vector \vec{r} .

Starting with equation (3.36) which I rewrite below,

$$\vec{H}_s(\vec{k}_{0r}) = \frac{1}{2} \int H_s(\vec{r}) \text{Exp}[i\vec{k}_{0r} \cdot \vec{r}] d^2r \quad (3.36)$$

where $H_s(\vec{r}) = H_s(r)\hat{\phi}$, $\vec{k}_{0r} \cdot \vec{r} = k_{0r}r \cos \phi$ and $d^2r = r dr d\phi$. Substituting these, I get,

$$H_s(\vec{k}_{0r}) = \frac{1}{2} \hat{\phi} \int_0^{2\pi} d\phi \left(\int_0^\infty dr H_s(r) r \text{Exp}[ik_{0r} r \cos \phi] \right) \quad (\text{D.1})$$

which using $\int_0^{2\pi} \text{Exp}[ik_{0r} r \cos \phi] d\phi = 2\pi J_0(k_{0r} r)$ ⁹³ simplifies to (J_0 denotes the Bessel function of zero order)^{61, 90}

$$H_s(\vec{k}_{0r}) = \hat{\phi} \pi \int_0^\infty r H_s(r) J_0(kr) dr \quad (\text{D.2})$$

Using equation (3.35) and the identities $\int_0^\infty J_0(bx) dx = \frac{1}{b}$ (if $n > -1$)⁶¹;

$\int_0^\infty \frac{J_0(x) dx}{\sqrt{x^2 + a^2}} = I_0\left(\frac{a}{2}\right) K_0\left(\frac{a}{2}\right)$ where I_0 and K_0 denote modified Bessel functions^{61, 90}.

$$\vec{H}_s(k_{0r}) = \hat{\phi} \left\{ \frac{-i\omega}{2} \sum_{n=1}^\infty q_n \left\{ \frac{1}{k_{0r}} - a_n R_0 I_0\left(\frac{k_{0r} a_n R_0}{2}\right) K_0\left(\frac{k_{0r} a_n R_0}{2}\right) \right\} \right\} \quad (\text{D.3})$$

and equation (D.3) is the same as equation (3.37).

In the limit of large k_{0r} , the $H_s(k_{0r})$ expands to (I used here the equation (9.7.5) of reference 90):

$$H_s(k_{0r} \rightarrow \infty) \sim \frac{1}{k_{0r}} - a_n R_0 \left[\frac{2}{2k_{0r} a_n R_0} + \frac{1}{2\left(2\frac{k_{0r} a_n R_0}{2}\right)^3} - \dots \right], \text{ which simplifies to}$$

$$\frac{1}{k_{0r}} - \frac{1}{k_{0r}} - \frac{1}{2(a_n R_0)^2 k_{0r}^3} - \dots, \quad (\text{D.4})$$

which to leading order goes as $\sim \frac{1}{k_{0r}^3}$.

In the limit of k_{0r} going to 0, the product term of modified Bessel functions in equation (D.3) show the logarithmic divergence term

$$H_s(k_{0r} \rightarrow 0) \sim \frac{1}{k_{0r}} + a_n R_0 \frac{\ln(k_{0r} a_n R_0 / 2)}{\Gamma(1)} \quad (D.5)$$

and (I used here the equations (9.6.7) and (9.6.8) of reference 90) in the limit of small k_{0r} , equation (D.3) diverges. These are the two limits that are referred to in the chapter 3.

GLOSSARY

A/D: Analog to Digital converter

AFM: Atomic Force Microscope

CMR: Colossal Magneto-resistive Materials

CNT: Carbon Nano-Tube

CryoSXM: Cryogenic Scanning X Microscope; general name for Oxford Instruments Microscopes

FFC: Frequency Following Circuit

FIB: Focus Ion Beam

FM: Frequency Modulation

HV: High Voltage Amplifiers

LDOS: Local Density of States

NSMM: Near-field Scanning Microwave Microscope

OVC: Outer Vacuum Chamber (the outer jacket of the cryostat)

PID: Proportional, Integrator and Derivative (in relation to feedback circuit of STM)

Q-loaded: The quality factor of resonator where losses due to coupling system are included besides the losses in the resonator

Q-unloaded: The quality factor of the resonator where losses only inside the resonator are included

SEM: Scanning Electron Microscope

STM: Scanning Tunneling Microscope

TOPS3: Particular name for the Cryogenic STM by Oxford Instruments

UHV: Ultra High Vacuum

VTI: Variable Temperature Insert (the space where the probe is inserted for low temperature experiments)

WRAPxxx: The commercial name for tips from Advanced Probing System where xxx stands for three digits assigned by the company

BIBLIOGRAPHY

- [1] S. M. Anlage, D. E. Steinhauer, B. J. Feenstra, C. P. Vlahacos and F. C. Wellstood, “*Near-Field Microwave Microscopy of Materials Properties*” in *Microwave Superconductivity*, edited by Harold Weinstock and Martin Nisenoff (Kluwer Academic Publishers, Boston) 2001, Chap. 10, p 239.
- [2] C. P. Vlahacos, R. C. Black, S. M. Anlage, A. Amar and F. C. Wellstood, “*Near-field scanning microwave microscope with 100 μ m resolution*”, *Appl. Phys. Lett.* **69**, p3272 (1996).
- [3] Constantine P. Vlahacos, “*A Near-Field Scanning Microwave Microscope*”, M.S. Thesis, Dept. of Physics, University of Maryland, College Park, Maryland, 1999.
- [4] Steven M. Anlage, C. P. Vlahacos, Sudeep Dutta and F. C. Wellstood, “*Scanning Microwave Microscopy of Active Superconducting Microwave Devices*”, *IEEE Trans. Appl. Supercond.* **7**, p3686 (1997).
- [5] D. E. Steinhauer, C. P. Vlahacos, S. K. Dutta, F. C. Wellstood and Steven. M. Anlage, “*Surface resistance imaging with a scanning near-field microwave microscope*”, *Appl. Phys. Lett.* **71**, p1736 (1997).
- [6] D. E. Steinhauer, C. P. Vlahacos, S. K. Dutta, B. J. Feenstra, F. C. Wellstood and Steven M. Anlage, “*Quantitative imaging of sheet resistance with a scanning near-field microwave microscope*”, *Appl. Phys. Lett.* **72**, p861 (1998).
- [7] C. P. Vlahacos, D. E. Steinhauer, S. K. Dutta, B. J. Feenstra, Steven M. Anlage and F. C. Wellstood, “*Quantitative topographic imaging using a near-field scanning microwave microscope*”, *Appl. Phys. Lett.* **72**, p1778 (1998).

- [8] Ashfaq S. Thanawalla, S. K. Dutta, C. P. Vlahacos, D. E. Steinhauer, B. J. Feenstra, Steven M. Anlage, F. C. Wellstood and Robert B. Hammond, “*Microwave near-field imaging of electric fields in a superconducting microstrip resonator*”, Appl. Phys. Lett. **73**, p2491 (1998).
- [9] Steven M. Anlage, D. E. Steinhauer, C. P. Vlahacos, B. J. Feenstra, A. S. Thanawalla, Wensheng Wu, Sudeep. K. Dutta and F. C. Wellstood, “*Superconducting Material Diagnostics using a Scanning Near-Field Microwave Microscope*”, IEEE. Trans. Appl. Supercond. **9**, p4127 (1999).
- [10] Wensheng Hu, A. S. Thanawalla, B. J. Feenstra, F. C. Wellstood and Steven M. Anlage, “*Imaging of microwave intermodulation fields in a superconducting microstrip resonator*”, Appl. Phys. Lett. **75**, p2824 (1999).
- [11] S. K. Dutta, C. P. Vlahacos, D. E. Steinhauer, A. S. Thanawalla, B. J. Feenstra, F. C. Wellstood, Steven M. Anlage and Harvey S. Newman, “*Imaging microwave electric fields using a near-field scanning microwave microscope*”, Appl. Phys. Lett. **74**, p156 (1999).
- [12] D. E. Steinhauer, C. P. Vlahacos, F. C. Wellstood, Steven M. Anlage, C. Canedy, R. Ramesh, A. Stanishevsky and J. Melngailis, “*Imaging of microwave permittivity, tunability, and damage recovery in (Ba, Sr)TiO₃ thin films*”, Appl. Phys. Lett. **75**, 3180 (1999).
- [13] D. E. Steinhauer, C. P. Vlahacos, F. C. Wellstood, S. M. Anlage, C. Canedy, R. Ramesh, A. Stanishevsky and J. Melngailis, “*Quantitative imaging of dielectric permittivity and tunability with a near-field scanning microwave microscope*”, Rev. Sci. Instrum. **71**, 2751 (2000).
- [14] Sheng-Chiang Lee, C. P. Vlahacos, B. J. Feenstra, Andrew Schwartz, D. E. Steinhauer, F. C. Wellstood and Steven M. Anlage, “*Magnetic permeability imaging of metals with a scanning near-field microwave microscope*”, Appl. Phys. Lett. **77**, p4404 (2000).
- [15] Vladimir V. Talanov, Robert Moreland, Andre Scherz, Andrew Schwartz and Youfan Liu, “*Scanning Near-Field Microwave Probe for In-line Metrology of Low-k Dielectrics*”, MRS Spring Meeting, Conference Proceedings (2004).

- [16] M. Tabib-Azar, R. Ciocan, G. Ponchak and S. R. LeClair, “*Transient thermography using evanescent microwave microscope*”, Rev. Sci. Instrum. **70**, p3387 (1999).
- [17] M. Tabib-Azar and D. Akinwande, “*Real-time imaging of semiconductor space-charge regions using high-spatial resolution evanescent microwave microscope*”, Rev. Sci. Instrum. **71**, p1460 (2000).
- [18] M. Tabib-Azar, P. S. Pathak, G. Ponchak, S. LeClair, “*Nondestructive superresolution imaging of defects and nonuniformities in metals, semiconductors, dielectrics, composites, and plants using evanescent microwaves*”, Rev. Sci. Instrum. **70**, p2783 (1999).
- [19] Y. G. Wang, M. E. Reeves, and F. J. Rachford, “*Simultaneous imaging of dielectric properties and topography in a $PbTiO_3$ crystal by near-field scanning microwave microscopy*”, Appl. Phys. Lett. **76**, p3295 (2000).
- [20] Y. G. Wang, M. E. Reeves, W. J. Kim, J.S. Horwitz and F. J. Rachford, “*Uniaxial dielectric anisotropy in $Ba_{0.5}Sr_{0.5}TiO_3$ films studied by evanescent-probe microscopy*”, Appl. Phys. Lett. **78**, p3872 (2001).
- [21] M. Abu-Teir, F. Sakran, M. Golosovsky, D. Davidov and A. Frenkel, “*Local contactless measurement of the ordinary and extraordinary Hall effect using near-field microwave microscopy*”, Appl. Phys. Lett. **80**, p1776 (2002).
- [22] H. Chang, C. Gao, I. Takeuchi, Y. Yoo, J. Wang, P. G. Schultz, X.-D. Xiang, R. P. Sharma, M. Downes and T. Venkatesan, “*Combinatorial synthesis and high throughput evaluation of ferroelectric/dielectric thin-film libraries for microwave applications*”, Appl. Phys. Lett. **72**, p2185 (1998).
- [23] H. Chang, I. Takeuchi and X. -D. Xiang, “*A low-loss composition region identified from a thin-film composition spread of $(Ba_{1-x-y}Sr_xCa_y)TiO_3$* ”, Appl. Phys. Lett. **74**, p1165 (1999).

- [24] S. Hyun, J. H. Cho, A. Kim, J. Kim, T. Kim and K. Char, “*Coexistence of metallic and insulating phases in epitaxial CaRuO_3 films observed by scanning microwave microscopy*”, Appl. Phys. Lett. **80**, p1574 (2002).
- [25] Hiroyuki Odagawa and Yasuo Cho, “*Measuring ferroelectric polarization component parallel to the surface by scanning nonlinear dielectric microscopy*”, Appl. Phys. Lett. **80**, p2159 (2002).
- [26] James C. Booth, “*Novel Measurements of the Frequency Dependent Microwave Surface Impedance of Cuprate Thin Film Superconductors*”, Ph.D thesis, Department of Physics, University of Maryland, College Park, Maryland (1996).
- [27] F. L. Pedrotti and L. S. Pedrotti, “*Introduction to Optics*” 2nd edition, Prentice Hall (1993).
- [28] J. W. Goodman, “*Introduction to Fourier Optics*”, McGraw Hill (1968).
- [29] W. A. Atia, “*Near Field Scanning Optical Microscopy: Theory, Design, and Application*”, Ph.D thesis, Department of Electrical Engineering, University of Maryland, College Park, Maryland, 1996.
- [30] Max Born and Emil Wolf, “*Principles of Optics: Electromagnetic Theory of Propagation, Interference and Diffraction of light*”, 6th edition, (Pergamon Press, 1980).
- [31] E. Betzig and J.K. Trautman, “*Near-Field Optics: Microscopy, Spectroscopy, and Surface Modification Beyond the Diffraction Limit*”, Science **267**, p189 (1992).
- [32] E. A. Ash and G. Nicholls “*Super-Resolution Aperture Scanning Microscope*”, Nature **237**, 510 (1972).

- [33] D. E. Steinhauer, “*Quantitative Imaging of Sheet Resistance, Permittivity, and Ferroelectric Critical Phenomena with a Near-Field Scanning Microwave Microscope*” Ph.D. thesis, Physics Department, University of Maryland, College Park, Maryland, 2000.
- [34] A. Kramer, F. Keilmann, B. Knoll and R. Guckenberger, “*The Coaxial Tip as a Nano-Antenna for Scanning Near-Field Microwave Transmission Microscopy*”, *Micron*, **27**, p413-417, (1996).
- [35] F. Keilmann, D. W. van der Weide, T. Eickelkamp, R. Merz and D. Stockle, “*Extreme sub-wavelength resolution with a scanning radio-frequency transmission microscope*”, *Optics Communications*, **129**, p15-18 (1996).
- [36] S. J. Stranick and P. S. Weiss, “*A versatile microwave-frequency-compatible scanning tunneling microscope*”, *Rev. Sci. Instrum.* **64**, p1232 (1993). There is Erratum to the paper published in *Rev. Sci. Instrum.* **64**, 2039 (1993).
- [37] S. J. Stranick, M. M. Kamna and P. S. Weiss, “*A low temperature, ultrahigh vacuum, microwave-frequency-compatible scanning tunneling microscope*”. *Rev. Sci Instrum.* **65**, p3211 (1994).
- [38] S. J. Stranick and P. S. Weiss, “*A tunable microwave frequency alternating current scanning tunneling microscope*”, *Rev. Sci. Instrum.* **65**, p918-921 (1994).
- [39] B. Knoll, F. Keilmann, A. Kramer and R. Guckenberger, “*Contrast of microwave near-field microscopy*”, *Appl. Phys. Lett.* **70**, p2667 (1997).
- [40] B. Michel, W. Mizutani, R. Schierle, A. Jarosch, W. Knop, H. Benedickter, W. Bachold and H. Rohrer, “*Scanning surface harmonic microscopy: scanning probe microscopy based on microwave field-induced harmonic generation*”, *Rev. Sci. Instrum.* **63**, 4080 (1992).
- [41] W. Mizutani, B. Michel, R. Schierle, H. Wolf and H. Rohrer, “*Scanning surface harmonic microscopy of self-assembled monolayers on gold*”, *Appl. Phys. Lett.* **63**, p147 (1993).

- [42] Greg P. Kochanski, “*Nonlinear Alternating-Current Tunneling Microscopy*”, Phys. Rev. Lett. **62**, 2285 (1989).
- [43] W. Seifert, E. Gerner, M. Stachel and K. Dransfeld, “*Scanning tunneling microscopy at microwave frequencies*”, Ultramicroscopy **42-44**, p379-387 (1992).
- [44] L. A. Bumm and P. S. Weiss, “*Small cavity nonresonant tunable microwave-frequency alternating current scanning tunneling microscope*”, Rev. Sci. Instrum. **66**, p4140 (1995).
- [45] W. Kreiger, T. Suzuki and M. Volcker, “*Generation of microwave radiation in the tunneling junction of a scanning tunneling microscope*”, Phys. Rev. B **41**, p10229 (1990).
- [46] M. Vokcker, W. Krieger, T. Suzuki and H. Walther, “*Laser-assisted scanning tunneling microscopy*”, J. Vac. Sci. Technol. B **9**, p541 (1991).
- [47] M. Volcker, W. Krieger and H. Walther, “*Laser-Driven Scanning Tunneling Microscope*”, Phys. Rev. Lett. **66**, 1717-1720 (1991).
- [48] M. Volcker, W. Krieger, and H. Walther, “*Detection of local conductivity by laser-frequency mixing in a scanning force microscope*”, J. Appl. Phys. **74**, p5426 (1993).
- [49] G. Nunes Jr. and M. R. Freeman, “*Picosecond Resolution in Scanning Tunneling Microscopy*”, Science **262**, 1029-1032 (1993).
- [50] G. Binning, H. Rohrer, Ch. Gerber, and E. Weibel, “*Surface studies by Scanning Tunneling Microscopy*”, Phys. Rev. Lett. **49**, p57 (1982).
- [51] J. Tersoff and N. D. Lang, “*Theory of Scanning Tunneling Microscopy*”, in Scanning Tunneling Microscopy, edited by Joseph A. Stroscio and William J. Kaiser, Academic Press (1993), chapter 1.

[52] Roland Wiesendanger, “*Scanning Probe Microscopy and Spectroscopy: Methods and Applications*”, Cambridge University Press (1994).

[53] J. Bardeen, “*Tunneling from a Many-Particle Point of View*”, Phys. Rev. Lett. **6**, p57 (1961).

[54] J. Tersoff and D. R. Hamann, “*Theory and Application for the Scanning Tunneling Microscope*”, Phys. Rev. Lett. **50**, p1998 (1983).

[55] S. M. Anlage, F. C. Wellstood, C. P. Vlahacos and D. E. Steinhauer. U.S Patent No. 5,900,618, issued May 4, 1999.

[56] Allan J. Melmed, “*The art and science and other aspects of making sharp tips*”, J. Vac. Sci. Technol. B **9** p601 (1991).

[57] A. J. Nam, A. Teren, T. A. Lusby and A. J. Melmed, “*Benign making of sharp tips for STM and FIM: Pt, Ir, Au, Pd, and Rh*”, J. Vac. Sci. Technol. **B** 13, p1556 (1995).

[58] The commercial company: *Advanced Probing Systems*; www.Advancedprobing.com

[59] The commercial company: *Custom Probes Unlimited*; www.customprobes.com.

[60] Clyde F. Coombs, Jr., “*Electronic Instrument Handbook*”, McGraw Hill, 2nd edition (1995).

[61] Murray R. Spiegel and John Liu, “*Mathematical Handbook of Formulas and Tables*”, 2nd edition, McGraw Hill (1999), p98.

[62] Chen Gao, Fred Duewer and X.-D.Xiang, “*Quantitative microwave evanescent microscopy*”, Appl. Phys. Lett. **75**, p3005-3007 (1999). There is Erratum to the paper published in Appl. Phys. Lett. **76**, p656 (2000).

[63] Xiao-Dong Xiang, Chen Gao, Peter. G. Schultz and Tao Wei, “*Scanning Evanescent Electro-Magnetic Microscope*” US patent# 6532806 B1, (2003).

[64] David M. Pozar, “*Microwave Engineering*”, 2nd edition, Wiley and Sons (1998)

[65] Samuel Y. Liao, “*Microwave Devices and Circuits*”, 3rd edition, Prentice-Hall (1990)

[66] E. Silva, M. Lanucara and R. Marcon, “*The effective surface resistance of superconductor/dielectric/metal structures*”, Supercond. Sci. Technol. **9**, p934 (1996).

[67] John Melngailis, “*Focus Ion Beam technology and applications*”, J. Vac. Sci. Technol. B **5**, p469 (1987).

[68] Private communication with Dr. Melngailis and John Barry of Institute for Research in Electronics and Applied Physics, University of Maryland, College Park, Maryland 20742.

[69] S. M. Sze, “*Physics of Semiconductor Devices*”, John Wiley and Sons (1969)

[70] Robert G. Wilson and George R. Brewer, “*Ion Beams with Applications to Ion Implantation*”, John Wiley and Sons (1973).

[71] T. Wu, S. B. Ogale, J. E. Garrison, B. Nagaraj, Amlan Biswas, Z. Chen, R. L. Greene, R. Ramesh, T. Venkatesan, and A. J. Millis “*Electroresistance and Electronic Phase Separation in Mixed-Valent Manganites*”, Phys. Rev. Lett. **86**, p5998 (2001).

- [72] M. Fath, S. Freisem, A. A. Menovsky, Y. Tomioka, J. Aarts and J. A. Mydosh, “*Spatially Inhomogeneous Metal-Insulator Transition in Doped Manganites*”, *Science* **285**, p1540 (1999).
- [73] Liuwan Zhang, Casey Israel, Amlan Biswas, R.L.Greene and Alex de Lozanne, “*Direct Observation of Percolation in a Manganite Thin Film*”, *Science* **298**, p805 (2002).
- [74] T. Becker, C. Streng, Y. Luo, V. Moshnyaga, B. Damaschke, N. Shannon and K. Samwer, “*Intrinsic Inhomogeneities in Manganite Thin Films Investigated with Scanning Tunneling Spectroscopy*”, *Phys. Rev. Lett.* **89**, p237203-1 (2002).
- [75] James C. Loudon, Neil D. Mathur and Paul A. Midgley, “*Charge-ordered ferromagnetic phase in $La_{0.5}Ca_{0.5}MnO_3$* ”, *Nature* **420**, p797 (2002).
- [76] Neil Mathur and Peter Littlewood, “*Mesoscopic Texture in Manganites*”, *Physics Today*, p25 (Jan. 2003).
- [77] V. Ravindranath, M. S. Ramachandra Rao, R. Suryanarayanan, G. Rangarajan, “*Evidence of electronic phase separation in Er^{3+} -doped $La_{0.8}Sr_{0.2}MnO_3$* ”, *Appl. Phys. Lett.* **82**, p2865 (2003).
- [78] Amlan Biswas, M. Rajeswari, R. C. Srivastava, Y. H. Li, T. Venkatesan, and R. L. Greene, “*Two-phase behavior in strained thin films of hole-doped manganites*”, *Phys. Rev. B* **61**, p9665 (2000).
- [79] Amlan Biswas, M. Rajeswari, R. C. Srivastava, T. Venkatesan, and R. L. Greene, “*Strain driven charge-ordered state in $La_{0.67}Ca_{0.33}MnO_3$* ”, *Phys. Rev. B* **63**, p184424 (2001).
- [80] K. A. Zaki, “*Measurements of the Equivalent Circuit Parameters of a Microwave Cavity Resonator*”, Lab write-up for ENEE 407, Dept. of Electrical Engineering, Univ. of Maryland, College Park.
- [81] Raymond S. Kwok and Ji-Fuh Liang, “*Characterization of High-Q Resonators for Microwave Filter Applications*”, *IEEE Trans. on MTT* **47**, p111 (1999).

- [82] N.D. Lang, “*Resistance of a one-atom contact in the scanning tunneling microscope*”, Phys. Rev. B **36**, p8173 (1987).
- [83] Neil W. Ashcroft and N. David Mermin, “*Solid State Physics*”, Saunders College Publishing (1976).
- [84] The commercial company: *Advanced Surface Microscopy, Inc.*; www.asmicro.com
- [85] M. Tabib-Azar, D.-P. Su, A Pohar, S. R. LeClair and G. Ponchak, “*0.4 μ m spatial resolution with 1GHz ($\lambda=30$ cm) evanescent microwave probe*”, Rev. Sci. Instrum. **70**, p1725 (1999).
- [86] T. Van Duzer and C. W. Turner, “*Principles of Superconductive Devices and Circuits*”, Elsevier North Holland, Inc. (1981).
- [87] Micro-Coax components, Inc. Box E, Collegeville, PA 19426; Ph: (215) 489 3700.
- [88] Simon Ramo, John R. Whinnery and Theodore van Duzer, “*Fields and Waves in Communication Electronics*”, 2nd edition, John Wiley & Sons (1984).
- [89] J. C. Booth, Dong Ho Wu, and Steven M. Anlage, “*A broadband method for the measurement of the surface impedance of thin films at microwave frequencies*”, Rev. Sci. Instrum. **65**, p2082 (1994).
- [90] M. Abramowitz and I. A. Stegun, “*Handbook of Mathematical Functions*”, Dover, (1972).
- [91] A. Imtiaz and S. M. Anlage, “*A novel STM-assisted microwave microscope with capacitance and loss imaging capability*”, Ultramicroscopy, **94** p209 (2003).
- [92] A. Imtiaz, M. Pollak, S. M. Anlage, J. D. Barry and J. Melngailis, “*Near-field microwave microscopy on nanometer length scale*”, Jour. of Appl. Phys., **97**, p044302 (2005).

- [93] *Mathematica* version 5; registered trademark of Wolfram Research.
- [94] Jin Au Kong, “*Electromagnetic Wave Theory*”, 2nd edition, John Wiley & Sons, Inc. (1990).
- [95] Ronold W. P. King, “*Electromagnetic field of a vertical dipole over an imperfectly conducting half-space*”, *Radio Science*, **25**, p 149 (1990)
- [96] Ronold W. P. King and Sheldon S. Sandler, “*The electromagnetic field of a vertical dipole in the presence of a three-layered region*”, *Radio Science*, **29**, p97 (1994).
- [97] R. E. Collin, “*Some Observations About the Near Zone Electric Field of a Hertzian Dipole Above a Lossy Earth*”, *IEEE. Trans. Antenn. and Propag.* **52**, p3133 (2004).
- [98] Ronold W. P. King, Margaret Owens and Tai Tsun Wu, “*Lateral Electromagnetic Waves*”, Springer-Verlag (1992).
- [99] Private communication with Dr. Mukovskii of Moscow Institute of Steel and Alloys, 117936 GSP-1, Leninskiy pr.4, Russian Federation.
- [100] Alexander Tselev, Charles M. Brooks, Steven M. Anlage, Haimei Zheng, Lourdes Salamanca-Riba, R. Ramesh and M. A. Subramanian, “*Evidence of power-law frequency dependence of intrinsic dielectric response in the $\text{CaCu}_3\text{Ti}_4\text{O}_{12}$* ”, arXiv:cond-mat/0308057 v4 5 Aug 2004
- [101] J. F. Mitchell, C. D. Ling, J. E. Millburn, D. N. Argyriou, A. Berger and M. Medarde, “*Magnetic phase diagram of layered manganites in the highly doped regime*”, *J. Appl. Phys.* **89**, p6618 (2001).
- [102] Private communication with Dr. Andrew Schwartz and Dr. Vladimir Talanov of Neocera, Inc., 10000 Virginia Manor Road, Beltsville, MD 20705, USA.

- [103] Alexander Tselev, Steven M. Anlage, Hans M. Christen, Robert L. Moreland, Vladimir V. Talanov and Andrew R. Schwartz, “*Near-field microwave microscope with improved sensitivity and spatial resolution*”, Rev. Sci. Instrum. **74**, p3167 (2003)
- [104] Steven M. Anlage, Vladimir Talanov and Andrew Schwartz, “*Principles of Near-Field Microwave Microscopy*”, to be published in “*Scanning Probe Microscopy: Electrical and Electromechanical Phenomena at the Nanoscale*” Springer-Verlag.
- [105] “*Handbook of Physics*”, Springer-Verlag (2000), edited by Walter Benenson, John W. Harris, Horst Stocker and Holger Lutz.
- [106] John D Jackson, “*Classical Electrodynamics*”, 3rd edition, (John Wiley & Sons, New York, 1999), Chapter 9, p408
- [107] in ‘Search and Discovery’ by Barbara Goss Levi, “*Learning about High- T_c Superconductors from Their Imperfections*”, Physics Today, p17 (March 2000).
- [108] Kathryn A. Moler, John R. Kirtley, D. G. Hinks, T. W. Li and Ming Xu, “*Images of Interlayer Josephson Vortices in $Tl_2Ba_2CuO_{6+\delta}$* ”, Science **279**, p1193 (1998).
- [109] C. W. Yuan, Z. Zheng, A. L. de Lozanne, M. Tortonese, D.A. Rudman and J. N. Eckstein, “*Vortex images in thin films of $YBa_2Cu_3O_{7-x}$ and $Bi_2Sr_2Ca_1Cu_2O_{8+x}$ obtained by low-temperature magnetic force microscopy*”, J. Vac. Sci. Technol. B **14**(2), p1210 (1996).
- [110] T. Cren, D. Roditchev, W. Sacks, J. Klein, J.-B. Moussy, C. Devile-Cavellin and M. Lagues, “*Influence of Disorder on the Local Density of States in High- T_c Superconducting Thin Films*”, Phys. Rev. Lett. **84**, p147 (2000).

Curriculum Vitae

Name: Atif Imtiaz

Permanent Address: 11420 Carroll Ave., Beltsville, MD 20705

Degree and date to be conferred: Ph.D., 2005

Title of Dissertation: Quantitative Materials Contrast at High Spatial Resolution With a Novel Near-Field Scanning Microwave Microscope.

Date of Birth: July 7th, 1975

Place of Birth: Karachi, Pakistan

Collegiate institutions attended

Institution	Dates attended	Degree	Date of Degree
State University of New York, Stony Brook	1994-1998	B.S., Physics	1998
University of Maryland	1998-2005	Ph.D., Physics	2005

Working Experience:

Research Assistant: Department of Physics, University of Maryland, College Park (1999 – Present).

Teaching Assistant: Department of Physics, University of Maryland, College Park (1998-1999).

Lab Assistant: Department of Physics, State University of New York, Stony Brook (1995-1997).

Professional Publications:

A. Imtiaz, M. Pollak, S. M. Anlage, J. D. Barry and J. Melngailis, “*Near-field microwave microscopy on nanometer length scale*”, Jour. of Appl. Phys., **97**, p044302 (2005).

A. Imtiaz and S. M. Anlage, “*A novel STM-assisted microwave microscope with capacitance and loss imaging capability*”, Ultramicroscopy, **94** p209 (2003).

Professional Presentations:

High Resolution Loss Imaging with Near-Field Scanning Microwave Microscope: -APS march meeting, Los Angeles, California, 2005

A Novel Scanning Near-Field Microwave Microscope with Loss Imaging Capability:
-APS march meeting, Montreal, Canada, 2004

Local contrast in $\text{La}_{0.67}\text{Ca}_{0.33}\text{MnO}_3$ thin film: evidence of phase segregation:
(Primary talk)-APS march meeting, Austin, Texas, 2003

Novel Scanning Near-Field Microwave Microscopes Capable of Imaging Semiconductors and Metals:- (Secondary talk)-APS march meeting, Austin, Texas, 2003

Evidence for phase segregation in $\text{La}_{0.67}\text{Ca}_{0.33}\text{MnO}_3$ thin CMR film:
-APS march meeting, Indianapolis, Indiana, March 2002

Near field Scanning Microwave Microscopy (NSMM) of Inhomogeneities in Oxide Materials:-APS march meeting, Seattle, Washington, March 2001